Fluidity Development of Coking Coal

Thesis submitted to the University of Nottingham for the Degree of
Doctor of Engineering
March 2022

George Thomas
Student ID: 14313956

Abstract

In most of the previous analytical studies on coking coal fluidity, single coal behaviour is well-documented but few studies have addressed coal blends regarding interactions in blends leading to possible non-additive behaviour. Many different techniques have been used to study single coals and blends, but of the two most promising are high temperature rheometry and ^{1}H NMR. However, there is little work reported to date on using these techniques to study coal blends and this is the primary focus of this investigation.

For rheometry, a novel cup geometry has been developed for its efficacy to complement the already established parallel plate (PP) geometry. A suite of 10 coals were studied and used throughout this project, initially to compare the PP and cup geometries. The PP suffered from sample loss, while the cup geometry displayed extended expansion due to the retaining walls and this can potentially provide a proxy for gas pressure. Complex viscosity profiles showed fair agreement between the two geometries for high fluidity coals and reasonable similarities for medium fluidity coals. One major benefit of the cup was found to be use of larger masses, compared to 1.5 g for the PP, with up to 3 g for medium and high fluidity coals, making it more favourable for investigating blends.

Using the cup geometry, a range of binary blends were studied and viscoelastic properties of the blends (minimum complex viscosity (η^*_{min}), complex viscosity (η^*) and tanδ) were compared with the development of gas pressure to quantify any interactions between coals, such as adsorption of fluid species on the remaining non-softening matrix. Significant deviations were found from additive behaviour for η^*_{min}, where both negative and positive interactions were found. Correlations with elastic modulus (G') and loss modulus (G") were used to rationalise that G' can provide information about interactions involving macromolecular changes and that G" can provide information about interactions involving mobile molecular entities. These were subsequently linked to the gas pressure, where it was found that volatile absorption was evident when blending non-coking coals with fluid exhibiting coals. Additionally, the use of the cup geometry has shown that blends exhibiting η^*_{min} of 2 – 3 x10^3 Pa s provide dangerous swelling. This was shown to be the limit of which sustained swelling occurred, or weak – semi cokes are formed due to volatile release from low η^* suspension formation.

High temperature ^{1}H NMR has been used to understand the mobile molecular behaviour of the 10 coals where %fluid hydrogen (H) and mobility of the fluid phase (T_{2L}) have been studied to quantify changes in such moieties. %Fluid H and T_{2L} at maximum %fluid H increased as a function of volatile matter content and bulk fluidity, apart from the high volatile coal 3 for the latter. %Fluid H exhibited similar generation profiles as a function temperature for all coals. For T_{2L}, non- and medium fluid coals exhibited maximum mobility at or below 400 ^{o}C, below that of maximum %fluid H, followed by a decay with increasing temperature, whilst high volatile coals exhibited maximum mobility close to maximum %fluid H. For blends, additive and non-additive behaviour was exhibited, where the coal with the highest mean vitrinite reflectance (MVR) and anomalous behaving coal 3 featured heavily in additive deviating blends with respect to %fluid H. For T_{2L}, fewer blends displayed additive behaviour, which was most prevalent for the majority of blends containing non-fluid coals. Consequently, it was evident that the apparent non-fluid coal 3 was distinct on possessing micro-fluidity detectable by ^{1}H NMR.

Limited correlations were found for single coals between rheometry and ^{1}H NMR, where G” and η* exhibited R^2 values of between 0.8 – 0.9 with the %fluid H. However, good correlations were found between G” (0.90 – 0.99) and η* (0.89 – 0.98) with %fluid H for medium fluidity coal blends. Consequently, viscous behaviour was predominantly dictated by mobile molecular entities, whereas elastic behaviour was dictated by bulk phenomena. Ultimately, NMR exhibited fewer deviations from additive behaviour compared with η^*_{min}.

Macroporosity and total porosity for the semi-cokes obtained exhibited good correlations with maximum plate gap ($R^2 > 0.9$), where the cup geometry could be used in future studies to predict porosity. This was due to good sample retention from the novel cup geometry. Regarding the microfluidity generated for coal 3, the semi-cokes had high microporosity, but low meso- and macroporosity, explaining why the fluid materials could not propagate through the bulk of the sample.

To my grandmother, Valerie, who inspired me to never stop learning

Acknowledgements

I would like to thank the following people, without whom this research would not have been possible:

- To the EPSRC and Tata Steel for funding this project and to the University of Nottingham for accepting me as a doctoral student.
- Supervisors at the University of Nottingham, Dr. Lee Stevens, Dr. Miguel Castro-Diaz and Prof. Colin Snape for all of their support and expert advice throughout this project.
- Industrial supervisors at Tata Steel, Bert Gols, Lucas Bleijendaal and Andre Oudhuis, for their industrial knowledge and expertise throughout this project, along with supplying the coals studied in this research.
- Dr. Lee Stevens for running and obtaining measurements from BET, MIP and strength testing.
- Umaru Musa for carbonising the coal pellets and performing ultimate elemental analysis.
- ETB technician, Adrian Quinn, for ensuring the smooth running of lab work
- My family who has supported and encouraged me through the past 4 years.
- My wonderful partner, Lily, who has been so patient and supported me over the course of this project.

Declaration

I declare that the research described in the following thesis was performed at the University of Nottingham, between October 2017 and December 2021, is my own work and has not been submitted for a degree at another institution.

Contents

List of Figures

List of Tables

Abbreviations:

BOF: Basic oxygen furnace

η^*: Complex viscosity

ddpm: Dial divisions per minute

EAF: Electric arc furnace

FID: Free induction decay

G”: Loss modulus

Tan(δ): Loss tangent

F_{Max}: Maximum fluidity

MVR: Mean vitrinite reflectance

η^*_{min}: Minimum complex viscosity

NMR: Nuclear magnetic resonance

PP: Parallel plate geometry

%Fluid H: Percentage of fluid hydrogen

δ: Phase angle

dL: Plate gap

PMRTA: Proton magnetic resonance thermal analysis

rf: radiofrequency

RSD: Relative standard deviation

SAOS: Small amplitude oscillatory shear

T_2: Spin-Spin relaxation time

T_{2G}: Spin-spin relaxation time of Gaussian of rigid phase

T_{2L}: Spin-spin relaxation time of Lorentzian or fluid phase

SD: Standard deviation

G’: Storage modulus

TMF: Temperature of maximum fluidity

T_{Resol}: Temperature of resolidification

T_{Soft}: Temperature of softening

Wt%: Weight percentage of coal addition

Chapter 1

Introduction

1.1. The Continuing Need for Coal in Iron and Steel Production

At the COP 26 summit in November 2021, all developed nations committed to the cessation of coal use in industry and energy generation (The Guardian, 2021). Although such commitments are vital for reduction of global temperatures, some industries are heavily reliant upon fossil fuels to produce valuable construction materials. As populations still increase and economies grow again post-COVID, there will be an ever-greater demand for such materials. With green and CCS technologies for such industries still in their infancy there is still significant need for fossil fuels.

The iron and steel industry is one such example, where the generation of raw iron still uses blast furnace technology, where transition to electric arc furnace (EAF) technology or carbon capture technologies (Global CCS Institute, 2017) such as the use of hydrogen (European Parliament, 2020), do not meet the production demand for this material (Liu et al, 2021). Therefore, it is predicted that the steel industry will be using coal for the foreseeable future unless policy implementation allows for significant subsidies or technology advances sufficient enough to allow the required product output to shift to greener alternatives (Financial Times, 2021). Green alternatives must be able to match this production rate to allow the industry to operate, and to enable the construction of buildings vital for everyday life. Although EAF furnaces are used on a large scale in the USA (70.6% of total steel production in 2020 (World Steel, 2021)), this requires sufficient quantities of recycled steel, which might not necessarily be in surplus (Singh, 2020). Therefore, the use of coal for iron and steel production will be the primary technology for years to come, where improvements of efficiency can reduce emissions (the IEA predicts that in 2030 68% of steel production will still be from blast furnace technology, (IEA, 2021)).

Coal is used for multiple purposes in the blast furnace, where two types are generally used to meet this demand. Low rank, sub-bituminous coal is used in the tuyeres to provide heat to the furnace to allow reduction reactions to take place (Bosenhofer et al, 2019). This coal is injected at the bottom of the furnace, where the hot gases can pass up through the layers of the furnace to feed the iron ore and coal with heat and an abundance of reducing gases (H_2 and CO) (Du, Chen & Lucas, 2010). High rank, bituminous coal is used at the top of the furnace for several reasons. This coal, also known as coking coal, acts as a reducing agent, a source of thermal energy, but most importantly as a permeable support to allow hot gases from the tuyeres to pass up through, but to also hold the heavy ferrous burden above (Diez, Alvarez & Barriocanal, 2002). This delicate balance between porosity and strength is vital for an efficient iron making process, where high quality coking coal is fundamental to this (Ghosh et al, 2018). Such coals develop fluidity at high temperature, along with volatile generation, which provides the final coke product with a porous structure (Geerdes, Chaigneau & Lingiardi, 2020).

As high quality, high rank coking coals have such unique properties, they are in low supply globally, with the majority being sourced from Australia (Alderman, 2013). The problems here then are multi-faceted. Due to the scarcity of these carbonaceous materials, prices are constantly increasing, giving rise to ever rising production costs of iron and steel (Kumar & Kumar, 2015). Additionally, with resources dwindling, there are worries that supply will not meet demand and insufficient coking coal would lead to halting of production. The third problem here is that, with the majority of coals being sourced from one nation, political tensions could lead to trade embargos and hence no access to high quality coking coals (Ozga-Blaschke, 2019). Conclusively the use of high-quality coking coals for the continuous operation of blast furnaces and production of iron is not feasible going forward. Due to the very high output of blast furnaces and conventional steel plants, transitioning to very new technologies such as direct reduction cannot be implemented in the near future (Ren et al, 2021). Therefore, lower quality coals with increased global supply and geographic variance are the logical way forwards in order for steel producers to remain productive and efficient (Tiwari, 2015).

The use of lower quality coals in the blast furnace is not a novel technique. Steel producers utilise lower rank coals in coal blends to increase the overall fluidity of the blend, along with reducing the cost of production (Saida et al, 2020). However, the addition rates of these coals are relatively low due to the unpredictable impact such samples have upon high rank coals. Consequently, the use of lower rank coals needs to be on a much larger scale to reduce the dependence upon high quality specimens. There are multiple differences between low rank and high rank coals, however an in-depth analysis into the geological and maceral differences is beyond the scope of this research. The use of low rank coals would be beneficial to coke making and iron making for multiple reasons, including the following. The abundance of low rank coals would reduce the dependence upon high rank coals from isolated geographical locations (Ryemshak & Jauro, 2013). Due to the lower quality of such samples, the overall cost of production would be optimised, which would be of particular importance going forward with increasing carbon taxes and post-COVID economic pressures (Das et al, 2018). There could also be a possibility to enhance the diversity of behaviours and characteristics of coke products (Tiwari et al, 2014). Researching such topics would additionally generate more information about the phenomena which these coals exhibit.

1.2. Importance of Fluidity

As mentioned above, the porosity of coke is fundamental to its quality and use in the blast furnace (Ghosh et al, 2018); pores too small and insufficient transmission of gas through the furnace is afforded. Pores too large and weak cokes are afforded, where the hot ferrous burden can fall through the furnace (Ghosh et al, 2018). This porosity is generated between 400 and 500 ^{o}C under inert atmosphere where the coal becomes fluid, and volatiles are generated. The generation of such gaseous species within the fluid matrix allows pores to form. The size and distribution of these is dependent upon the viscosity of the fluid material generated, which ultimately determines the strength of pore walls (Duffy et al, 2007). Hence, understanding the fluidity development of coking coals is fundamental to understanding the quality of the resultant coke. The development of porous structure and fluidity is expanded on further in chapter 2 (literature review).

As such, measuring fluidity of coking coals is a very good and valuable way in understanding the quality of the coke that will be produced (Kumar et al, 2008). Not enough fluidity, and insufficient porosity is afforded. Too fluid, and the coal forms pores that coalesce and reduce the strength of the coke (Castro-Diaz et al, 2015). Therefore, having a measure of the fluidity of the coal before complete carbonisation and utilisation in the coke oven and blast furnace can significantly optimise efficiency and coke quality, as opposed to performing large scale carbonisation tests in pilot scale ovens, which is energy intensive along with generating a significant amount of CO_2 (North et al, 2018). As such, the quality of low rank coals can be assessed using fluidity measurements, where only small samples are required, ultimately improving the efficiency of the steel making process (Mochizuki et al, 2017).

Industry standards are presently used to test the fluidity of coals, which is predominantly Gieseler plastometry (this is expanded upon in the literature review (chapter 2) and chapter 4) (Flores et al, 2020; Frage et al, 2020; Mochizuki, Naganuma & Tsubouchi, 2018; Yang et al, 2018). This technique provides a single value of maximum fluidity which can provide the coke maker with vital information about how the coal would behave on the industrial scale in relation to the resultant porosity (Rees & Pierron, 1955). However, due to previously stated problems with using high quality coals such as geographical isolation and price, steel producers use blends where multiple different coals are used (Yuan et al, 2020). This can help drive down cost, improve coke performance through variability in coal properties and reduce dependence upon one coal producer. However, the fluidity of blends of coals has always been an elusive topic due to the complexity of fluid phase of these carbonaceous materials where the resultant fluidity of the blend is not necessarily a summation of that of the individual single coals (Das et al, 2018; Zhang et al, 2021).

Studies have been performed upon the assessment of coking coal blend fluidity and the relationship with that of the single coals to identify links and causes to the deviations from expected behaviour (Das et al, 2018; Flores et al, 2020). The successful development of a model that could accurately predict blend fluidity would save many steel producers a significant amount of time and financial investment. There has always been a need for such a predictive model, and hence the continual research into coal science despite political pressure to move towards green technology.

In the late 1990s and early 2000s there was a significant amount of novel work into this field of coking coal blend fluidity due to the growth of the steel industry and the increasing scarcity of good coking coals. Significant progress was made in this period where the major molecular and chemical contributors to coal fluidity were identified, oscillatory shear rheometry was developed for the study of coals and links between fluid hydrogen and bulk fluidity were solidified (Castro Diaz et al, 2007; Castro Diaz et al, 2007; Castro Diaz et al, 2008; Duffy et al, 2007; Nomura et al, 1999; Steel et al, 2004). Despite political pressure, coking coal is still needed to make high quality steel, essential for construction and economic growth, and increasing the efficiency of the coke making and steel making process would significantly reduce the carbon footprint of this essential manufacturing process (Na et al, 2021; Zhang et al, 2021). Therefore, in order for the targets of the Paris agreement and COP 26 to be met (Garvey, Norman & Barrett, 2022; Griffin & Hammond, 2021; Ren et al, 2021), the use of coking coal in the steel industry must be made more efficient, and the best way to do this is to understand the interactions between coals during their fluid phase and develop accurate predictive models to reduce the need for large scale tests along with the use of lower rank, more geographically accessible coals.

As the majority of coking coal used in Europe for steel making is sourced from Australia (in 2020, Australia exported 63% of total exported coking coal globally (Euracoal, 2021)), the shipping of this raw material presents a big problem in relation to emissions (Chen et al, 2022; Matyjaszek et al, 2018). Nations such as Poland have vast resources of good coking coals which could be used in Europe as opposed to Australian derivatives (Duda & Fidalgo, 2021). The main issue here is the lack of understanding of how these coals would impact the coke quality, where implementing new coals could be very costly for a steel maker if production has to be halted due to low quality coke due to lack of understanding of fluid behaviour (Jiao et al, 2018; Matyjaszek et al, 2018; Salcedo et al, 2020; Suopajarvi et al, 2018). Therefore, this research project has been developed with consideration of the impacts of many different facets of the steel making process and how to optimise the coke making process to afford a more efficient industry.

1.3. Project Rationale

This project was developed to ultimately provide more structurally relevant data to possibly develop and feed into new models to predict coking coal blend behaviour using two very unique techniques; high temperature rheometry and high temperature ^{1}H NMR. Although there is a range of literature on the study of single coals with these techniques, and in some cases using both techniques, there has never been a comprehensive study using both techniques to study blends of coals (Castro Diaz et al, 2005; Castro Diaz et al, 2007; Castro Diaz et al, 2008; Castro Diaz et al, 2012; Castro-Diaz et al, 2015; Castro Diaz et al, 2016; Duffy et al, 2007; Duffy et al, 2007; Duffy et al, 2013; Duffy, Mahoney & Steel, 2010; Edecki et al, 2007; Kokonya et al 2013; Karen et al, 2017; Steel et al, 2006; Steel et al, 2014; Steel et al, 2017; Yoshida et al, 1999; Yoshida et al, 2002). It is believed here that a holistic approach to the study of blends using information of both micro- and macro-fluidity can provide vital information that could optimise the coke making process, along with expanding the knowledge base of coke science and hopefully develop accurate fluidity models.

To fully understand the complexity of coking coal fluidity, the range of data obtained should be expanded where only a single methodology for rheometry has been used hitherto (Castro Diaz et al, 2005; Castro Diaz et al, 2007; Castro Diaz et al, 2008; Castro Diaz et al, 2012; Castro-Diaz et al, 2015; Castro Diaz et al, 2016; Duffy et al, 2007; Duffy et al, 2007; Duffy et al, 2013; Duffy, Mahoney & Steel, 2010; Edecki et al, 2007; Kokonya et al 2013; Karen et al, 2017; Steel et al, 2006; Steel et al, 2014; Steel et al, 2017; Yoshida et al, 1999; Yoshida et al, 2002). Rheology provides very valuable information and is a very complex technique, therefore developing a new methodology could be very beneficial for coke making along with improving the knowledge base for coal scientists. This methodology development would subsequently enable a database of properties to be generated which could be used to compare the coals. This would allow for correlations to be made with previous techniques, including Gieseler plastometry, and understand what coking properties are important to focus on when considering blend fluidity. Additionally, only complex viscosity (which can be defined as a material's resistance to deformation and the flow of the material (Castro Diaz et al, 2015)), and in some cases tanδ (also known as the loss tangent, tanδ can be defined as a ratio between the viscous and elastic behaviour of a material. As tanδ exceeds 1, the material becomes more fluid-like, and more solid-like as tanδ decreases below 1 (Castro Diaz et al, 2012)), have been used in previous studies (Castro Diaz et al, 2005; Castro Diaz et al, 2007; Castro Diaz et al, 2008; Castro Diaz et al, 2012; Castro-Diaz et al, 2015; Castro Diaz et al, 2016; Duffy et al, 2007; Duffy et al, 2007; Duffy et al, 2013; Duffy, Mahoney & Steel, 2010; Edecki et al, 2007; Kokonya et al 2013; Karen et al, 2017; Steel et al, 2006; Steel et al, 2014; Steel et al, 2017; Yoshida et al, 1999; Yoshida et al, 2002), so the comparison of other viscoelastic parameters can be performed.

Armed with a database of viscoelastic information, along with a new methodology, the complexity of blend fluidity can be tackled. Information of the compositions within the blend can be compared and studied to understand trends within the blend, and subsequently with other blends. The new information of the single coals can also be used to map against the blends to test if these systems do obey linear regressions with respect to fluidity, or if there are deviations. The deviations, if present, can be studied in detail and theories developed as to the fluid behaviour. Correlations between the viscoelastic parameters can also be performed at the deviations where such relationships could aid in the development of theories and subsequent models.

Although there has been limited research upon the rheological study of coking coal blends, there have been no comprehensive studies using high temperature ^{1}H NMR, despite the value of the information provided by this technique (Castro Diaz et al, 2005; Castro Diaz et al, 2016; Maroto-Valer et al, 1998; Maroto-Valer, Andresen & Snape, 1997; Maroto-Valer, Andresen & Snape, 1997; Maroto-Valer, Andresen & Snape, 1998; Sakurovs, 2000; Snape & Martin, 2000). Due to the very small mass permissible in the ^{1}H NMR capsule, there will be no methodology development, which is unnecessary due to the lack of implementation of this technique for coal blends. Single coals will be studied to provide a base level of micro-fluidity and to build a database of micro-fluidity which can be used to test blends. Blends will then be tested where the development of micro-fluidity and its mobility can be understood as a function of temperature and compared against the single coals. Due to the lack of previous research in this field, detailed comparisons will be made between single coals and blends to understand if a logical linear relationship is found between fluidity and mobility with composition.

As hydrogen species have been shown to be major contributors to fluidity (Castro Diaz et al, 2016; Maroto-Valer et al, 1998; Maroto-Valer, Andresen & Snape, 1997; Maroto-Valer, Andresen & Snape, 1997; Maroto-Valer, Andresen & Snape, 1998; Sakurovs, 2000; Snape & Martin, 2000), the results from ^{1}H NMR can be mapped against rheological behaviour to understand if deviations from expected behaviour are due to intrinsic fluid matter generation or bulk phenomena. These relationships, along with inter-technique relationships, can be used to develop models which can hopefully more accurately predict blend fluidity. This will also be paired with porosity investigations, where relationships between porosity and fluidity have been identified before and could help in elucidating causes behind anomalous fluid behaviour (Duffy et al, 2007; Duffy et al, 2013; Steel et al, 2006; Steel et al, 2014; Karen et al, 2017).

1.4. Aim and Objectives

The literature reviewed in general in chapter 2, and in detail in chapters 4 – 6, identified only very limited use of rheology and ^{1}H NMR to study coal blends. Therefore, the project aim is:

- To expand the use, understanding and methodology of rheometry and ^{1}H NMR to single coals and binary blends in order to provide structurally relevant data for predictive models.

The specific objectives are:

1) To test a new cup geometry for high temperature rheometry which has never been used for coking coal fluidity analysis.
2) To use rheometry to examine coking coals with different parameters, such as complex viscosity, tan(δ) and plate gap to build a database of properties.
3) To test single coals using ^{1}H NMR to complement the rheological property database to provide structurally relevant data to test expected behaviour of blends.
4) To test binary blends using rheometry and ^{1}H NMR to understand their behaviour and the coal-coal interactions.
5) To map experimental blend data over predicted behaviour from the polymer blending rule to test linear behaviour.

1.5. Thesis Structure

As this research has developed new methodologies and studied novel systems (the use of ^{1}H NMR for the study of blends) there has been a significant amount of novel information generated. Therefore, the data chapters have been structured as research manuscripts to be published, along with a short, generalised literature review (chapter 2) to briefly describe the relevant coal science and basics of coal fluidity, along with previous findings in this field. In depth literature reviews have been provided within the data chapters (chapters 4 – 6) to give a clearer path through this research. Short discussions have also been provided within the data chapters (chapters 4 – 6), however in order to provide a holistic view of this research, the main discussion (chapter 7) compares the two techniques. Here, the comparison for both single coals and blends has been performed to fully appreciate the link between micro- and macro-fluidity. Porosity tests, being a confirmatory analysis of the findings, has been provided in the discussion chapter.

Due to the significant amount of data generated from this research, only pertinent graphs presenting experimental findings have been provided in the main text. Graphs linked to correlations and relationships between parameters have been provided in the appendices.

1.6. Rheological and ^{1}H NMR Parameter Definition

Due to the complex nature of high temperature rheometry and solid state ^{1}H NMR, the parameters associated with these techniques, and used throughout this thesis, will be defined here. Additive behaviour has also been defined due to its use throughout this research.

1.6.1. High Temperature Rheometry

Complex viscosity and tanδ have been described above on page 6, so do not require definition here. Sol point is defined as the temperature at which tanδ exceeds 1 (hence the material becomes more fluid-like at this temperature). Gel point is defined as the temperature at which tanδ reduces below 1 (hence the material becomes more solid-like at this temperature). Storage modulus (G') is a measure of the elastic response of a material and can provide information about the rigid, solid nature of the sample. Loss modulus (G") is a measure of the viscous response of a material and can provide information about the fluid nature of the sample (Barnes, Hutton & Walters, 1989).

1.6.2. High Temperature Solid State ^{1}H NMR

%Fluid hydrogen (%Fluid H) is a measure of the proportion of fluid phase in a sample. The spin-spin relaxation time of the fluid phase (T_{2L}) is a measure of the mobility of the fluid phase (as T_{2L} increases, the fluid phase become more mobile) (Steel et al, 2004).

1.6.3. Additive Behaviour

Additive behaviour occurs when the measured parameter of a blend (complex viscosity, %fluid H, etc.) is a weighted average of the measured parameter of the individual components (Duffy et al, 2010).

1.7. References

Alderman, J.K., 2013. Future industrial coal utilization: forecasts and emerging technological and regulatory issues. In *The Coal Handbook: Towards Cleaner Production* (pp. 85-101). Woodhead Publishing.

Barnes, H.A., Hutton, J.F. and Walters, K. 1989. *An introduction to rheology*, *Volume 3*. 1st Edition. Amsterdam: Elsevier.

Bösenhofer, M., Wartha, E.M., Jordan, C., Feilmayr, C., Stocker, H., Hauzenberger, F., Rieger, J., Tjaden, S., Walk, A. and Harasek, M. 2019. Suitability of pulverised coal testing facilities for blast furnace applications. *Ironmaking & Steelmaking*. ***47****(5)*, pp. 574 - 585

Castro Díaz, M., Duffy, J.J., Snape, C.E. and Steel, K.M. 2007. The shear-rate dependent viscoelastic properties of coal during carbonisation. *International Conference on Coal Science and Technology*. *28th – 31st August 2007*. Nottingham.

Castro Díaz, M., Duffy, J.J., Snape, C.E. and Steel, K.M. 2007. Use of high-temperature, high-torque rheometry to study the viscoelastic properties of coal during carbonization. *Journal of Rheology*. ***51***(5), pp.895-913.

Castro Díaz, M., Edecki, L., Steel, K.M., Patrick, J.W. and Snape, C.E. 2008. Determination of the effects caused by different polymers on coal fluidity during carbonization using high-temperature ^{1}H NMR and rheometry. *Energy & fuels*. ***22***(1), pp.471-479.

Castro Díaz, M., Steel, K.M., Drage, T.C., Patrick, J.W. and Snape, C.E. 2005. Determination of the effect of different additives in coking blends using a combination of in situ high-temperature ^{1}H NMR and rheometry. *Energy & fuels*. ***19***(6), pp.2423-2431.

Castro Díaz, M., Uguna, C.N., Cheeseman, B., Barker, J. and Snape, C.E. 2016. Investigation of the fluid behavior of asphaltenes and toluene insolubles by high-temperature proton nuclear magnetic resonance and rheometry and their application to visbreaking. E*nergy & Fuels*. **30***(*3), pp.2012-2020.

Castro Díaz, M., Zhao, H., Kokonya, S., Dufour, A. and Snape, C.E. 2012. The effect of biomass on fluidity development in coking blends using high-temperature SAOS rheometry. E*nergy & fuels*. ***26(***3), pp.1767-1775.

Castro-Díaz, M., Vega, M.F., Barriocanal, C. and Snape, C.E. 2015. Utilization of carbonaceous materials to restore the coking properties of weathered coals. *Energy & Fuels*. ***29***(9), pp.5744-5749.

Chen, W., Zhang, Q., Wang, C., Li, Z., Geng, Y., Hong, J. and Cheng, Y. 2022. Environmental sustainability challenges of China's steel production: Impact-oriented water, carbon and fossil energy footprints assessment. *Ecological Indicators*. ***136,*** p.108660.

Das, B., Suresh, A., Dash, P.S., Chandra, S., Diaz, M.C., Stevens, L.A. and Snape, C.E., 2018. Understanding the unusual fluidity characteristics of high ash Indian bituminous coals. *Fuel Processing Technology*. ***176,*** pp.258-266.

Dıez, M.A., Alvarez, R. and Barriocanal, C. 2002. Coal for metallurgical coke production: predictions of coke quality and future requirements for cokemaking. *International Journal of Coal Geology*. ***50***(1-4), pp.389-412.

Du, S.W., Chen, W.H. and Lucas, J.A. 2010. Pulverized coal burnout in blast furnace simulated by a drop tube furnace. *Energy*. ***35***(2), pp.576-581.

Duda, A. and Fidalgo Valverde, G. 2021. The Economics of Coking Coal Mining: A Fossil Fuel Still Needed for Steel Production. *Energies*. ***14***(22), p.7682.

Duffy, J.J., Díaz, M.C., Snake, C.E., Mahoney, M.R. and Steel, K.M. 2007, January. Combined use of rheometry and microscopy to understand pore structure development during coal carbonization. In: *International Conference on Coal Science and Technology. 28th – 31st August 2007*. Nottingham.

Duffy, J.J., Díaz, M.C., Snape, C.E., Steel, K.M. and Mahoney, M.R. 2007. Understanding the mechanisms behind coking pressure: Relationship to pore structure. *Fuel*. ***86***(14), pp.2167-2178.

Duffy, J.J., Mahoney, M.R. and Steel, K.M. 2010. Influence of coal thermoplastic properties on coking pressure generation: Part 2–A study of binary coal blends and specific additives. *Fuel*. ***89***(7), pp.1600-1615.

Duffy, J.J., Scholes, O., Mahoney, M.R. and Steel, K.M. 2013. Influence of thermoplastic properties on coking pressure generation: Part 3–Evidence and role of pore coalescence in the mechanism for pressure generation. *Fuel*. ***103***, pp.711-718.

Edecki, L., Diaz, M.C., Patrick, J.W. and Snape, C.E. 2007. Determination of the effects caused by different polymers on coal fluidity during carbonisation using high-temperature ^{1}H NMR and rheometry. In: *International Conference on Coal Science and Technology. 28th – 31st August 2007*. Nottingham.

Euracoal. 2021. EURACOAL Market Report 2021 no.1. [Online]. [Accessed: 03/03/22] Available at: https://euracoal.eu/library/coal-market-reports/

European Parliament. 2020. The potential of hydrogen for decarbonising steel production. [Online].]Accessed: 18/01/2022]. Available at https://www.europarl.europa.eu/RegData/etudes/BRIE/2020/641552/EPRS_BRI(2020)641552_EN.pdf

Financial Times. 20201. ‘Green Steel’: The race to clean up one of the world’s dirtiest industries. [Online]. [Accessed: 21/03/22]. https://www.ft.com/content/46d4727c-761d-43ee-8084-ee46edba491a

Flores, B., Agra, A., Gums, A., da Silva, G., Osório, E. and Vilela, A. 2020. Thermoplastic interaction of ultra-high fluidity Brazilian coal with components of blends. *Journal of Materials Research and Technology*. ***9***(3), pp.2737-2743.

Fraga, M., Flores, B., Osório, E. and Vilela, A. 2020. Evaluation of the thermoplastic behavior of charcoal, coal tar and coking coal blends. *Journal of Materials Research and Technology*. ***9***(3), pp.3406-3410.

Garvey, A., Norman, J.B. and Barrett, J. 2022. Technology and material efficiency scenarios for net zero emissions in the UK steel sector. *Journal of Cleaner Production*. ***333***, p.130216.

Geerdes, M., Chaigneau, R. and Lingiardi, O. 2020. *Modern Blast Furnace Ironmaking: An Introduction (2020)*. Ios Press.

Ghosh, B., Sahoo, B.K., Chakraborty, B., Manjhi, K.K., Das, S.K., Sahu, J.N. and Varma, A.K. 2018. Influence of coke structure on coke quality using image analysis method. *International Journal of Coal Science & Technology*. ***5***(4), pp.473-485.

Global CCS Institute. 2017. CCS: A necessary technology for decarbonising the steel sector. [Online]. [Accessed: 18/01/2022]. Available at: https://www.globalccsinstitute.com/news-media/insights/ccs-a-necessary-technology-for-decarbonising-the-steel-sector/

Griffin, P.W. and Hammond, G.P. 2021. The prospects for ‘green steel’making in a net-zero economy: A UK perspective. *Global Transitions*. ***3***, pp.72-86.

The Guardian. 2021. Cop26 ends in climate agreement despite India watering down coal resolution. [Online]. [Accessed: 18/01/2022]. Available at: https://www.theguardian.com/environment/2021/nov/13/cop26-countries-agree-to-accept-imperfect-climate-agreement#:~:text=Cop26%20ends%20in%20climate%20agreement%20despite%20India%20watering%20down%20coal%20resolution,-This%20article%20is&text=Countries%20have%20agreed%20a%20deal,in%20the%202015%20Paris%20agreement.

IEA. 2021. Iron and Steel Tracking Report. [Online]. [Accessed: 18/01/2022]. Available at: https://www.iea.org/reports/iron-and-steel

Jiao, H., Wang, M., Kong, J., Yan, D., Guo, J. and Chang, L. 2018. Contribution of single coal property to the changes of structure and reactivity of chars from blending coking. *Journal of analytical and applied pyrolysis*. ***134***, pp.114-121.

Karen, M., Robin, E., David, R. and Merrick, R. 2017. Use of rheometry and micro-CT analysis to understand pore structure development in coke. *Fuel Processing Technology*. ***155***, pp. 106-113

Kokonya, S., Castro-Díaz, M., Barriocanal, C. and Snape, C.E. 2013. An investigation into the effect of fast heating on fluidity development and coke quality for blends of coal and biomass. *Biomass and bioenergy*. ***56***, pp.295-306.

Kumar, D. and Kumar, D., 2015. *Management of coking coal resources*. Elsevier.

Kumar, P.P., Barman, S.C., Singh, S. and Ranjan, M. 2008. Influence of coal fluidity on coal blend and coke quality. *Ironmaking & Steelmaking*. ***35***(6), pp.416-420.

Liu, W., Zuo, H., Wang, J., Xue, Q., Ren, B. and Yang, F. 2021. The production and application of hydrogen in steel industry. *International Journal of Hydrogen Energy*. ***46***(17), pp.10548-10569.

Maroto-Valer, M.M., Andrésen, J.M. and Snape, C.E. 1997. In-situ 1H NMR investigation of particle size, mild oxidation, and heating regime effects on plasticity development during coal carbonization. *Energy & fuels*. ***11***(1), pp.236-244.

Maroto-Valer, M.M., Andrésen, J.M. and Snape, C.E. 1997. Quantification by in situ ^{1}H NMR of the contributions from pyridine-extractables and metaplast to the generation of coal plasticity. *Fuel*. ***76***(13), pp.1301-1308.

Maroto-Valer, M.M., Andrésen, J.M. and Snape, C.E. 1998. In situ ^{1}H NMR study of the fluidity enhancement for a bituminous coal by coal tar pitch and a hydrogen-donor liquefaction residue. *Fuel*. ***77***(9-10), pp.921-926.

Maroto-Valer, M.M., Taulbee, D.N., Andrésen, J.M., Hower, J.C. and Snape, C.E. 1998. The role of semifusinite in plasticity development for a coking coal. *Energy & fuels*. ***12***(5), pp.1040-1046.

Matyjaszek, M., Wodarski, K., Krzemień, A., García-Miranda, C.E. and Sánchez, A.S. 2018. Coking coal mining investment: Boosting European Union's raw materials initiative. *Resources Policy*. ***57***, pp.88-97.

Mochizuki, Y., Naganuma, R. and Tsubouchi, N. 2018. Influence of inherently present oxygen-functional groups on coal fluidity and coke strength. *Energy & Fuels*. ***32***(2), pp.1657-1664.

Mochizuki, Y., Naganuma, R., Uebo, K. and Tsubouchi, N. 2017. Some factors influencing the fluidity of coal blends: Particle size, blend ratio and inherent oxygen species. *Fuel Processing Technology*. ***159***, pp.67-75.

Na, H., Sun, J., Qiu, Z., He, J., Yuan, Y., Yan, T. and Du, T. 2021. A novel evaluation method for energy efficiency of process industry—A case study of typical iron and steel manufacturing process. *Energy*. ***233***, p.121081.

Nomura, S., Kato, K., Komaki, I., Fujioka, Y., Saito, K. and Yamaoka, I. 1999. Viscoelastic properties of coal in the thermoplastic phase. *Fuel*. ***78***(13), pp.1583-1589.

North, L., Blackmore, K., Nesbitt, K. and Mahoney, M.R. 2018. Models of coke quality prediction and the relationships to input variables: a review. *Fuel*. ***219***, pp.446-466.

Ozga-Blaschke, U. 2019. Change in the status of coking coal on the EU list of critical raw materials (2017). *Polityka Energetyczna*, ***22(3).*** Pp. 71-82.

Rees, O.W. and Pierron, E.D. 1955. *Effect of diluents on the plastic properties of coal as measured by the Gieseler plastometer. Circular no. 197.* Urbana, Illinois: Illinois State Geological Survey.

Ren, M., Lu, P., Liu, X., Hossain, M.S., Fang, Y., Hanaoka, T., O'Gallachoir, B., Glynn, J. and Dai, H. 2021. Decarbonizing China’s iron and steel industry from the supply and demand sides for carbon neutrality. *Applied Energy*. ***298***, p.117209.

Ryemshak, S.A. and Jauro, A. 2013. Proximate analysis, rheological properties and technological applications of some Nigerian coals. *International Journal of Industrial Chemistry*. ***4***(1), pp.1-7.

Saida, S., Chakravaty, S., Sahu, R., Das Biswas, R. and Chakravarty, K. 2020. Laboratory-Scale Tests for the Utilization of High Ash Non-Coking coal in Coke-Making Process. *Transactions of the Indian institute of metals*. ***73***(5), pp.1257-1263.

Sakurovs, R. 2000. Some factors controlling the thermoplastic behaviour of coals. *Fuel*. ***79***(3-4), pp.379-389.

Salcedo, E.R., Sánchez, S.M., Merchán, W.N., Cabrejo, O.G., Bermúdez, M.A. and Neita, J.S.G. 2020. A Predictive Model for the Anisotropy Index of Semi-Coke Derived from the Properties of Colombia's Eastern Cordillera Coals. *Ingeniería y ciencia*. ***16***(32), pp.109-134.

Singh, R., 2020. *Applied welding engineering: processes, codes, and standards*. Butterworth-Heinemann.

Snape, C.E. and Martin, S.C. 2000, March. Quantifying fluidity development and mobility in coals by in situ ^{1}H NMR. In *Prepr. Symp. Am. Chem. Soc. Div. Fuel Chem*. ***45***(2), pp. 205-210).

Steel, K.M., Dawson, R.E., Jenkins, D.R., Pearce, R. and Mahoney, M.R. 2017. Use of rheometry and micro-CT analysis to understand pore structure development in coke. *Fuel Processing Technology*. ***155***, pp.106-113.

Steel, K.M., Diaz, M.C., Duffy, J.J., Snape, C.E. and Mahoney, M.R. 2014. Influence of thermoplastic properties on coking pressure generation: Part IV–Further evidence of the role of bubble coalescence in the mechanism for pressure generation. *Fuel*. ***129***, pp.102-110.

Steel, K.M., Diaz, M.C., Patrick, J.W. and Snape, C.E. 2004. Use of rheometry and ^{1}H NMR spectroscopy for understanding the mechanisms behind the generation of coking pressure. *Energy & fuels*. ***18***(5), pp.1250-1256.

Steel, K.M., Diaz, M.C., Patrick, J.W. and Snape, C.E. 2006. Evidence for network formation during the carbonization of coal from the combination of rheometry and ^{1}H NMR techniques. *Fuel*. ***85***(12-13), pp.1821-1830.

Suopajärvi, H., Umeki, K., Mousa, E., Hedayati, A., Romar, H., Kemppainen, A., Wang, C., Phounglamcheik, A., Tuomikoski, S., Norberg, N. and Andefors, A. 2018. Use of biomass in integrated steelmaking–Status quo, future needs and comparison to other low-CO2 steel production technologies. *Applied Energy*. ***213***, pp.384-407.

Tiwari, H.P., Banerjee, P.K., Saxena, V.K., Sharma, R., Haldar, S.K. and Verma, S. 2014. Efficient way to use of non-coking coals in non-recovery coke making process. *Metallurgical Research & Technology*. ***111***(4), pp.211-220.

Tiwari, H.P., Sharma, R., Haldar, S.K., Verma, S., Paul, S. and Das, P.S. 2015. An approach to maximize the use of non-coking coal in non-recovery coke making. *Coke and Chemistry*. ***58***(2), pp.58-63.

World Steel. 2021. World Steel in Figures 2021. [Online]. [Accessed: 14/01/2022]. Available at: https://www.worldsteel.org/en/dam/jcr:976723ed-74b3-47b4-92f6-81b6a452b86e/World%2520Steel%2520in%2520Figures%25202021.pdf

Yang, G., Shi, T., Zhang, Q., Cao, Y., Zhang, W., Wu, X., Li, J. and Yang, J. 2018. An index of fluidity-temperature area for evaluating cohesiveness of coking coal by Gieseler fluidity characterization. *Fuel Processing Technology*. ***177***, pp.1-5.

Yoshida, T., Iino, M., Takanohashi, T. and Katoh, K. 1999. Study on thermoplasticity of Coking Coals from Solvent Extraction and Viscoelasticity Measurements. *International Journal of the Society of Materials Engineering for Resources*. ***7***(2), pp.301-311.

Yoshida, T., Takanohashi, T., Iino, M. and Katoh, K. 2002. Temperature-variable dynamic viscoelastic measurements for coal blends of coking coal with slightly coking coal. *Fuel processing technology*. ***77***, pp.275-283.

Yuan, Y., Qu, Q., Chen, L. and Wu, M. 2020. Modeling and optimization of coal blending and coking costs using coal petrography. *Information Sciences*. ***522***, pp.49-68.

Zhang, L., Wang, G., Xue, Q., Zuo, H., She, X. and Wang, J. 2021. Effect of preheating on coking coal and metallurgical coke properties: A review. *Fuel Processing Technology*. ***221***, p.106942.

Zhang, X., Jiao, K., Zhang, J. and Guo, Z. 2021. A review on low carbon emissions projects of steel industry in the World. *Journal of Cleaner Production*. ***306***, p.127259.

Zhou, S., Peng, T. and Ou, X. 2021. A review of CO2 emissions reduction technologies and low-carbon development in the iron and steel industry focusing on China. *Renewable and Sustainable Energy Reviews*. ***143***, p.110846.

Chapter 2

Literature Review

2.1. Introduction

At the beginning of this PhD project, the steel industry was one of the largest manufacturing industries in the world at a net worth of $900 billion (Angel, 2018), equating to 1.6 billion tonnes in 2017. Despite the impacts of COVID-19 upon construction projects and economic growth along with political pressure to cut coal use, steel production has increased to almost 1.9 billion tonnes in 2020 (World Steel, 2021). Hence, the consumption of raw materials is at an all-time high, with 73% of steel production coming from primary raw material conversion in 2021 (World Steel, 2021), such as the *Basic Oxygen Furnace (BOF:* a process which describes the production of iron from its ore, rather than just a blast furnace) *(World Coal Association, 2018)*, showing that steel production from the electric arc furnace, and other such techniques, are going to be very minor producers in comparison in the near future *(*this has been emphasized by the insignificant reduction in use of oxygen furnace techniques to 74% in 2017 (World Coal Association, 2018)). Coking coal is one of the said raw materials, but it is unique as it behaves differently to coal used for power generation. Due to such unique behaviour, this raw material is not in abundance, and a very small percentage of this is known to be good coking coal. Therefore, steel companies endeavour to utilise all grades of coal to produce a blend which has a range of properties but is also economically beneficial.

Numerous publications are released each year on coking coal science, many of which attempt to rationalise the chemistry behind fluid entities. The major factors influencing fluidity have been clarified well, but only on singular coals, which is a far stretch from accomplishing this for blends. Due to the complex nature of coal-coal interaction in blends, authors have yet to rationalise the non-additive behaviour of binary coal blends. Many different techniques have been used to study blends, but the two most promising are high temperature ^{1}H NMR (also known as *proton magnetic resonance thermal analysis (PMRTA))*, and rheometry; these techniques can elucidate valuable physical information. However, there is little work being performed using these techniques, which beggars the question; why are blends not studied using said analytical tools? Due to the complexity of these techniques, detailed literature reviews have been provided in the dedicated data chapters 4 – 6. This general literature review focuses on the basics of coking coal and factors which influence its fluidity.

2.2. What is Coking Coal?

Understanding the techniques to study coking coal is very useful, but one must have a good knowledge of the material they are examining before delving too deep. Unlike coal used in power plants to generate electricity, coking coal has unique properties that make it very useful in the manufacture of iron and steel. These properties include acting as a reducing agent, allowing the reduction of iron ore to iron to take place; it also acts as a heat source, providing heat to the reaction; and the coking coal provides a permeable support, allowing hot, reducing gases to pass up through into the furnace as well as supporting the hot metal burden (Diez, Alvarez & Barriocanal, 2002). Although the first two roles can be replaced by other fossil fuels and carbon-based derivatives, the latter has only been known to be akin to coke, hence coking coal is likely to be used for many years to come in steel production. Demand for this material is at an all-time high with steel production at the greatest it has ever been, which is highlighted in Figure 2.1 below which shows the consumption of crude steel, which is proportional to that of coking coal (World Steel, 2017; World Steel, 2018; World Steel, 2021). The production of crude steel in 2020 shows that coking coal demand is at an all-time high and shows little sign of slowing from the upward trend shown in Figure 2.1. Demand is dictated by unique properties which cannot be replicated by the use of other materials, although this has been researched extensively (Trinkel et al, 2015; Mollah et al, 2015; Wei et al, 2017). Other research has focused on the blending of coking coal with additives such as plastics (Melendi-Espina et al, 2015), binders (coal tar and pitch) (Nomura & Arima, 2017) and other coal extracts (Chang et al, 2014) but has yet to prove fruitful in comparison.

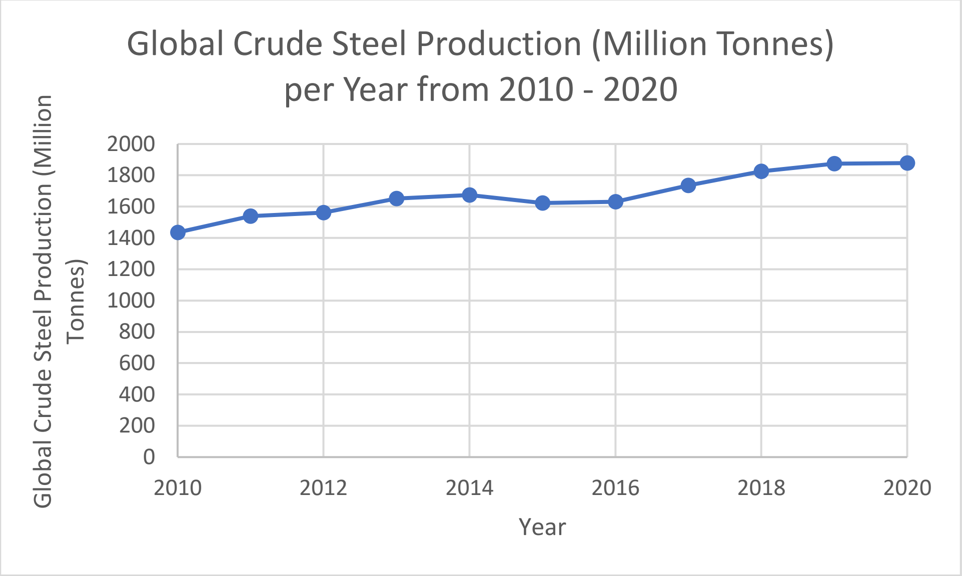

Figure 2.1: Global crude steel production in million tonnes from 2010 to 2020 (World Steel, 2021)

As stated above, coke acts as a permeable support within the blast furnace, but this can only be achieved using ‘good’ coking coals. Although this is quite a broad specification, good coking coals have specific properties. In order for the permeable support to be made, pores need to be formed within the structure of the coking coal; this is performed by a series of thermoplastic events as the coal is heated, or carbonised. These processes are associated with the fluidity of the coal which has been studied intensely for years, but there has still yet to be clear rationale for the causes of the fluidity development (Jenkins & Mahoney, 2015). This is made even more trialling due to the blending of coking coals in industry in order to achieve a bulk coal system which has the ideal characteristics needed to make high quality steel (Jenkins & Mahoney, 2015). Blending also has the benefit of reducing the reliance upon a few sources of coal, and the incorporation of lesser coking coals, reducing the price of the operation. Hence, there are many different methods to measure the different parameters of fluidity development in coking coal, such as Gieseler plastometry (Guelton, 2017), thermal gravimetric analysis (TGA) (Flores et al, 2017), dilatometry (Nomura, 2018), rheometry (Castro-Diaz et al, 2012) and high temperature ^{1}H NMR (Xie et al, 2015), among many others. Of these technologies, ^{1}H NMR and rheometry are the most useful in studying the fluidity of coking coal, due to the information that is ascertained, and the possibility of studying blends, rather than just single coals.

2.3. Use in Coke Ovens and the Blast Furnace

Coking coal is used in the blast furnace, typically in the *BOF (Geerdes, Chaigneau & Kurunov, 2015)*, to produce iron which can then be treated to make steel (Bodsworth, 1963). Unlike a research lab where very small masses of coking coal are used in rheometers and plastometers, industry heats the coking coal in large ovens known as *coke ovens (ThyssenKrupp, 2018)*. Such industrial ovens are capable of carbonising large amounts of coal at a time, where they are arranged in rows of up to 70 in one coke oven battery. Each oven has typical dimensions of 15 to 20 m in length, 7 to 9 m in height, 0.4 to 0.6 m in width, and typical wall thickness of 0.1 m (Yang, Raipala & Holappa, 2014). In this set up, large amounts of coal are heated to produce the vital, porous material known as coke, which is then quenched to maintain the structure of the material. There are different types of coke oven, but this is beyond the scope of this review, however Figures 2.2 and 2.3 below shows a typical coke oven set up (Tata Steel, 2011).

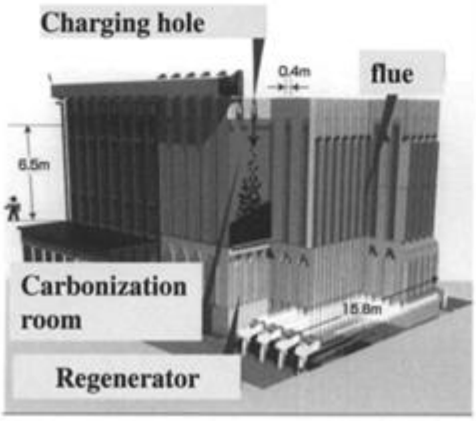

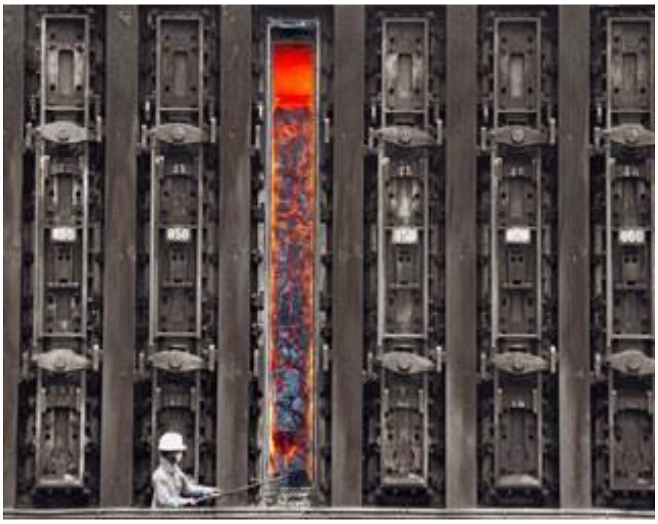

Figure 2.2 (left): Open Coke Oven (Tata Steel, 2011); Figure 2.3 (right): Typical Coke Oven Set Up (Kasai & Tsutsui, 2008)

Once the coke has been quenched, it is then moved to the blast furnace, where it is inserted through the top of the furnace, along with iron ore and limestone (Geerdes, Chaigneau & Kurunov, 2015). The coke and iron ore are layered around the edge of the furnace to provide good surface contact between the materials when they eventually meet the cohesive zone (Geerdes, Chaigneau & Kurunov, 2015). In the cohesive zone, the intense temperatures begin to degrade the coke, which produces carbon monoxide (CO) which then reacts with the iron ore at high temperatures to initiate reduction reactions (Geerdes, Chaigneau & Kurunov, 2015). As the partially reduced iron ore starts to drip down from the cohesive zone to the bed of coke, large amounts of reductive gases pass up through, aiding the final reduction of the iron ore, where the carbon content of the iron starts to increase from reaction with coke (Geerdes, Chaigneau & Kurunov, 2015). Hot metal can then pass down through the porous structure of the coke and into the deadman zone, which is called such due to the little effect this domain has on the whole process (Geerdes, Chaigneau & Kurunov, 2015).

The raceway is the zone just in front of the tuyeres where hot blast is blown into the furnace, providing oxygen into the system, as well as blowing soot and dust into the furnace, which then encompasses some of the small coke particles. Coke and coal fines can accumulate behind the raceway, forming a bird’s nest, which is an impermeable zone of coke; therefore, fines can cause a severe problem for blast furnace operation (Geerdes, Chaigneau & Kurunov, 2015). However, as the coke is blown through and away from the raceway, there is a stagnant zone in the centre of the furnace, and molten iron accumulates in this zone until it is removed from the furnace via the tap holes (Geerdes, Chaigneau & Kurunov, 2015) (see Figure A1 in Appendix A). Conclusively, it can be noted that the role of coke within the blast furnace is imperative, and the process to produce it must be understood in order to produce high quality metallurgical materials (Bodsworth, 1963; ThyssenKrupp, 2018).

2.4. Basics of Coal Fluidity

It is well known that coking coal has thermoplastic properties, giving rise to its fluid behaviour, and thus the porous structure of the coke used in the blast furnace (Meng et al, 2017). The porous structure is vital for the coke’s use in the blast furnace, but it must also have integral strength to support the burden (Saito et al, 2018). Not only this, but such viscoelastic behaviour is also key to obtaining information about the quality of the coal itself. However, to understand such behaviour, we need to know the physical changes that occur at the molecular level, as well as the macromolecular changes. Although those of the macromolecular form can be monitored easily with devices such as Gieseler plastometers and dilatometers, the molecular changes are far more difficult to obtain. Techniques such as TGA can provide information about the nature of the volatiles given off during the carbonisation process (Suopajarvi et al, 2017), particularly when coupled with mass spectrometry as the composition of such volatiles can also be determined. However, such techniques can only provide simple information about the volatile products, but little information about the reactivity of such volatiles. High temperature ^{1}H NMR can study the fixed and mobile hydrogen within a coal sample, and hence can provide very insightful information about the physical changes that occur during coking coal carbonization (Castro Diaz et al, 2007).

Using the techniques described above, the fluid events occurring in coking coal as it's heated can be observed and measured. These include softening, maximum fluidity (F_{Max}) and resolidification (Zubkova, Strojwas & Jozwiak, 2017). There are standard procedures to measure such events, which have been used extensively in industry by steel manufacturers to grasp the quality of the coking coal. Such procedures include plastometry, which measures the resistance of a material to rotation, either from variable torque or fixed. In industry, Gieseler plastometers are used to measure such resistance, which gives a measure of fluidity as the coal is heated. Standard experimental parameters are usually a heating rate of 3 ^{o}Cmin^{-1} once at 300 ^{o}C and a torque of 10^{-5} Nm. Using such a technique, the maximum fluidity can be determined where the stirrer increases speed as the coal softens, and slows as the coal resolidifies, with maximum speed at maximum fluidity (Loison, Foch & Boyer, 1989).

For analysis such as rheometry and Gieseler plastometry, the important variables are fluidity (viscosity) and temperature. These are best observed on a plot of complex viscosity or Gieseler fluidity vs. temperature, like that shown in Figure A2 in Appendix A (the former is obtained from oscillatory rheometry). In this plot it can be observed that as the coal is heated initially, there is a decrease in viscosity, or increase in fluidity in the case for Gieseler plastometry. This is attributable to the initial generation of volatile species within the coal (Vega et al, 2017), comprising mostly of light hydrocarbons (Zhou et al, 2017). As the temperature reaches 400-430 ^{o}C, the viscosity starts to significantly drop to maximum fluidity; this is due to many reasons, such as the transfer of hydrogen radicals (Sakurovs, 2003), the number of volatiles generated, any additives, alkyl chain substitution (Vivero et al, 2005) and amount of aromaticity (where lamellar structures begin to move over one another) (Meng et al, 2017). Once the maximum fluidity has been achieved, the viscosity begins to increase rapidly as the coking coal starts to resolidify; radicals begin to form crosslinks and become absorbed into the structure of the now porous coke, but volatiles are still generated through the resolidification period (Sakurovs, 2003).

As mentioned above, fluidity development occurs through many factors, including the generation of volatiles from within the structure of the coking coal. These volatiles become mobile as the coal is heated; evidence for which can be sought using solvents to extract these small molecular groups from coal (Gavo, Garcia & Diez, 2016). Numerous papers have been written on the swelling of coals with emphasis on the volatile and pyrolysis products (Tran et al, 2016); these show that when the volatile matter is extracted the swelling of the coal is significantly reduced (Tran et al, 2016). This suggests that the overall swelling of the coal during heating is due to the generation of the metaplast, where the weight distribution of this fraction changes at different points through the temperature transition, and the gaseous products are trapped by the metaplast (Tran et al, 2016). The metaplast is a liquid component generated during heating of the coking coal over a range of temperatures during the fluidity development (Tran et al, 2016). The volatile matter generated during the fluidity development has a low molecular weight, below 1000 Da for some coals, suggesting that such coals' matter is comprised of small molecular species, rather than large maceral groups (Stanger et al, 2015).

2.5. Petrographic Properties

2.5.1. Maceral Composition

Before traversing further into the discrete physical changes during the plastic stage of coke production, one must understand the basic structure of the material. Although a black, oblique material upon initial inspection, coal has a very dynamic and complicated structure which can give rise to varied properties. But in a brief description, coal is a very large polymer comprised of many fused aromatic rings. These fused rings form large structures which are known as macerals, derived from the parent plant, and vary in size and properties, giving coal very diverse properties (Meyers, 1981). However, there are many different macerals, but they come under three main types: vitrinite, inertinite and exinite (Meyers, 1981). Each type has unique properties, giving rise to a wide variation in the ranks of coal, from lignite to anthracite. The macerals important for the positive fluidity behaviour of coking coals are vitrinite and exinite, leading to the softening and plasticising of the coal upon heating. The inertinite macerals are, by definition, inert in the coking process, but release volatiles (Das, 2001). Although inert, the inertinite macerals play an important part in the fluidity development, where these macerals contain inert organic components (Das, 2001). In many equations to predict the strength and quality of a coking blend, the amount of inert material within the blend is an important factor to consider, as some inert material can help to maintain the strength of the coke in the furnace through different mechanisms (Chen & Ma, 2002).

Unlike vitrinite and exinite, inertinite shows very little thermoplastic behaviour upon heating; in fact, inertinite has a suppressing effect on the fluidity of the other macerals (Yu, Lucas & Wall, 2007). This has been shown to be caused by the structure of the macerals within the inertinite group, which have large aromatic clusters with very little substitution onto the fused rings. The aromatic fractions have large amounts of crosslinking, which of course prevents the aromatic clusters from undergoing a parallel arrangement, leading to the unique plastic behaviour of good coking coals (Alonso et al, 1999; Diessel & Smyth, 1998). Therefore, for a coal to have good caking properties, it must contain macerals which have large aromatic networks, but with cleavable links between them to allow for mobility of these large components (Alonso et al, 1999). Figure A3 in appendix A shows the difference between low and high rank coals; low rank coals have lots of substitution onto the aromatic rings and lots of oxygen functional groups and crosslinking. High rank coals have a laminar structure to the aromatic macromolecules, allowing these to form parallel arrangements, enhancing fluidity (Bonijolyy, Oberlin & Oberlin, 1982). Of course, the formation of crosslinking between the aromatic components is vital for a coking coal as resolidification needs to occur for the porous structure to maintain its strength, and thus be used in the blast furnace to support the hot metal burden (Alonso et al, 1999). However, inertinites do have some thermoplastic behaviour over a range of temperatures; *Alonso et al (1999)* found that 90% of the char material composed of inertinite macerals had melted over the temperature transition.

Although aromatic structures occur readily in inertinites, they are still required for fluidity to occur. In high rank prime coking coals, there are large amounts of vitrinite macerals which have expansive aromatic structures, giving rise to Van der Waals forces between the macromolecules (Mallya & Stock, 1986). In such macerals, crosslinking is rare due to the lack of heteroatomic material. In lower rank vitrinite macerals, there is a larger amount of oxygen, giving rise to smaller aromatic structures, containing a more considerable fraction of phenolic groups. Consequently, the process of resolidification in these macerals takes place via crosslinking, reducing the fluidity (Alonso et al, 1999). However, the amount of oxygen in the maceral will vary from coal to coal; *Chen & Ma (2002)* found that the vitrinite fraction of a particular coal had the greatest amount of oxygen, despite being the most important maceral for the caking behaviour. However, *Chen & Ma (2002)* also concluded that the inertinite macerals were the least important component when considering the plasticity of the coking coal.

It goes without saying that the petrography of the coal is very important when considering the quality of the coking coal. Particular geological periods give rise to good coking coals, whereas others give rise to poor caking abilities. For example, the Jurassic period gave rise to poor coking coals, mostly due to the high content of inertinite in these coals, whereas those from the Carboniferous period have good caking behaviour (Chen & Ma, 2002). However, it has been noted that high fluid coals can give rise to weak cokes, and so the fluid content (from vitrinite macerals) needs to be controlled, and the presence of inert macerals is necessary (Vega et al, 2017). Even if coals come from the same geological period and location, the behaviour of the coals can be different. *Vega et al (2017)* showed that two American coals from the same geological period had different oxidation characteristics, caused by the difference in porosity in the maceral structures. Another cause of differences in oxidation has been known to be the presence of FeS_2 within the coal, which can catalyse the formation of oxygen substituents within the carbon network, accelerating oxidation, and thus decreasing fluidity (Vega et al, 2017; Beamish & Theiler, 2017).

2.5.2. Analysing Macerals

The most efficient way to measure the content of macerals within a coal is by reflectance methods, including Fourier Transform Infrared (FTIR) (Li et al, 2007), optical microscopy (Scott et al, 2000) and vitrinite reflectance, which measures the amount of incident light reflected from vitrinite macerals (Marino, Marshak & Mastalerz, 2015). Analysing the macerals within coking coals can identify the important features required for a good coking coal, where each maceral group has specific properties and chemical structures (Nomura et al, 2000). Upon studying the reflectance of macerals, *Taylor (1966)* found that the vitrinite group could be split into two, where vitrinite A had a much higher reflectance, vitrinite B being very laminar. *Nomura et al (2000)* studied the structural differences between Goonyella and Witbank coals, being good and slightly coking coals, respectively. It was found that Goonyella has larger aromatic structures within the maceral layers, compared to Witbank which had longer alkyl chains between the aromatic components (Nomura et al, 2000). Table 2.1 below shows the sub-group macerals which comprise the major types.

Table 2.1: Maceral Types and Their Sub-Group Compositions (Winans & Crellin, 1984; Dyrkacz et al, 1991)

Maceral Type	Sub-Group Macerals
Liptinite (Exinite)	Sporinite Cutinite Resinite
Inertinite	Fusinite Semi-Fusinite Macrinite Semi-Macrinite Micrinite
Vitrinite	Telinite 1 Telinite 2 Desmocollinite Telocollinite Gelocollinite Corpocollinite

From the analyses described above, the differences between the macerals can be distinguished, and the contribution towards coal properties identified. When considering the visual differences, the three maceral types can be recognised. Figure 2.4 below shows an optical micrograph of coal showing the individual maceral groups with definitive compositions (Permana, Ward & Gurba, 2013).

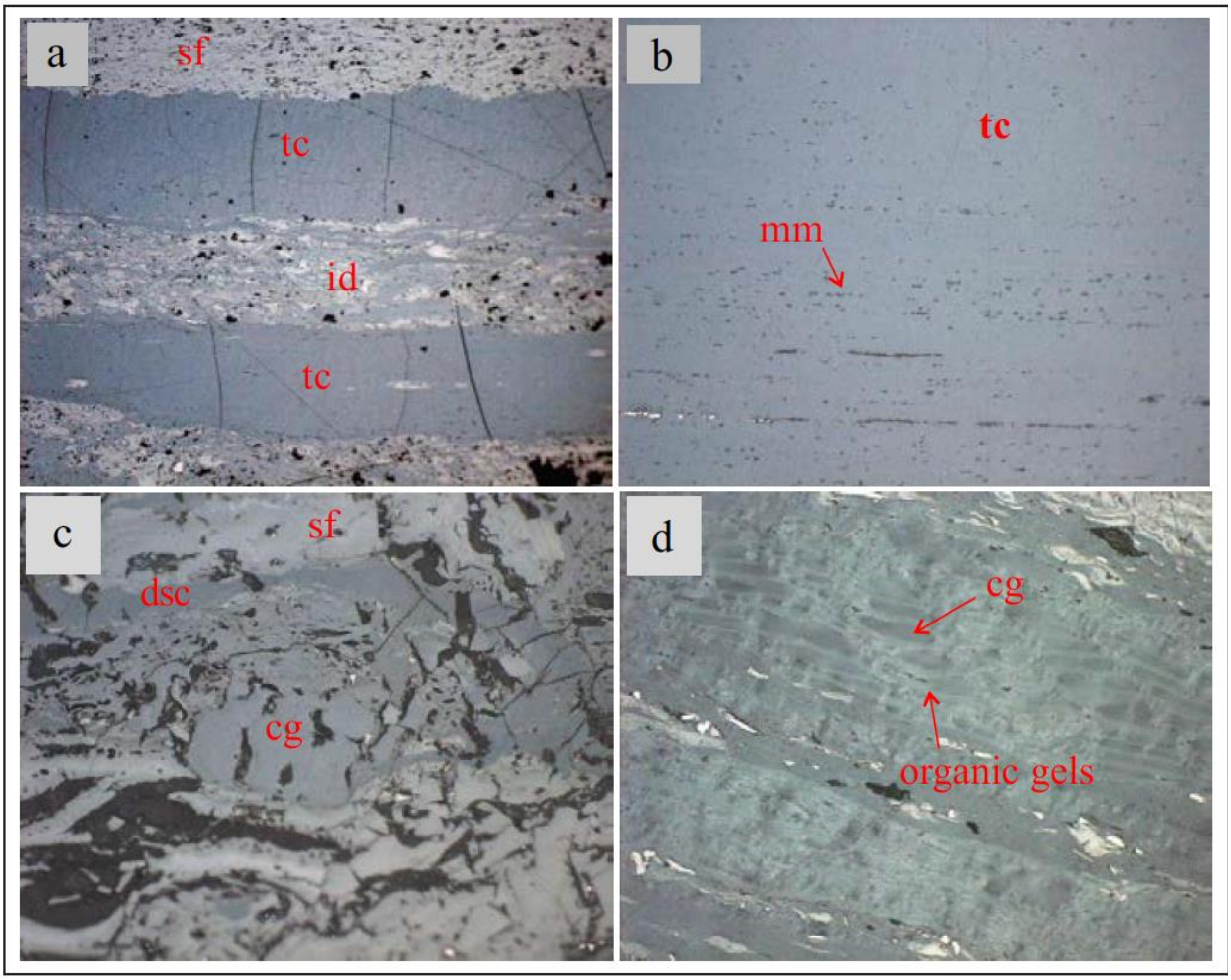

Figure 2.4: Optical micrograph of Coking Coal Showing the Individual Maceral Groups, including corpogelinite (cg), desmocollinite (dsc), inertodetrinite (id), mineral matter (mm), organic gel infillings, semifusinite and telocollinite (tc). (Permana, Ward & Gurba, 2013)

2.6. Literature on Properties of Coking Coal

The majority of literature on coking coal fluidity is based upon using additives to enhance the fluidity, such as coal tar, pitch and extracted volatile matter from the coal (Swietlik et al, 1999; Fernandez et al, 2009; Maroto-Valer, Andresen & Snape, 1998; Clemens & Matheson, 1995; Qin et al, 2016), as well as the study of single coals, pristine (Yang et al, 2018; Xie et al, 2018) and oxidised (Vega et al, 2017). Such literature has thoroughly researched the effect of additives upon the fluidity of coking coal, mostly in that such substances can provide a source of donatable hydrogen (Swietlik et al, 1999), as hydrogen transfer is a vital process for fluidity to occur (see section 2.7.2. *Hydrogen and Hydrogen Donation Transfer*). However, there is a harmony between the generation of hydrogen and the absorbance of such species which cause the recombination of radicals, and the overall process of coke production (Swietlink et al, 1999). For coal tar pitch used, there tends to be a small proportion of aromatic structures and a lack of methyl groups, and therefore there is a low donation of hydrogen from such additives (Swietlik et al, 1999; Diez et al, 1999). Other literature has focussed upon the optimisation of fluidity of coking coals and the overall factors that affect the process (Sakurovs, 2000).

However, there appears to be a lack of literature on blends of coking coals, and the interactions between the components giving rise to the fluidity observed. There are authors who have performed studies upon the interaction between two coals in a binary system, which has given limited insight into the interactions between them (Sakurovs, 2003). This is likely due to the small sample sizes permissible in analytical equipment where studying binary and multi-component blends has proven to be rather difficult. Yet, iron and steel producers use blends of coals which contain multiple different components and subsequently exhibit complex fluid behaviour. Therefore, the latter part of this review will focus upon the nature of coking coals and the physical properties giving rise to its unique properties.

2.7. Factors Influencing Coking Coal Fluidity

2.7.1. The Metaplast

As stated previously, the metaplast is generated during the plastic state of the coking coal during heating. The generation of the metaplast is vital for the formation of the porous matrix formed after resolidification of the coking coal (Xie et al, 2016). As the metaplast forms, it reduces the porosity of the coal, and volatiles are generated throughout the heating regime (Xie et al, 2015; Xie et al, 2016). As the gas is stuck within the metaplast, bubbles form, and the fluid swells, with maximum swelling occurring at maximum volatile generation during the resolidification period. This process results in the porous structure that we know as coke, and how these events unfold will dictate the strength of the coke (Xie et al, 2015; Xie et al, 2016). The formation of the metaplast ends at around 500 ^{o}C, and at higher temperatures (>600 ^{o}C) the volatile generation slows, coinciding with the contraction of the coal, giving rise to the porous product (Xie et al, 2015).

It has been disputed that the metaplast acts as a hydrogen donor component (Yoshidaand et al, 2001), where the hydrogen acts as a vital volatile component for fluidity to occur. Nevertheless, authors have argued over the composition of such liquid phases, with some insisting that they consist of small molecular species (Miura et al, 2001), others that the metaplast contains large macromolecules with weights above 10,000 Da (John et al, 1994). Such large species could be products of the agglomeration of lots of small molecules, which become mobile during heating (Mullins et al, 2012). But it has also been shown that the metaplast itself undergoes pyrolysis reactions, where volatiles are generated and crosslinking occurs (Stanger et al, 2016). *Stanger et al (2016)* proposed that the metaplast is actually comprised of a series of structural monomers which form the fluid phase, which rationalises the volatile generation and solvent extraction of the metaplast. However, it is widely accepted that the formation of the metaplast occurs when the macromolecules degrade under pyrolysis to give rise to the liquid fraction (Shui et al, 2011). As the metaplast forms from the macro, polyaromatic components, the fluid phase provides a medium in which the aromatic sections can rearrange and commence the resolidification (Shui et al, 2011).

As the metaplast provides the medium for resolidification to occur, it is vital for the formation of coke with high mechanical strength, as well as the porous structure which has allowed it to be used extensively in the iron and steel industry (Shui et al, 2011). In low rank coals which contain large amounts of oxygen substituents (-OH, -COOH, -CO), there is little metaplast formed due to the high propensity for crosslinking (Shui et al, 2011; De La Puente et al, 1998). The metaplast is formed from the cleavage of bonds of the macromolecular structure within the macerals, and therefore if the crosslinking is extensive, these will have a lower affinity to break (due to high bond enthalpies) and form a fluid phase (De La Puente et al, 1998). All in all, the metaplast is an integral part of the thermoplastic behaviour of coking coal, where it accounts for almost half of all fluid material during the fluidity development of coal (Snape & Martin, 2000).

2.7.2. Hydrogen and Hydrogen Donation Transfer

The role of hydrogen in fluidity development is paramount, and for many reasons. The amount of fluid hydrogen in the coal is a good indication of the quality of the coking coal; the higher the amount of fluid hydrogen during the plastic phase, the better the coal to an extent, but too high and the resultant material will be too brittle for use (Snape & Martin, 2000). During the softening period of the coking coal, bonds are cleaved, and it has been found that R-H bonds are responsible for fluidity development through the softening stage (Solomon et al, 1989). In fact, the donation of hydrogen into the plastic phase will stabilise the thermoplastic behaviour, preventing early resolidification. As coal is heated, radicals form, and mobile hydrogen can quench such species, preventing cross-linking (Snape & Martin, 2000). Therefore, the monitoring of the fluid hydrogen is an efficient method of studying the fluidity of the coking coal. With the metaplast consisting of small organic fractions, the mobile hydrogen will increase with greater fluidity (Snape & Martin, 2000).

The fraction of hydrogen within coking coal can be adversely affected by oxidation; as oxidation increases the amount of hydrogen decreases (Bend, Edwards & Marsh, 1989). As the amount of oxidation increases, the volatile generation decreases, which has deleterious effects on the final coke properties, again showing that hydrogen is a vital elemental component for fluidity (Bend, Edwards & Marsh, 1989). There have been attempts to understand the outcome of inserting hydrogen-rich components to coking coal to observe the fluidity generated. *Sakurovs et al (2000)* studied mixtures of polymers and coal, where different polymers gave varied outcomes on the fluidity of the coking coal. Of four different polymers, polyacrylnitrile proved to enhance the fluidity the best, the three other plastics either having no effect, or reducing the fluidity (Sakurovs, 2000). Other authors, such as *Uzumkesici et al (1999),* have shown that polymers like polyethylene donate hydrogen into the blend due to their aliphatic nature, compared to aromatic based polymers which absorb hydrogen. Polyethylene and polystyrene were added as the aliphatic and aromatic polymers, respectively. It was found that additive aliphatic groups have little effect upon the fluidity up to a weight percentage (wt%) of 10%, whereas polystyrene had a deleterious effect above 2wt% (Uzumkesici et al, 1999).

Ultimately, hydrogen is important due to the stabilisation of the radical reactions that occur during the pyrolysis of coking coal (Dominguez et al, 2001). The small molecular species generated at the softening stage are rich in hydrogen, due to the organic framework that they originated from. These hydrogen-donating species will sequester radical formation within the structure, eventually turning them into solvating components, preventing early resolidification (Dominguez et al, 2001). Therefore, the generation of hydrogen, and small molecular species, is vital for maintenance of the fluid state. The radical formation within the coal will increase relative to temperature and can only be reduced by hydrogen transfer reactions from the fluid phase via free radical reactions. The increased presence of the radical species leads to recombination, and eventually crosslinking and a reduction of fluidity (Dominguez et al, 2001).

Hence, the dominant presence of hydrogen within the coal during the fluid phase is paramount for thermoplastic events to occur and be maintained (Dominguez et al, 2001).

2.8. Conclusion

Coking coal is a complex material due to its unique role in the blast furnace, but also due to the fluidity that is generated upon heating of the coking coal to between 400 and 500 °C. Over this temperature range, the coal has a wide range of viscoelastic properties which give rise to the porous structure that is known as coke. Such fluid properties are dictated by multiple factors which have been discussed in the above review. These include the fluid fraction known as the metaplast, which has caused controversy between authors surrounding its composition, between small monomers to large macromolecular structures as large as 10,000 Da. However, the most likely scenario is that the metaplast is generated from the pyrolysis of the large maceral matrices. The other major contributor to fluidity is donatable hydrogen, as the R-H bonds within the coal structure are cleaved during the fluidity development. The importance of hydrogen has been demonstrated via the addition of hydrogen donors and absorbers, where the fluidity has been either enhanced or hindered, respectively. Research has focused upon the properties of individual coals with emphasis upon coal fluidity, rather than the intricacies of blends of many different coals used to produce blast furnace coke.

2.9. References

Alonso, M.J.G., Borrego, A.G., Alvarez, D. and Menéndez, R. 1999. Pyrolysis Behaviour of Pulverised Coals at Different Temperatures. *Fuel*. **78**(13), pp.1501-1513.

Angel, M. Reuters. 2018. Worldsteel Raises Forecast for 2018 Global Steel Demand Growth to 1.8 Percent. [Online]. [Accessed: 28/6/18]. Available at: https://www.reuters.com/article/us-global-steel-demand/worldsteel-raises-forecast-for-2018-global-steel-demand-growth-to-1-8-percent-idUSKBN1HO1DY

Beamish, B. and Theiler, J. 2017. Assessing the reactivity of pyrite. *In: Aziz, N. and Kininmonth, B. ed. Proceedings of the 2017 Coal Operators' Conference. 8-10th February 2017, Wollongong*. Wollongong: Mining and Environmental Engineering, University of Wollongong. pp. 391-394.

Bend, S.L., Edwards, I.A.S. and Marsh, H. 1989. The Effects of Oxidation and Weathering on Coal Combustion. *American Chemical Society, Division of Fuel Chemistry, Preprints*. ***34***(3), pp.923-930.

Bodsworth, C. 1963. *Physical chemistry of iron and steel manufacture*. Harlow: Longmans.

Bonijoly, M., Oberlin, M. and Oberlin, A. 1982. A Possible Mechanism for Natural Graphite Formation. *International Journal of Coal Geology*. ***1***(4), pp.283-312.

Cardott, B.J. and Curtis, M.E. 2018. Identification and Nanoporosity of Macerals in Coal by Scanning Electron Microscopy. *International Journal of Coal Geology*. ***190***, pp.205-217.

Castro Díaz, M, Edecki, L., Steel, K.M., Patrick, J.W. and Snape, C.E. 2007. Determination of the Effects Caused by Different Polymers on Coal Fluidity during Carbonization using High-Temperature 1H NMR and Rheometry. *Energy & Fuels*. ***22***(1), pp.471-479.

Castro Díaz, M., Zhao, H., Kokonya, S., Dufour, A. and Snape, C.E. 2012. The Effect of Biomass on Fluidity Development in Coking Blends Using High-Temperature SAOS Rheometry. *Energy & Fuels*. ***26***(3), pp.1767-1775.

Chang, C.M., Whang, T.J., Huang, D.S., Wang, D.H., Tsai, S.T. and Hung, M.T. 2014. Thermoplasticity and Strength Improvement of Coking Coal by Addition of Coal Extracts. *Fuel*. ***117***, pp.364-371.

Chen, P. and Ma, J. 2002. Petrographic Characteristics of Chinese Coals and Their Application in Coal Utilization Processes. *Fuel*. ***81***(11-12), pp.1389-1395.

Clemens, A.H. and Matheson, T.W. 1995. The Effect of Selected Additives and Treatments on Gieseler Fluidity in Coals. *Fuel*. ***74***(1), pp.57-62.

Das, T.K. 2001. Evolution Characteristics of Gases during Pyrolysis of Maceral Concentrates of Russian Coking Coals. *Fuel*. ***80***(4), pp.489-500.

De La Puente, G., Marbán, G., Fuente, E. and Pis, J.J. 1998. Modelling of Volatile Product Evolution in Coal Pyrolysis. The Role of Aerial Oxidation. *Journal of Analytical and applied Pyrolysis*. ***44***(2), pp.205-218.

Diessel, C.F.K. and Smyth, M. 1998. Chapter 9: Technological Applications. In: Taylor, G.H., Teichmüller, M., Davis, A.C.F.K., Diessel, C.F.K., Littke, R. and Robert, P. ed(s). *Organic Petrology*. Stuttgart: Schweizerbart Science Publishers, pp. 519-613.

Dıez, M.A., Alvarez, R. and Barriocanal, C. 2002. Coal for Metallurgical Coke Production: Predictions of Coke Quality and Future Requirements for Cokemaking. *International Journal of Coal Geology*. ***50***(1-4), pp.389-412.

Dıez, M.A., Domınguez, A., Barriocanal, C., Alvarez, R., Blanco, C.G. and Canga, C.S. 1999. Hydrogen Donor and Acceptor Abilities of Pitches from Coal and Petroleum Evaluated by Gas Chromatography. *Journal of Chromatography A*. ***830***(1), pp.155-164.

Domınguez, A., Blanco, C.G., Barriocanal, C., Alvarez, R. and Dıez, M.A. 2001. Gas Chromatographic Study of the Volatile Products from Co-Pyrolysis of Coal and Polyethylene Wastes. *Journal of Chromatography A*. ***918***(1), pp.135-144.

Dyrkacz, G.R., Bloomquist, C.A.A., Ruscic, L. and Crelling, J.C. 1991. An Investigation of the Vitrinite Maceral Group in Microlithotypes using Density Gradient Separation Methods. *Energy & fuels*. ***5***(1), pp.155-163.

Duffy, J.J., Mahoney, M.R. and Steel, K.M. 2010. Influence of Coal Thermoplastic Properties on Coking Pressure Generation: Part 2–A Study of Binary Coal Blends and Specific Additives. *Fuel*. ***89***(7), pp.1600-1615.

Fernández, A.M., Barriocanal, C., Díez, M.A. and Alvarez, R. 2009. Influence of Additives of Various Origins on Thermoplastic Properties of Coal. *Fuel*. ***88***(12), pp.2365-2372.

Flores, B.D., Flores, I.V., Guerrero, A., Orellana, D.R., Pohlmann, J.G., Diez, M.A., Borrego, A.G., Osório, E. and Vilela, A.C. 2017. Effect of Charcoal Blending with a Vitrinite Rich Coking Coal on Coke Reactivity. *Fuel Processing Technology*. ***155***, pp.97-105.

Gayo, F., García, R. and Diez, M.A. 2016. Modelling the Gieseler Fluidity of Coking Coals Modified by Multicomponent Plastic Wastes. *Fuel*. ***165***, pp.134-144.

Geerdes, M., Chaigneau, R. and Kurunov, I. 2015. *Modern Blast Furnace Ironmaking: An Introduction. 3rd Edition*. Amsterdam: IOS Press.

Guelton, N. 2017. The Prediction of the Gieseler Characteristics of Coal Blends. *Fuel*. ***209***, pp.661-673.

Jenkins, D.R. and Mahoney, M.R. 2015. A Mechanistic Model for the Softening of Coking Coal and Its Use for Predicting the Dilatation of Blends. *Fuel*. ***153***, pp.585-594.

John, P., Johnson, C.A., Parker, J.E., Smith, G.P., Herod, A.A., Li, C.Z., Humphrey, P., Chapman, J.R. and Kandiyoti, R. 1994. Molecular Masses up to 270 000 u in Coal and Coal-Derived Products by Matrix Assisted Laser Desorption Ionization Mass Spectrometry (MALDI-ms). *Fuel*. ***73***(10), pp.1606-1616.

Kasai, K. and Tsutsui, Y. 2008. Recent Technology of Coke Oven Refractories. *Nippon Steel Technical Report No. 98*. **42**, p.37.

Li, Z., Fredericks, P.M., Rintoul, L. and Ward, C.R. 2007. Application of Attenuated Total Reflectance Micro-Fourier Transform Infrared (ATR-FTIR) Spectroscopy to the Study of Coal Macerals: Examples from the Bowen Basin, Australia. *International Journal of Coal Geology*. ***70***(1-3), pp.87-94.

Loison, R., Foch, P. and Boyer, A. 1989. *Coke: Quality and Production. 2nd Edition*. Oxford: Elsevier.

Mallya, N. and Stock, L.M. 1986. The Alkylation of High Rank Coals. Non-Covalent Bonding Interactions. *Fuel*. ***65***(5), pp.736-738.

Mariño, J., Marshak, S. and Mastalerz, M. 2015. Evidence for Stratigraphically Controlled Paleogeotherms in the Illinois Basin Based on Vitrinite-Reflectance Analysis: Implications for Interpreting Coal-Rank Anomalies. *AAPG Bulletin*. ***99***(10), pp.1803-1825.

Maroto-Valer, M.M., Andrésen, J.M. and Snape, C.E. 1998. In Situ 1H NMR Study of the Fluidity Enhancement for a Bituminous Coal by Coal Tar Pitch and a Hydrogen-Donor Liquefaction Residue. *Fuel*. ***77***(9-10), pp.921-926.

Melendi-Espina, S., Alvarez, R., Diez, M.A. and Casal, M.D. 2015. Coal and Plastic Waste Co-Pyrolysis by Thermal Analysis–Mass Spectrometry. *Fuel Processing Technology*. ***137***, pp.351-358.

Meng, F., Gupta, S., Yu, J., Jiang, Y., Koshy, P., Sorrell, C. and Shen, Y. 2017. Effects of Kaolinite Addition on the Thermoplastic Behaviour of Coking Coal during Low Temperature Pyrolysis. *Fuel Processing Technology*. ***167***, pp.502-510.

Meyers, R.A. 1981. Coal Structure. In: Meyers, R.A. ed. *Coal Handbook*. New York: Marcel Dekker Inc.

Miura, K., Shimada, M., Mae, K. and Sock, H.Y. 2001. Extraction of Coal Below 350 C in Flowing Non-Polar Solvent. *Fuel*. ***80***(11), pp.1573-1582.

Mollah, M.M., Jackson, W.R., Marshall, M. and Chaffee, A.L. 2015. An Attempt to Produce Blast Furnace Coke from Victorian Brown Coal. *Fuel*. ***148***, pp.104-111.

Mullins, O.C., Sabbah, H., Eyssautier, J., Pomerantz, A.E., Barré, L., Andrews, A.B., Ruiz-Morales, Y., Mostowfi, F., McFarlane, R., Goual, L. and Lepkowicz, R. 2012. Advances in Asphaltene Science and the Yen–Mullins Model. *Energy & Fuels*. ***26***(7), pp.3986-4003.

Nomura, M., Kidena, K., Hiro, M. and Murata, S. 2000. Mechanistic Study on the Plastic Phenomena of Coal. *Energy & fuels.* ***14***(4), pp.904-909.

Nomura, S. 2018. The Effect of Binder (Coal Tar and Pitch) on Coking Pressure. *Fuel.* ***220**,* pp.810-816.

Nomura, S. and Arima, T. 2017. Influence of Binder (Coal Tar and Pitch) Addition on Coal Caking Property and Coke Strength. *Fuel Processing Technology.* ***159***, pp.369-375.

Permana, A.K., Ward, C.R. and Gurba, L.W. 2013. Maceral characteristics and vitrinite reflectance variation of the high rank coals, South Walker Creek, Bowen Basin, Australia. *Indonesian Journal on Geoscience*, ***8***(2), pp.63-74.

Qin, L., Han, J., Fang, K., Chen, X. and Wu, G. 2016. Enhanced Metallurgical Coke Quality Through Incorporation of the Pitch during Biomass/Coal Co-Carbonization. *In: Kim, Y.H. Proceedings of the 2016 5th International Conference on Sustainable Energy and Environment Engineering (ICSEEE 2016), 12-13th November 2016, Zhuhai*. Hong Kong: Atlantis Press.

Saito, Y., Miyamoto, Y., Ono, Y., Numazawa, Y., Matsuo, S., Matsushita, Y., Aoki, H. and Hayashizaki, H. 2018. Effect of Volatile Matter and Thermoplastic Components on Softening and Swelling Behavior in Carbonization of Coal. *The Iron and Steel Institute of Japan International.* ***58***(4), pp.660-666.

Sakurovs, R. 2000. Some Factors Controlling the Thermoplastic Behaviour of Coals. *Fuel.* ***79***(3-4), pp.379-389.

Sakurovs, R. 2003. Interactions between Coking Coals in Blends. *Fuel.* ***82***(4), pp.439-450.

Scott, A.C., Cripps, J.A., Collinson, M.E. and Nichols, G.J. 2000. The Taphonomy of Charcoal Following a Recent Heathland Fire and Some Implications for the Interpretation of Fossil Charcoal Deposits. *Palaeogeography, Palaeoclimatology, Palaeoecology.* ***164***(1-4), pp.1-31.

Shui, H., Li, H., Chang, H., Wang, Z., Gao, Z., Lei, Z. and Ren, S. 2011. Modification of Sub-Bituminous Coal by Steam Treatment: Caking and Coking Properties. *Fuel processing technology*. ***92***(12), pp.2299-2304.

Snape, C.E. and Martin, S.C. 2000. Quantifying Fluidity Development and Mobility in Coals by In-Situ ^{1}H NMR. *Preprints of Papers – American Chemical Society, Division of Fuel Chemistry*. ***45***(2), pp. 205-210.

Solomon, P.R., Best, P.E., Yu, Z.Z. and Deshpande, G.V. 1989. A Macromolecular Network Model for Coal Fluidity. *Abstracts of Papers of the American Chemical Society*. ***198***(67), pp. 895-906

Stanger, R., Borrowdale, J., Smith, N., Xei, W., Tran, Q.A., Lucas, J. and Wall, T. 2015. Changes in Solvent-Extracted Matter for Heated Coal during Metaplast Formation using High-Range Mass Spectrometry. *Energy & Fuels*. ***29***(11), pp.7101-7113.

Stanger, R., Tran, Q.A., Attalla, T., Smith, N., Lucas, J. and Wall, T. 2016. The Pyrolysis Behaviour of Solvent Extracted Metaplast Material from Heated Coal using LDI-TOF Mass Spectroscopy Measurements. *Journal of analytical and applied pyrolysis*. ***120***, pp.258-268.

Suopajärvi, H., Dahl, E., Kemppainen, A., Gornostayev, S., Koskela, A. and Fabritius, T. 2017. Effect of Charcoal and Kraft-Lignin Addition on Coke Compression Strength and Reactivity. *Energies*. ***10***(11), p.1850.

Świetlik, U., Gryglewicz, G., Machnikowska, H., Machnikowski, J., Barriocanal, C., Alvarez, R. and Dıez, M.A. 1999. Modification of Coking Behaviour of Coal Blends by Plasticizing Additives. *Journal of Analytical and Applied Pyrolysis*. ***52***(1), pp.15-31.

TATA Steel. 2011. COSMOS (Coke Oven Scheduling and Heating Monitoring System) + Autospot. [Online]. [Accessed: 03/08/18]. Available From: http://automationtatasteel.com/html/COSMOS.html

Taylor, G.H., 1966. The electron microscopy of vitrinites. In: Given, P.H. ed. Coal Science. Washingon, D. C.: *American Chemical Society*. pp. 274-283.

ThyssenKrupp Industrial Solutions AG. 2018. Coke Plant Technologies. [Online]. [Accessed: 28/6/18]. Available at: https://www.thyssenkrupp-industrial-solutions.com/media/products_services/coke_plants/tkis_coke_plant_technologies.pdf

Tran, Q.A., Stanger, R., Xie, W., Smith, N., Lucas, J. and Wall, T. 2016. Linking Thermoplastic Development and Swelling with Molecular Weight Changes of a Coking Coal and Its Pyrolysis Products. *Energy & Fuels*. ***30***(5), pp.3906-3916.

Trinkel, V., Kieberger, N., Bürgler, T., Rechberger, H. and Fellner, J. 2015. Influence of Waste Plastic Utilisation in Blast Furnace on Heavy Metal Emissions. *Journal of Cleaner Production*. ***94***, pp.312-320.

Uzumkesici, E.S., Casal-Banciella, M.D., McRae, C., Snape, C.E. and Taylor, D. 1999. Co-Processing of Single Plastic Waste Streams in Low Temperature Carbonisation. *Fuel*. ***78***(14), pp.1697-1702.

Vega, M.F., Fernández, A.M., Díaz-Faes, E. and Barriocanal, C. 2017. Improving the Properties of High Volatile Coking Coals by Controlled Mild Oxidation. *Fuel*. ***191***, pp.574-582.

Vega, M.F., Fernández, A.M., Díaz-Faes, E., Casal, M.D. and Barriocanal, C. 2017. The Effect of Bituminous Additives on the Carbonization of Oxidized Coals. *Fuel Processing Technology*. ***156***, pp.19-26.

Vivero, L., Barriocanal, C., Alvarez, R. and Diez, M.A. 2005. Effects of Plastic Wastes on Coal Pyrolysis Behaviour and the Structure of Semicokes. *Journal of Analytical and Applied Pyrolysis*. ***74***(1-2), pp.327-336.

Wei, R., Zhang, L., Cang, D., Li, J., Li, X. and Xu, C.C. 2017. Current Status and Potential of Biomass Utilization in Ferrous Metallurgical Industry. *Renewable and Sustainable Energy Reviews*. ***68***, pp.511-524.

Winans, R.E. and Crelling, J.C. 1984. Chemistry and characterization of coal macerals: overview. In: Winans, R.E. and Crelling, J.C. eds. *Chemistry and Characterization of Coal Macerals*. Washington, D. C.: American Chemical Society, pp. 1-20

World Coal Association. 2018. How Is Steel Produced. [Online]. [Accessed: 28/6/18]. Available at: https://www.worldcoal.org/coal/uses-coal/how-steel-produced

World Steel Association. 2017. World Steel in Figures 2017. [Online]. [Accessed: 28/6/18]. Available at: https://www.worldsteel.org/media-centre/press-releases/2017/world-steel-in-figures-2017.html

World Steel Association. 2018. World Crude Steel Output Increases by 5.3% in 2017. [Online]. [Accessed: 03/08/18]. Available at: https://www.worldsteel.org/media-centre/press-releases/2018/World-crude-steel-output-increases-by-5.3--in-2017.html

World Steel. 2021. World Steel in Figures. [Online]. [Accessed: 21/02/2021]. Available at: https://worldsteel.org/wp-content/uploads/2021-World-Steel-in-Figures.pdf

Xie, W., Stanger, R., Tran, Q.A., Smith, N., Wall, T. and Lucas, J. 2018. Impact of Coal Pyrolysis Products as a Rheological Additive on Thermoplasticity of a Coking Coal. *Energy & Fuels*. ***32***(4), pp.4382-4390.

Xie, W., Stanger, R., Wall, T.F., Lucas, J.A. and Mahoney, M.R. 2015. Associations of Physical, Chemical with Thermal Changes during Coking as Coal Heats–Experiments on Coal Maceral Concentrates. *Fuel*. ***147***, pp.1-8.

Xie, W., Wall, T., Lucas, J., Mahoney, M. and Stanger, R. 2016. Thermo-Swelling Behaviour of Australian Coking Coals from Different Basins: Relating to Rank and Maceral Compositions. *Energy & Fuels*. ***30***(12), pp.10126-10135.

Yang, G., Shi, T., Zhang, Q., Cao, Y., Zhang, W., Wu, X., Li, J. and Yang, J. 2018. An Index of Fluidity-Temperature Area for Evaluating Cohesiveness of Coking Coal by Gieseler Fluidity Characterization. *Fuel Processing Technology*. ***177***, pp.1-5.

Yang, Y., Raipala, K. and Holappa, L. 2014. Ironmaking. In: Seetharaman, S., McLean, A., Guthrie, R. and Sridhar, S. eds. *Treatise on Process Metallurgy, Volume 3: Industrial Processes.* Oxford: Elsevier, pp. 2-86.

Yoshidaand, T., Takanohashi, T., Iino, M. and Katoh, K. 2001. Dynamic Viscoelastic Measurement of Coal Extracts and Residues. *Energy & fuels.* ***15***(1), pp.170-175.

Yu, J., Lucas, J.A. and Wall, T.F. 2007. Formation of the Structure of Chars during Devolatilization of Pulverized Coal and Its Thermoproperties: A Review. *Progress in Energy and Combustion Science.* ***33***(2), pp.135-170.

Zhou, Q., Liu, Q., Shi, L., Yan, Y. and Liu, Z. 2017. Behaviours of Coking and Radicals during Reaction of Volatiles Generated from Fixed-Bed Pyrolysis of a Lignite and a Subbituminous Coal. *Fuel Processing Technology.* ***161***, pp.304-310.

Zubkova, V., Strojwas, A. and Jozwiak, M. 2017. The Influence of Long-Term Storage on Thermal Behaviour of Lower Rank Coal on the Example of Polish Coal. Part 1. The Influence of Long-Term Storage (LTS) of a Lower Rank Coal on Changes in Volume of Carbonized Charge and Changes in Structural Chemical Parameters of Pyrolysis Products. *Fuel.* ***188***, pp.79-89.

Chapter 3

Materials & Methods

A methods section has been provided to give an overview of the techniques used for this research. Each results chapter contains a methods section which provides the specific experimental details for the samples analysed.

3.1. Materials

A suite of 10 coals were provided by Tata Steel to be tested under various analytical techniques. Tata Steel provided the following properties of the coals which could be used to compare the samples and help understand phenomena in viscosity and fluid hydrogen measurements. Properties provided were volatile matter content (%), ash content (%), inertinite content (%), vitrinite content (%), mean vitrinite reflectance (MVR), free swelling index, dilatation (%) and maximum Gieseler fluidity (ddpm). Properties are displayed in Table 3.1 below.

Table 3.1: Properties of the 10 coals tested in this study including volatile matter content, ash content, inertinite content, vitrinite content, mean vitrinite content, free swelling index, dilatation and Gieseler fluidity. These were provided by Tata Steel.

Coal #	Volatility – Dry Ash Free Basis (%)	Ash – Dry Basis (%)	Inertinite (%)	Vitrinite (%)	Mean Vitrinite Reflectance	Free Swelling Index	Dilatation (%)	Fluidity (ddpm)
1	17.6	10.8	48.4	51.6	1.36	3	6	0
2	19.1	8.2	55.4	44.6	1.23	5	-22	3
3	39.9	4.2	1.6	96.4	0.65	6.5	17	22
4	22.4	9.2	32.2	67.8	1.10	9.5	62	440
5	18.7	5.8	31.2	68.8	1.41	9	70	130
6	29.9	8.6	25	73	0.95	7.5	152	3700
7	25.6	6.4	14.6	85.2	1.15	9	253	8400
8	32.4	6.5	17.4	76.8	0.97	8.5	300	30000
9	36.7	7.5	1.8	93.8	0.74	8.5	168	29400
10	32.4	8.4	18.4	74	0.93	8	182	30000

3.2. Methods

3.2.1. Sample Preparation

Upon delivery, coals were placed in a freezer to mitigate any effects of oxidation. Coals were then manually crushed and sieved to achieve a particle size range of 53 – 212 μm. Samples were kept in a freezer throughout the project to mitigate oxidation.

3.2.2. Rheology

A Rheometric RDA III high temperature rheometer has been used to measure the viscoelastic and expansion behaviour of coal samples, where this instrument has been used in previous studies for measuring coal fluidity development (Castro-Diaz et al, 2005; Castro-Diaz et al, 2007; Castro-Diaz et al, 2007; Castro-Diaz et al, 2008; Castro-Diaz et al, 2012; Castro-Diaz et al, 2015; Castro-Diaz et al, 2018). Coal pellets of 25 mm diameter and varying thickness, dependent upon mass, were made using a 25 mm die and a Carver manual hydraulic press. Pellets were formed under 5 tonnes of force. Pellets were placed on the geometry and a force of 200 g was applied by the top plate to ensure contact between sample and rheometer. Geometry was dependent upon the study where a serrated parallel plate (PP) and smooth cup (with serrated top plate) have been used throughout the project. Experimental details have been provided for each chapter. Temperature range (350 – 500 ^{o}C) and heating rate (3 ^{o}C min^{-1}) for each test was set before each measurement through the environmental controller, within the Rheometric software on the host computer. Samples were heated by an internal forced convection oven and through two resistive heater guns mounted above and below the sample. Temperature was measured by the environmental controller, where platinum resistance thermocouples were used to directly measure the temperature within the oven. The difference between the commanded temperature of the environmental controller and the measured temperature by the thermocouples controlled the temperature changes through feedback to the environmental controller.

Samples were held in place by generically a top fixture, or plate, and bottom fixture, or plate (where a PP and cup geometry have been used throughout this research). The top plate was connected to a transducer. The transducer was connected to an internal torsion bar, where movement of the internal torsion bar sent a signal to the environmental controller and allowed movement in the top plate to allow constant contact with the sample and mitigated damage to the transducer, moving the plate up if a force exceeding 20 g was measured (exerted by the sample upon the plate). Additionally, this movement allowed the measurement of plate gap. The motor, which was connected to the bottom fixture, provided oscillatory shear, pre-determined by the host computer. The frequency and strain amplitude of the oscillatory shear were entered into the host computer which allowed the motor to apply the correct oscillatory shear. A frequency of 1 Hz was used, which has been used throughout coking coal fluidity studies, and a maximum strain of 0.1%. Strain was optimised through strain sweep tests (see Figure B1, Appendix B), where the applied strain during testing had to be within the linear viscoelastic range of the coking coal.

As the sample was deformed, the torque measured by the transducer allowed measurements of viscosity to be made. Torque was measured every 10 seconds by the transducer to allow a change in temperature of the system. The stress and strain were subsequently measured by the following equations for the PP (Morrison, 2001):

$$\dot{\gamma} = \frac{R\Omega}{H} \tag{3.1}$$

$$\tau = \frac{2T}{\pi R^2}\left[\frac{3}{4} + \frac{dln\left({}^{T}/_{2\pi R^3}\right)}{dln\dot{\gamma}_R}\right] \tag{3.2}$$

Where:

$\dot{\gamma}$ = *Strain rate* (s^{-1})

τ = *Stress (Pa)*

r = Plate radius

Ω = *Frequency* (s^{-1})

H = Sample height (m)

T = Torque (Nm)

And for the cup (Morrison, 2001):

$$\tau = \frac{T}{2\pi R^2 L\kappa^2} \tag{3.3}$$

$$\dot{\gamma} = \frac{\kappa\Omega}{(1-\kappa)} \tag{3.4}$$

Where:

L = Length of bob/plate (m)

κ = Ratio of plate radius to cup radius

The stress and strain from the above equations could then be used in the following equations to calculate viscoelastic parameters (Barnes, Hutton and Walters, 1989):

$$\eta^* = G^*/\omega \tag{3.5}$$

$$G^* = \tau^*/\gamma^* \tag{3.6}$$

$$G' = G^*\cos(\delta) \tag{3.7}$$

$$G'' = G^*\sin(\delta) \tag{3.8}$$

$$G''/G' = tan\delta \tag{3.9}$$

Where:

η = Complex viscosity (Pa s)*

G = Complex modulus (Pa)*

τ = Stress (Pa)

γ = Strain

G' = Storage modulus (Pa)

G" = Loss modulus (Pa)

Tan(δ) = Loss tangent

The aforementioned calculations were performed automatically by the software. After each test, the data, stored on the Rheometrics software datasheet, was copied into Excel files to enable analysis and graph plotting. All viscoelastic and expansion data was measured as a function of temperature.

The two fixtures, or plates, were held in place by retainers and could be removed via a screwable knob. After each test, the fixtures were removed and cleaned. Samples were placed onto the fixtures prior to testing. The plate gap was calibrated before each test by the environmental controller by measuring the zero-distance between the fixtures and setting the minimum working plate gap to 2.3 mm to reduce damage to the transducer. Samples were either placed carefully on the PP, or inserted into the cup, prior to testing. The PP was only used in the geometry comparison chapter (chapter 4), but the novel cup has been used in chapters 4 and 5.

3.2.3. NMR

Up to 200 mg of coal were packed into boron nitride capsules and capped with a screw lid to contain samples. Capsules were inserted horizontally into the stator within the Doty 200 MHz ^{1}H probe and used with a Bruker MLS 300 MHz instrument, used in previous studies for the analysis of coking coal fluidity development (Castro-Diaz et al, 2008; Castro-Diaz et al, 2018). Dry nitrogen was blown through the capsule region at 35 dm^{3}min^{-1} to heat the sample. Air was blown at a heating rate of 60 dm^{3}min^{-1} to ensure that the region below the capsule was maintained below 50 ^{o}C, and 20 dm^{3}min^{-1} of air was used to keep the region below the sample container and probe exterior to maintain the temperature below 110 ^{o}C. The sample region temperature was monitored via an independent thermocouple, and the temperature controlled via an independent temperature controller. Temperature had to be increased manually every 3 minutes to maintain a heating rate of 3 ^{o}Cmin^{-1}. 100 scans were performed with a cycle delay of 0.3 s. As temperature was controlled independently and acquisitions performed manually, acquisitions were performed every 10 ^{o}C from 360 to 500 ^{o}C. Prior to each accumulation of data, the probe was tuned and matched to ensure the frequency of radiofrequency (rf) signal matched that of the protons, where turning of two prongs underneath the probe allowed the adjustment of the tuning frequency.

A solid echo pulse sequence ($90^o – \tau – 90^o$) was used to determine the difference in peak width with increasing temperature. This echo pulse sequence refocussed the spin of the protons, where two intense rf pulses, which were out of phase from each other, were subjected upon the sample, separated by a time interval, τ. This provided a distribution of spins, where upon the second pulse of rf an echo was generated. The first pulse aligned the spins of protons into the same plane. The spins then precessed in different directions, and at time τ the second rf pulse was subjected upon the protons. During the precession time, the spins interfered with one another (Hahn, 1950). Upon the second rf pulse the echo generated allowed the interference between spins to be measured (Garvey et al, 2006).

The echo spectrum (in the form of free induction decay, FID), in the time domain, was deconvoluted using a Fourier transform using the Bruker TopSpin software, to generate a spectrum in the frequency domain. 0-order phasing was then performed, followed by baseline correction using the TopSpin software, in order for the spectrum to be analysed. The spectrum was converted to ASCII format using NUTS software. This then allowed the spectrum area of Lorentzian (mobile protons) and Gaussian (rigid protons) contributions to be calculated using Origin software, based on a high-performance computer which was logged into and accessed virtually to perform the deconvolution. The areas of Lorentzian and Gaussian contributions then allowed for calculation of %fluid H:

$$\%Fluid\ H = \frac{A_L}{A_L + A_G}\ x\ 100 \tag{3.10}$$

Where:

A_L = *Area of Lorentzian contribution*

A_G = *Area of Gaussian contribution*

The width of the Gaussian and Lorentzian peaks at half-height, where mobility was denoted as T_2 for the Lorentzian (T_{2L}) and Gaussian (T_{2G}) contributions, provided the mobility of the rigid (Gaussian) and mobile (Lorentzian) phases:

$$T_2 = \frac{1}{\pi H_{1/2}} \tag{3.11}$$

Where:

T_2 = *Mobility (μs)*

$H_{1/2}$ = *Width at half-height of peak* (s^{-1})

Figure D1 (appendix D) details an example of a deconvoluted spectrum, showing the experimental spectrum, a predicted spectrum which could be integrated, Lorentzian component and Gaussian component.

3.2.4. Carbonisation of Coal Pellets for Porosity Analysis

Coal pellets were prepared from 3 g samples of 52 – 212 µm coal sample and compressed using a Carver manual press under 5 tonnes of force using a 25 mm die. The pellets were then placed in a tubular furnace and heated to 1000 ^{o}C at a heating rate of 3 ^{o}C min^{-1}. Nitrogen was used as the heat transfer gas with a flow rate of 1dm^{3} min^{-1}.

3.2.5. Pycnometry

Skeletal density and volume of the coke samples was performed using a Micromeritics AccuPyc II 1340 Pycnometer. Helium was used as the gas displacement medium. Prior to analysis, the Pycnometer was purged with helium by venting out the chamber and system with helium several times. The lid to the chamber was greased to ensure a good seal. The sample cell volume was then calibrated to ensure accurate measurements. This was performed using the empty cell and then two calibrated spherical weights with known volume and mass. The cell was filled with helium and then vented to obtain the volume of the empty and filled cell. This was performed 20 times in each case.

Coke samples were split into chunks of varying size, not exceeding 12.5 mm width (in order to fit into 10 cm^{3} sample cell), placed in vials and dried in a vacuum oven for 24 hours at 120 ^{o}C to ensure that samples were dry prior to analysis. Samples were taken out of the vacuum oven and weighed as quickly as possible prior to analysis to mitigate moisture development on the samples. Samples were then placed in the 10 cm^{3} sample cell and placed within the Pycnometer. The samples were purged 20 times using helium and subsequently 20 cycles of analysis were performed to obtain an averaged skeletal density of the coke samples (Kostas et al, 2020). The skeletal volume and density from the report generated by the Micrometrics software were recorded at the end of each test.

3.2.6. BET

Microporosity information was obtained utilising BET (Brunauer, Emmet and Teller) where a Micromeritics ASAP 2420 was used, and CO_2 was used as the adsorbate to obtain CO_2 isotherms. Prior to analysis approximately 250 mg of sample was weighed into a sample tube and degassed to remove adsorbed moisture and other gases under high vacuum at 120 ^{o}C for 15h. Isotherms were carried out at 0 ^{o}C from 0.00005 to 0.35 relative pressure (P/P_0). The surface area and micropore volume was calculated using the Dubinin-Radushkevich model using Microactive Software V5.0 (Kostas et al, 2020).

3.2.7. MIP

A Micromeritics Autopore IV Series instrument was used to obtain the bulk density and porosity of coke samples. 3 g coke samples were vacuum dried at 120 ^{o}C for 48 hours in a vacuum oven. Samples were subsequently loaded into a 5 mL solid penetrometer, 0.392 mL stem volume, then sealed. Mercury intrusion was measured from 0 to 4137 bar. The Washburn equation was used to convert the volume of mercury intrusion to pore volume for slit and angular pores. A contact angle of 151.5 ^{o} and surface tension of 475.5 mN m^{-1} for mercury intrusion in the coke samples was used to provide pore size distribution from 231 μm (macropores) to 2 nm (mesopores). Correlation methods were applied by running a blank penetrometer to remove any intrusion detected from an empty penetrometer (Li et al, 2021).

3.2.8. Strength Testing

An Instron 5969 dual column tabletop universal testing system equipped with a 50 kN load cell was used to test the strength of coke samples. Samples were carbonised at 1000 ^{o}C in nitrogen to form approximately 25 mm diameter coke discs (see section 3.2.4). A compression speed of 0.0167 mm sec^{-1} was used with a maximum compression load of 14.6 kN. Maximum compression load of samples was obtained through averaging the load of the first 10 fractures. Strength was obtained through the following equation (Qiao et al, 2016):

$$\sigma_c = (4F/\pi D^2)(H/D) \tag{3.12}$$

Where:

σ_c: Compressive strength (Pa)

F: Maximum compressive load (N)

D: Diameter of coke pellets (m)

H: Height of coke pellets (m)

3.2.8. Ultimate Analysis

The fractional mass of hydrogen of the fresh coals was determined using a LECO CHN-628 elemental analyser. 2,5-(Bis(5-tert-butyl-2-benzo-oxazol-2-yl)thiophene (BBOT) was used as a standard. 0.075 g of fresh coal was weighed into foil cups for analysis. Samples were combusted in oxygen at 950 ^{o}C and the hydrogen content determined by detection of H_2O by infrared cells. All single coals were analysed in triplicate to provide the fractional mass of hydrogen in the fresh coals.

3.3. References

Barnes, H.A., Hutton, J.F. and Walters, K. 1989. *An introduction to rheology*, *Volume 3*. 1st Edition. Amsterdam: Elsevier.

Castro Díaz, M., Zhao, H., Kokonya, S., Dufour, A. and Snape, C.E. 2012. The Effect of Biomass on Fluidity Development in Coking Blends Using High-Temperature SAOS Rheometry. *Energy & Fuels*. ***26***(3), pp.1767-1775.

Castro-Díaz, M., Duffy, J.J., Snape, C.E. and Steel, K.M. 2007. The Shear-Rate Dependent Viscoelastic Properties of Coal during Carbonisation. In: *International Conference on Coal Science and Technology*. *28th – 31st August 2007*. Nottingham.

Castro-Díaz, M., Duffy, J.J., Snape, C.E. and Steel, K.M. 2007. Use of High-Temperature, High-Torque Rheometry to Study the Viscoelastic Properties of Coal during Carbonization. *Journal of Rheology*. ***51***(5), pp.895-913.

Castro-Díaz, M., Edecki, L., Steel, K.M., Patrick, J.W. and Snape, C.E. 2008. Determination of the Effects Caused by Different Polymers on Coal Fluidity during Carbonization using High-Temperature 1H NMR and Rheometry. *Energy & Fuels*. ***22***(1), pp.471-479.

Castro-Díaz, M., Steel, K.M., Drage, T.C., Patrick, J.W. and Snape, C.E. 2005. Determination of the Effect of Different Additives in Coking Blends using a Combination of in situ High-Temperature 1H NMR and Rheometry. *Energy & Fuels*. ***19***(6), pp.2423-2431.

Castro-Díaz, M., Vega, M.F., Barriocanal, C. and Snape, C.E. 2015. Utilization of Carbonaceous Materials to Restore the Coking Properties of Weathered Coals. *Energy & Fuels*. ***29***(9), pp.5744-5749.

Castro-Diaz, Miguel., Snape, C., Florentino-Madiedo, L., Diaz-Faes, E. and Barriocanal, C. 2018. Importance of Biomass and Binder Selection for Coking Briquette Preparation: Their Effect on Coal Thermoplastic Properties. *Energy & Fuels*. ***32***(10), pp.10727-10736.

Garvey, C.J., Parker, I.H., Simon, G.P. and Whittaker, A.K., 2006. The hydration of paper studied with solid-state magnetisation-exchange ^{1}H NMR spectroscopy. *Wood Research and Technology - Holzforschung*. ***60***(4), pp. 409-416

Hahn, E.L. 1950. Spin echoes. *Physical review*. ***80***(4), p.580.

Kostas, E.T., Durán-Jiménez, G., Shepherd, B.J., Meredith, W., Stevens, L.A., Williams, O.S., Lye, G.J. and Robinson, J.P. 2020. Microwave pyrolysis of olive pomace for bio-oil and bio-char production. *Chemical Engineering Journal*. ***387***, p.123404.

Li, W., Stevens, L.A., Uguna, C.N., Vane, C.H., Meredith, W., Tang, L., Li, Q. and Snape, C.E. 2021. Comparison of the impact of moisture on methane adsorption and nanoporosity for over mature shales and their kerogens. *International Journal of Coal Geology*. ***237***, p.103705.

Morrison, F.A. 2001. *Understanding rheology*. New York: Oxford: Oxford University Press.

Qiao, X., Zhang, Y., Wang, Y., Zhao, Y., Sun, Y., Dong, Y., Jia, J. and Zhao, X. 2016. Preparation of High-Strength Gasified Coke Used for DRI from Low Rank Coal. In *XVIII International Coal Preparation Congress, 28th June – 1st July 2016, Saint-Petersburg, Russia.* Springer, Cham., pp. 531-536.

Chapter 4

A Rheometric Cup Geometry to Study the Viscoelastic Behaviour of Coking Coals

Abstract

A cup geometry for the rheometric study of coking coals at high temperature under controlled strain small amplitude oscillatory shear (SAOS) has been studied for its efficacy to complement the already established parallel plate geometry, which has been used extensively to quantify fluidity development. A suite of 10 coals were studied with the parallel plate and cup geometries to compare complex viscosity, storage modulus, loss modulus and plate gap profiles. For high fluidity coals, the parallel plate geometry gave significant contraction during softening due to sample loss, while the cup geometry displayed extended expansion due to the retaining walls and this can potentially provide a proxy for gas pressure. Complex viscosity profiles showed agreement between the two geometries for high fluidity coals and reasonable similarities for medium fluidity coals. Low and non-fluid coals displaying high complex viscosity gave differences, due to slip effects, which were also responsible for the differences in medium and high fluidity coals before softening and after resolidification. Larger masses can be used with the cup geometry compared to 1.5 g for the parallel plate, with up to 3 g for medium and high fluidity coals, making it more favourable for investigating blends.

4.1. Introduction

Blast furnace coke is formed from coking coals through fluidity development where thermoplastic events take place, transforming relatively small coal particles into a matrix of coherent coke, containing segregated pores (Guerrero, Diez & Borrego, 2015; Jenkins & Mahoney, 2015). Historically, the transitions during fluidity development and resolidification have been measured through empirical techniques such as Gieseler plastometry (Guerrero, Diez & Borrego, 2015; Jenkins & Mahoney, 2015). Coking coal has a ternary role in the blast furnace; acting as a reducing agent, a heat source and a permeable support, allowing hot gases to pass vertically and holding the heavy ferrous burden within the furnace (Diez, Alvarez & Barriocanal, 2002). The first two roles could be performed by other carbon-based materials; however, the latter has only been shown to be performed by coking coal, and as such is in high demand (World Steel Association, 2017). Research has been performed into using other materials which could replace coking coal as a permeable support, such as polymers (Melendi et al, 2011) and charcoal (MacPhee et al, 2009), however no suitable alternatives have been found (Mollah et al, 2015; Trinkel et al, 2015; Wei et al, 2017). Blending coals with additives has also been investigated including biomass (Kokonya et al, 2013), polymers (Castro Diaz et al, 2008; Melendi et al, 2007; Melendi-Espina et al, 2015), binders (Guerrero, Diez & Borrego, 2015) and coal extracts (Jenkins & Mahoney, 2015) in order to improve coal fluidity but have all fallen short of the quality required for a good coke.

4.1.1. Studying Coal Fluidity

The Gieseler plastometer comprises a metal cup and a spinning needle with horizontal pins to provide a rake-like fixture with constant torque around the inner circumference, where the frequency of rotation is inversely proportional to viscosity i.e., directly proportional to fluidity (Guelton, 2017). Although this technique gives a quantitative indication as to the relative fluidity of coals, it does not provide any viscoelastic information and the spinning needle is measuring only at the circumference of the cup and around the pins of the needle (Adeleke et al, 2007; Clemens & Matheson, 1995). It has been shown that polymer and colloid systems exhibit a boundary slip layer where the interface between the sample and the wall generate a layer of reduced viscosity (Yoshimura & Prod’homme, 1988). However, Gieseler plastometry is used throughout the steel industry to understand the fluidity of coals, where good reliability has been found with this technique.

High temperature rheometry has been used to study the fluidity and viscoelastic changes in coking coals where the technique has provided information about the macromolecular changes in the coal (Duffy et al, 2007). Oscillatory shear rheometry operates by applying a sinusoidal strain to a sample and measuring the stress response to provide information on the viscoelastic properties of the materials (Barnes, Hutton & Walters, 1989). The difference in angle between the maxima in stress and strain is denoted as δ (phase angle) where this will vary between 0 and 90^o for a viscoelastic material. For a purely solid, elastic material, the phase angle will be 0^o as any strain applied to the sample is instantly translated through its structure as stress. For a purely fluid, viscous material any applied strain is dissipated through the structure and any resultant stress is delayed in its application (Ferry, 1980). As such, purely viscous materials exhibit δ values of 90^o. At δ values of 45^o, there are equal contributions of viscous and elastic behaviour. The elastic and viscous nature of the materials can be quantified from the applied stress and strain using the cosine and sin functions of the phase angle, as shown in Equation 4.1.

$$G' = \left[\frac{\tau_0 cos(\delta)}{\gamma_0}\right];\ G'' = \left[\frac{\tau_0 sin(\delta)}{\gamma_0}\right] \tag{4.1}$$

Where:

G' = Storage (elastic) modulus (Pa)

G'' = Loss (viscous) modulus (Pa)

τ_0 = Maximum stress (Pa)

γ_0 = Maximum strain

δ = Phase angle (^{o})

The storage modulus (G') defines the elastic behaviour of the sample and the loss modulus (G") defines the viscous behaviour of the sample, where these parameters can be compared to understand the behaviour of the material as a ratio as shown in Equation 4.2 below.

$$G''/G' = tan\delta \tag{4.2}$$

Where:

Tanδ = Loss tangent

When tanδ increases above 1, the material is behaving more viscous and fluid-like (sol point), and when it decreases below 1 the material is behaving more elastic and solid-like (gel point) (Barnes, Hutton & Walters, 1989).

Complex viscosity (η*) has been used previously as a direct comparison with Gieseler fluidity, where lower values of viscosity indicate greater fluidity. This parameter is hence used to study coking coals, which is calculated from the complex modulus and frequency of oscillation as shown in Equations 4.3 and 4.4.

$$\eta^* = G^*/\omega \tag{4.3}$$

$$G^* = \tau^*/\gamma^* \tag{4.4}$$

Where:

η^* = *Complex viscosity (Pa s)*

G^* = *Complex modulus (Pa)*

τ^* = *Maximum stress (Pa)*

γ^* = *Maximum strain*

ω = *Frequency (Hz, s^{-1})*

Additionally, the complex modulus is utilised to calculate the storage and loss moduli throughout rheological testing as shown in Equations 4.5 and 4.6.

$$G' = G^*\cos(\delta) \tag{4.5}$$

$$G'' = G^*\sin(\delta) \tag{4.6}$$

4.1.2. Previous Rheometric Studies of Coal Fluidity

In all previous research on coking coals, only the serrated parallel plate geometry has been used due to its ease of use, the reduction of slip from the serrated plates and its use prior for the study of polymers (Lin & Winter, 1991). *Nomura et al (1999)* first implemented the technique with a serrated parallel plate for the study of coking coals to examine their thermoplastic behaviour and has not been changed since (Nomura et al, 1999). A vast range of coals have been investigated with the serrated parallel plate geometry to understand the thermoplastic changes and viscosity, where coking coals give minimum complex viscosity

(η^*_{min}) between 10^3 – 10^5 Pa s (Castro Diaz et al, 2005; Castro Diaz et al, 2007; Castro Diaz et al, 2007; Castro-Diaz et al, 2018; Duffy et al, 2007; Melendi et al, 2007; Steel et al, 2009; Steel et al, 2014). There is also particular interest in studying non-coking, non-fluid coals in coke blends to optimise the cost of production and minimise the swelling from high fluidity coals (Das et al, 2018).

From rheometry, the three main thermoplastic phases of coals can be observed. Softening occurs first where initial maceral movement occurs along with volatile generation. This is indicated by an initial maximum followed by a reduction in complex viscosity. As the temperature increases gradually, bonds are cleaved within the aromatic structure giving rise to free radicals, which are stabilised by small, mobile hydrogen species. Maceral movement increases to a point where the fluid phase, or metaplast, is fully formed indicated by η^*_{min} (maximum fluidity) and there is a stable state of hydrogen donation and absorption. This lasts for a very short temperature range as the hydrogen species are bound and polymerisation reactions occur where larger free radicals recombine to begin the formation of the macromolecular structure. This latter stage, known as resolidification, involves significant cross-linking, giving rise to a reduction in fluidity, indicated by an increase in complex viscosity after η^*_{min}. Essentially, C-H bonds within the aromatic structures are replaced with higher energy C-C bonds (Loison, Foch & Boyer, 2014; Riazi & Gupta, 2016).

A wide range of rheological experimental conditions have been used to identify factors affecting fluidity of coking coals. For example, *Castro Diaz et al (2007)* found that increasing the heating rate gave rise to a higher temperature of maximum fluidity (TMF), along with a greater fluidity (lower η^*_{min}) and fluidity range (Castro Diaz et al, 2007). Further, an increased heating rate used for blends of coals and biomass was found to increase the overlap of the fluidity ranges (Castro Diaz et al, 2012). Additionally, plate gap measurements can probe the expansion of high fluid coals (Duffy et al, 2007). The use of 53 – 212 μm particle size range was found optimal for the rheometric study of coals using the serrated parallel plate, where <53 μm particles restricted the bulk fluid movement through the sample (Das et al, 2018; Kok et al, 1998). Rheometry has also been used to understand if pore development and fluidity could be linked, where large pores were prevalent in high fluidity coals, with low fluidity coals generating less porosity, comparatively (Meng et al, 2017; Steel et al, 2017). This correlation between porosity and fluidity was also found when testing coals using rheometry and CT analysis where *Steel et al (2017)* found that high fluidity coals generate large, coalesced pores which are detrimental to the coke strength, when compared to low fluidity coals (Steel et al, 2017). Good coking coals generate sufficient fluidity, with η^*_{min} of approximately 10^4 Pa s, to give rise to large, segregated pores (compared to small pores generated in low fluidity coals and large, merged pores in high fluidity coals), enhancing the strength of the coke (Duffy et al, 2010). The serrated parallel plate geometry has also been used to understand the effect of additives on fluidity, where the addition of coal tar can enhance fluidity of coals, whereas biomass reduced fluidity (Castro Diaz et al, 2015), due to the low softening temperature of the biomass, forming char before coals soften appreciably and absorbing the fluid material generated from coals (Castro Diaz et al, 2015). Attempts have been made to obtain indicative measurements of bulk effects of coals from rheometry, however only predictive models from low mass samples have been developed from rheological data (Steel et al, 2004; Steel et al, 2006).

4.1.3. Geometric Comparisons and Scope of this Study

One of the major differences between Gieseler plastometry and rheometry is that high temperature rheometry uses a small amplitude oscillatory shear to remain within the viscoelastic range of the coal, whereas the Gieseler plastometer has a high rotation speed to measure small changes in fluidity (Nomura et al, 1999). Correlations have been found between Gieseler fluidity and tanδ from parallel plate rheometry for some coals, with some discrepancies for medium fluidity coals (Yoshida et al, 2000).

As an alternative to the parallel plate, a geometry comprised of a 26 mm inner diameter cup along with a top serrated plate has been used here that draws comparisons with the couette geometry. The couette geometry utilises a smooth bob instead of a top plate, where this has been used extensively for low viscosity samples such as polymer dispersions (Laun, Bung & Schmidt, 1991), gels (Medina-Banuelos et al, 2017), gums (Benkhelifa, Alvarez & Flick, 2008) and food stuffs (Medina-Banuelos et al, 2017). However, there have been few investigations into the comparisons between serrated parallel plate and couette geometries for their use to study viscoelastic materials. Of the papers that have made comparisons, the majority have investigated colloid suspensions where agreements have been found (Park et al, 2011; Yoshimura et al, 1987)). As the cup geometry is a completely novel geometry, the couette geometry has only been used as a simple diagrammatic comparison with the parallel plate, cup and Gieseler plastometer.

Figure 4.1 depicts the side cross-section view of the four previously mentioned techniques: parallel plate (a), cup (b) and couette (c) geometries used for oscillatory rheometry and Gieseler plastometry (d). The cup and couette geometries can be compared to Gieseler where the sample is contained within smooth walls. Additionally, the sides of the serrated plate (cup geometry) or smooth bob (couette geometry) can be in contact with sample at the geometry surface, akin to that of the needle in Gieseler. Comparisons between the cup and parallel plates can be drawn, where a top serrated plate is used to measure the elastic and viscous response of the material for both geometries, along with the plate gap to monitor the expansion of the sample.

In this study we compare the parallel plate and cup geometries to understand the differences affecting the η^*, $\tan(\delta)$ and dilatation measured. Ten coals of differing properties have been used to ensure that the novel geometry is suitable for a range of samples, from low fluidity, non-swelling samples to high fluidity, swelling coals, along with an exemplary prime coking coal. The use of an alternative geometry can potentially expand the range of information obtained from coals and increase the sample size studied from 1.5 g to 3 g (increasing pellet thickness from 2.5 mm to 5 mm), allowing more representative measurements to be made for blends.

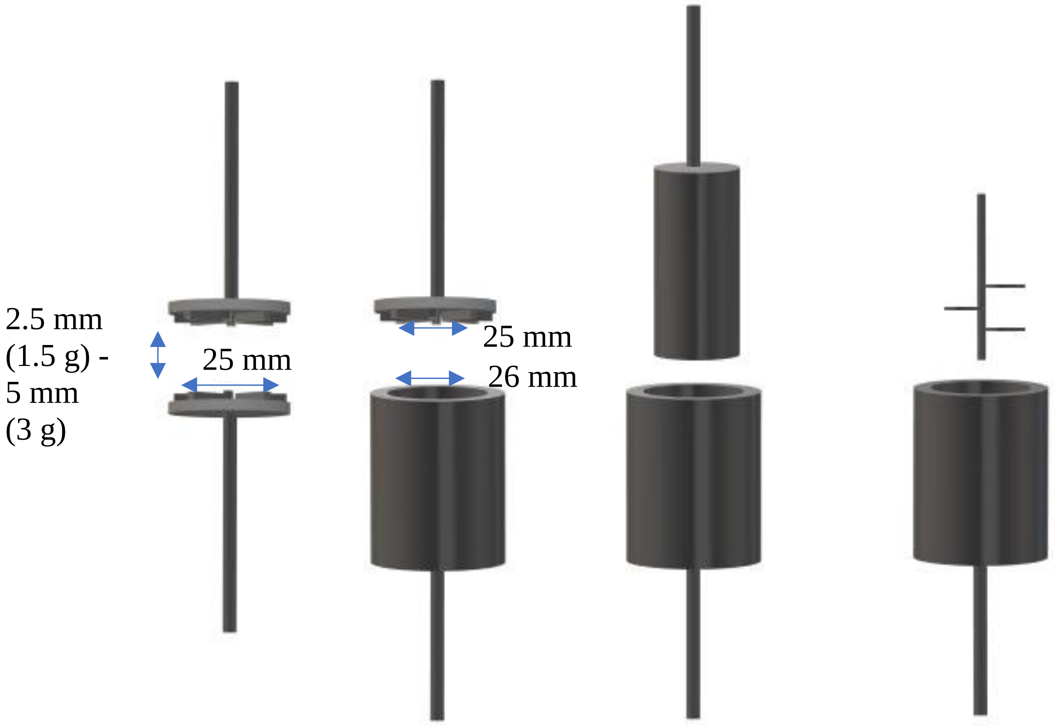

Figure 4.1: Diagram of side view of sample measurement in (from left to right) A) Parallel plate geometry (rheometry), B) Cup geometry (rheometry), C) Couette geometry (rheometry) and D) Gieseler plastometry.

4.2. Experimental

A suite of 10 coals with varying fluidity and coking properties were tested. Relevant coal properties including volatile matter, ash content, maceral composition, free swelling index, dilatation (measured using Audibert-Arnu dilatometer) and maximum Gieseler fluidity, are listed in Table 3.1 (chapter 3.1). Temperatures of softening, maximum fluidity and resolidification obtained by the Gieseler plastometer are presented in Table B1 (appendix B). Coals were manually crushed and sieved to achieve a particle size range of 53 – 212 μm. Pellets were formed using a 25 mm die and 5 tonnes of force applied to the coal sample to achieve a bulk density of 1200 kg m^{-3} (+/- 80 kg m^{-3}). Masses of 1.5 g were used to compare the geometries, and 3 g used to investigate the impact of mass with the cup geometry. Single tests were used to compare the coals and five tests were carried out on coals 5 (medium fluidity) and 9 (high fluidity) to assess repeatability.

A Rheometric RDA III high temperature strain-controlled rheometer was used to obtain rheological data to compare the cup and PP geometries. Strain sweep tests were performed at softening, maximum fluidity and resolidification of coal 4 to ensure measurements were made within the linear viscoelastic region of the samples (Figure B1, Appendix B). Consequently, tests were performed using a strain of 0.1% (0.36 ^{o} angle swing) and a frequency of 1 Hz. Coals were heated at a heating rate of 3 ^{o}Cmin^{-1} from 350 to 500 ^{o}C where nitrogen was used to ensure tests were performed in an inert atmosphere. Strain was applied through the bottom plate (PP) or cup (cup), and the resultant stress was measured by the top plate to calculate complex viscosity (η^*) and tan(δ) from Equations 4.1 – 4.6. A constant force of 200 g was applied to the sample to reduce slip and a sensitivity of 20 g was used to ensure the top plate could move in response to expansion and contraction. Plate gap measurements were made throughout the test to understand how the coal samples expanded and contracted.

The point of softening was identified as a maximum in complex viscosity before the increase in fluidity (decrease in complex viscosity) moving towards maximum fluidity. Maximum fluidity was identified as the minimum in complex viscosity (η^*_{min}). Resolidification was identified as the point at which complex viscosity ceased to increase. A graphical example of this is shown in Figure 4.2. Values of minimum complex viscosity (η^*_{min}) were also checked using a binomial fitting, the 1st differential of which provided the temperature of maximum fluidity (TMF) and η^*_{min}. All viscoelastic data was smoothed using the Savitzky – Golay method, where a third order polynomial was fitted to every 10 data points, through a linear least squares method, and the smoothed values calculated from the coefficients of the polynomial to reduce the scatter of rheological data.

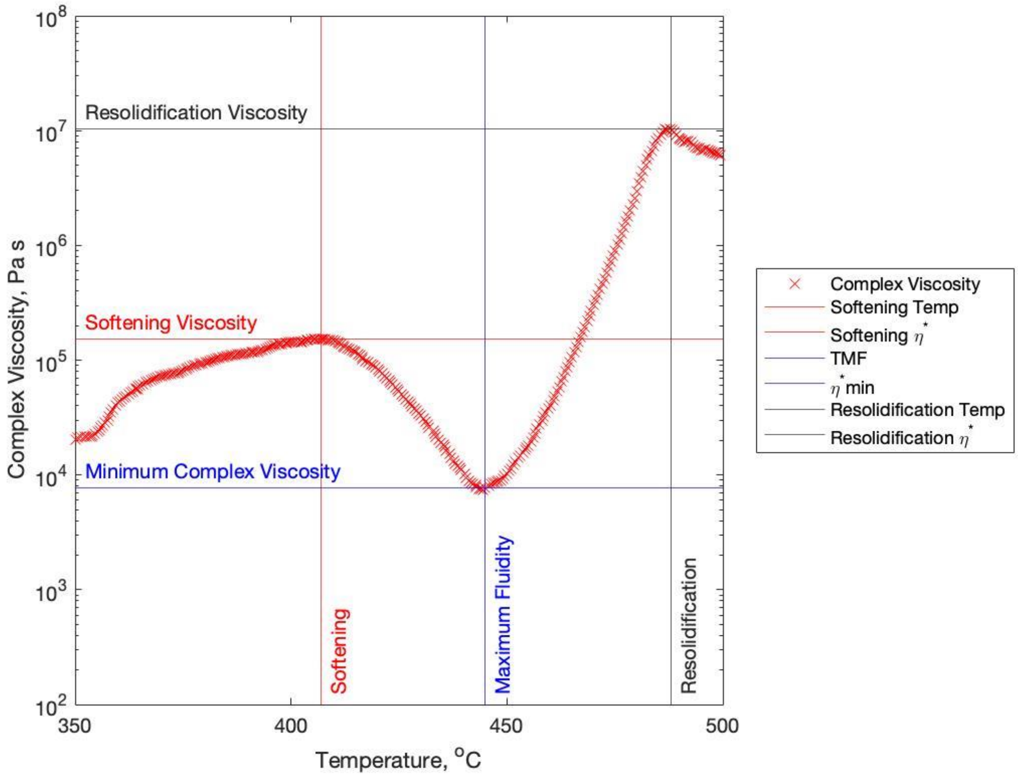

Figure 4.2: Example of the complex viscosity softening, maximum fluidity and resolidification measurements (coal 10 measured with the PP geometry at 1.5 g).

4.3. Results and Discussion

4.3.1. Repeatability

The repeatability of the PP and cup geometry measurements were determined using a medium fluidity coal (coal 5) and a high fluidity coal (coal 9). It was assumed that the standard deviations (SDs) obtained from these tests could then be applied to the other coals for identifying any significant differences between the geometries. Both coals were tested five times in each geometry, and the relative standard deviations (RSDs) calculated for η*, tanδ and plate gap. Figure 4.3 shows the variation of complex viscosity with temperature for both coals and geometries. Table 4.1 lists the mean values and RSDs for the complex viscosity (at points of softening, maximum fluidity and resolidification), tanδ and plate gap measurements for the two coals with both geometries.

Table 4.1: Relative standard deviations (RSDs) of repeat tests of coal 5 and 9 in the PP and cup geometries for η^**, tan*δ *and plate gap. For* η^**, RSDs at softening, maximum fluidity (*η^*_{Min}*) and resolidification were calculated. For tan*δ*, RSDs at sol point, maximum tan*δ*, gel point and tan*δ *at 500 °C (where medium fluidity coals did not exhibit a gel point due to high softening temperature). For plate gap, RSDs were calculated at the maximum during softening (PP) or at maximum fluidity (cup. As* η^* *are presented using* $\log_{10}$ *axes, the errors have been given in both a standard and* $\log_{10}$ *% (the latter in brackets).*

Coal/Geometry	η^* (Pa s)			*Tan*δ			*Plate Gap (mm)*
	Softening	*Maximum Fluidity*	*Resolidification*	*Sol Point*	*Max Tan*δ	*Gel Point*	*Maximum*
Coal 5/PP	6.13 x 10^5 Pa s +/- 33.2% (1.5%)	1.94x10^4 Pa s +/- 9.39% (1.0%)	4.57x10^5 Pa s +/- 13. 3% (1.1%)	448 +/- 1.79%	2.93 +/- 8.1%	N/A	119% +/- 6.1%
Coal 5/Cup	5.33x10^4 Pa s +/- 51.7% (1.7%)	1.03x10^4 Pa s +/- 12.9% (1.1%))	3.44x10^5 Pa s +/- 6.15% (0.8%)	455 +/- 1.85%	3.03 +/- 10.5%	N/A	152% +/- 5.9%
Coal 9/PP	2.89x10^5 Pa s +/- 15.6 (1.2)	1.95x10^3 Pa s +/- 23.3% (1.4%)	2.83x10^6 Pa s +/- 21.1% (1.3%)	412+/- 0.57 %	2.94 +/- 32.5%	434 +/- 2.65%	107% +/- 4.9%
Coal 9/Cup	6.81x10^4 Pa s +/- 14.4% (1.2)	3.03x10^3 Pa s +/- 17.5% (1.2)	1.64x10^6 Pa s +/- 1.03% (0.01%)	414 +/- 1.78%	3.12 +/- 54.2%	436 +/- 2.78%	130% +/- 8.2%

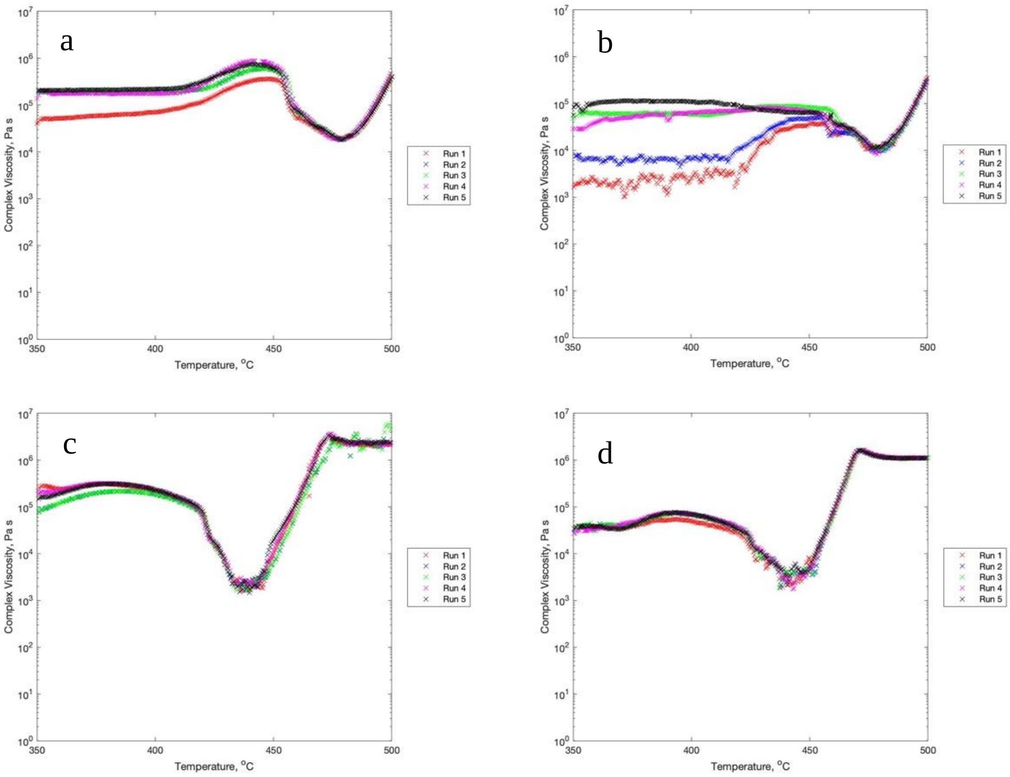

Figure 4.3: Complex viscosity as a function of temperature for a) coal 5 measured by the PP, b) coal 5 measured by the cup, c) coal 9 measured by the PP and d) coal 9 measured by the cup

The cup geometry exhibited greater variability prior to softening due to increased propensity for variable slip to occur due to increased contact surface area, compared with the PP (Figure 4.3 above) and this is most noticeable for coal 5 due to the higher temperature of softening and lower fluidity, compared with coal 9. However, despite this low temperature variability, the RSDs were lower for the cup for coal 9, compared with the PP over the softening range for measured complex viscosities (Table 4.1). All RSDs for measured complex viscosities of both PP and cup were less than 1.7%, logarithmic scale, which complex viscosity was plotted as.

Maximum tanδ RSDs were significantly high, particularly for coal 9, which was due to the fluctuations and low values in G’ (where tanδ = G’/G”). Consequently, lower G’ values were found for coal 9, compared with coal 5, as a function of higher fluidity. The gel point for coal 5 could not be measured due to complete resolidification occurring at temperatures greater than 500 °C. RSDs for plate gap were greater for the PP for coal 5 due to sample displacement from lack of retaining walls, compared with the cup.

4.3.2. Comparisons between the PP and Cup Geometries with 1.5 g Samples for Viscoelastic Properties

4.3.2.1. Complex Viscosity

For each geometry, the correlations between the measured values of G', G'' and η^* at temperatures of softening, maximum fluidity and resolidification were high ($R^2 > 0.98$) so, therefore, only η^* is considered for comparing the two geometries. The viscoelastic data for coals 1 – 10 at softening, maximum fluidity and resolidification are listed in Table 4.2, and their behaviour is presented in Figures 4.4a – j for the two geometries. Coals 1 – 3 exhibit very little fluidity, with differences being found between the geometries for these coals due to the slip of the solid pellet in the cup leading to lower values of η^* (increased slip, reducing the measured viscosity). However, increases in complex viscosity occurred during resolidification, suggesting that both PP and cup were sensitive to elastic changes (Figures 4.4a-c).

For the medium fluidity coal 4, apart from differences during initial stages of softening due to slip in the cup, no significant differences were evident during the fluid range (Figure 4.4d). For coal 5, the differences during resolidification could again be due to slip effects in the cup (Figure 4.4e).

Coals 6 – 10 all display high fluidity with η^*_{min} values between $10^3 – 10^4$ Pa s, and all showed similar trends in η^* during softening, maximum fluidity and resolidification with generally good agreement between the two geometries with differences only being evident at the onset of softening and when resolidification was close to completion (Figures 4.4f-j). For example, for coals 8 and 9, differences were found between the geometries on initial softening (as for all coals) where the cup detected a later onset of softening. For coal 9, during resolidification, the cup measured a greater rate of increase in elastic behaviour, compared with the PP.

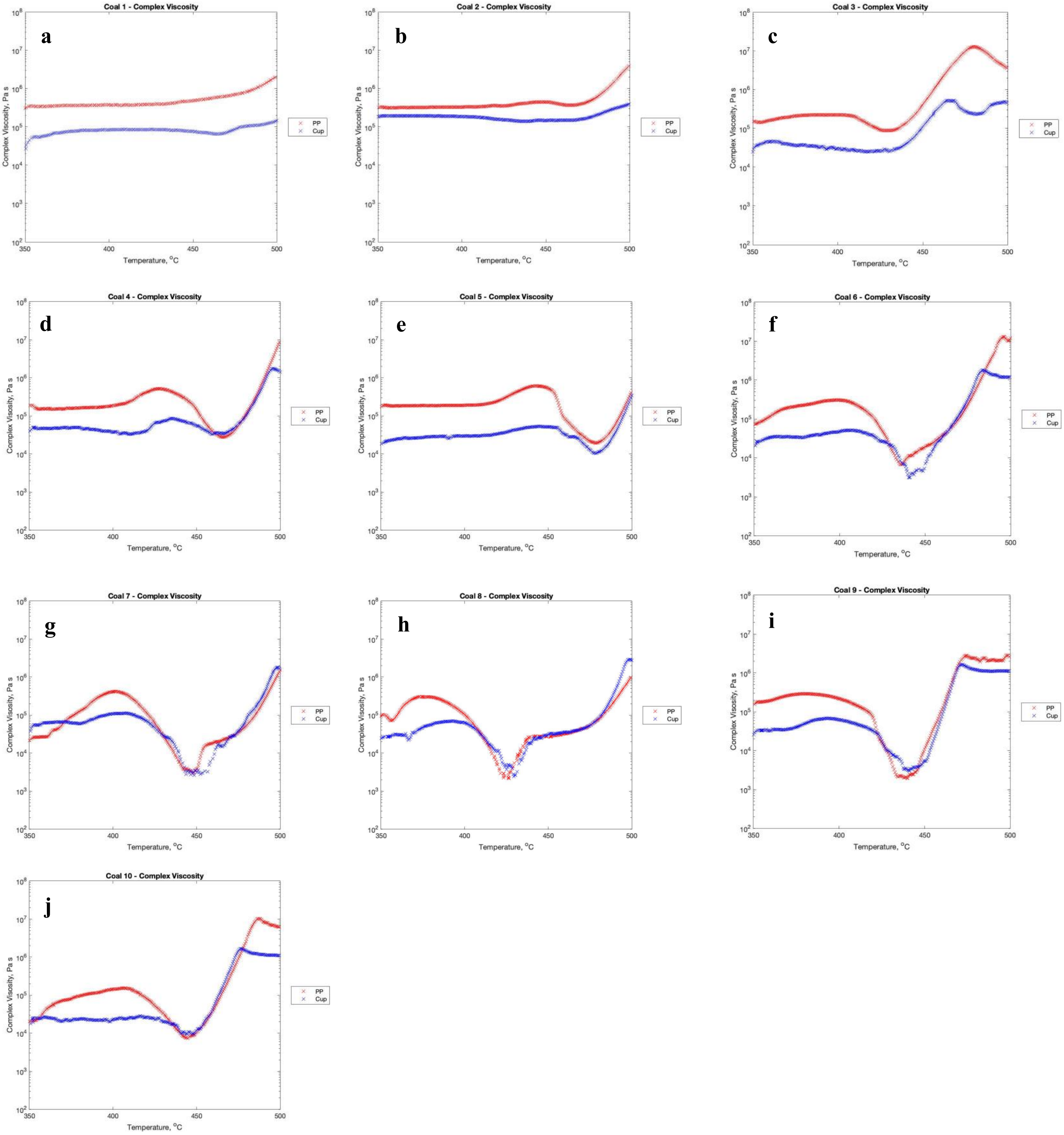

Figure 4.4: Complex viscosity as a function of temperature for PP and cup geometries at 1.5 g for a) coal 1, b) coal 2, c) coal 3, d) coal 4, e) coal 5, f) coal 6, g) coal 7, h) coal 8, i) coal 9, j) coal 10.

Further evidence of agreement between the two geometries is provided by the correlations between the PP and cup measurements for softening, maximum fluidity and resolidification for both complex viscosity and temperature. Table 4.3 lists the R^2 values for these correlations, which are presented in Appendix B (Figures B2a - f). Since coal 1 did not exhibit any viscoelastic behaviour (consistent with the measurement of 0 ddpm from Gieseler fluidity), and hence no measurable value for viscosity and temperature, only coals 2 – 10 were used in the correlations. At softening, Table 4.3 indicates that reasonable agreement was found for viscosity measurements (R^2 = 0.82) and good agreement for temperatures of softening (R^2 = 0.97). At maximum fluidity, both viscosity (η^*_{Min}) and temperatures showed good agreement (R^2 = 0.98; R^2 = 0.99). For resolidification, there was little agreement for viscosity measurements (R^2 = 0.11), but reasonable agreement was obtained for temperature (R^2 = 0.89). R^2 values are presented in Table 4.3 below and correlation plots can be found in Figures B2a – f, Appendix B.

Table 4.2: Values of η^* at softening, maximum fluidity and resolidification for coals 1 – 10 measured by the PP and cup geometries.

Coal	Geom	Softening		Maximum Fluidity		Resolidification	
		η* (Pa s)	Temp (ºC)	η* (Pa s)	Temp (ºC)	η* (Pa s)	Temp (ºC)
1	PP	N/A	N/A	N/A	N/A	N/A	N/A
	Cup	N/A	N/A	N/A	N/A	N/A	N/A
2	PP	4.50x10^5	449	3.69x10^5	464	4.16x10^6	500
	Cup	1.50x10^5	454	1.50x10^5	465	4.01x10^5	500
3	PP	2.25x10^5	403	8.73x10^4	429	1.29x10^7	480
	Cup	4.04x10^4	369	2.58x10^4	428	5.27x10^5	465
4	PP	5.19x10^5	428	2.79x10^4	463	9.76x10^6	500
	Cup	8.55x10^4	436	3.39x10^4	466	1.76x10^6	496
5	PP	5.28x10^5	443	2.24x10^4	478	4.45x10^5	500
	Cup	1.76x10^5	445	1.58x10^4	480	1.97x10^5	500
6	PP	3.07x10^5	398	6.87x10^3	436	1.30x10^7	496
	Cup	5.20x10^4	407	3.03x10^3	443	1.81x10^6	484
7	PP	4.18x10^5	401	3.48x10^3	444	1.53x10^6	500
	Cup	1.13x10^5	407	2.34x10^3	450	1.80x10^6	499
8	PP	3.02x10^5	378	2.30x10^3	425	1.01x10^6	500
	Cup	7.00x10^4	393	3.94x10^3	427	2.92x10^6	498
9	PP	1.17x10^5	395	2.23x10^3	435	2.19x10^7	494
	Cup	5.25x10^4	393	1.61x10^3	436	1.90x10^6	475
10	PP	1.52x10^5	407	7.72x10^3	445	1.03x10^7	488
	Cup	2.83x10^4	416	9.42x10^3	445	1.67x10^6	477

Table 4.3: Cross-geometry correlations R^2 correlations for temperatures complex viscosity at softening, maximum fluidity and resolidification.

		PP					
		η^* Soft	T Soft	η^*_{Min}	TMF	η^* Resol	T Resol
Cup	η^* Soft	0.82					
	T Soft		0.97				
	η^*_{Min}			0.98			
	TMF				0.99		
	η^* Resol					0.11	
	T Resol						0.89

4.3.2.2. Tanδ

The sol point, maximum tanδ, the temperature of maximum tanδ and the gel point are listed in Table 4.4, and plots of tanδ as a function of temperature shown in Figures 4.5a – j. The sol point is where a material starts to behave predominantly as a fluid, as opposed to a solid, identified as the point at which tanδ increases above 1 where the viscous forces exceed that of the elastic forces. Gel point is where a material behaves predominantly as a solid, after behaving as a fluid, and hence tanδ decreases below 1. Coals 1 – 3 did not exhibit sol and gel points as insufficient fluidity was developed and so, by definition, there is good agreement between the two geometries (Figures 4.5a-c). For coals 4 – 10, sol points were within 5 °C between the two geometries, as were the temperatures of maximum tanδ (Table 4.4). Further, all the fluidity coals exhibited good agreement between the PP and cup geometries from 350 °C to the sol point (Figures 4.5d-j), however, excessive scatter for tanδ at values *ca.* >2 make comparisons in maximum tanδ difficult. For coals 4 and 5 measured by the PP, the gel point was above 500 °C, where this was also the case for coal 5 measured by the cup. For all the high fluidity coals, there was some deviation in gel points where the cup generally measured a lower gel point, possibly due to the coal sample resolidifying more at the walls. However, correlating the 4 parameters between the geometries gave R^2 values above 0.95 for the fluid coals (Table 4.5, the correlation plots are shown in Appendix B (Figures B3a – d). Therefore, tanδ is most useful to help understand the initial softening behaviour of the coals.

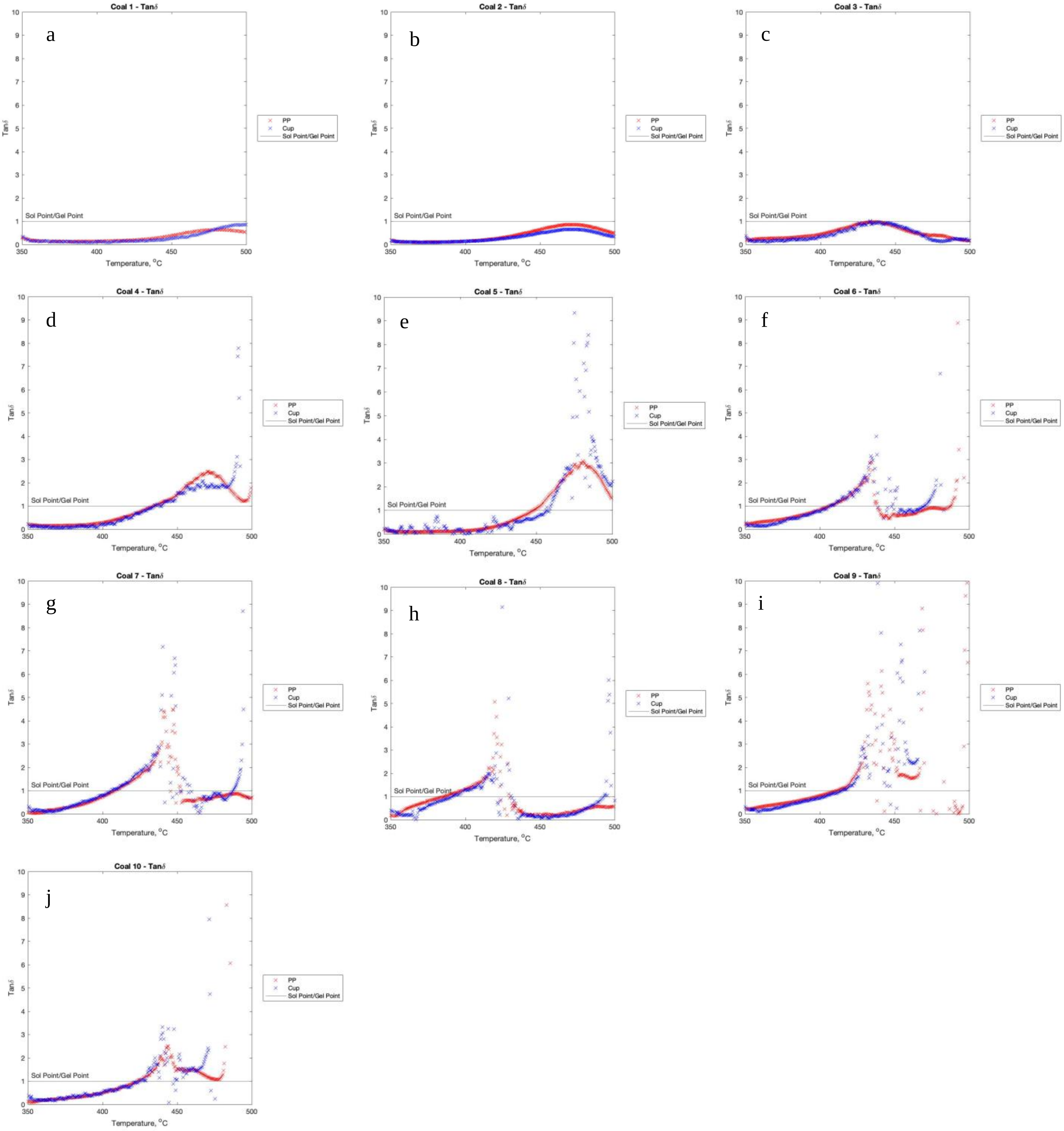

Figure 4.5: Tanδ as a function of temperature for PP and cup geometries at 1.5 g for a) coal 1, b) coal 2, c) coal 3, d) coal 4, e) coal 5, f) coal 6, g) coal 7, h) coal 8, i) coal 9, j) coal 10.

Table 4.4: Sol point, maximum tanδ, temperature of maximum tanδ and gel point as measured by tanδ from PP and cup geometries.

Coal	Geometry	Sol Point (oC)	Max Tanδ	Max Tanδ Temperature (°C)	Gel Point (oC)
1	PP	N/A	0.633	478	N/A
	Cup	N/A	0.853	497	N/A
2	PP	N/A	0.855	469	N/A
	Cup	N/A	0.649	469	N/A
3	PP	N/A	0.961	434	N/A
	Cup	N/A	0.935	437	N/A
4	PP	435	2.18	467	>500
	Cup	435	1.91	467	493
5	PP	450	2.92	477	>500
	Cup	446	3.03	482	>500
6	PP	407	2.91	434	439
	Cup	406	3.14	434	439
7	PP	409	3.25	442	452
	Cup	406	2.89	437	460
8	PP	386	3.71	419	430
	Cup	391	2.87	420	431
9	PP	409	2.94	431	434
	Cup	406	3.11	427	430
10	PP	423	2.17	444	486
	Cup	426	2.3	442	473

Table 4.5: Correlation values for PP – Cup R^2 correlation comparisons for sol point (coals 4 – 10), maximum tanδ (max tanδ, coals 1 – 10), temperature of maximum tanδ (Max Tanδ T, coals 1 – 10) and gel point (coals 6 – 10).

		PP			
		Sol Point	Max Tanδ	Max Tanδ T	Gel Point
Cup	Sol Point	0.99			
	Max Tanδ		0.95		
	Max Tanδ T			0.97	
	Gel Point				0.95

4.3.2.3. Gieseler Fluidity

Correlation R^2 values for complex viscosity and tanδ with Gieseler fluidity are listed in Tables 4.6 and 4.7. Figures B4a – j and B5a – h in Appendix B present the correlation plots. Softening temperatures and sol points showed good correlations with Gieseler softening temperature, with R^2 values >0.9. Similarly, R^2 values above 0.9 were found between

Gieseler TMF and temperature of maximum tanδ, as well as with complex viscosity TMF. For resolidification, only complex viscosity showed any correlation with Gieseler temperature of resolidification, where the cup exhibited a higher R^2 value of 0.85, compared with 0.72 for the PP. Gel point showed no correlation with temperatures of resolidification from Gieseler plastometry.

Reasonable correlations exist between log(η^*_{min}) and log(Gieseler fluidity), with R^2 values of 0.96 and 0.87 for the PP and cup, respectively (Table 4.6). However, for the five high fluidity coals, the ordering differed (Figures B4a – j, Appendix B), coals 8-10 had similar Gieseler fluidities (Table 3.1) but coal 10 had a significantly higher η^*_{min} than coals 8 and 9 (Table 4.2). This was due to the maximum rotation of the instrument of 30000 ddpm, so sensitivity above this was not possible. Coal 7 had a similar η^*_{min} to coals 8 and 9, but it had a lower Gieseler fluidity. These differences for the high fluidity coals could have arisen from how fluidity is measured, i.e., high torque, spinning needle (Gieseler) as opposed to an oscillating plate/cup at small oscillatory amplitude shear rates (Nomura et al, 1999). Here, strain sweep tests show that at a strain of 1%, G' and G" begin to drop, showing that the material is outside of the linear viscoelastic range. Therefore, at high torque and frequencies, it is possible that the macromolecular structures in the coals are forced apart, breaking intermolecular bonds, which for high fluidity coals could give rise to increased measured fluidity and loss of viscoelastic behaviour (Nomura et al, 1999).

Tanδ only showed correlations with Gieseler fluidity for sol point and maximum tanδ temperature, when compared with Gieseler softening temperature and TMF, respectively (Table 4.7). However, maximum tanδ and gel point showed no correlation with the respective Gieseler parameters (fluidity and resolidification temperature). Lack of correlation for maximum tanδ was due to the scatter in this parameter, as iterated before where η^*_{min} should be used for maximum fluidity measurements. For gel point, the differences were due to the intrinsic differences between the parameters; Gieseler measures empirical fluidity (any change in torque) whereas gel point measures the point at which the coal behaves more like a solid compared with a fluid (tanδ < 1).

Table 4.6: Correlation R^2 values between complex viscosity and Gieseler fluidity parameters (coals 2, 4 – 10 were used for the correlations since Gieseler fluidities were only obtained for these samples).

	Gieseler Fluidity		Gieseler T Soft		Gieseler TMF		Gieseler T Resol		Log(Gieseler Fluidity)	
Parameter	PP	Cup	PP	Cup	PP	Cup	PP	Cup	PP	Cup
η^*_{min}	0.41	0.43								
Tsoft			0.97	0.93						
TMF					0.92	0.92				
T resol							0.72	0.85		
Log(η^*_{min})									0.96	0.87

Table 4.7: Correlation R^2 values between tanδ and Gieseler fluidity parameters.

	Gieseler Fluidity		Gieseler T Soft		Gieseler TMF		Gieseler T Resol	
Parameter	PP	Cup	PP	Cup	PP	Cup	PP	Cup
Max Tanδ	0.48	0.44						
Sol Point			0.94	0.91				
Max Tanδ T					0.90	0.93		
Gel Point							0.15	0.31

4.3.2.4. Coal Property Correlations with Viscoelastic Measurements

Tables 4.8 and 4.9 below list the R^2 values found for the correlations between complex viscosity and tanδ parameters with volatile matter content and rank and these correlations are shown in Appendix B (Figures B6 – B9).

Table 4.8: Correlation R^2 values for complex viscosity with volatile matter content and mean vitrinite reflectance for both PP and cup geometries (based on correlations with coals 2 – 10, since coal 1 did not show any viscoelastic behaviour).

	Volatile Matter		MVR	
Parameter	PP	Cup	PP	Cup
η* soft	0.89	0.87	0.85	0.89
η* min	0.39	0.5	0.25	0.34
η* resol	0.64	0.36	0.76	0.32

Table 4.9: Correlation R^2 values for tanδ with volatile matter content and rank for both PP and cup geometries (based on tanδ values in Table 4.4).

	Volatile Matter		MVR	
Parameter	PP	Cup	PP	Cup
Sol Point	0.73	0.72	0.64	0.64
Max Tanδ	0.24	0.25	0.12	0.12
Gel Point	0.15	0.75	0.21	0.64

4.3.2.4.1. Volatile Matter

Complex viscosity at softening showed a correlation with volatile matter for both the PP and cup geometries, where R^2 values of 0.89 and 0.87 were found (Table 4.8; R^2 values below 0.9 as the low-softening coal 3 had the highest volatile matter). However, the minimum complex viscosity and resolidification viscosities did not correlate with volatile matter content, although only using the fluid coals, 4 – 10, some correlations were found for both geometries. At minimum complex viscosity, R^2 values of 0.39 and 0.5 were found for the PP and cup but increased to 0.80 and 0.64 when only coals 4 – 10 were used. At resolidification R^2 values of 0.64 and 0.36 were found for the two geometries but changed to 0.62 and 0.68 when only coals 4 – 10 were used.

Maximum tanδ did not show any correlation with volatile matter due to the scatter in the data (Appendix B, Figure B8c & d, R^2 0<0.25). However, the sol point showed moderate correlation, with R^2 values of 0.73 and 0.72 for the PP and cup geometries. Gel point gave R^2 values of 0.18 and 0.75 for the PP and cup. The low value for the PP was likely due to fewer coals exhibiting a gel point in this geometry, where the cup measured a gel point for coal 4, unlike the PP (Table 4.9).

4.3.2.4.2. Mean Vitrinite Reflectance

At softening, viscosity correlated reasonably well with MVR (R^2 values of 0.85 for the PP and 0.89 for the cup, Table 4.8). At maximum fluidity, no correlation was found with R^2 values of 0.25 and 0.34 for the PP and cup geometries (Table 4.8). At resolidification, the PP showed a better correlation between complex viscosity and MVR, with an R^2 value of 0.76 (compared with 0.32 for the cup). No correlations were found between tanδ and MVR with all R^2 values below 0.65.

4.3.3. Plate Gap

Expansion and contraction of coals under carbonisation was measured using an Audibert-Arnu dilatometer, where the three parameters obtained are contraction (contraction of the coal during softening), dilatation (difference between the beginning coal thickness and the end of swelling) and swelling (difference between maximum contraction and maximum swelling). In the rheometry tests, the top plate exerted a constant force of 200 g throughout the test to ensure sufficient contact with the sample to enable measurements to be made, and a sensitivity of 20 g (where if the sample exerts > 20 g force against the top plate, the top plate moves up, measured as an increase in plate gap). For the plate gap measurements, initial expansion occurs from volatile release (prior to softening), followed by a contraction (akin to the standard Audibert-Arnu dilatation test) when softening occurs. Swelling then occurs, but this is dependent on geometry. Fluid material was displaced in the PP during softening, giving rise to a maximum in swelling during softening. For the cup, in contrast, the volatile force allowed the expansion of the sample at maximum fluidity to be obtained. For the PP, all coals exhibited a decrease at maximum fluidity and during resolidification due to fluid displacement by the top plate.

Due to the differences between plate gap measurements (from the PP and cup geometries) and the Arnu-Audibert dilatometer the two different techniques were compared using dilatation (from the dilatometer) and compared against the swelling in the plate gap. These two measurements were used as this has similarities where a needle or plate is forced upwards by an expanding coke sample to reach a maximum, thus this maximum can be compared.

Tables 4.10 – 4.12 detail the plate gap values, plate gap temperatures and dilatation information for coals 1 – 10. All plate gap values are given as percentages with respect to the initial thickness of the coal pellet. An example of a plate gap measurement is shown in Figure 4.6, where the four events are labelled for the PP (red) and cup (blue) geometries. Figures 4.7a – j show the plate gap variations as a function of temperature for all the coals. For the cup, the medium fluidity high rank coal 5 (MVR = 1.41) showed continuous expansion, where rank and reduced pore coalescence restricted sample displacement by the top plate, suggesting such a coal exerts high gas and coke pressure. The other fluid coals (4, 6 – 10) showed contractions after maximum fluidity due to pore coalescence and weak coke strength. Therefore, dilatation measurements were taken at the point where there was no more decrease in plate gap (apart from coal 5 measured by the cup, where dilatation was taken at the point at which there was no further increase in plate gap).

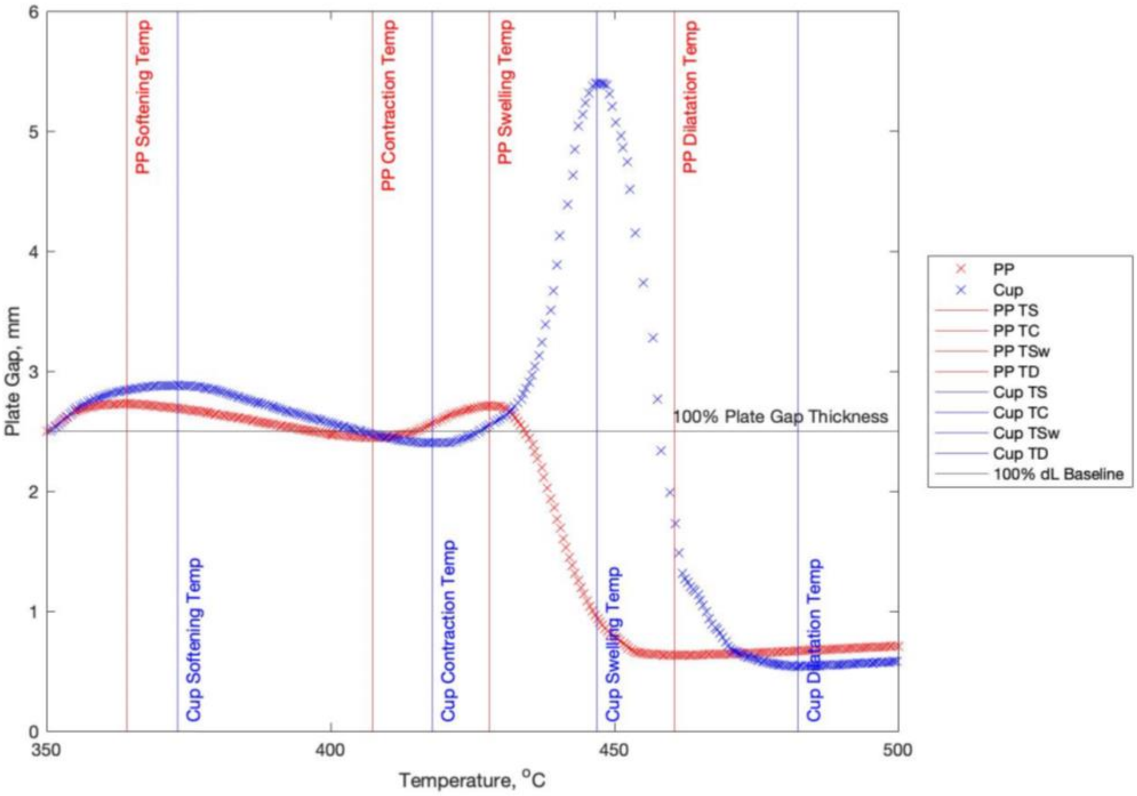

Figure 4.6: Example of plate gap measurements for the high fluidity coal 7 for the PP and cup geometries. Plate gap values were obtained at the temperatures indicated.

Table 4.10: Temperatures of plate gap measurements at maximum swelling

Plate Gap	Temp Max Swelling	
Coal	PP	Cup
1	440	448
2	416	412
3	429	424
4	458	466
5	467	500
6	428	440
7	428	447
8	411	430
9	420	438
10	358	446

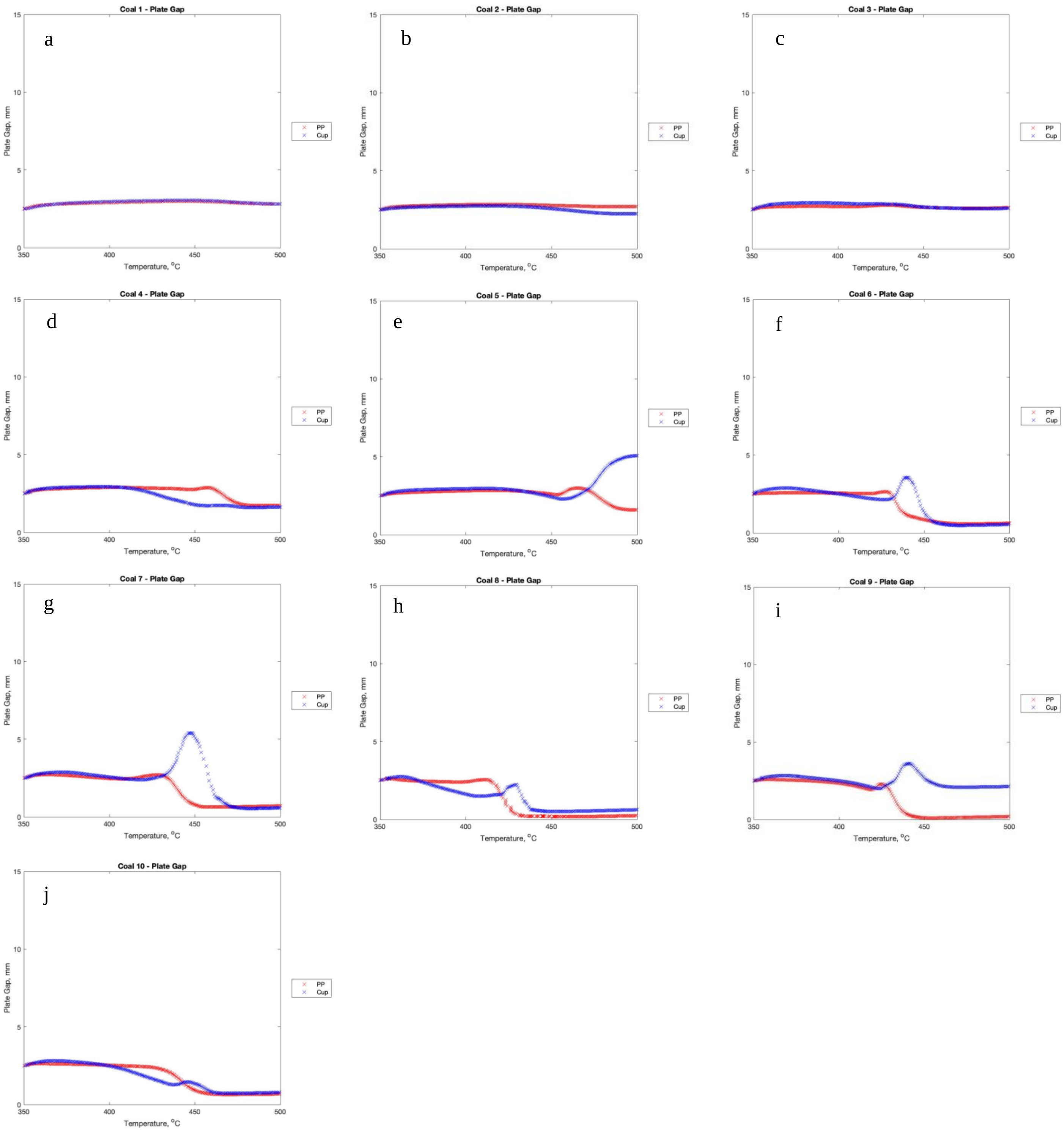

Figure 4.7: Plate gap as a function of temperature for PP and cup geometries at 1.5 g for a) coal 1, b) coal 2, c) coal 3, d) coal 4, e) coal 5, f) coal 6, g) coal 7, h) coal 8, i) coal 9, j) coal 10.

4.3.3.1. Geometry Comparison

Coals 1-3 gave good agreement between the two geometries due to their virtual lack of contraction and expansion (Coal 2 showed some deviation after 450 ^{o}C). Small differences were found for the medium fluidity coal 4. However, coal 5 showed the greatest differences of all the coals, due to gas pressure from the sample in the cup giving rise to continuous increases in plate gap to 500 ^{o}C when resolidification occurred. All the high fluidity coals, apart from coal 8, showed agreement between the geometries up to softening.
Correlation plots are shown in Appendix B (Figures B10a & b) and values are listed in Table 4.13. Correlations between the geometries for temperatures and values for swelling were 0.54 and 0.10, respectively.

Table 4.11: Plate gap measurements: Maximum swelling

Plate Gap	Max Swelling (%)	
Coal	PP	Cup
1	120	122
2	114	110
3	112	115
4	115	70
5	119	152
6	106	142
7	109	216
8	102	90
9	107	130
10	105	58

Table 4.12: Dilatation percentage, temperature of softening, temperature of contraction and temperature of dilatation for measurements from the Audibert-Arnu dilatation test

Dilatation	Dilatation (%)	Temp of Softening (^{o}C)	Temp of Contraction (^{o}C)	Temp of Dilatation (^{o}C)
1	6	442	490	490
2	-22	404	447	470
3	17	366	425	443
4	62	394	440	466
5	70	427	460	488
6	152	352	402	449
7	253	362	400	473
8	300	334	378	487
9	168	352	404	452
10	182	352	398	446

During resolidification, coals 4, 6 – 10 were displaced by the force of the top plate, but through different mechanisms for the two geometries. For the PP, samples were displaced due to lack of retaining walls, therefore displacement occurred during softening where fluid material poured over the sides of the plate. For the cup, sample was displaced due to weak semi-coke strength. The force of the top plate was able to push through the weak semi-coke, where these samples had likely formed coalesced pores. The fact that displacement does not occur in the cup until during resolidification suggests that it could be used as a proxy for gas pressure for these coals.

Table 4.13: R^2 values for inter-geometry correlations of temperature of swelling (TSwell) and swelling plate gap (Swel).

	T Swell	Swel
R^2	0.54	0.1

Table 4.14: R^2 values for geometry – dilatometry correlations, with the following parameters. Dilatometry: Temperature of dilatation (T Dil) and dilatation (Dil). Plate gap: Temperature of swelling (T Swell) amd swelling plate gap (Swel).

Dilatometry	T Dil		Dil (%)	
Plate Gap	PP	Cup	PP	Cup
T Swell	0.46	0.37		
Swel			0.81	0.18

4.3.3.1.1. Comparisons with Dilatometry

Correlation plots are shown in Appendix B (Figure B11a – d) and the R^2 values are listed in Table 4.14. Comparing plate gap measurements with dilatometry, there were no strong correlations, although the PP showed an R^2 of 0.81 between swelling in the rheometer and dilatation in the dilatometer. Conversely, the cup afforded no correlation for either temperature or magnitude of swelling with dilatation. A contributary factor for the poor correlation for the cup was the continuous expansion of coal 5 (maximum swelling in cup of 151.9%), where this sample exhibited a dilatometry dilatation of only 70% but exhibited the greatest expansion of the 10 coals in rheometry tests. Indeed, removing coal 5 from the correlation of cup swelling with dilatation increases the R^2 value from 0.18 to 0.60. Coal 8 exhibited the greatest dilatometry dilatation of 300%, but with a plate gap increase of only 90% in the cup (102% in the PP).

4.3.4. Cup geometry with 3 g samples

4.3.4.1. Complex Viscosity – Comparing 1.5 g and 3 g

The effect of mass was studied with the cup geometry, where plate gap measurements showed that this geometry retains the entire coke sample up to maximum fluidity, unlike the PP. To understand the impact of mass upon the measurements of fluidity, a low fluidity coal, medium fluidity coal and two high fluidity coals were studied using 1.5 g and 3 g in the cup geometry. Table 4.15 details the values of η* for coals 3, 4, 6 and 10 for 1.5 g and 3 g samples at softening, maximum fluidity and resolidification, respectively. Figure 4.8a – d details the complex viscosity as a function of temperature plots for the 4 data sets.

Table 4.15: Values of η and temperatures of softening, maximum fluidity and resolidification for coals 3, 4, 6 and 10 using the cup geometry with 3 g samples.*

Coal	Softening		Maximum Fluidity		Resolidification	
1.5 g	η* (Pa s)	*Temp (°C)*	η* (Pa s)	*Temp (°C)*	η* (Pa s)	*Temp (°C)*
3	4.04×10^4	369	2.58×10^4	428	5.27×10^5	465
4	8.55×10^4	436	3.39×10^4	466	1.76×10^6	496
6	5.20×10^4	407	3.03×10^3	443	1.81×10^6	484
10	2.83×10^4	416	9.42×10^3	445	1.67×10^6	477
3 g						
3	4.83×10^4	375	4.91×10^4	429	2.79×10^6	468
4	8.02×10^4	445	8.75×10^3	468	1.61×10^6	494
6	6.10×10^4	419	3.78×10^3	444	1.54×10^6	480
10	1.02×10^5	411	1.28×10^4	447	3.19×10^6	480

The lack of fluidity for coal 3 for both 1.5 and 3 g samples (Figures 4.4c and 4.8a*)* suggests any differences were due to slip effects. There was an agreement for temperature of resolidification (465 °C), although 3 g gave a greater rate of increase in η* (Figures 4.8a), in common with coals 4, 6 and 10, due to the greater mass of resolidifying material. Differences were found for coal 4 (Figures 4.4d and 4.8b) during pre-softening (< 438 °C) due to slip effects and maximum fluidity (457 °C – 478 °C), where the 3 g sample exhibited a lower η^*_{min}, but agreement was found during resolidification (478 °C – 496 °C).

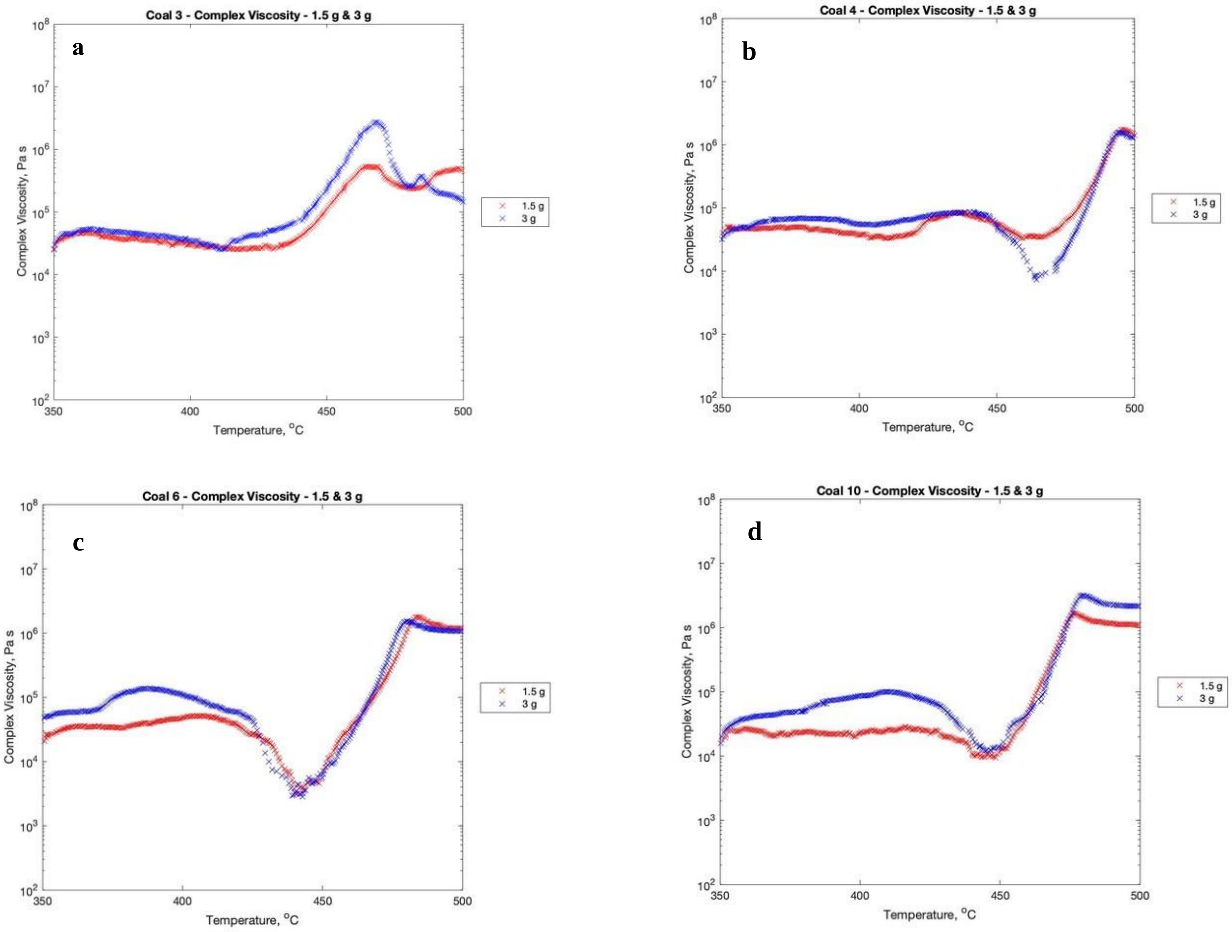

Figure 4.8: Complex viscosity as a function of temperature for 1.5 and 3 g samples measured in the cup geometry for coals a) 3, b) 4, c) 6 and d) 10.

At softening, the 3 g sample for coal 6 gave a higher temperature of maximum η* by 12 °C, compared to the 1.5 g sample (Figures 4.4f and 4.8c). This was possibly due to the increased mass of fluid material enhancing the effects of slip at low temperatures, but agreement was found at maximum fluidity and during resolidification (Figures 4.4f and 4.8c, 443 – 484 °C). The values of η* were significantly different for coal 10 where increased values were found for the 3 g sample (Figures 4.4j and 4.8d). The 3 g sample gave a greater rate of decrease in η* during softening to maximum fluidity due to increased volume of fluid material. η^*_{min} showed agreement between the 1.5 and 3 g samples with respect to temperature and magnitude (Figures 4.4j and 4.8d).

Overall, agreement obtained between the 1.5 g and 3 g samples for the medium and high fluidity coals during maximum fluidity and resolidification showed that an increased mass can be used.

4.3.4.2. Tanδ

Table 4.16 details the sol point, maximum tanδ, temperature of maximum tanδ and gel point for the 1.5 g and 3 g samples of coals 3, 4, 6 and 10 tested in the cup geometry. Figure 4.9a – d present tanδ as a function of temperature plots for these samples.

Table 4.16: Sol point, maximum tanδ, temperature of maximum tanδ and gel point for tanδ measurements of 1.5 g and 3 g samples of coals 3, 4, 6 and 10.

1.5 g	Sol Point (^oC)	Max Tanδ	Max Tanδ T	Gel Point (^oC)
Coal 3	N/A	0.935	437	N/A
Coal 4	435	1.91	467	493
Coal 6	406	3.14	434	439
Coal 10	426	2.3	442	473
3 g				
Coal 3	437	1.12	442	450
Coal 4	443	5.15	472	491
Coal 6	404	4.25	443	475
Coal 10	421	3.13	444	476

Agreements were found between 1.5 g and 3 g as follows. *Coal 3:* Agreements were found from 350 ^oC to maximum tanδ (350 ^oC – 450 ^oC), and after resolidification (490 ^oC – 500 ^oC). Here, the peak in tanδ between 450 – 470 ^oC correlates with resolidification in η*, therefore likely due to slip. *Coal 4:* Agreements were found between the geometries from 350 ^oC to the sol point, where significant scatter was found after tanδ = 2. *Coal 6*: Agreements were found between 1.5 g and 3 g from 350 ^oC to 415 ^oC, where after significant scatter was found. *Coal 10:* Akin to coal 6, agreements were found through the sol point and up to a temperature of 438 ^oC. Again, due to scatter, agreements could not be concluded for maximum tanδ or gel point. Comparing tanδ measurements for 1.5 g and 3 g for coals 3, 4, 6 and 10, it was found that, overall, increasing mass increased the temperature range in which tanδ was above 1. The only exception to this was the temperature range in which tanδ was above 1 for coal 4, where 1.5 g gave a greater range compared with 3 g. Overall, the temperature range of tanδ > 1 was increased by 12 ^oC (excluding coal 3, as this did not show a sol point at 1.5 g). This suggests that increasing mass reduces the temperature at which the coal becomes predominantly fluid, with fluid forces greater than elastic forces at the sol point. Maximum tanδ showed greater values for all 4 coals at 3 g, compared with 1.5 g, suggesting increased mass reduces the elastic forces at maximum fluidity. However, maximum tanδ temperatures were greater at 3 g, which would suggest that full fluidity onset occurs at a higher temperature, possibly due to temperature gradient across the pellet. Gel point also showed a greater temperature at 3 g, compared with 1.5 g, again possibly due to the temperature gradient across the pellet being greater. There was good agreement between 1.5 g and 3 g up to sol point. However, past the sol point, there was significant scatter, therefore the impact of mass of upon maximum tanδ and gel point could not be concluded.

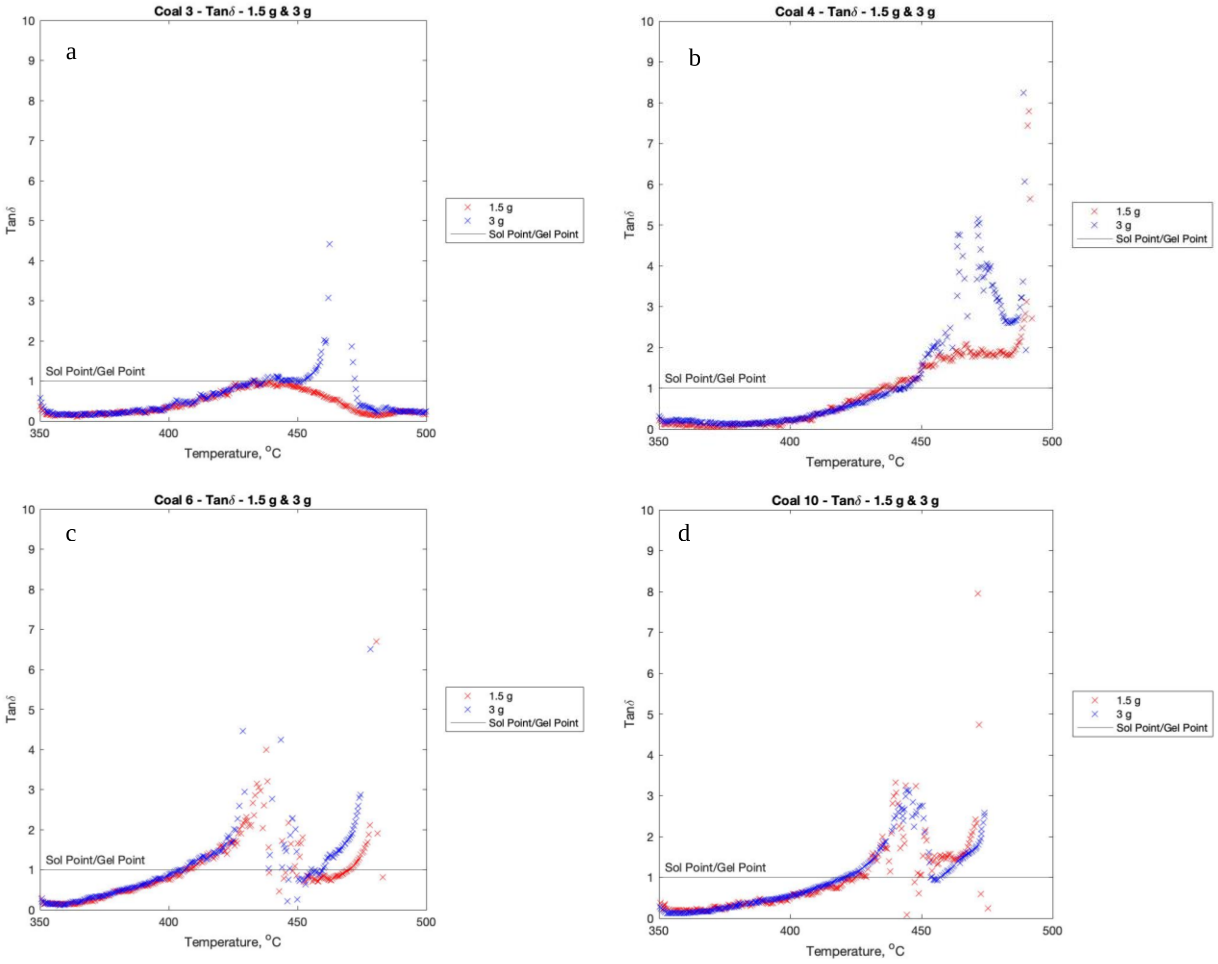

Figure 4.9: Tanδ as a function of temperature for 1.5 and 3 g samples measured in the cup geometry for coals a) 3, b) 4, c) 6 and d) 10.

4.3.4.3. Plate Gap

Table 4.17 details the maximum plate gap information for coals 3, 4, 6 and 10 tested in the cup geometry. Figures 4.10a – d show the variation in plate gap with temperature.

Table 4.17: Plate gap measurements for coals 3, 4, 6 and 10 using 1.5 and 3 g samples measured in the cup geometry, showing temperature of swelling (TSw) and swelling plate gap (Sw).

1.5 g	TSw (°C)	Sw (%)
3	424	115
4	466	70
6	440	142
10	446	58
3 g		
3	443	97
4	499	187
6	447	188
10	443	144

Comparing the 1.5 g and 3 g plate changes, Figure 4.10 indicates that the magnitude of the plate gap changes for the 3 g samples were considerably greater than for the 1.5 g samples. The initial plate gap is twice as large due to the disc being twice as thick as shown in Figure 4.10 below. Clearly, increased gas pressure provided enhanced swelling for the 3 g samples for coal 4, 6 and 10. Further, temperatures of swelling occurred at a greater temperature, apart from coal 10. Coal 4 displayed the largest change with significant expansion occurring with 3 g and no reduction in plate gap after maximum fluidity was evident, akin to coal 5 at 1.5 g in the cup, showing excessive gas pressure which gave enhanced swelling with the 3 g samples. There was also enhanced retention of coal sample for coals 6 and 10, evident from the final plate gap measurements at 500 °C, indicated in Figure 4.10. Overall, the greater magnitude of the plate gap changes with the 3 g samples could be advantageous for studying blends.

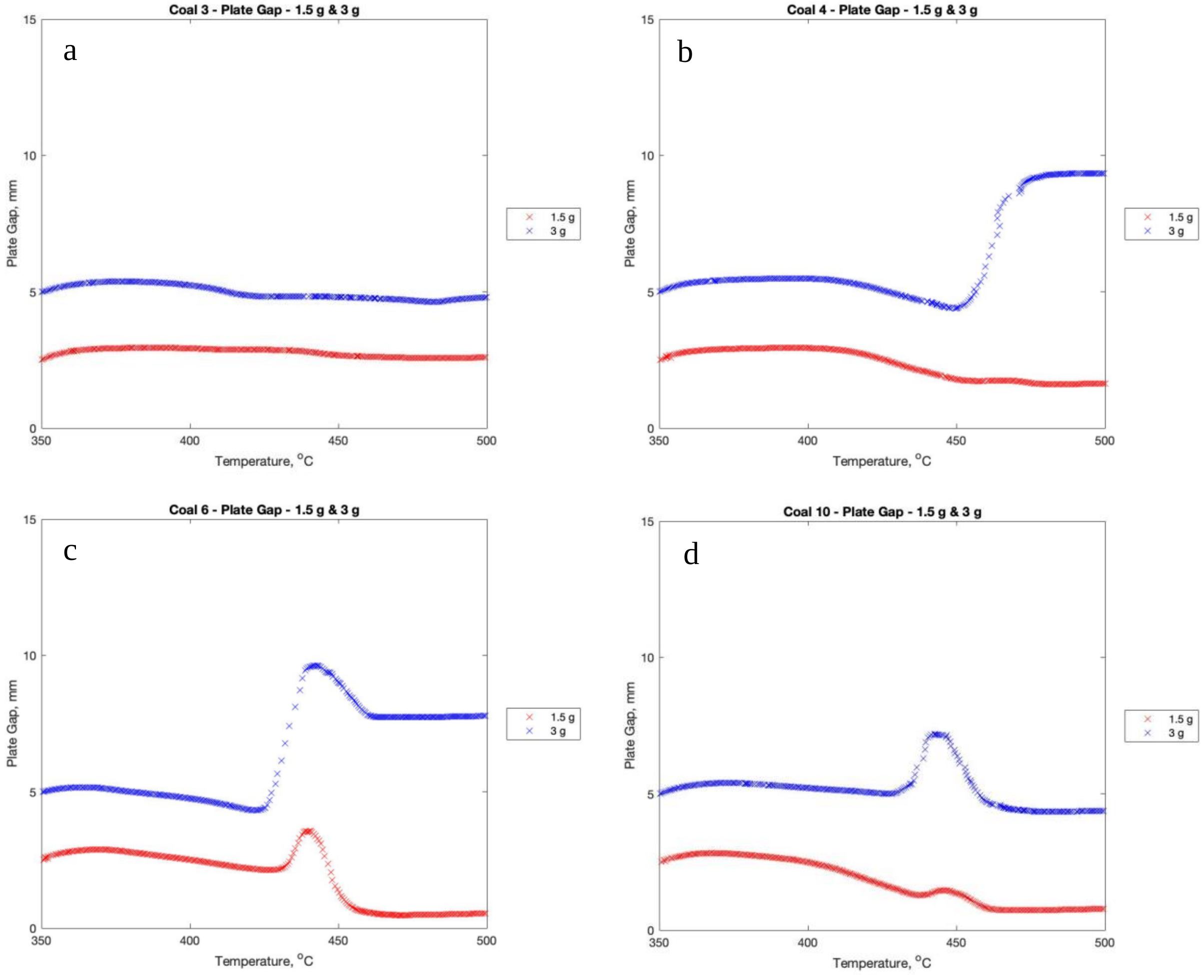

Figure 4.10: Plate gap as a function of temperature for the 1.5 and 3 g samples in the cup geometry for coals a) 3, b) 4, c) 6 and d) 10.

4.4. Conclusions

For η* measurements there was particularly good agreement between the geometries at maximum fluidity. There was no agreement with Gieseler measurements, apart from log-log correlations, therefore results from either geometry should not be expected to agree with those from Gieseler. Tanδ also showed good agreement for the two geometries, however there was significant scatter for this parameter at maximum fluidity, and there was no correlation between gel point and resolidification temperature from Gieseler. Due to the presence of retaining walls for the cup there was no agreement between the geometries for plate gap measurements, where the force of volatile release and coke expansion was directly applied against the cup, as opposed to horizontal release in the PP. However, future research could focus on understanding if the cup geometry can provide a proxy for gas pressure. The cup geometry has shown to accommodate a greater mass compared with the PP due to retaining walls, where reasonable agreement was found between 1.5 g and 3 g for η* measurements. The use of a larger mass would provide more representative results (compared with 1.5 g) and would be extremely beneficial for studying coking coal blends.

4.5. References

Adeleke, A.O., Makan, R.S., HND, P. and Ibitoye, S.A. 2007. Studies on the Gieseler Plastometry Parameters of the American Pittson Coal for Metallurgical Cokemaking at the Ajaokuta Steel plant, Nigeria. *Pacific Journal of Science and Technology*. ***8***(2), pp.208-211.

Barnes, H.A., Hutton, J.F. and Walters, K. 1989. *An introduction to rheology, Volume 3*. 1st Edition. Amsterdam: Elsevier.

Benkhelifa, H., Alvarez, G. and Flick, D. 2008. Development of a Scraper-Rheometer for Food Applications: Rheological Calibration. *Journal of Food Engineering*. ***85***(3), pp.426-434.

Castro Díaz, M., Zhao, H., Kokonya, S., Dufour, A. and Snape, C.E. 2012. The Effect of Biomass on Fluidity Development in Coking Blends Using High-Temperature SAOS Rheometry. *Energy & Fuels*. ***26***(3), pp.1767-1775.

Castro-Díaz, M., Duffy, J.J., Snape, C.E. and Steel, K.M. 2007. The Shear-Rate Dependent Viscoelastic Properties of Coal during Carbonisation. In: *International Conference on Coal Science and Technology*. *28th – 31st August 2007*. Nottingham.

Castro-Díaz, M., Duffy, J.J., Snape, C.E. and Steel, K.M. 2007. Use of High-Temperature, High-Torque Rheometry to Study the Viscoelastic Properties of Coal during Carbonization. *Journal of Rheology*. ***51***(5), pp.895-913.

Castro-Díaz, M., Edecki, L., Steel, K.M., Patrick, J.W. and Snape, C.E. 2008. Determination of the Effects Caused by Different Polymers on Coal Fluidity during Carbonization using High-Temperature 1H NMR and Rheometry. *Energy & Fuels*. ***22***(1), pp.471-479.

Castro-Díaz, M., Steel, K.M., Drage, T.C., Patrick, J.W. and Snape, C.E. 2005. Determination of the Effect of Different Additives in Coking Blends using a Combination of in situ High-Temperature 1H NMR and Rheometry. *Energy & Fuels*. ***19***(6), pp.2423-2431.

Castro-Díaz, M., Vega, M.F., Barriocanal, C. and Snape, C.E. 2015. Utilization of Carbonaceous Materials to Restore the Coking Properties of Weathered Coals. *Energy & Fuels*. ***29***(9), pp.5744-5749.

Castro-Diaz, Miguel., Snape, C., Florentino-Madiedo, L., Diaz-Faes, E. and Barriocanal, C. 2018. Importance of Biomass and Binder Selection for Coking Briquette Preparation: Their Effect on Coal Thermoplastic Properties. *Energy & Fuels*. ***32***(10), pp.10727-10736.

Clemens, A.H. and Matheson, T.W. 1995. The Effect of Selected Additives and Treatments on Gieseler Fluidity in Coals. *Fuel*. ***74***(1), pp.57-62.

Das, B., Suresh, A., Dash, P.S., Chandra, S., Díaz, M.C., Stevens, L.A. and Snape, C.E. 2018. Understanding the Unusual Fluidity Characteristics of High Ash Indian Bituminous Coals. *Fuel Processing Technology*. ***176***, pp.258-266.

Dıez, M.A., Alvarez, R. and Barriocanal, C. 2002. Coal for Metallurgical Coke Production: Predictions of Coke Quality and Future Requirements for Cokemaking. *International Journal of Coal Geology*. ***50***(1-4), pp.389-412.

Duffy, J.J., Castro-Diaz, M., Snake, C.E., Mahoney, M.R. and Steel, K.M. 2007. Combined Use of Rheometry and Microscopy to Understand Pore Structure Development during Coal Carbonization. In*: International Conference on Coal Science and Technology.28th – 31st August 2007*. Nottingham.

Duffy, J.J., Castro-Diaz, M., Snape, C.E., Steel, K.M. and Mahoney, M.R. 2007. Understanding the Mechanisms Behind Coking Pressure: Relationship to Pore Structure. *Fuel*. ***86***(14), pp.2167-2178.

Duffy, J.J., Mahoney, M.R. and Steel, K.M. 2010. Influence of Coal Thermoplastic Properties on Coking Pressure Generation: Part 2–A study of Binary Coal Blends and Specific Additives. *Fuel*. ***89***(7), pp.1600-1615.

Ferry, J.D. 1980. *Viscoelastic Properties of Polymers*. 3rd Edition. New York: Wiley.

Guelton, N. 2017. The Prediction of the Gieseler Characteristics of Coal Blends. *Fuel*. ***209***, pp.661-673.

Guerrero, A., Diez, M.A. and Borrego, A.G. 2015. Influence of Charcoal Fines on the Thermoplastic Properties of Coking Coals and the Optical properties of the Semicoke. *International Journal of Coal Geology*. ***147***, pp.105-114.

Jenkins, D.R. and Mahoney, M.R. 2015. A Mechanistic Model for the Softening of Coking Coal and Its Use for Predicting the Dilatation of Blends. *Fuel*. ***153***, pp.585-594.

Kök, M.V., Özbas, E., Karacan, O. and Hicyilmaz, C. 1998. Effect of Particle Size on Coal Pyrolysis. *Journal of Analytical and Applied Pyrolysis*. ***45***(2), pp.103-110.

Kokonya, S., Castro-Díaz, M., Barriocanal, C. and Snape, C.E. 2013. An Investigation into the Effect of Fast Heating on Fluidity Development and Coke Quality for Blends of Coal and Biomass. *Biomass and bioenergy*. ***56***, pp.295-306.

Laun, H.M., Bung, R. and Schmidt, F. 1991. Rheology of Extremely Shear Thickening Polymer Dispersions (Passively Viscosity Switching Fluids). *Journal of Rheology*. ***35***(6), pp.999-1034.

Lin, Y.G. and Winter, H.H. 1991. High-Temperature Recrystallization and Rheology of a Thermotropic Liquid Crystalline Polymer. *Macromolecules*. ***24***(10), pp.2877-2882.

Loison, R., Foch, P. and Boyer, A., 2014. *Coke: quality and production*. Elsevier.

MacPhee, J.A., Gransden, J.F., Giroux, L. and Price, J.T. 2009. Possible CO2 Mitigation via Addition of Charcoal to Coking Coal Blends. *Fuel Processing Technology*. ***90***(1), pp.16-20.

Medina-Bañuelos, E.F., Marín-Santibáñez, B.M., Pérez-González, J., Malik, M. and Kalyon, D.M. 2017. Tangential Annular (Couette) Flow of a Viscoplastic Microgel with Wall Slip. *Journal of Rheology*. ***61***(5), pp.1007-1022.

Melendi-Espina, S., Alvarez, R., Diez, M.A. and Casal, M.D. 2015. Coal and Plastic Waste Co-Pyrolysis by Thermal Analysis–Mass Spectrometry. *Fuel Processing Technology*. ***137***, pp.351-358.

Melendi, S., Diez, M.A., Alvarez, R. and Barriocanal, C. 2011. Plastic Wastes, Lube Oils and Carbochemical Products as Secondary Feedstocks for Blast-Furnace Coke Production. *Fuel Processing Technology*. ***92***(3), pp.471-478.

Melendi, S., Diez, M.A., Alvarez, R., Castro, M., Steel, K. and Snape, C.E. 2007. Rheological Behaviour of Coal Modified by Waste Plastics and Lubricating Oils. In: *International Conference on Coal Science and Technology. 28th – 31st August 2007*. Nottingham.

Meng, F., Gupta, S., French, D., Koshy, P., Sorrell, C. and Shen, Y. 2017. Characterization of Microstructure and Strength of Coke Particles and Their Dependence on Coal Properties. *Powder Technology*. ***320***, pp.249-256.

Mollah, M.M., Jackson, W.R., Marshall, M. and Chaffee, A.L. 2015. An Attempt to Produce Blast Furnace Coke from Victorian Brown Coal. *Fuel*. ***148***, pp.104-111.

Nomura, S., Kato, K., Komaki, I., Fujioka, Y., Saito, K. and Yamaoka, I. 1999. Viscoelastic Properties of Coal in the Thermoplastic Phase. *Fuel*. ***78***(13), pp.1583-1589.

Park, H.O., Bricker, J.M., Roy, M.J. and Butler, J.E. 2011. Rheology of Oscillating Suspensions of Non-Colloidal Spheres at Small and Large Accumulated Strains. *Physics of Fluids*. ***23***(1), p.013302.

Riazi, M.R and Gupta, R. 2016. *Coal to Metallurgical Coke. In Coal Production and Processing Technology*. CRC Press, pp. 377–396.

Steel, K.M., Castro-Diaz, M., Duffy, J.J. and Snape, C.E. 2009. Use of Oscillatory Shear Rheometry and Thermogravimetric Analysis to Examine the Microstructural Changes during Coal Pyrolysis/Carbonization for the Prediction of IRSID Strength Indices. *Energy & Fuels*. ***23***(4), pp.2111-2117.

Steel, K.M., Castro-Diaz, M., Duffy, J.J., Snape, C.E. and Mahoney, M.R. 2014. Influence of Thermoplastic Properties on Coking Pressure Generation: Part IV–Further Evidence of the Role of Bubble Coalescence in the Mechanism for Pressure Generation. *Fuel*. ***129***, pp.102-110.

Steel, K.M., Castro-Diaz, M., Patrick, J.W. and Snape, C.E. 2004. Use of Rheometry and 1H NMR Spectroscopy for Understanding the Mechanisms Behind the Generation of Coking Pressure. *Energy & Fuels*. ***18***(5), pp.1250-1256.

Steel, K.M., Castro-Diaz, M., Patrick, J.W. and Snape, C.E. 2006. Evidence for Network Formation during the Carbonization of Coal from the Combination of Rheometry and 1H NMR Techniques. *Fuel*. ***85***(12-13), pp.1821-1830

Steel, K.M., Dawson, R.E., Jenkins, D.R., Pearce, R. and Mahoney, M.R. 2017. Use of Rheometry and Micro-CT Analysis to Understand Pore Structure Development in Coke. *Fuel Processing Technology*. ***155***, pp.106-113.

Trinkel, V., Kieberger, N., Bürgler, T., Rechberger, H. and Fellner, J. 2015. Influence of Waste Plastic Utilisation in Blast Furnace on Heavy Metal Emissions. *Journal of Cleaner Production*. ***94***, pp.312-320.

Wei, R., Zhang, L., Cang, D., Li, J., Li, X. and Xu, C.C. 2017. Current Status and Potential of Biomass Utilization in Ferrous Metallurgical Industry. *Renewable and Sustainable Energy Reviews*. ***68***, pp.511-524.

World Steel Association. 2017. World Steel in Figures 2017. [Online]. [Accessed: 30/3/2020]. Available at: https://www.worldsteel.org/media-centre/press-releases/2017/world-steel-in-figures-2017.html

Yoshida, T., Iino, M., Takanohashi, T. and Katoh, K. 2000. Study on Thermoplasticity of Coals by Dynamic Viscoelastic Measurement: Effect of Coal Rank and Comparison with Gieseler Fluidity. *Fuel*. ***79***(3-4), pp.399-404.

Yoshimura, A. and Prud'homme, R.K. 1988. Wall Slip Corrections for Couette and Parallel Disk Viscometers. *Journal of Rheology*. ***32***(1), pp.53-67.

Yoshimura, A.S., Prud'homme, R.K., Princen, H.M. and Kiss, A.D. 1987. A Comparison of Techniques for Measuring Yield Stresses. *Journal of Rheology*. ***31***(8), pp.699-710.

Chapter 5

High Temperature Small Amplitude Oscillatory Shear Rheometry on Binary Blends using the Cup Geometry

Abstract

Given that little previous work has addressed the rheological behaviour of coal blends, a range of binary blends composed of coals with varying properties have been studied here to understand the impacts of blending upon deviations from additive behaviour, where a novel cup geometry has been used which facilitates larger sample sizes than the traditional parallel plate geometry and also provides a proxy for gas pressure of coking coals during softening since the sample is retained within the cup. Significant deviations were found from additive behaviour for η^*_{min}, where both negative and positive interactions were found. C1-C10(50wt%), a blend of a non-softening coal with a softening coal ($\eta^*_{min} < 10^4$ Pa s) exhibited significantly increased η^*_{min}, 132% greater than predicted. Conversely, a blend of two softening coals, C6-C10(75wt%), afforded a η^*_{min} 95.9% lower than predicted. These were subsequently linked to the plate gap changes, where it was found that fluid material adsorption was evident when blending non-coking coals with fluid exhibiting coals. Additionally, the use of the cup geometry has shown that coals exhibiting η^*_{min} of 2 – 3 x10^3 Pa s provide sustained plate gap expansion. This was shown to be the limit of which sustained expansion occurred, or weak – semi cokes are formed due to volatile release from low viscosity suspension formation. Additionally, such suspension formation, and subsequent possible clustering of inert material, led to non-linear reductions in η^*, particularly for blends of non-softening and high fluidity coals.

5.1. Introduction

Due to the ever-increasing cost and scarcity of prime coking coals, steel manufacturers prefer to use blends of coals. This provides a wider range of properties, reduced operational and material costs, and reduced reliance upon a single source (de Cordova, Madias & Barreiro, 2016). As such, research is required into the effect of blending coals upon the fluidity of blends. Fluidity development is fundamental to coke quality, as outlined in the previous chapter (Castro-Diaz et al, 2005; Castro-Diaz et al, 2007; Castro-Diaz et al, 2007; Castro-Diaz et al, 2007; Castro-Diaz et al, 2012; Castro-Diaz et al, 2018; Das et al, 2018; Duffy et al, 2007; Lin & Winter, 1991; Melendi et al, 2007; Nomura et al, 1999; Steel et al, 2009; Steel et al, 2014; Steel et al, 2017). Although there has been extensive research into fluidity of single coals with rheometry and Gieseler fluidity, there has been limited experimental work on blends and understanding the complex interactions between blend constituents. Some work has been performed on intense modelling using rheological data (Guelton, 2017), but few experimental results have shown the success of these models. Additionally, any work on blends using rheometry has only used the parallel plate (PP) geometry and 1.5 g sample size (Castro-Diaz et al, 2005; Castro-Diaz et al, 2007; Castro-Diaz et al, 2007; Castro-Diaz et al, 2007; Castro-Diaz et al, 2012; Castro-Diaz et al, 2018; Das et al, 2018; Duffy et al, 2007; Duffy, Mahoney & Steel, 2010; Lin & Winter, 1991; Melendi et al, 2007; Nomura et al, 1999; Steel et al, 2004; Steel et al, 2006; Steel et al, 2009; Steel et al, 2014; Steel et al, 2017).

Significant experimental work has been performed upon the blending of coking coals with additives, such as plastics, biomass, binders, coal extracts and charcoal (Castro-Diaz et al, 2008; Flores et al, 2017; Fraga et al, 2020; Guerrero, Diez & Borrego, 2015; Jenkins & Mahoney, 2015; Kokonya et al, 2013; Melendi et al, 2007; Melendi-Espina et al, 2015). The only work to extensively study blends experimentally has been on binary blends, where the mixing of two coals did not necessarily agree with additive behaviour, and has mostly shown that negative interactions occur between coals with dissimilar rank and properties (reduced fluidity) (Das et al, 2018; Diez, Alvarez & Fernandez, 2012; Duffy et al, 2010; Eremin, Kuprygin & Kukolev, 2016; Kumar et al, 2008; Mochizuki et al, 2017; Steel et al, 2004; Steel et al, 2006; Steel et al, 2014; Takanohashi et al, 2006; Tiwari, Banerjee & Saxena, 2013). This additive behaviour, known as the ‘polymer blending rule’ was developed by *Duffy, Mahoney & Steel (2010),* which takes into account the complex viscosity (η^*) of each constituent and the proportion (wt%) of each constituent, as shown in Equation 5.1:

$$ln\,\eta^* = \varphi_1\, ln\,\eta_1{}^* + \varphi_2\, ln\,\eta_2{}^* \tag{5.1}$$

Where:
η^* = Complex viscosity
φ = Component Fraction in Blend

Although some agreements have been found with the polymer blending rule, this model does not take into account interactions between components (Kumar et al, 2008). These observations have led to numerous theories to be developed to understand the interactions between coals. *Neavel (1982)* suggested that as one coal resolidifies, the aromatic structures release mobile hydrogen species, stabilizing the radicals generated from volatile release from the other blended coal (where such radicals start the resolidification process) (Neavel, 1982). *Sakurovs (2003)* suggested that fluid matter generated from lignite macerals within the coal do not interact with those generated by other coals in the blend. Additionally, inert and resolidified material within the blend act as absorbents of volatile matter, reducing the overall fluidity of the blend. Further, differences in rank lead to early softening of a high rank coal (and later resolidification for low rank coal), where rank has been shown to correlate well with temperature of softening and maximum fluidity (Yoshida et al, 2000).

Such interactions have been shown to be slightly overcome by increasing the heating rate, where *Takanohashi et al (2006)* found that the overlap of softening range was improved, along with a slower rate of volatilisation. This overlap of softening range was also shown to improve the fluidity of blends of coal with biomass samples, where *Castro Diaz et al (2015)* tested a range of biomass samples with good coking coals. However, such mitigating steps cannot be easily incorporated into an industrial coking facility. *Guelton (2017)* attempted to incorporate many factors into a multi-component coking coal blend model, yet there was little agreement with experimental Gieseler fluidity measurements. This was found to be due to the non-additive nature of coal fluidity; however, TMFs could be predicted from the model.

Many studies have attempted to predict coking coal fluidity using Gieseler plastometry (Mochizuki et al, 2017; Nasirudeen & Jauro, 2011), where a range of conclusions have been found. *Diaz-Faes et al (2007)* found that there was little agreement between experimental and predicted fluidity values, where a range of binary, ternary and quaternary blends were tested. *Shaik et al (2019)* tested low rank Indian coals with prime coking coals and found large reductions in fluidity which did not correlate with expansion. *Krzesinska, Smedowski & Szeluga, (2013)* tested a range of Polish coals in binary and ternary blends and found disagreements with linear behaviour. *Flores et al (2020)* found that adding an ultra-high fluidity coal to a blend could actually increase the maximum fluidity of the blend. Interestingly, few studies have shown positive interactions between coals where fluidity of blends increased when compared with additive behaviour from the single coals.

Although the rheological studies on coal blends have provided very useful viscoelastic information, there has been little thought to the methodology. All literature to date has utilised the serrated parallel plate geometry with 1.5 g sample size (Castro-Diaz et al, 2005; Castro-Diaz et al, 2007; Castro-Diaz et al, 2007; Castro-Diaz et al, 2007; Castro-Diaz et al, 2012; Castro-Diaz et al, 2018; Das et al, 2018; Duffy et al, 2007; Duffy, Mahoney & Steel, 2010; Lin & Winter, 1991; Melendi et al, 2007; Nomura et al, 1999; Steel et al, 2004; Steel et al, 2006; Steel et al, 2009; Steel et al, 2014; Steel et al, 2017). In the previous chapter, it was shown that a greater mass could be used of up to 3 g with the novel cup geometry. Not only does this provide more representative measurements of viscoelasticity, but also reduces the error in composition and in some cases, can provide a proxy for gas pressure through plate gap measurements (this was not possible for the parallel plate due to the lack of retaining walls, and subsequent release of volatile matter). Therefore, the cup geometry has been used here to measure coking coal blends at an increased mass of 3 g to understand the impact of coal interactions on η*, G’ and G”, and generation of gas pressure through plate gap measurements.

5.2. Experimental

The suite of 10 coals described and used in chapter 4 were used to make 18 blends with varying fluidities and behaviours (see Table 3.1 for coal properties and Gieseler fluidity information can be found in Table B1, Appendix B). Samples were also prepared using the methodology described in chapter 4. Masses of 3 g were used to test the blends in the novel cup geometry, as this was shown to be beneficial in single coal studies. Single tests were used to understand the fluidity development of the blends and five tests were carried out on a blend of 50wt% coal 5 50wt% coal 6 (C5-C6(50wt%)), where this blend showed significant deviation from additive behaviour. The relative standard deviation (RSD) of these repeated tests was used to calculate experimental error and to subsequently identify significant differences between experimental and predicted viscoelastic parameters. The experimental conditions used in chapter 4 were used here, where only the cup geometry was used.

18 different blends were tested with varying compositions to test the polymer blending rule and understand the interactions between different coals where properties varied significantly. Table 5.1 below details the blends tested, the compositions, and the blend notation (this notation has also been used for blends tested using high temperature NMR, chapter 6) along with the category of the blend (i.e., blend of coals with similar coking properties).

Table 5.1: Blends tested with compositions, notations and blend category

Blend (Coal X: Coal Y)	Compositions Tested (Wt% Coal Y)	Blend Notation (CX-XY(Wt% Coal Y))	Blend Category
Coal 4: Coal 5	25, 50, 75	C4-C5(Wt% Coal 5)	Blends with Coals of Similar Properties
Coal 6: Coal 10	25, 50, 75	C6-C10(Wt% Coal 10)	
Coal 1: Coal 4	50, 55, 70, 75, 80, 85	C1-C4(Wt% Coal 4)	Blends with Non-Softening Coals
Coal 1: Coal 10	50, 70, 75, 80, 85	C1-C10(Wt% Coal 10)	
Coal 2: Coal 6	25, 50, 75	C2-C6(Wt% Coal 6)	
Coal 2: Coal 8	25, 50, 75	C2-C8(Wt% Coal 8)	
Coal 4: Coal 6	25, 50, 75	C4-C6(Wt% Coal 6)	Blends with Medium Fluidity Coal 4
Coal 4: Coal 10	25, 50, 75	C4-C10(Wt% Coal 10)	
Coal 5: Coal 6	25, 50, 75	C5-C6(Wt% Coal 6)	Blends with Medium Fluidity Coal 5
Coal 5: Coal 8	25, 37.5, 50, 62.5	C5-C8(Wt% Coal 8)	
Coal 5: Coal 10	25, 50, 75	C5-C10(Wt% Coal 10)	
Coal 3: Coal 4	50, 70, 75, 80, 85	C3-C4(Wt% Coal 4)	Coal 3 with Medium Fluidity Coals
Coal 3: Coal 5	50, 75, 87.5	C3-C5(Wt% Coal 5)	
Coal 3: Coal 6	50, 62.5, 75	C3-C6(Wt% Coal 6)	Coal 3 with High Fluidity Coals
Coal 3: Coal 7	50, 62.5, 75, 87.5	C3-C7(Wt% Coal 7)	
Coal 3: Coal 8	37.5, 50, 62.5, 75	C3-C8(Wt% Coal 8)	
Coal 3: Coal 9	50, 75, 87.5	C3-C9(Wt% Coal 9)	
Coal 3: Coal 10	50, 62.5, 75	C3-C10(Wt% Coal 10)	

5.3. Results and Discussion

In this study, η*, G', G", tanδ and plate gap have been used to understand the impacts of blending on fluidity and expansion. Tanδ exhibited significant scatter during maximum fluidity in chapter 4, therefore this parameter has been primarily used to understand the softening (through sol point) and resolidification (through gel point) stage of coal blends (where RSD of both sol point and gel point were below 1%), and maximum tanδ has not been discussed here (sol point is defined as the temperature at which tanδ exceeds 1. Gel point is defined as the temperature at which tanδ reduces below 1 (after sol point)). Sol point and gel point have been used here as they provide definitive markers for when the coal behaves predominantly as a fluid, and when solid behaviour consecutively dominates. Minimum complex viscosity (η^*_{min}) was used to understand changes at maximum fluidity. G' and G" have not been discussed in detail here, as good correlations were found for single coals with η^*_{min}, therefore only η^*_{min} has been discussed in detail. G' and G" have been correlated with η^*_{min} and plate gap to identify differences in elastic and viscous behaviour to confirm interactions and mechanisms between coals in blends.

η^*_{min} for the 18 blends tested here have been presented as a function of composition in order to understand deviations from additive behaviour and rationalise interactions behind such differences. Plots of η* and tanδ for all 18 blends as a function of temperature can be found in Appendix C (Figures C1 – 18, Appendix C) to show how fluidity developed throughout the heating regime and broadly show changes during softening and resolidification. Plots of sol point and gel point as a function of composition can be found in Appendix C, Figures C1c – C18c.

Plots of minimum G' and G" as a function of blend composition can be found in Figures C19 – C36 in Appendix C. Correlation matrices between η^*_{min}, minimum G' and minimum G" for the groups of blends can be found in Figures C37 – C43. In summary, all correlations between η* with G' and G" exhibited R^2 values > 0.9. Blends of non-softening coals 1 & 2 afforded improved correlations with G', compared with G". Hence, elastic behaviour was exhibited more readily in blend behaviour of these blends (through mechanisms such as maceral crosslinking and suspension formation) compared with viscous behaviour. All other blends exhibited improved correlations with G", suggesting that viscous behaviour was exhibited more readily in blend behaviour (through mechanisms such as hydrogen donation and fluid material adsorption), compared with elastic behaviour.

5.3.1. Errors and Relative Standard Deviations (RSDs)

C5-C6(50wt%) was tested 5 times to obtain a relative standard deviation (RSD), and hence determine significant differences between experimental and predicted η^*_{min}. Figure 5.1 details η^* as a function of temperature for C5-C6(50wt%). It was found that an RSD of 19.6% was found for the repeated tests for η^*_{min}. Therefore, agreement was confirmed if the %difference between experimental and predicted (additive behaviour) η^*_{min} was within 38.8% (1.59% log basis), where 95% confidence limits was used (hence agreement was within 1.96 RSDs (Altman & Bland, 2003)). Table 5.2 below details the experimental η^*_{min}, predicted η^*_{min} (calculated from the polymer blending rule) and 95% confidence percentage limits for experimental results (38.8% of experimental η^*_{min}). These have been given for CX-CY(50wt%) blends as an example.

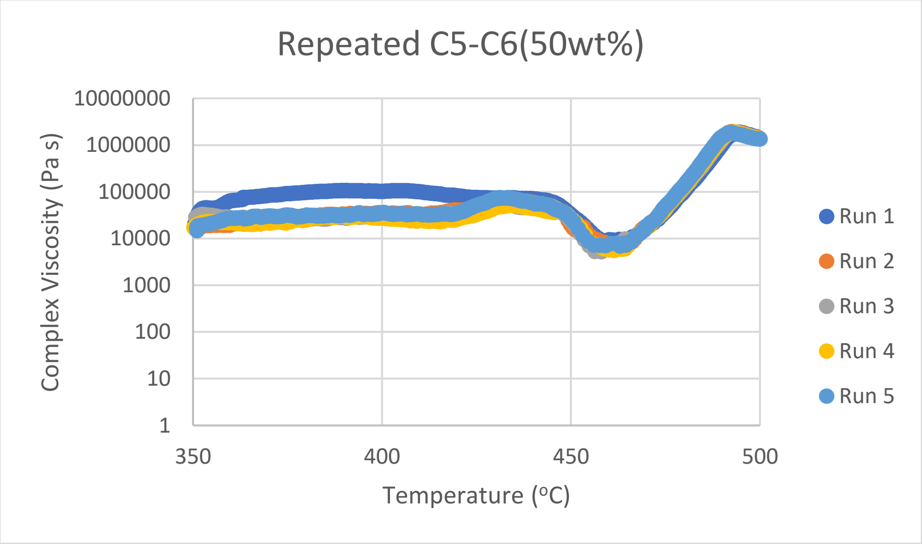

Figure 5.1: η as a function of temperature for repeated C5-C6(50wt%) samples*

Table 5.2: Experimental η^*_{min}, lower limit of experimental error (95% confidence limit), upper limit of experimental error (95% confidence limit) and predicted η^*_{min}. Values are provided for CX-CY(50wt%) as an example.

Blend	Experimental η*min (Pa s)	Lower Limit Experimental (Pa s)	Upper Limit Experimental (Pa s)	Predicted η*min (Pa s)
C4-C5(50wt%)	1.08×10^4	6.61×10^3	1.50×10^4	5.65×10^3
C6-C10(50wt%)	2.65×10^3	1.62×10^3	3.68×10^3	6.81×10^3
C1-C4(50wt%)	4.31×10^4	2.64×10^4	5.98×10^4	3.07×10^4
C1-C10(50wt%)	1.80×10^5	1.10×10^5	2.50×10^5	3.71×10^4
C2-C6(50wt%)	2.13×10^4	1.30×10^4	2.96×10^4	1.70×10^4
C2-C8(50wt%)	3.47×10^3	2.12×10^3	4.82×10^3	1.08×10^4
C4-C6(50wt%)	2.25×10^3	1.38×10^3	3.12×10^3	5.64×10^3
C4-C10(50wt%)	5.53×10^3	3.38×10^3	7.68×10^3	1.06×10^4
C5-C6(50wt%)	8.07×10^3	4.94×10^3	1.12×10^4	3.63×10^3
C5-C8(50wt%)	1.84×10^3	1.13×10^3	2.55×10^3	2.30×10^3
C5-C10(50wt%)	1.12×10^4	6.85×10^3	1.55×10^4	6.83×10^3
C3-C4(50wt%)	5.83×10^4	3.57×10^4	8.09×10^4	1.87×10^4
C3-C5(50wt%)	2.19×10^4	1.34×10^4	3.04×10^4	1.20×10^4
C3-C6(50wt%)	3.22×10^4	1.97×10^4	4.47×10^4	1.20×10^4
C3-C7(50wt%)	4.67×10^4	2.86×10^4	6.48×10^4	1.06×10^4
C3-C8(50wt%)	6.78×10^3	4.15×10^3	9.41×10^3	7.60×10^3
C3-C9(50wt%)	3.48×10^4	2.13×10^4	4.83×10^4	8.57×10^3
C3-C10(50wt%)	5.64×10^4	3.45×10^4	7.83×10^4	2.26×10^4

N.B. 95% confidence limits of 38.8% were determined by 1.96 RSDs of repeated tests

Sol and gel point exhibited low RSDs of 0.37% and 0.167%, respectively. Therefore, agreement between experimental and predicted sol point and gel point were found to be 1.96 RSDs (95% confidence limits), hence within 0.73% and 0.33%, respectively. Table 5.3 below details the experimental sol point and gel point, lower and upper confidence limits of experimental sol point and gel point and predicted sol point and gel point (calculated from the polymer blending rule). These have been given for CX-CY(50wt%) blends as an example.

Table 5.3: Experimental sol point, lower confidence limit and upper confidence limit of experimental sol point, predicted sol point, experimental gel point, lower confidence limit and upper confidence limit of experimental gel point and predicted gel point Values are provided for CX-CY(50wt%) as an example.

	Sol Point				Gel Point			
Composition	Experimental (ºC)	Lower Limit (ºC)	Upper Limit (ºC)	Predicted (ºC)	Experimental (ºC)	Lower Limit (ºC)	Upper Limit (ºC)	Predicted (ºC)
C4-C5(50wt%)	448.0	444.7	451.3	444.6	499.4	497.8	501.0	495.3
C6-C10(50wt%)	407.0	404.0	410.0	413.5	475.0	473.5	476.5	476.0
C1-C4(55wt%)	*471.4*	467.9	474.9	*463.8*	*500.0*	498.4	501.6	*494.9*
C1-C10(50wt%)	462.0	458.6	465.4	458.0	485.0	483.4	486.6	487.8
C2-C6(50wt%)	434.0	430.8	437.2	#######	483.0	481.4	484.6	######
C2-C8(50wt%)	429.5	426.4	432.6	#######	480.2	478.6	481.8	######
C4-C6(50wt%)	423.0	419.9	426.1	421.8	473.9	472.4	475.4	483.6
C4-C10(50wt%)	426.5	423.4	429.6	431.8	481.9	480.3	483.5	483.0
C5-C6(50wt%)	431.0	427.8	434.2	426.2	489.9	488.3	491.5	488.3
C5-C8(50wt%)	430.6	427.4	433.8	435.6	491.0	489.4	492.6	486.9
C5-C10(50wt%)	434.4	431.2	437.6	436.2	491.4	489.8	493.0	487.8
C3-C4(50wt%)	435.1	431.9	438.3	436.5	484.1	482.5	485.7	477.3
C3-C5(50wt%)	458.0	454.6	461.4	444.9	497.1	495.5	498.7	491.0
C3-C6(50wt%)	423.5	420.4	426.6	418.1	470.0	468.5	471.5	470.3
C3-C7(50wt%)	421.5	418.4	424.6	419.4	475.5	474.0	477.0	461.8
C3-C8(50wt%)	418.0	414.9	421.1	427.5	466.5	465.0	468.0	468.9
C3-C9(50wt%)	426.5	423.4	429.6	419.9	466.7	465.2	468.2	467.3
C3-C10(50wt%)	432.5	429.3	435.7	428.1	470.6	469.1	472.1	469.7

 # Coal 2 did not exceed tanδ = 1, hence no sol point or gel point was exhibited. Therefore, predicted values could not be obtained for sol point and gel point for coal 2 blends. C1-C4(50wt%) also did not exceed tanδ = 1, therefore no sol point or gel point was exhibited. The experimental and predicted values and errors have been provided for C1-C4(55wt%). N.B. 95% confidence limits of 0.73% and 0.33% were determined by 1.96 RSDs of repeated tests.

Maximum plate gap exhibited an RSD of 7.32%. Therefore, agreement between experimental and predicted maximum plate gap was found to be within 14.3% (1.96 RSDs). Table 5.4 below details the experimental maximum plate gap, lower and upper confidence limits of experimental maximum plate gap and predicted maximum plate gap (calculated from the polymer blending rule). These have been given for CX-CY(50wt%) blends as an example.

Table 5.4: Experimental maximum plate gap, lower and upper confidence limits of experimental maximum plate gap and predicted maximum plate gap. Values are provided for CX-CY(50wt%) as an example.

Blend	Experimental Max. Plate Gap (mm)	Lower Limit (mm)	Upper Limit (mm)	Predicted Max. Plate Gap (mm)
C4-C5(50wt%)	10.2	8.8	11.7	10.8
C6-C10(50wt%)	9.3	7.9	10.6	7.8
C1-C4(50wt%)	5.6	4.8	6.4	7.5
C1-C10(50wt%)	5.3	4.5	6.0	5.8
C2-C6(50wt%)	7.3	6.2	8.3	7.6
C2-C8(50wt%)	11.9	10.2	13.6	6.4
C4-C6(50wt%)	13.3	11.4	15.2	9.5
C4-C10(50wt%)	9.8	8.4	11.2	7.7
C5-C6(50wt%)	10.7	9.1	12.2	10.9
C5-C8(50wt%)	11.7	10.0	13.4	9.8
C5-C10(50wt%)	9.9	8.5	11.3	9.1
C3-C4(50wt%)	5.8	4.9	6.6	7.4
C3-C5(50wt%)	5.4	4.6	6.2	8.8
C3-C6(50wt%)	5.4	4.7	6.2	7.5
C3-C7(50wt%)	6.1	5.2	6.9	6.6
C3-C8(50wt%)	8.2	7.0	9.3	6.4
C3-C9(50wt%)	5.4	4.7	6.2	5.5
C3-C10(50wt%)	5.4	4.6	6.2	5.7

N.B. 95% confidence limits of 14.3% were determined by 1.96 RSDs of repeated tests.

Throughout this study, the confidence limits detailed above, for examples of 50:50 blends, have been used to determine significant differences from additive behaviour, and ultimately assess the efficacy of the polymer blending rule.

5.3.2. Viscoelastic Behaviour of Blends

5.3.2.1. Similar Coal Blends

Blends with similar coals (similarities with respect to rank, softening profile and volatile matter content) have been discussed first, since it has been shown previously that such blends exhibit additive behaviour (Duffy, Mahoney & Steel, 2010; Steel et al, 2006).

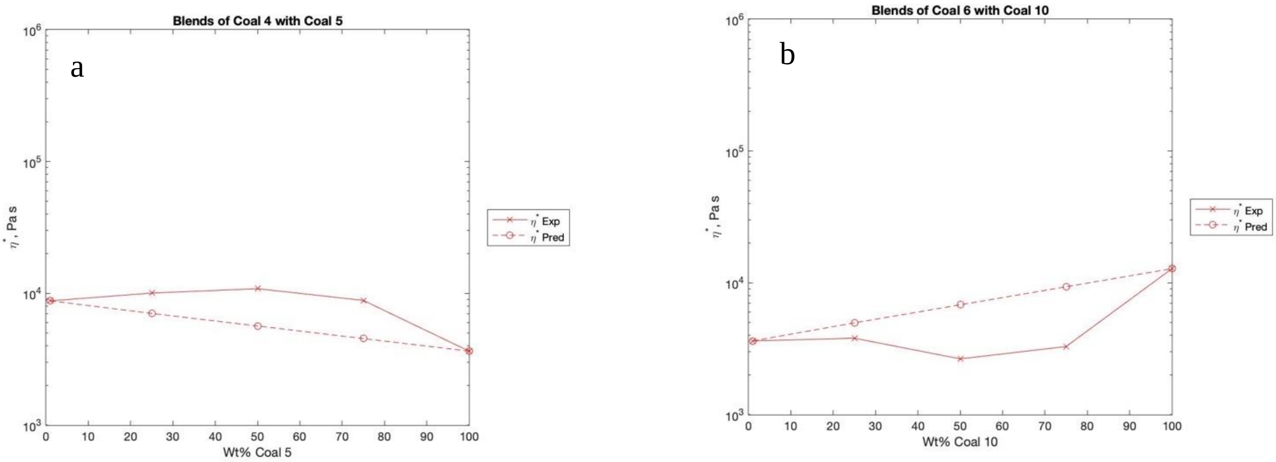

Figure 5.2: Minimum η^* (a, top left) as a function of composition for blends of C4-C5 (a) and C6-C10 (b)

Figures 5.2a & b above detail the η^*_{min} as a function of composition for C4-C5 (a) and C6-C10 (b). Figures C1 and C2 (Appendix C) exhibit the η^* and tanδ as a function of temperature for C4-C5 (C1a & C1b) and C6-C10 (C2a & C2b). Figure C1c and C2c detail the sol point and gel point as a function of composition for C4-C5 and C6-C10, respectively. It should be noted that C4-C5 and C6-C10 were the only blends studied here utilising two similar coals.

η^*

The C4-C5 blends (Figure 5.2a) afforded negative impacts upon fluidity (increased η^*_{min}) at C4-C5(50wt%) and C4-C5(75wt%) (63.0% (5193 Pa s) and 64.3% (8838 Pa s) greater than predicted values). Interestingly, there was a difference of 13 ^{o}C in the TMFs of the two coals, where it was possible that coal 5 absorbed fluid material generated by softening coal 4 (absorption mechanism), and inhibited fluid propagation through the sample. For the high fluidity coal blend, C6-C10 (Figure 5.2b) there was only a difference of 2 ^{o}C in the TMFs of the two coals, and a difference of 0.02 in MVR. The resultant η^*_{min} exhibited increased fluidity at C6-C10(50wt%) and C6-C10(75wt%) (88.0% (4163 Pa s) and 95.9% (6051 Pa s) lower than predicted values), showing that blending these two coals gave rise to positive interactions, most likely due to the almost perfect overlapping of softening profiles (this is shown in the η^* as a function of temperature plots in the Appendix C, Figure C2a). If it is unlikely that increased fluidity was due to additional fluid material, then lower viscosity was possibly due to loss of solid structure (in line with reduced G' in Figure C20a, Appendix C), where 'fluid pockets' could link and form channels between macromolecular structures. The lack of solid structure through linking of fluid pockets afforded a suspension of macromolecular species in a matrix of molecular fluid entities, where inert material could flow with the fluid material, which subsequently gave rise to non-additive fluidity. If the suspension theory holds, then there could be a clustering of solid particles within the fluid matrix, giving rise to segregated phases. Therefore, the fluid material moves to the edges of the coal mass, giving rise to non-linear reduced measured η^* (suspension mechanism).

Sol Point and Gel Point

Comparing the tanδ profiles of the C4-C5 samples (see Figure C1c, Appendix C), there was a difference of 9 °C between the sol points of coals 4 (sol point = 440 °C) and 5 (sol point = 449 °C). Significant differences of 0.756% (3.3 °C), 0.770% (3.5 °C) and 1.054% (4.8 °C) compared with predicted values were found here, with decreased values at C4-C5(25wt%) and increased values at C4-C5(50wt%) and C4-C5(75wt%). Gel point increased for all C4-C5 compositions by 0.54% (2.7 °C), 0.83% (4.1 °C) and 0.47% (2.3 °C) compared with additive behaviour, with resolidification pushed to a higher temperature. Comparing the tanδ profiles of the C6-C10 samples (see Figure C2c, Appendix C), there appeared to be more of a contribution from coal 6 to the sol point (giving rise to reduced sol point at C6-C10(50wt%) and C6-C10(75wt%) by 1.6% (6.4 °C) and 1.7% (7.0 °C)). C6-C10(25wt%) exhibited agreement with additive behaviour. For the gel point, there was only a difference of 1.1 °C between gel point of coal 6 and coal 10, therefore little difference between gel point of the blends, which was confirmed by agreement between blend gel points and additive behaviour. Reduced sol point for C6-C10 was in line with reduced η^*_{min}.

5.3.2.2. Overall Summary of Discrepancies to Additive Behaviour

Interestingly, there were differences between the experimental η^*_{min} and predicted values for similar coals, where previous studies have found reasonable agreement between such (Steel et al, 2006). Additionally, work with rheometry on coal blends has found mostly negative interactions between coals (reduced fluidity), where here it was found that two very similar high fluidity coals provide positive interactions (enhanced fluidity).

The polymer blending rule assumes that there are only perfectly additive interactions between the coals, where deviations show that negative and positive interactions are present. The differences to the polymer blending rule were quantified by calculating the percentage difference for each composition (excluding single coals) between experimental and predicted values. Agreement was defined as being within the error of the experimental values with 95% confidence (1.96 RSDs), which for η^*_{min} was 38.8%% (1.59% on log basis) for the individual values (where an RSD of 19.6% was obtained from repeated tests of C5-C6(50wt%)). Table 5.5 details the 50:50wt% individual blends, percentage difference between experimental and predicted values, and whether there was agreement to provide an overview of agreements and differences from additive behaviour. Log(%difference) have also been provided, as η^* and η^*_{min} have been provided on log axes. A full break down of differences for each composition can be found in Appendix C, Table C2 with linear and log %differences.

Table 5.5: Percentage differences for η^*_{min} for 50:50wt% blends compared to polymer blending rule

Blend	% Difference	Log(%Difference)	Agreement? (Yes/No)
C4-C5	63.0%	1.80%	No
C6-C10	88.0%	1.94%	No
C1-C4	33.6%	1.53%	Yes
C1-C10	132%	2.12%	No
C2-C6	22.4%	1.35%	Yes
C2-C8	103%	2.01%	No
C4-C6	85.8%	1.93%	No
C4-C10	62.7%	1.80%	No
C5-C6	75.8%	1.88%	No
C5-C8	22.8%	1.36%	Yes
C5-C10	48.4%	1.68%	No
C3-C4	103%	2.01%	No
C3-C5	58.2%	1.76%	No
C3-C6	91.4%	1.96%	No
C3-C7	126%	2.10%	No
C3-C8	11.5%	1.06%	Yes
C3-C9	121%	2.08%	No
C3-C10	85.8%	1.93%	No

N.B. Agreement between experimental and additive behaviour was defined as being within 38.8% (linear) and 1.59% (log)

Differences have also been calculated for sol point and gel point along with agreement with the additive behaviour. Agreement between experimental and additive behaviour values was defined as being within 0.733% and 0.325% for sol point and gel point, respectively. 50:50wt% blends have been detailed as examples in Table 5.6 below, where individual composition differences and agreements for the two parameters can be found in Appendix C (Table C3).

Table 5.6: Absolute difference and %difference for sol point and gel point for 50:50 blends, with agreements highlighted

Composition	Sol Point			Gel Point		
	Diff (^oC)	Diff (%)	Agreement (Yes/No)	Diff (^oC)	Diff (%)	Agreement (Yes/No)
C4-C5(50wt%)	3.5	0.8	No	4.1	0.8	No
C6-C10(50wt%)	6.4	1.6	No	1.1	0.2	Yes
C1-C4(50wt%)	N/A	N/A	N/A	N/A	N/A	N/A
C1-C10(50wt%)	4.0	0.9	No	2.8	0.6	No
C2-C6(50wt%)	N/A	N/A	N/A	N/A	N/A	N/A
C2-C8(50wt%)	N/A	N/A	N/A	N/A	N/A	N/A
C4-C6(50wt%)	1.2	0.3	Yes	9.7	2.0	No
C4-C10(50wt%)	5.3	1.2	No	1.1	0.2	Yes
C5-C6(50wt%)	4.8	1.1	No	1.6	0.3	Yes
C5-C8(50wt%)	5.0	1.2	No	4.1	0.8	No
C5-C10(50wt%)	1.8	0.4	Yes	3.6	0.7	No
C3-C4(50wt%)	1.5	0.3	Yes	6.8	1.4	No
C3-C5(50wt%)	N/A	N/A	N/A	N/A	N/A	N/A
C3-C6(50wt%)	5.4	1.3	No	0.2	0.0	Yes
C3-C7(50wt%)	2.1	0.5	Yes	13.7	2.9	No
C3-C8(50wt%)	9.5	2.3	No	2.3	0.5	No
C3-C9(50wt%)	6.6	1.5	No	0.6	0.1	Yes
C3-C10(50wt%)	4.4	1.0	No	0.8	0.2	Yes

N.B: Agreement between experimental and additive behaviour values was defined as being within 0.733% and 0.325% for sol point and gel point, respectively.

Table 5.5 above showed that, for 50:50wt% blends, there were only 4 blends that showed agreement with the polymer blending rule (C1-C4, C2-C6, C5-C8 and C3-C8). Overall, of the 64 compositions tested here, 46 of these showed significant deviations from additive behaviour. Hence there was generally poor accuracy for the polymer blending rule for predicting η^*_{min}. For sol point (Table 5.6), C4-C6, C5-C10, C3-C4 and C3-C7 were the only 50:50wt% blends to show agreement with additive behaviour. For gel point (Table 5.6 above), C6-C10, C4-C10, C5-C6, C3-C6, C3-C9 and C3-C10 exhibited agreements with additive behaviour. Overall, 12 compositions exhibited agreements with additive behaviour with respect to sol point, and 13 compositions exhibited agreements with additive behaviour with respect to gel point, out of the 64 compositions tested.

Due to the complex nature of coking coals under carbonisation, it is difficult to visualise and model such systems. One possible way of visualising these samples is by defining the different coals in rheological terms, as opposed to a simple value of fluidity, which could enable a better understanding and prediction of interactions. This was also suggested by *Steel et al (2006)* however here a more comprehensive study of coking coal blends has been performed, along with a novel cup geometry which can accommodate a greater mass (where the couette geometry is used in other industries to study gels (Coussot et al, 2009), emulsions (Ovarlez et al, 2008) and suspensions (Ahuja & Singh, 2009)). High fluidity coals, at maximum fluidity, are suspensions of macromolecular species (inertinite containing macerals) in a fluid matrix mostly composed of molecular fluid entities. Medium fluidity, higher rank coals are composed of macromolecular mass with ‘pockets’ of fluidity, where the linking of these pockets leads to increased fluidity (this can be seen as the opposite of high fluidity coals), where higher rank specimens contain larger sized macromolecules and more segregated fluid pockets (Diaz-Faes et al, 2007). Non – fluidity coals are mostly inert, macromolecular species with very segregated, small pockets of molecular fluid entities. These can be visualised more like a sponge-like substance at maximum fluidity, where the holes are micro-pockets of volatile matter or mobile fluid entities, but due to the elastic forces of the pore walls, these fluid pockets cannot link. From this, it is possible that blending coals, as opposed to perfectly mixing these systems, there are isolated suspensions. For example, if a non-softening coal is blended with a high fluidity coal, the inert, macromolecular structures prevent the flow and connection of the high fluidity metaplast (along with absorbing fluid material through the ‘sponge-like’ macromolecular structures). As such, the measured η^* is higher due to the lack of propagation of fluid material through the coke sample. And when high fluidity coals are in abundance, the inert, solid particles of non-fluid coal become part of the low viscosity suspension, leading to non-additive behaviour where such inert particles can cluster and allow the fluid material to propagate to the edge of the sample.

5.3.2.3. Agreement with Additive Behaviour

Although there were significant deviations from the polymer blending rule, indicated above, there were some agreements for individual compositions. From Table C2 in Appendix C, the following compositions showed agreement with the polymer blending rule with respect to η^*_{min}, detailed in Table 5.7 below.

Table 5.7: List of blends which show agreement with the polymer blending rule

Blend	% Difference	Agreement? (Yes/No)
C1-C4(50wt%)	33.6	Yes
C2-C6(50wt%)	22.4	Yes
C2-C8(25wt%)	0.8	Yes
C4-C5(25wt%)	35.2	Yes
C6-C10(25wt%)	26.7	Yes
C4-C6(25wt%)	8.7	Yes
C4-C10(25wt%)	13.9	Yes
C5-C6(75wt%)	24.2	Yes
C5-C8(37.5wt%)	10.1	Yes
C5-C8(50wt%)	22.0	Yes
C5-C8(62.5wt%)	26.1	Yes
C3-C4(85wt%)	14.7	Yes
C3-C6(75wt%)	31.9	Yes
C3-C7(75wt%)	11.4	Yes
C3-C8(50wt%)	11.5	Yes
C3-C8(75wt%)	26.3	Yes
C3-C9(87.5wt%)	9.4	Yes

N.B. Agreement between experimental and additive behaviour was defined as being within 38.8%

The following sections highlight the deviations from additive behaviour, as the overall behaviour of the blends tested here has been summarised above. This discussion has been divided into groups of blends, dependent upon constituent coals. Where significant deviations have been found, compared with additive behaviour, these have been highlighted and quantified by %difference from the experimental value. For η^*_{min}, significant differences were greater than 38.8%, for sol point greater than 0.73% and for gel point greater than 0.33%. To highlight the deviations for fluidity, plots of η^*_{min} as a function of composition have been detailed in the text below in Figures 5.3 – 5.7. Plots of sol point and gel point as a function of composition can be found in Figures C1c – C18c, Appendix C.

5.3.2.4. Blends with Non – Softening Coals 1 & 2

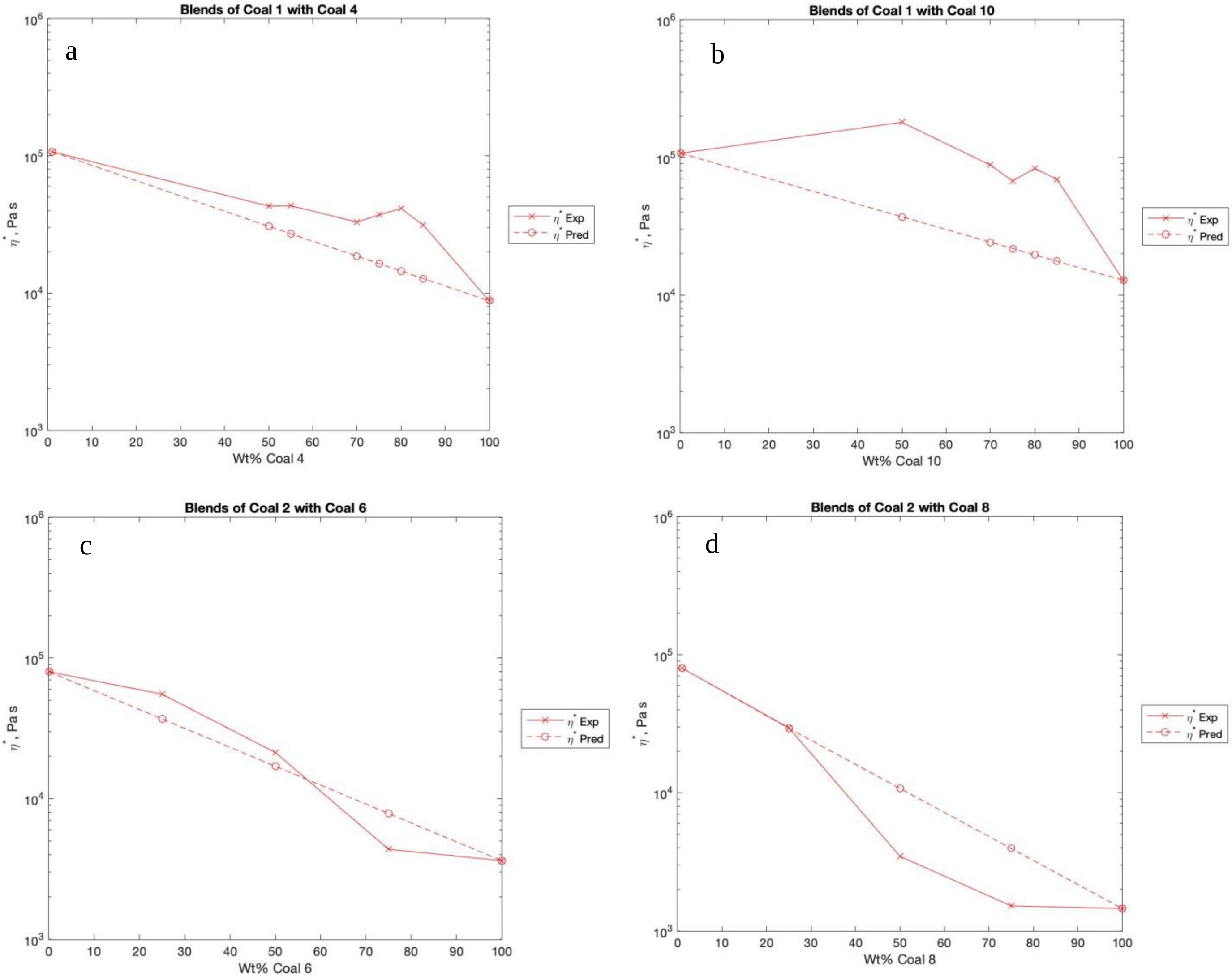

Figure 5.3: η^*_{min} *as a function of composition for C1-C4(a), C1-C10(b), C2-C6 (c) and C2-C8(d)*

Figures 5.3a - d detail the η^*_{min} as a function of composition for C1-C4 (a), C1-C10 (b), C2-C6 (c) and C2-C8 (d). Figures C3 – C6 (Appendix C) exhibit the η^* and $\tan\delta$ as a function of temperature for C1-C4 (C3a & C3b), C1-C10 (C4a & C4b), C2-C6 (C5a & C5b) and C2-C8 (C6a and C6b). Figure C3c, C4c, C5c and C6c detail the sol point and gel point as a function of composition for C1-C4, C1-C10, C2-C6 and C2-C8, respectively.

η^*

Coal 1 blends: Medium fluidity coal 4 and high fluidity coal 10 were blended with non-softening coal 1 (C1-C4 (Figure 5.3a) and C1-C10 (Figure 5.3b), where both blends afforded negative impacts upon fluidity and subsequent disagreements with the polymer blending rule. Disagreements for C1-C4 ranging from 46.3% (16315 Pa s) to 96.3% (26886 Pa s) were found for C1-C4(55wt%), C1-C4(70wt%), C1-C4(75wt%), C1-C4(80wt%) and C1-C4(85wt%) (Table C2, Appendix C). Disagreements for C1-C10 ranging from 102% (45787 Pa s) to 132% (143099 Pa s) were found for C1-C10(50wt%), C1-C10(70wt%), C1-C10(75wt%), C1-C10(80wt%) and C1-C10(85wt%) (see Table C2, Appendix C). Interestingly, these negative impacts were exacerbated with C1-C10. This was most noticeable at C1-C10(50wt%), where C1-C4 exhibited agreements with the polymer blending rule (at C1-C4(50wt%)), but significantly increased η^*_{min} was found for C1-C10, when compared with the additive behaviour. Additionally, both blends exhibited a peak in η^*_{min} (compared with additive behaviour) at 80wt%. The mechanism thought to be behind this is the adsorption of fluid material by coal 1.

Coal 2 blends: Unlike coal 1, the only disagreements found with the polymer blending rule were positive interactions (i.e., increased fluidity), few examples of which in literature have been documented. Such decreases in η^*_{min}, compared with additive behaviour, were lower than predicted. These decreases in η^*_{min} were found at C2-C6(75wt%) (see Figure 5.3c), C2-C8(50wt%) and C2-C8(75wt%) (Figure 5.3d), with differences of 22.4% (4281 Pa s), 103% (7304 Pa s) and 89% (2439 Pa s) (Table C2, Appendix C) compared with additive behaviour. For these blends, it is thought that the inert material is clustered and a low-viscosity suspension forms giving rise to non-linear decreases in η^*. Interestingly, previous studies utilising non-fluid coals have found negative interactions where reduced fluidity has been found (Mochizuki et al, 2017).

Sol Point and Gel Point

Although no sol point was observed for C1-C4(50wt%)), increased addition of coal 1 led to increased sol point for the other blends, likely due to the adsorption mechanism (Figure C3c, Appendix C), where increases ranged from 0.7% (3.0 ^{o}C) to 1.6% (7.6 ^{o}C) (Table C3, Appendix C). For gel point there was no trend with composition, with increased values at C1-C4(55wt%), C1-C4(75wt%), C1-C4(80wt%) and C1-C4(85wt%) with differences from additive behaviour ranging from 0.3% (1.6 ^{o}C) to 1.0% (5.1 ^{o}C), and a decreased value at C1-C4(70wt%) of 1.1% (5.4 ^{o}C) compared with additive behaviour (see Table C3, Appendix C). For C1-C10 (Figure C4c, Appendix C), sol point exhibited increased values, compared with additive behaviour, at C1-C10(50wt%) of 0.9% (4.0 ^{o}C) and C1-C10(80wt%) of 0.8% (3.6 ^{o}C), and reduced values at C1-C10(70wt%) of 1.4% (6.2 ^{o}C), C1-C10(75wt%) of 1.8% (7.7 ^{o}C) and C1-C10(85wt%) of 1.6% (6.8 ^{o}C). Reduced gel point was found for all composition, with differences ranging from 0.4% (1.9 ^{o}C) to 1.0% (4.7 ^{o}C) (Table C3, Appendix C).

Coal 2 did not exhibit a sol point or gel point, so predicted values could not be obtained. However, from the experimental results shown in Figures C5c (Appendix C) (C2-C6) and C6c (Appendix C) (C2-C8) it can be shown that there was almost linear behaviour in sol point and gel point for C2-C6(25wt%), C2-C6(50wt%) and C2-C6(75wt%), where a sol point and gel point was observed. For C2-C8, there were significant deviations from linear behaviour, particularly at C2-C8(75wt%), which was in line with the reduced $\eta*_{min}$. Therefore, the increased fluidity could have been due to early softening from hydrogen donation from coal 8 to coal 2 (mobilising some macerals in coal 2).

5.3.2.5. Blends of Medium Fluidity Coal 4

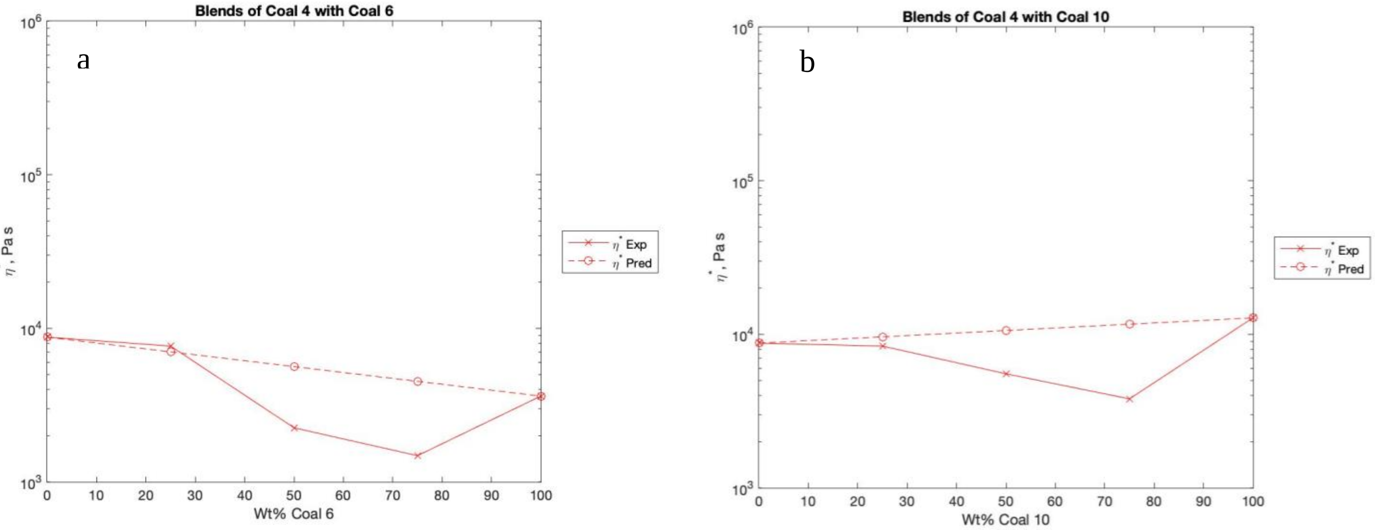

Figure 5.4: $\eta*_{min}$ as a function of composition for C4-C6 (a) and C4-C10 (b)

Figures 5.4a & b above detail the $\eta*_{min}$ as a function of composition for C4-C6 (a) & C4-C10 (b). Figures C7 & C8 (Appendix C) exhibit the η* and tanδ as a function of temperature for C4-C6 (C7a & C7b) & C4-C10 (C8a & C8b). Figure C7c & C8c detail the sol point and gel point as a function of composition for C4-C6 & C4-C10, respectively.

*η**

Medium fluidity coal 4 exhibited η^*_{min} that would suggest it would be a good coking coal (~10^4 Pa s, although with a slightly lower MVR than prime coking coal 5). Therefore, coal 4 (MVR = 1.1) was blended with lower rank, higher volatile coals to understand how interactions between these different coals impacted the blend behaviour. Blending coal 4 with coal 6 (MVR = 0.95), and coal 10 (MVR = 0.93), afforded very similar results in η^*_{min}. Reduced η^*_{min} was found (when compared with additive behaviour) at C4-C6(50 – 75wt%) (see Figure 5.4a) and C4-C10(50 - 75wt%) (Figure 5.4b), with differences of 85.8% (3384 Pa s) - 101% (3036 Pa s) and 62.7 (5058 Pa s) – 102% (7843 Pa s), respectively (Table C2, Appendix C). Agreement with the polymer blending rule was found at C4-C6(25wt%) and C4-C10(25wt%). There was a difference of 21 – 23 ^oC between the TMFs of the medium fluidity coal 4 and high fluidity coals 6 and 10, along with a difference of 0.15 – 0.17 in MVR, respectively. Therefore, it was expected that reduced fluidity would be found (increased η^*_{min}) for any differences to the polymer blending rule, unlike the reduced η^*_{min} found here. Therefore, deviations from additive behaviour were rank and TMF independent. The likely mechanisms for enhanced fluidity here were hydrogen donation along with suspension formation.

Sol Point and Gel Point

C4-C6 exhibited agreement between experimental and predicted sol point at C4-C6(50wt%) but increases at C4-C6(25wt%) of 0.8% (3.4 ^oC) and C4-C6(75wt%) of 1.3% (5.4 ^oC) (Figure C7c, Appendix C and Table C3, Appendix C). For gel point, there were decreases at C4-C6(25wt%) of 0.5% (2.5 ^oC) and C4-C6(50wt%) of 2.0% (9.7 ^oC) (see Table C3, Appendix C). Therefore, blending at 50:50 did not impact softening, but did impact resolidification, likely due to early crosslinking. For C4-C10, reduced sol point was found for all compositions with differences to additive behaviour of 1.0% (4.5 ^oC) – 1.2% (5.3 ^oC) (hydrogen donor effect and suspension formation) (see Figure C8c, Appendix C and Table C3, Appendix C)). For gel point, there were small reductions in experimental values at C4-C10(25wt%) of 0.5% (2.6 ^oC) and C4-C10(75wt%) of 0.4% (1.9 ^oC) (early crosslinking), and agreement at C4-C10(50wt%) with additive behaviour (Figure C7c and Table C3, Appendix C).

5.3.2.6. Blends of Medium Fluidity, High Rank Coal 5

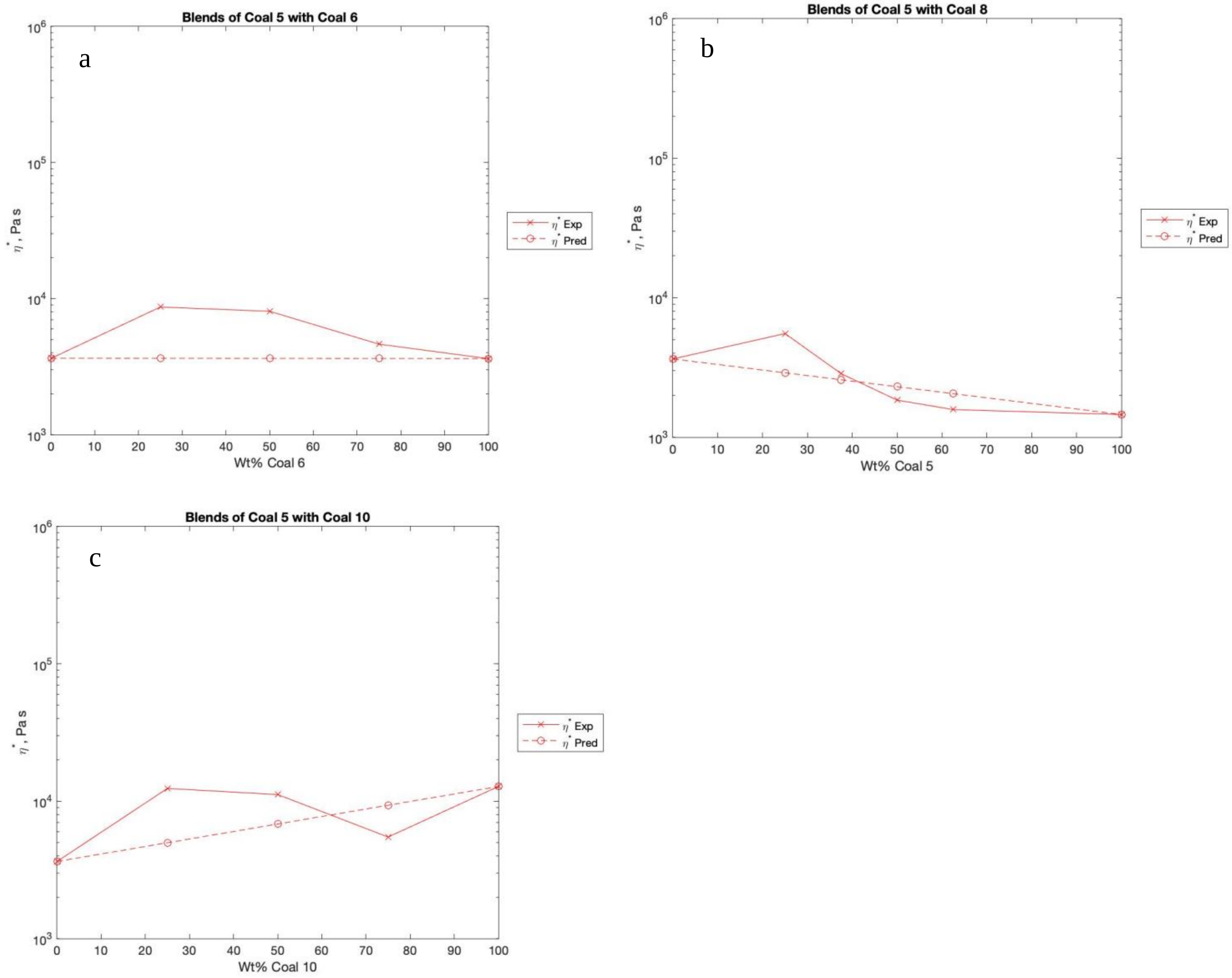

Figure 5.5: η^*_{min} as a function of composition for C5-C6 (a), C5-C8 (b) and C5-C10 (c)

Figures 5.5a - c above detail the η^*_{min} as a function of composition for C5-C6 (a), C5-C8(b) & C5-C10 (c). Figures C9, C10 & C11 (Appendix C) exhibit the η* and tanδ as a function of temperature for C5-C6 (C9a & C9b), C5-C8 (C10a & C10b) & C5-C10 (C11a & C11b). Figure C9c, C10c & C11c detail the sol point and gel point as a function of composition for C5-C6, C5-C8 & C5-C10, respectively. Prime coking coal 5 (MVR = 1.41) was blended with high fluidity coals 6 (MVR = 0.95), 8 (MVR = 0.97) and 10 (MVR = 0.93) to show how blending a prime coking coal with high fluidity, low rank coals impacted the behaviour of the blends.

*η**

Increases in η^*_{min} at C5-C6(25wt%), of 81.9% (5040 Pa s), and C5-C6(50wt%), of 75.8% (4438 Pa s) (Table C2, Appendix C), could have arisen from early crosslinking mechanism, where the abundance of macromolecular structures in coal 5 were crosslinked to, blocking fluid propagation (see Figure 5.5a). Agreement was found with additive behaviour at C5-C6(75wt%). Increases in η^*_{min} at C5-C8(25wt%), of 62.7% (2641 Pa s), compared with the polymer blending rule was due to the same reasons given for C5-C6 blends (early crosslinking to coal 5 macerals, giving rise to enhanced elastic behaviour). Agreement was found at other compositions (see Figure 5.5b). Two different behaviours as a function of composition were found for C5-C10 (see Figure 5.5c). Increases in η^*_{min} at C5-C10(25wt%), of 85.2% (7404 Pa s), and C5-C10(50wt%), of 48.4% (4355 Pa s), along with reductions in η^*_{min} at C5-C10(75wt%) of 52.1% (3862 Pa s), compared with additive behaviour (Table C2, Appendix C). Reduced fluidity was likely due to the same mechanisms mentioned above for both C5-C6 and C5-C8 (crosslinking and volatile absorption). At C5-C10(75wt%), increased fluidity was likely caused by the suspension mechanism (Figure 5.5c).

Sol Point and Gel Point

For C5-C6 (see Figure C9c, Appendix C), agreement was found at C5-C6(25wt%) for sol point but increases at C5-C6(50wt%), of 1.1% (4.8 ^oC), and C5-C6(75wt%), of 0.8% (3.2 ^oC), compared with additive behaviour (Table C3, Appendix C). For gel point, an increase in temperature was found at C5-C6(25wt%), of 0.9% (4.5 ^oC), a decrease at C5-C6(75wt%), 0.4% (2.0 ^oC), and agreement at C5-C6(50wt%) with predicted behaviour (Table C3, Appendix C). For C5-C8 (see Figure C10c, Appendix C), reductions in sol point were found at C5-C8(50wt%), of 1.2% (5.0 ^oC), and C5-C8(62.5wt%), of 2.7% (11.1 ^oC), with agreement at C5-C8(25wt%) and C5-C8(37.5wt%) compared with additive behaviour (Table C3, Appendix C). The reverse trend was found for gel point, where increases in temperature were found at C5-C8(50wt%), of 0.8% (4.1 ^oC), and C5-C8(62.5wt%), of 1.9% (9.3 ^oC), however there was also increases in gel point at C5-C8(25wt%), of 0.4% (1.7 ^oC) (along with agreement at C5-C8(37.5wt%)) compared with additive behaviour (Table C3, Appendix C). For C5-C10 (Figure C11c, Appendix C), additive behaviour for sol point was observed for all blends. There appeared to be a link between gel point and η^*_{min}, where increased gel point (compared with additive behaviour) was in line with increased η^*_{min}, and vice versa. Increases in gel point were found at C5-C10(25wt%), of 1.0% (4.8 ^oC), and C5-C10(50wt%), of 0.7% (3.6 °C), and reductions in gel point at C5-C10(75wt%), of 0.7% (3.5 °C), compared with predicted behaviour (Table C3, Appendix C).

5.3.2.7. Blends with Coal 3

It was found in the study of 10 single coals utilising a novel cup geometry (chapter 4) that the high vitrinite coal 3 exhibited very little viscoelastic behaviour. Therefore, this coal was outlined for in depth blend testing to understand if blending could elucidate more valuable information to rationalise the behaviour of this coal. It is thought that coal 3 develops micro-fluidity, where fluid material cannot propagate to the bulk scale, and is segregated into very small pockets. This is also to be explored in later chapters.

5.3.2.7.1. Blends with Low Fluidity, High Volatile Coal 3 with Medium Fluidity Coals

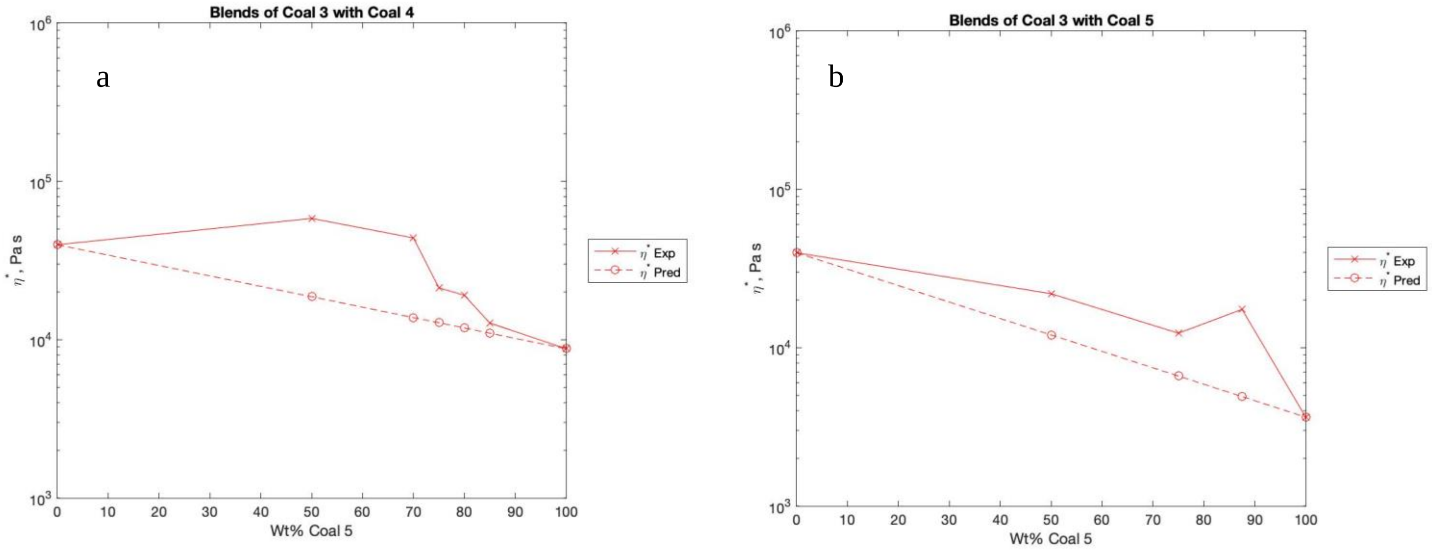

Figure 5.6: η^*_{min} as a function of composition for C3-C4 (a) and C3-C5 (b)

Figures 5.6a & b above detail the η^*_{min} as a function of composition for C3-C4 (a) & C3-C5(b). Figures C12 & C13 (Appendix C) exhibit the η^* and tanδ as a function of temperature for C3-C4 (C12a & C12b) & C3-C5 (C13a & C13b). Figure C12c and C13c detail the sol point and gel point as a function of composition for C3-C4 and C3-C5, respectively.

η^*

C3-C4 afforded increases in η^*_{min} over the range C3-C4(50 – 80wt%) with a range of differences from 46.6% (7211 Pa s) to 104% (30099 Pa s), but agreement with the polymer blending rule at C3-C4(85wt%) (Figure 5.6a and Table C2, Appendix C). As coal 3 resolidification temperature occurred during softening and maximum fluidity of coal 4, reduced fluidity was likely due to the adsorption mechanism. For C3-C5 differences in TMF and MVR were even greater for this medium fluidity coal, of 59 ^{o}C (TMF) and 0.76 (MVR) (when compared with coal 4, see Figure 5.6b)). Consequently, increases in η^*_{min} were found for all compositions, with difference between 58.2% (9876 Pa s) and 112% (12534 Pa s), compared with additive behaviour (Table C2, Appendix C). The mechanisms thought to be behind this were early crosslinking (where coal 5 contained large macromolecular structures, where early crosslinking would lead to rapid increases in η^* and elastic behaviour), absorption and micro-fluidity segregation (a coal 3 effect). C3-C5(50wt%) did not exhibit a η^*_{min}.

Sol Point and Gel Point

For C3-C4, additive behaviour for sol point at C3-C4(50wt%) and C3-C4(75wt%) was observed, along with reductions in sol point at C3-C4(70wt%), of 1.5% (6.5 ^{o}C), C3-C4(80wt%), of 1.3% (5.8 ^{o}C), and C3-C4(85wt%), of 2.3% (10.1 ^{o}C), compared with additive behaviour (see Figure C12c and Table C3, Appendix C). At gel point, agreement was only found at C3-C4(85wt%), where increases in gel point were found at all other compositions (with differences ranging from 0.7% (3.2 ^{o}C) to 1.6% (8.0 ^{o}C) compared with additive behaviour (Table C3, Appendix C)). Increased gel point suggested that there were still fluid entities present to mitigate early crosslinking up to C3-C4(80wt%). For C3-C5, significantly increased values were found for sol point with differences of 2.9% (13.1 ^{o}C) and 2.0% (9.1 ^{o}C), along with increases in gel point of 1.2% (6.0 ^{o}C) and 0.9% (4.5 ^{o}C) compared with additive behaviour (C3-C5(50wt%) did not exhibit a sol point or gel point) (Figure C13c and Table C3, Appendix C). The differences between C3-C4 and C3-C5 were likely due to the increased rank of coal 5, where early crosslinking was possibly exacerbated by the increased size of macromolecular structures.

5.3.2.7.2. Blends of Coal 3 with High Fluidity Coals

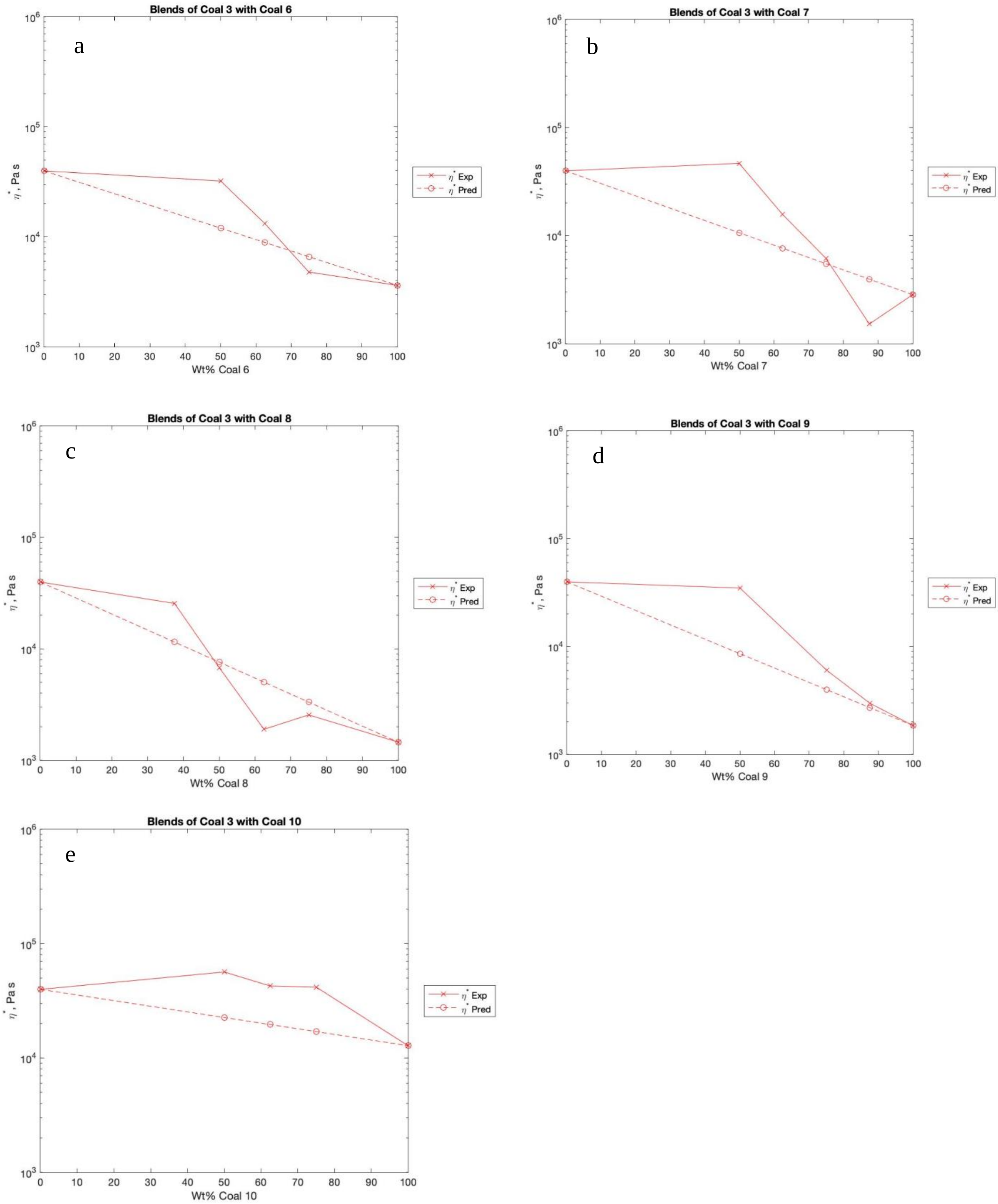

Figure 5.7: η^*_{min} (a) as a function of composition for C3-C6 (a), C3-C7 (b), C3-C8 (c), C3-C9 (d) and C3-C10 (e)

Figures 5.7a - e above detail the η^*_{min} as a function of composition for C3-C6 (a), C3-C7 (b), C3-C8 (c), C3-C9 (d) and C3-C10 (e). Figures C14 - C18 (Appendix C) exhibit the η* and tanδ as a function of temperature for C3-C6 (C14a & C14b), C3-C7 (C15a & C15b), C3-C8 (C16a & C16b), C3-C9 (C17a & C17b) and C3-C10 (C18a & C18b). Figure C14c, C15c, C16c, C17c and C18c detail the sol point and gel point as a function of composition for C3-C6, C3-C7, C3-C8, C3-C9 and C3-C10, respectively.

*η**

There were differences of 23 ^{o}C and 0.3 in TMF and MVR between coal 3 and coal 6, giving rise to an increase in η^*_{min} at C3-C6(50wt%) of 91.4% (20200 Pa s) compared with additive behaviour (Table C2, Appendix C), possibly due to the absorption mechanism along with early crosslinking and segregation of micro-fluid pockets (coal 3). Agreements were found with η^*_{min} for experimental and predicted values at C3-C6(62.5wt%) and C3-C6(75wt%) (Figure 5.7a).

Two different behaviours exhibited by C3-C7 suggested that the individual coals dictated the overall behaviour of the blend. Differences in TMF and MVR of 30 ^{o}C and 0.50 were found, which was likely the cause of increased η^*_{min} at C3-C7(50wt%) and C3-C7(62.5wt%) (see Figure 5.7b). Absorption and early crosslinking, along with micro-fluidity segregation, were likely mechanisms behind fluidity reduction for C3-C7(50wt%) and C3-C7(62.5wt%), with differences of 126% (36045 Pa s) and 69.1% (8075 Pa s) compared with additive behaviour. Reduction in η^*_{min} at C3-C7(82.5wt%) of 88.9% (2431 Pa s) was likely due to the suspension mechanism (Table C2, Appendix C).

There was a difference of 36 ^{o}C in TMF between coal 3 and coal 8, along with a difference of 0.22 in MVR, giving rise to some reduction in fluid matter generation through the absorption and fluidity segregation mechanism for C3-C8(37.5wt%), with an increase in η^*_{min} of 75.9% (14061 Pa s), compared with additive behaviour (see Table C2, Appendix C). Conversely, enhanced fluidity at C3-C8(62.5wt%) (with a difference of 90.5% (3132 Pa s) (Table C2, Appendix C)) was due to ‘fluid pockets’ linking and clustering of solid material from low viscosity suspension formation (Figure 5.7c).

Differences of 15 ^{o}C and 0.11 were found in TMF and MVR between coals 3 and 9. Despite reduced differences in the aforementioned parameters compared with other blends of coal 3 with high fluidity coals, an increase in η^*_{min} was found at C3-C9(75wt%) of 41.1% (2057 Pa s) compared with additive behaviour (Figure 5.7d and Table C2, Appendix C). Segregation of micro-fluidity of coal 3 could have given rise to reductions in fluidity at C3-C9(50wt%) of 121% (26270 Pa s) compared with additive behaviour.

C3-C10 exhibited the most significant negative differences for all high fluidity coals blended with coal 3. Differences in TMF and MVR of 25 ^{o}C and 0.28 existed between coals 3 and 10, where it was likely that the higher η^*_{min} for coal 10, compared with coals 6 – 9, was a significant factor in the reduced fluidity of this blend (Figure 5.7e). This would rationalise the suspension mechanism, where increased η^*_{min} of coal 10 could not afford a suspension to cluster coal 3 solid material. Additionally, the segregation of micro-fluidity in coal 3, particularly towards C3-C10(50wt%), could have been another factor that caused increased η^*_{min}. Increases in η^*_{min} ranging from 74.0% (22988 Pa s) and 85.8% (33884 Pa s) were found here.

Sol Point and Gel Point

Increases in sol point, compared with additive behaviour, were found for all compositions of C3-C6 (ranging from 1.3% (5.4 ^{o}C) to 1.5% (6.2 ^{o}C) (Table C3, Appendix C)), likely due to the difference in the sol point of the two coals. For gel point, agreement with additive behaviour was found at C3-C6(50wt%), along with reductions in gel point at C3-C6(62.5wt%) and C3-C6(75wt%) of 0.9% (4.3 ^{o}C) and 0.8% (3.8 ^{o}C), respectively (Figure C14c and Table C3, Appendix C).

Significant increases in sol point, compared with additive behaviour, were found at all compositions of C3-C7 apart from C3-C7(50wt%) (see Figure C15c, Appendix C), ranging from 0.5% (2.1 ^{o}C) to 4.0% (17 ^{o}C) (Table C3, Appendix C). Again, this was likely due to the absorption mechanism. Increases in gel point were found at all compositions, compared with additive behaviour, ranging from 2.9% (13.7 ^{o}C) to 5.2% (25.1 ^{o}C) (Table C3, Appendix C), which could possibly have been due to suspension formation with higher additions of coal 7, due to lack of surface area of solid material for radicals to crosslink to, due to clustering of coal 3.

Interesting results for sol point were exhibited for C3-C8, where reductions in sol point, compared with additive behaviour, were found at all compositions (ranging from 1.5% (6.3 ^{o}C) to 3.9% (15.8 ^{o}C) (see Table C3, Appendix C)), suggesting positive interactions between the coals during softening, along with a possible suspension mechanism (mitigating negative impacts of coal 3). Increase in gel point, compared with additive behaviour, was found at C3-C8(75wt%) of 2.1% (10.1 ^{o}C) (Table C3, Appendix C), likely due to the same mechanisms proposed for C3-C7 (Figure C16c, Appendix C). For C3-C9, increases in sol point, compared with additive behaviour, were found at all compositions of 1.0% (4.1 ^{o}C) to 1.6% (6.8 ^{o}C) (see Figure C17c and Table C3, Appendix C). For gel point, agreement was found at C3-C9(50wt%), and small reductions in gel point at C3-C9(75wt%) and C3-C9(87.5wt%) of 1.2% (5.6 ^{o}C) and 1.1% (5.1 ^{o}C), when compared to predicted behaviour, likely due to early crosslinking (see Table C3, Appendix C). Increases at all compositions for sol point were found for C3-C10, ranging from 1.0% (4.4 ^{o}C) to 1.7% (7.5 ^{o}C), when compared with additive behaviour (see Figure C18c and Table C3, Appendix C). For gel point, agreements with predicted values were exhibited at C3-C10(50wt%) and C3-C10(75wt%), with reduction in gel point at C3-C10(62.5wt%) of 1.0% (4.7 ^{o}C) (Table C3, Appendix C).

5.3.2.8. Confirmatory Correlations between η^*_{min}, G' and G"

Although G' and G" have not been discussed in detail (due to the high correlations between G' and G" with η^*_{min} for single coals), correlations were made between the three viscoelastic parameters to understand if changes in elastic and viscous behaviour could confirm particular interactions and mechanisms behind non-additive behaviour. Table 5.8 details the correlation R^2 values for the sets of blends described above. Correlation matrices for these correlations are shown in Figures C37 – C43, Appendix C. Correlations between η^* with G' and G" for single coals have also been given for reference (Table 5.8).

Table 5.8: Correlation R^2 values between η^*_{min} vs G' and G"

Blend Set	η^*_{min} – G' Correlation	η^*_{min} – G" Correlation
Coal 1 Blends	0.98	0.93
Coal 2 Blends	0.99	0.96
Similar Coal Blends	0.93	1.00
Coal 4 Blends	0.91	1.00
Coal 5 Blends	0.91	1.00
Coal 3 with Medium Fluidity Coals	0.94	0.95
Coal 3 with High Fluidity Coals	0.97	0.98
Single Coals	0.99	1.00

From the correlations detailed above in Table 5.8, it was found that there was a high degree of correlation for all blend types, with $R^2 > 0.9$. Notable highlights from the correlations were as such. Blends with coals 1 and 2 exhibited better correlations between η* and G', compared with G", likely due to the increased inertinite content of coals 1 and 2. Improved correlations between η* and G" were observed for all other blends, compared with G'. The lowest correlation R^2 values were found for coal 4 and coal 5 blends, with 0.91 for correlations between G' and η*. With all R^2 values > 0.9, a multitude of mechanisms likely occurred to afford deviations from additive behaviour, such as maceral crosslinking, suspension formation, fluid matter adsorption and hydrogen donation.

5.3.3. Plate Gap Measurements

From chapter 4 it was found that much greater expansion was observed using the cup geometry, when compared with the PP, due to sample displacement from the latter. Hence, this could act as a proxy for gas pressure and help understand the expansion of the coal and the force that these samples exert during carbonisation. Additionally, as expansion is linked to η^*_{min}, examining differences to additive behaviour could help in understanding the factors impacting coal - coal interactions. Therefore, measurements of plate gap at maximum expansion were plotted as a function of composition to show which blends exhibited non-additive expansion and indicate the interactions that occur. For example, when reduced expansion is found for some samples, this will support theories as to adsorption of fluid material, and the subsequent reduction of fluidity. Plots of plate gap as a function of temperature have also been provided in Figures C44 – C49, Appendix C, to identify which blends exhibited continuous expansion as found for coal 5 with 1.5 g and coal 4 with 3 g (chapter 4.3.2.5 and 4.3.3.3). Agreement with additive behaviour was defined as being within 14.3% (95% confidence limit with an RSD of 7.32%).

5.3.3.1. Blends of Similar Coals

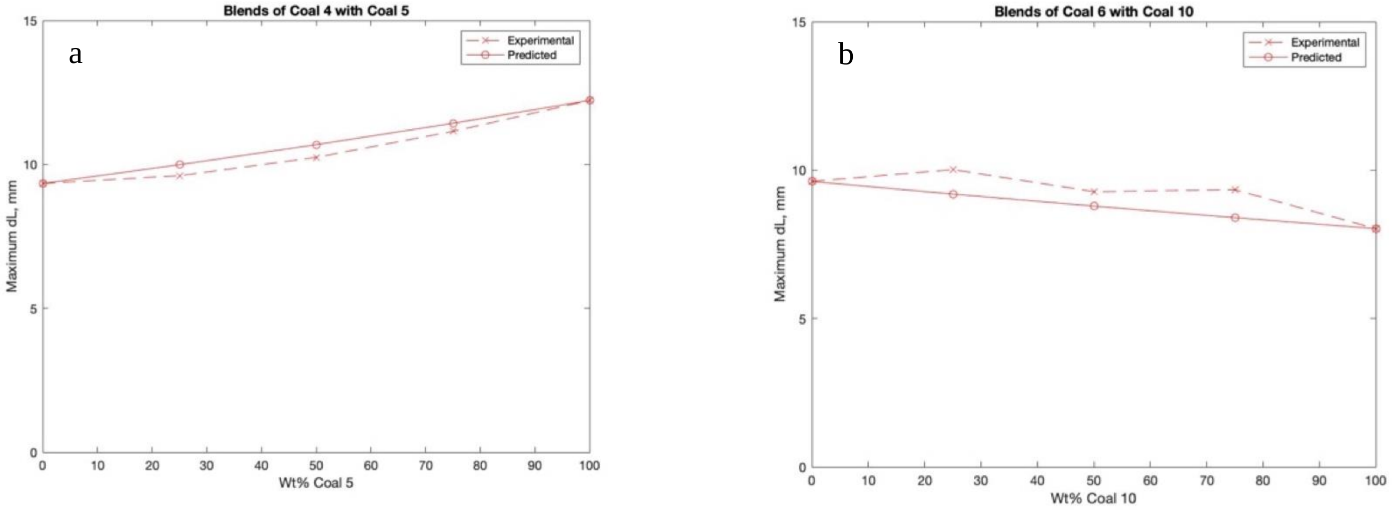

Figure 5.8: Plate gap at maximum expansion as a function of composition for C4-C5 (a) and C6-C10 (b)

Figures 5.8a and b detail the maximum plate gap as a function of composition plots for blends of C4-C5 and C6-C10. Figures C44a and C44b (Appendix C) detail the plate gap as a function of temperature for blends of C4-C5 and C6-C10. Blending two medium fluidity coals (with MVR > 1), continuous expansion was found for all samples (Figure C44a), increasing almost linearly with composition from C4-C5(0wt%) to C4-C5(100wt%) (Figure 5.8a). This was in line with the difference in η^*_{min} of the two coals (8770 Pa s – coal 4 to 3640 Pa s – coal 5), where expansion increased with decreasing η^*_{min}. Agreement was found with predicted values from linear behaviour for all compositions (Table C4, Appendix C). For C6-C10 (Figures 5.8b), all samples showed significantly increased maximum expansion, implying that volatiles were trapped within the blends of C6-C10, compared to volatile escape from the single coals tested separately. This was highlighted by significantly greater expansion than predicted at C6-C10(50wt%) and C6-C10(75wt%), by 15.5% (1.4 mm) and 25.7% (2.4 mm) compared with predicted, respectively (see Table C4, Appendix C). All compositions of C6-C10 did show a drop in plate gap during resolidification (see Figure C44b) due to volatile escape (through low viscosity suspension) and subsequent reduced coke and gas pressure, where η^*_{min} ranged from 2650 Pa s (50:50wt%) to 12800 Pa s (100wt% coal 10).

5.3.3.2. Blends with Non-Softening Coals 1 and 2

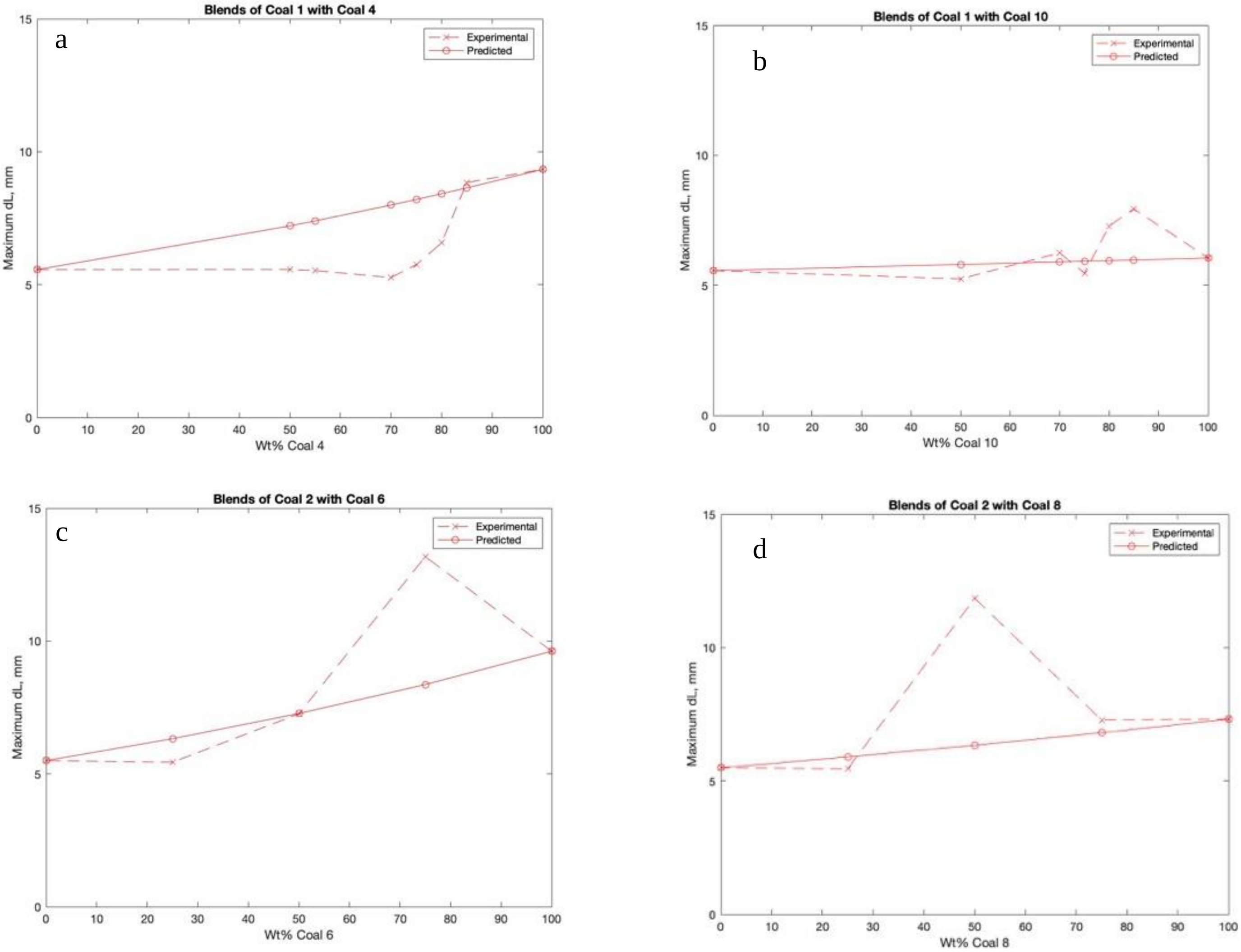

Figure 5.9: Plate gap at maximum expansion as a function of composition plots for C1-C4 (a), C1-C10 (b), C2-C6 (c) and C2-C8 (d)

Figures 5.9a – d detail the maximum expansion plate gap as a function of composition for blends of C1-C4, C1-C10, C2-C6 and C2-C8. Figures C45a – d (Appendix C) detail the plate gap as a function of temperature plots for blends of C1-C4, C1-C10, C2-C6 and C2-C8. C1-C4 (Figure 5.9a) and C1-C10 (Figure 5.9b) afforded different plate gap expansion, despite similar trends in η^*_{min} for these two blends. C1-C4 exhibited almost no change in expansion up to C1-C4(70wt%), followed by an increase at C1-C4(85wt%) (significant reductions in plate gap, compared with additive behaviour, of 33.8% (1.9 mm), 55.8% (2.9 mm), 46.0% (2.6 mm) and 30.6% (2.0 mm) were found at C1-C4(50wt% - 80wt%) (Table C4, Appendix C)). This supports an absorption mechanism, restricting expansion at coal 1 addition over 15wt%.

For C1-C10, additive behaviour up to C1-C10(75wt%) was found. Interestingly, there was enhanced expansion at C1-C10(80wt%) and C1-C10(85wt%), with differences to additive behaviour of 18.3% (1.3 mm) and 24.7% (2.0 mm), respectively (Table C4, Appendix C). This could be rationalised, as coal 10 did not show as significant expansion when compared with the medium fluidity coals. Adding a small amount of inert coal, C1-C10(80-85wt%), increased η^*_{min} to retain volatile matter, and subsequent build-up of gas pressure leading to sustained expansion (Figure C45b, Appendix C), where increased elastic forces prevent pores from coalescing. With relatively high MVR, this could have been caused by crosslinks between macromolecular structures, in line with the correlation between η^*_{min} and G' for coal 1 blends.

C2-C6 (Figure 5.9c) displayed similar trends in plate gap as those in $\eta^*_{min;}$ drop in expansion at C2-C6(25wt%) and increase in expansion at C2-C6(50 – 75wt%). This would suggest that the maximum expansion here was due, in part, to reduced η^*_{min}, allowing larger pores to develop, which was restricted significantly at C2-C6(25wt%) due to lack of fluidity from coal 2 (a significant difference of 34.8% (4.6 mm) between experimental and predicted values was found here, see Table C4, Appendix C). Interestingly, at C2-C6(75wt%), the maximum expansion was greater here compared with coal 6 (a significant difference of 20.1% (1.1 mm) between experimental and predicted values was found here, see Table C4 (Appendix C)). This could be due to the same mechanism proposed for C1-C10: coal 2 increases the η^*_{min}, retains volatile matter and reduces the pore size to an extent that internal coke pressure is increased, compared with 100wt% coal 6, where large, coalesced pores form due to lower η^*_{min} and subsequent volatile release. This was emphasised in plots of plate gap as a function of temperature, where C2-C6(25wt%) exhibited sustained expansion, plateauing at resolidification, whereas coal 6 exhibited a drop in plate gap during resolidification, due to coalesced pores and reduced coke pressure (Figure C45c, Appendix C)).

For C2-C8 (Figure 5.9d) maximum expansion was found at C2-C8(50wt%). This, again, was possibly due to the due to reduced pore size and subsequent increase in internal coke pressure as a function of low fluidity (high η^*_{min}). This was also shown in the plots of plate gap as a function of temperature, where C2-C8(50wt%) exhibited expansion greater than double that of any other C2-C8 blend tested (Figure C45d, Appendix C). This would also suggest that a particular range of fluidity, or η^*_{min}, is required to allow significant expansion to occur and sustain the expanded coke pellet throughout the test (without sample displacement due to weak coke strength). Consequently, disagreement with additive behaviour was only found at C2-C8(50wt%) by 45.9% (5.4 mm, Table C4, Appendix C).

5.3.3.3. Blends with Medium Fluidity Coal 4

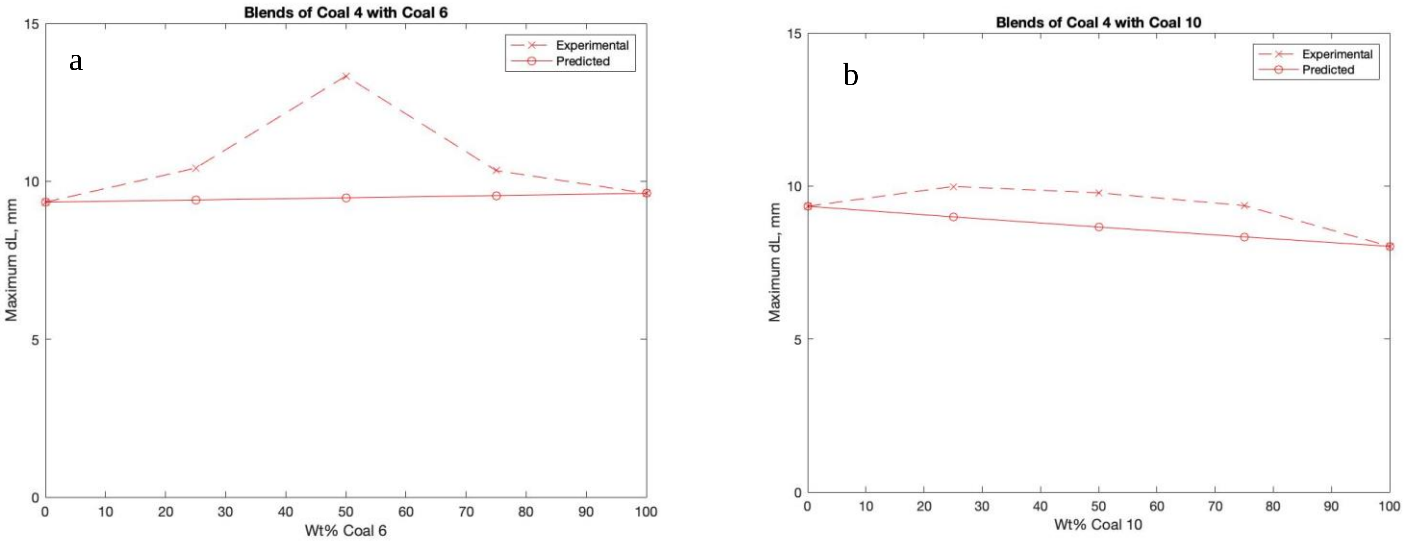

Figure 5.10: Plate gap at maximum expansion as a function of composition for blends of C4-C6 (a) and C4-C10 (b)

Figures 5.10a and b detail maximum plate gap expansion as a function of composition for blends of C4-C6 and C4-C10. Figures C46a and C46b (Appendix C) detail plate gap as a function of temperature for blends of C4-C6 and C4-C10.

C4-C6(50wt%) exhibited the greatest expansion (28.9% (3.9 mm) greater than predicted, see Table C4 (Appendix C)), with retention of the entire sample, suggesting increased gas pressure (see Figure 5.10a). At C4-C6(75wt%) reduced maximum plate gap was found, probably due to reduced η^*_{min} (allowing volatile matter escape). The significant expansion at C4-C6(50wt%) suggested that the reduction in η^*_{min} (to 2250 Pa s), to a limit, allowed sufficiently large pores to form but mitigated excessive pore coalescence and volatile matter release (note that the η^*_{min} at C4-C6(75wt%) was found to be 1480 Pa s and semi-coke displacement occurred (Figure C46a, Appendix C). C4-C10 (see Figure 5.10b) exhibited enhanced maximum expansion at all compositions, but small reductions in plate gap after resolidification (Figure C46b, Appendix C), again demonstrating the impact of blending with a high fluidity coal. Disagreements with additive behaviour were found at C4-C6(50wt%) and all C4-C10 compositions of 28.9% (3.9 mm), 14.7% (1.5 mm), 21.3% (2.1 mm) and 26.6% (2.5 mm), respectively (Table C4, Appendix C).

5.3.3.4. Blends with High Rank, Medium Fluidity Coal 5

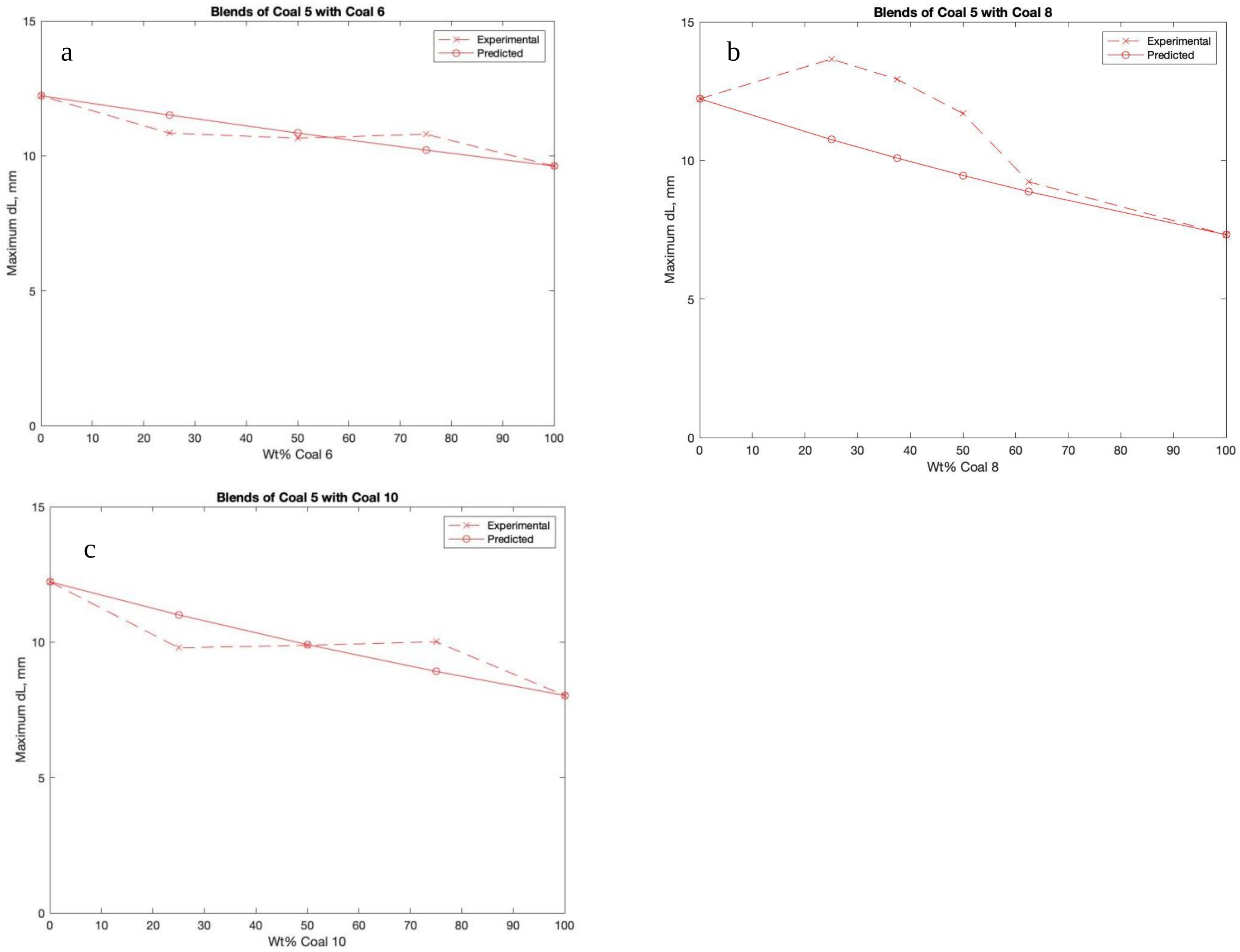

Figure 5.11: Plate gap at maximum expansion as a function of composition for C5-C6 (a), C5-C8 (b) and C5-C10 (c)

Figures 5.11a – c detail maximum expansion plate gap as a function of composition plots for blends of C5-C6, C5-C8 and C5-C10. Figures C47a – c detail plate gap as a function of temperature for blends of C5-C6, C5-C8 and C5-C10.

C5-C6 (see Figures 5.11a) and C5-C10 (see Figures 5.11c) afforded similar changes in plate gap as a function of temperature; sustained expansion was found up to C5-C6(75wt%) (see Figure C47a, Appendix C) and C5-C10(75wt%) (see Figure C47c, Appendix C), where the η^*_{min} (4630 Pa s and 5490 Pa s, respectively) was low enough to allow large pores to form but mitigate volatile release (see Figure 47a, Appendix C). As, by definition, coal 5 swelled more than high volatile coals, the greatest expansion was found for the single coal 5, compared with any of the constituent blends. Additionally, the expansion for C5-C10(75wt%) was less than that for C5-C6(75wt%), corresponding with the comparatively reduced η^*_{min} for C5-C6(75wt%). However, the increased maximum expansion was 24.2% (2.4 mm) greater than predicted for C5-C10(75wt%), compared with agreement for C5-C6(75wt%), when compared with additive behaviour.

For C5-C8 (Figure 5.11b), maximum sustained expansion was found at C5-C8(25wt%), where plate gap was found to be greater than that of 100wt% coal 5 (Figure 47b, Appendix C). Enhanced maximum expansion was found up to C5-C8(50wt%) due to the very high volatile matter content of coal 8, but sustained expansion was only found at C5-C8(25wt%) (see Figure 47c, Appendix C). Disagreements with additive behaviour were found at C5-C8(25wt%), C5-C8(37.5wt%), C5-C8(50wt%) and C5-C10(75wt%) ranging from 16.5% (1.9 mm) to 24.2% (2.4 mm) (Table C4, Appendix C).

5.3.3.5. Blends with Coal 3

5.3.3.5.1. Blends with Coal 3 and Medium fluidity coals 4 and 5

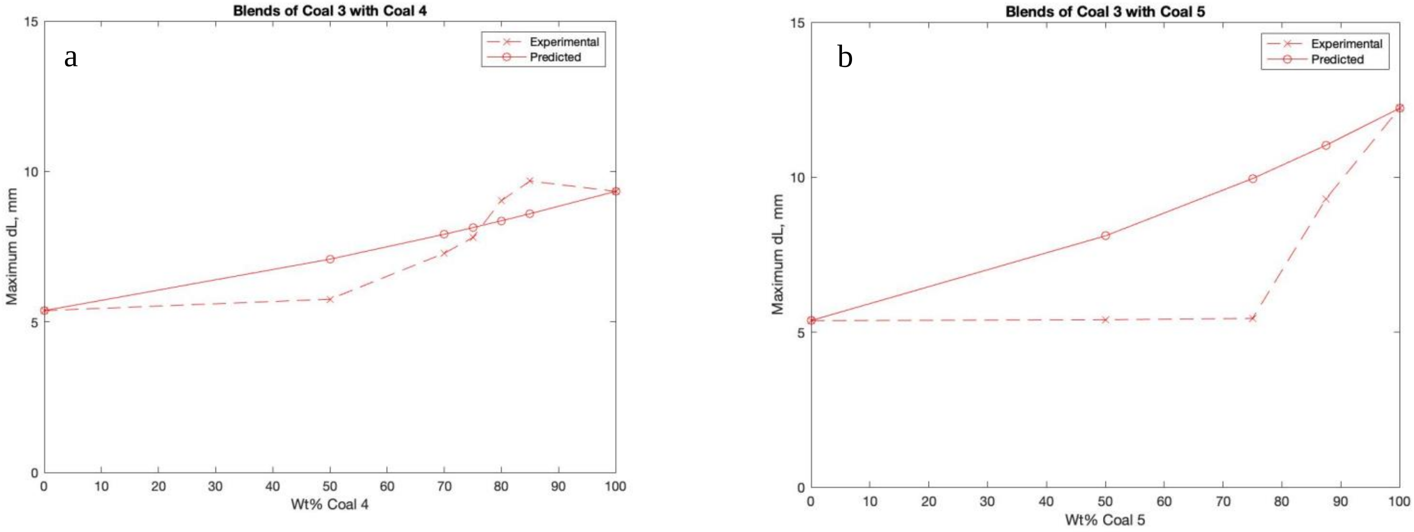

Figure 5.12: Plate gap at maximum expansion as a function of composition for C3-C4 (a) and C3-C5 (b)

Figures 5.12a and b detail the plate gap as a function of composition for C3-C4 and C3-C5. Figures C48a and C48b (Appendix C) detail plate gap as a function of temperature for C3-C4 and C3-C5. C3-C4 (Figures 5.12a) and C3-C5 (Figure 5.12b) plate gap measurements appeared to show similar trends to that shown in η^*_{min} measurements. For C3-C4, maximum expansion was found when the η^*_{min} of the blends was closest to the polymer blending rule (C3-C4(85wt%)), and vice versa for minimum expansion for C3-C4(50wt%). For C3-C5, all blends showed increased η^*_{min} (compared with additive behaviour), which was highlighted in plate gap where reduced expansion was afforded. Again, these blends suggested that expansion of coal samples was a function of η^*_{min} (lower η^*_{min}, greater expansion). Differences to additive behaviour were found at C3-C4(50wt%) and all C3-C5 compositions of 27.8% (1.6 mm), 62.9% (3.4 mm), 93.2% (5.1 mm) and 22.2% (2.1 mm), respectively (see Table C4, Appendix C).

5.3.3.5.2. Blends with Coal 3 with High Fluidity Coals

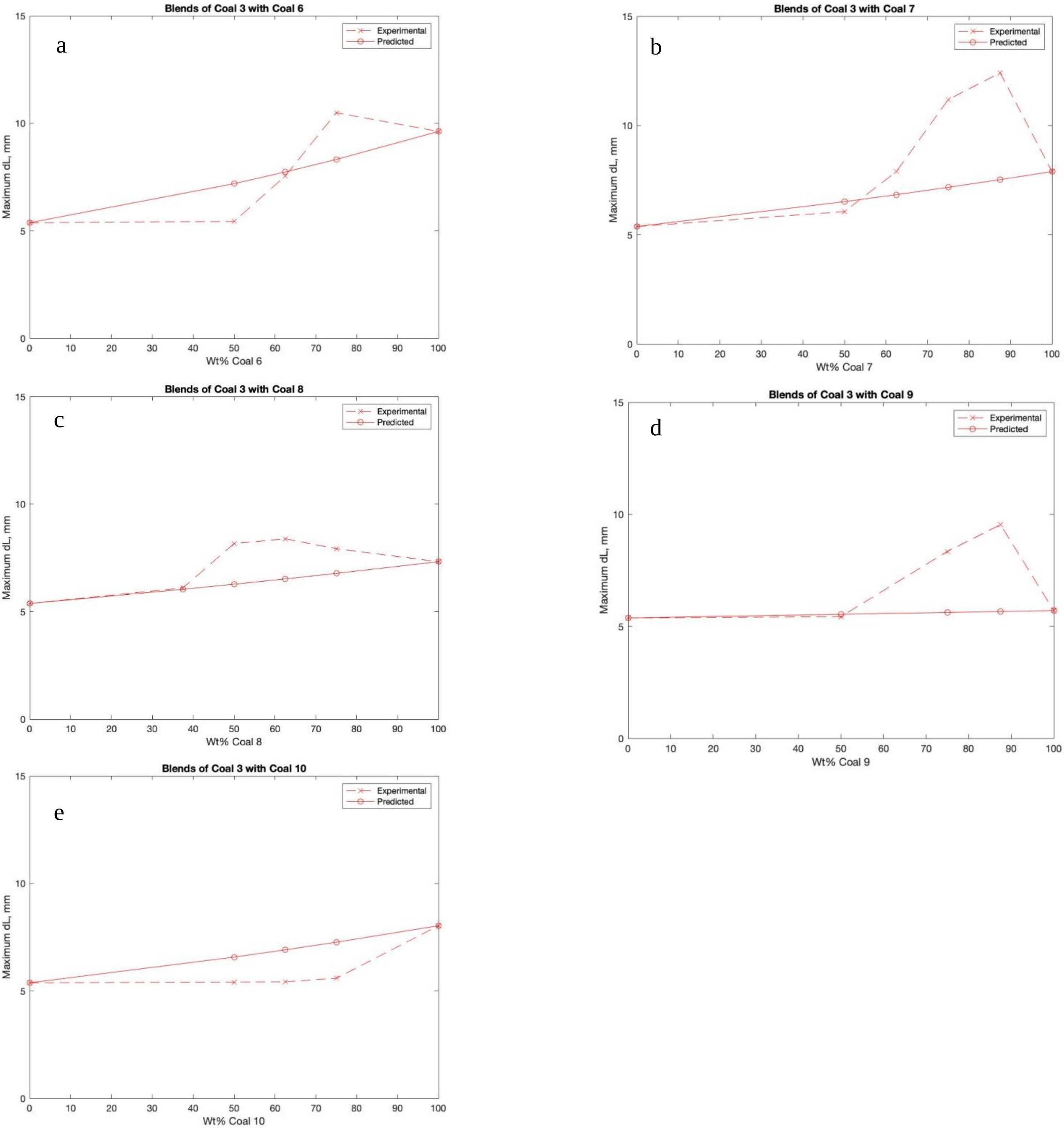

Figure 5.13: Plate gap at maximum expansion as a function of composition for C3-C6 (a), C3-C7 (b), C3-C8 (c), C3-C9 (d) and C3-C10 (e)

Figures 5.13a – e detail the plate gap at maximum expansion as a function of composition for C3-C6, C3-C7, C3-C8, C3-C9 and C3-C10. Figures C49a – e (Appendix C) detail plate gap as a function of temperature plots for C3-C6, C3-C7, C3-C8, C3-C9 and C3-C10.

The plate gap increase appeared to be a function of η^*_{min}, where increased fluidity gave rise to increasing plate gap. C3-C6(50wt%) provided a maximum expansion 38% (2.1 mm) lower than predicted (see Table C4, Appendix C) where a η^*_{min} of 3.22×10^4 Pa s was recorded (see Table C2, Appendix C). Maximum sustained expansion was found at C3-C6(75wt%) (see Figure C49a, Appendix C and Figure 5.13a above) with a η^*_{min} of 4780 Pa s, which provided an enhanced maximum plate gap 18.4% (1.9 mm) greater than predicted (see Table C4, Appendix C). C3-C6(100wt%) exhibited a decrease during resolidification, due to lower η^*_{min} of 3620 Pa s.

For C3-C7 (see Figures 5.13), maximum sustained expansion occurred at C3-C7(75wt%) (with an increased maximum expansion 35.1% (3.9 mm) greater than predicted (Table C4, Appendix C). However, the greatest expansion was found for C3-C7(82.5wt%) (with an increase of 38.9% (4.8 mm) compared to predicted behaviour (Table C4, Appendix C)) where a drop in plate gap during resolidification was found (Figure C49b, Appendix C). This was rationalised in η^*_{min}, where C3-C7(75wt%) provided a value of 6160 Pa s (sustained expansion), compared with 1520 Pa s for C3-C7(82.5wt%) (semi-coke displacement). This also supports the suspension mechanism theory, where a non-linear decrease in η^* through loss of elastic structure through suspension formation and subsequent clustering of inert material allows volatile release.

For C3-C8 (Figure 5.13c) drops in plate gap during resolidification were found from C3-C8(62.5wt%) (Figure C49c, Appendix C). Again, this was rationalised by the drop in η^*_{min} from C3-C8(50wt%) (sustained expansion) to C3-C8(62.5wt%) (semi-coke displacement), where η^*_{min} values dropped from 6760 Pa s to 1900 Pa s, respectively. Hence, once a low viscosity suspension forms, volatile release can occur, there is very little contribution of elastic behaviour from coal 3 (due to clustering of solid particles) and formation of weak semi-coke occurs. Enhanced maximum expansion was found at C3-C8(50wt%) and C3-C8(62.5wt%) with differences of 22.2% (1.8 mm) and 21.4% (1.8 mm) compared with predicted values, respectively (Table C4, Appendix C).

Unlike the other blends of coal 3 with high fluidity coals, C3-C9 (see Figures 5.13d) and C3-C10 (see Figures 5.13e) did not exhibit reduced η^*_{min} when compared with the polymer blending rule. Despite this, excessive, sustained expansion was found for all compositions for

C3-C9 (see Figure C49d, Appendix C) with increased expansion of 32.6% (2.7 mm) and 40.6% (3.9 mm) compared with additive behaviour at C3-C9(75wt%) and C3-C9(87.5wt%) (see Table C4, Appendix C). Maximum sustained expansion occurred when η^*_{min} reached 2980 Pa s, whereas coal 9 (which exhibited semi-coke displacement) afforded η^*_{min} of 1850 Pa s. For C3-C10, very limited expansion was found, which was found to be due to a high η^*_{min} of 41600 Pa s at C3-C10(75wt%), where coal 10 possessed the greatest η^*_{min} of the high fluidity coals. Again, there appeared to be a η^*_{min} limit at which sustained expansion stopped (see Figure C49e, Appendix C) and semi-coke displacement started (due to the release of volatile matter due to low η*). Agreement was found with predicted values for all C3-C10 compositions.

5.3.4. Connections Between Viscoelastic Parameters and Plate Gap

Overviewing the plate gap expansion and the samples which exhibited sustained expansion, and those which exhibited semi-coke displacement during resolidification, a link was found with η^*_{min}. In order for a continuous expansion to occur, η^*_{min} had to be above 2000 - 3000 Pa s. The closer the η^*_{min} to the limit, the greater the final expansion of the sample, due to large pores within the fluid matrix. However, below 2000 - 3000 Pa s, there was possibly insufficient elastic force to segregate the pores to an extent that internal coke pressure and gas pressure could build up. Consequently, sample displacement occurred through top plate force pushing through the weak semi-coke formed. One possible mechanism that could attribute to this is the propagation of volatile matter through the sample. If the sample had a low enough η^*_{min}, volatile matter could travel to the surface of the fluid sample and be released. If the η^*_{min} is not below the limit (2000 - 3000 Pa s), the elastic force of the viscoelastic material withholds the volatile matter within the sample, stopping propagation, and allowing internal gas pressure to build through pore generation and expansion.

For blending non-similar coals, the mechanism behind this was likely to be suspension formation. If sufficient fluid material was generated by a high fluidity coal, inert material could be suspended in the low viscosity matrix, a non-linear drop in viscosity occurred due to clustering of inert material, and volatile matter could propagate through the low viscosity fluid matrix. This was highlighted by plotting η^*_{min} vs maximum expansion plate gap (Figure 5.14 below), where plate gap increased almost exponentially as the η* reaches 2000 – 3000 Pa s. The limit for sustained expansion zone, with respect to η^*_{min}, is shown in the plot, where the closer to this zone, the greater the maximum expansion plate gap. At or below the limit, it was likely that sufficient fluid material was generated to form a suspension and cluster the inert material.

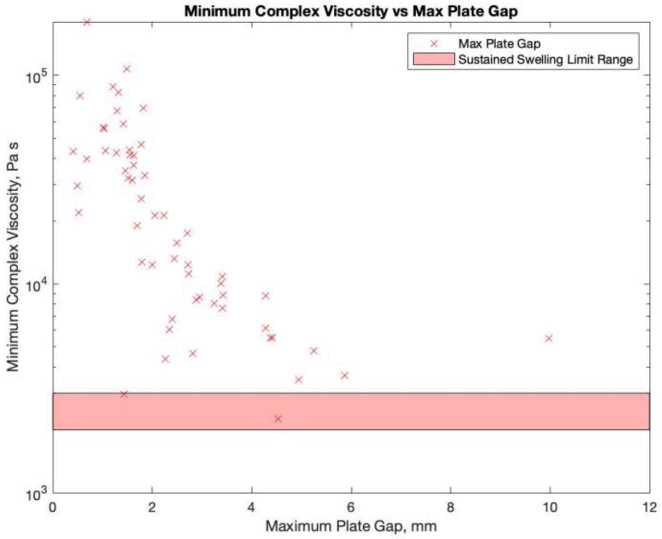

Figure 5.14: η^*_{min} as a function of maximum expansion plate gap for blends that exhibit sustained expansion (with η^* limit range (red zone) for sustained expansion to occur)

5.4. Conclusions

Using the novel cup geometry, samples could be tested at 3 g, as opposed to 1.5 g (found in all previous literature using the PP geometry), providing more representative analysis of viscoelastic behaviour and reducing the error in blend composition. Most blends tested here afforded non-linear behaviour, including those with similar coking properties and those with non-coking coals, likely due to prevention of fluid propagation and fluid material adsorption, or hydrogen donation effects and suspension formation, where such mechanisms were also in line with correlations with G’ and G”. Interestingly, enhanced fluidity was found in many blends tested here, supporting a possible suspension mechanism theory leading to non-linear decreases in η* through the clustering of inert material.

Blending non-softening coals with high fluidity coals gave rise to sustained expansion, due to the adsorption of fluid material and limiting gas release, and subsequent increased internal gas pressure within the sample. Blends of medium fluidity and high fluidity coals also provided enhanced expansion due to trapped volatile matter in the blend, compared to testing the coals separately. Conversely, blends of non-softening and medium fluidity coals provided a suppression on expansion due to fluid material adsorption. For some blends there appeared to be a limit at which sustained expansion was not achieved, and the force of the top plate could force through the weak-semi coke formed (suggested to be the point at which low viscosity suspension formed). Subsequently it was possible that highly viscous samples (with low η^*_{min}) allowed the escape of volatile matter through the low viscosity fluid matrix of suspensions, giving rise to weak, coalesced pores and subsequent reduced internal gas pressure. A limit of 2000 – 3000 Pa s was found to dictate if sustained expansion occurred, where η^*_{min} lower than the limit, a weak semi-coke was formed due to suspension formation.

5.5. References

Adeleke, A.O., Makan, R.S., HND, P. and Ibitoye, S.A. 2007. Studies on the Gieseler Plastometry Parameters of the American Pittson Coal for Metallurgical Cokemaking at the Ajaokuta Steel plant, Nigeria. *Pacific Journal of Science and Technology*, ***8***(2), pp.208-211.

Ahuja, A. and Singh, A. 2009. Slip velocity of concentrated suspensions in Couette flow. *Journal of Rheology*. ***53***(6), pp.1461-1485.

Altman, D.G. and Bland, J.M. 2003. Interaction revisited: the difference between two estimates. *Bmj*. ***326***(7382), p.219.

Barnes, H.A., Hutton, J.F. and Walters, K. 1989. *An introduction to rheology, Volume 3*. 1st Edition. Amsterdam: Elsevier.

Castro Díaz, M., Zhao, H., Kokonya, S., Dufour, A. and Snape, C.E. 2012. The Effect of Biomass on Fluidity Development in Coking Blends Using High-Temperature SAOS Rheometry. E*nergy & Fuels*. 2***6(***3), pp.1767-1775.

Castro Diaz, Miguel., Snape, C., Florentino-Madiedo, L., Diaz-Faes, E. and Barriocanal, C. 2018. Importance of Biomass and Binder Selection for Coking Briquette Preparation: Their Effect on Coal Thermoplastic Properties. *Energy & Fuels*. ***32****(10), pp.10727-10736.*

Castro-Díaz, M., Duffy, J.J., Snape, C.E. and Steel, K.M. 2007. The Shear-Rate Dependent Viscoelastic Properties of Coal during Carbonisation. In: *International Conference on Coal Science and Technology. 28th – 31st August 2007. Nottingham.*

Castro-Díaz, M., Duffy, J.J., Snape, C.E. and Steel, K.M. 2007. Use of High-Temperature, High-Torque Rheometry to Study the Viscoelastic Properties of Coal during Carbonization. *Journal of Rheology*. ***51***(5), pp.895-913.

Castro-Díaz, M., Edecki, L., Steel, K.M., Patrick, J.W. and Snape, C.E. 2008. Determination of the Effects Caused by Different Polymers on Coal Fluidity during Carbonization using High-Temperature ^{1}H NMR and Rheometry. *Energy & Fuels*. ***22***(1), pp.471-479.

Castro-Díaz, M., Steel, K.M., Drage, T.C., Patrick, J.W. and Snape, C.E. 2005. Determination of the Effect of Different Additives in Coking Blends using a Combination of in situ High-Temperature ^{1}H NMR and Rheometry. *Energy & Fuels*. ***19***(6), pp.2423-2431.

Clemens, A.H. and Matheson, T.W. 1995. The Effect of Selected Additives and Treatments on Gieseler Fluidity in Coals. *Fuel*. ***74***(1), pp.57-62.

Coussot, P., Tocquer, L., Lanos, C. and Ovarlez, G. 2009. Macroscopic vs. local rheology of yield stress fluids. *Journal of Non-Newtonian Fluid Mechanics*. ***158***(1-3), pp.85-90.

Das, B., Suresh, A., Dash, P.S., Chandra, S., Díaz, M.C., Stevens, L.A. and Snape, C.E. 2018. Understanding the Unusual Fluidity Characteristics of High Ash Indian Bituminous Coals. *Fuel Processing Technology*. ***176***, pp.258-266.

de Cordova, M., Madias, J. and Barreiro, J. 2016. Review on Modelling of Coal Blends for Prediction of Coke Quality. In: Ashburn, R. E. ed. *Proceedings of the Iron & Steel Technology Conference, 16-19th May 2016, Pittsburgh, PA.* Warrendale, PA: Association for Iron and Steel Technology.

Diaz-Faes, E., Barriocanal, C., Diez, M. A. and Alvarez, R. 2007. Characterisation of Different Origin Coking Coals and Their Blends by Gieseler Plasticity and TGA. *Journal of Analytical and Applied Pyrolysis.* ***80**(1),* pp. 203 – 208.

Diez, M.A., Alvarez, R. and Fernandez, M. 2012. Biomass Derived Products as Modifiers of the Rheological Properties of Coking Coals. *Fuel*. ***96***, pp. 306 – 313.

Duffy, J.J., Diaz, M.C., Snake, C.E., Mahoney, M.R. and Steel, K.M. 2007. Combined Use of Rheometry and Microscopy to Understand Pore Structure Development during Coal Carbonization. In: *International Conference on Coal Science and Technology.28th – 31st August 2007. Nottingham*.

Duffy, J.J., Mahoney, M.R. and Steel, K.M. 2010. Influence of Coal Thermoplastic Properties on Coking Pressure Generation: Part 2–A Study of Binary Coal Blends and Specific Additives. *Fuel*. ***89***(7), pp.1600-1615.

Eremin, A.Y., Kuprygin, V.V. and Kukolev, Y.B. 2016. Viscoplastic Properties of Binary and Multicomponent Coal Blends. *Coke and Chemistry*. ***59***(3), pp.69-73.

Flores, B., Agra, A., Gums, Alessandro., da Silva, G., Osorio, E. and Vilela, A. Thermoplastic Interaction of Ultra High Fluidity Brazilian Coal with Components of Blends. 2020. *Journal of Materials Research and Technology.* ***9**(3),* pp. 2737 – 2743.

Flores, B.D., Flores, I.V., Guerrero, A., Orellana, D.R., Pohlmann, J.G., Diez, M.A., Borrego, A.G., Osório, E. and Vilela, A.C. 2017. Effect of Charcoal Blending with a Vitrinite Rich Coking Coal on Coke Reactivity. *Fuel Processing Technology*. ***155***, pp.97-105.

Fraga, M., Flores, B., Osorio, E. and Vilela, A. 2020. Evaluation of the Thermoplastic Behaviour of Charcoal, Coal Tar and Coking Coal Blends. *Journal of Materials Research and Technology.* ***9**(3), pp. 3406 – 3410.*

Guelton, N. 2017. The Prediction of the Gieseler Characteristics of Coal Blends. *Fuel*. ***209***, pp.661-673.

Guerrero, A., Diez, M.A. and Borrego, A.G. 2015. Influence of Charcoal Fines on the Thermoplastic Properties of Coking Coals and the Optical properties of the Semicoke. *International Journal of Coal Geology*. ***147,*** pp.105-114.

Jenkins, D.R. and Mahoney, M.R. 2015. A Mechanistic Model for the Softening of Coking Coal and Its Use for Predicting the Dilatation of Blends. *Fuel*. ***153***, pp.585-594.

Kokonya, S., Castro-Díaz, M., Barriocanal, C. and Snape, C.E. 2013. An Investigation into the Effect of Fast Heating on Fluidity Development and Coke Quality for Blends of Coal and Biomass. *Biomass and bioenergy*. ***56***, pp.295-306.

Krzesinska, M., Smedowski, L. and Szeluga, U. 2013. Synergistic Effects on Pyrolysis of Binary and Ternary Coal Blends Studied by Means of Dynamic Mechanical Thermal Analysis and Gieseler Plastometer. *Journal of Analytical and Applied Pyrolysis.* ***100****,* pp. 127 – 136.

Kumar, P.P., Barman, S.C., Singh, S. and Ranjan, M. 2008. Influence of Coal Fluidity on Coal Blend and Coke Quality. *Ironmaking & Steelmaking*. ***35***(6), pp.416-420.

Lin, Y.G. and Winter, H.H. 1991. High-Temperature Recrystallization and Rheology of a Thermotropic Liquid Crystalline Polymer. *Macromolecules*. ***24***(10), pp.2877-2882.

Melendi-Espina, S., Alvarez, R., Diez, M.A. and Casal, M.D. 2015. Coal and Plastic Waste Co-Pyrolysis by Thermal Analysis–Mass Spectrometry. *Fuel Processing Technology*. ***137***, pp.351-358.

Melendi, S., Diez, M.A., Alvarez, R., Castro, M., Steel, K. and Snape, C.E. 2007. Rheological Behaviour of Coal Modified by Waste Plastics and Lubricating oils. In: *International Conference on Coal Science and Technology. 28th – 31st August 2007. Nottingham.*

Mochizuki, Y., Naganuma, R., Uebo, K. and Tsubouchi, N. 2017. Some Factors Influencing the Fluidity of Coal Blends: Particle Size, Blend Ratio and Inherent Oxygen Species. *Fuel Processing Technology*. ***159***, pp.67-75.

Nasirudeen, M. B. and Jauro, A. 2011. Quality of Some Nigerian Coals as Blending Stock in Metallurgical Coke Production. *Journal of Minerals & Materials Characterisation & Engineering.* ***10****(1),* pp. 101 – 109.

Neavel, R.C. 1982. Coal plasticity mechanism: inferences from liquefaction studies. In: Gorbaty, M. L., Larsen, J. W. and Wender, I. eds. *Coal science.* Cambridge, Massachusetts: Academic Press, pp. 1-19.

Nomura, S., Kato, K., Komaki, I., Fujioka, Y., Saito, K. and Yamaoka, I. 1999. Viscoelastic Properties of Coal in the Thermoplastic Phase. *Fuel*. ***78***(13), pp.1583-1589.

Ovarlez, G., Rodts, S., Ragouilliaux, A., Coussot, P., Goyon, J. and Colin, A. 2008. Wide-gap Couette flows of dense emulsions: Local concentration measurements, and comparison between macroscopic and local constitutive law measurements through magnetic resonance imaging. *Physical Review E.* ***78***(3), p.036307.

Sakurovs, R. 2003. Interactions between Coking Coals in Blends. *Fuel*. ***82***(4), pp.439-450.

Shaik, S., Chakravarty, S., Mishra, P. R., Sahu, R. and Chakravarty, K. 2019. Caking Ability Tests for Coal Blends in Process to Utilize the Indian Origin Coals. *Transactions of the Indian Institute of Metal.* ***72*** *(12),* pp. 3129 – 3137.

Steel, K.M., Castro Diaz, M., Patrick, J. W. and Snape, C.E. 2004. Use of Rheometry and ^{1}H NMR Spectroscopy for Understanding the Mechanisms behind the Generation of Coking Pressure. *Energy & Fuels.* ***18***, pp.1250 – 1256

Steel, K.M., Dawson, R.E., Jenkins, D.R., Pearce, R. and Mahoney, M.R. 2017. Use of Rheometry and Micro-CT Analysis to Understand Pore Structure Development in Coke. *Fuel Processing Technology*. ***155***, pp.106-113.

Steel, K.M., Diaz, M.C., Duffy, J.J. and Snape, C.E. 2009. Use of Oscillatory Shear Rheometry and Thermogravimetric Analysis to Examine the Microstructural Changes during

Coal Pyrolysis/Carbonization for the Prediction of IRSID Strength Indices. *Energy & Fuels*. ***23***(4), pp.2111-2117.

Steel, K.M., Diaz, M.C., Duffy, J.J., Snape, C.E. and Mahoney, M.R. 2014. Influence of Thermoplastic Properties on Coking Pressure Generation: Part IV–Further Evidence of the Role of Bubble Coalescence in the Mechanism for Pressure Generation. *Fuel*. ***129***, pp.102-110.

Steel, K.M., Diaz, M.C., Patrick, J.W. and Snape, C.E. 2006. Evidence for Network Formation during the Carbonization of Coal from the Combination of Rheometry and ^{1}H NMR Techniques. *Fuel*. ***85***(12-13), pp.1821-1830.

Takanohashi, T., Shishido, T., Saito, I., Masaki, K., Dobashi, A. and Fukada, K. 2006. Synergistic Effect of Coal Blends on Thermoplasticity Evaluated using a Temperature-Variable Dynamic Viscoelastic Measurement. *Energy & fuels*. ***20***(6), pp.2552-2556.

Tiwari, H.P., Banerjee, P.K. and Saxena, V.K. 2013. A Novel Technique for Assessing the Coking Potential of Coals/Coal Blends for Non-Recovery Coke Making Process. *Fuel*. ***107***, pp.615-622.

Todoschuk, T., Dofasco, A., Giroux, L. and Wing, K. 2019, June. *Coal Rheology – A Practical Approach for Industry.* In *Proc. 4th European Steel Technology and Application Days Conference, 24th June – 28th June 2019, Dusseldorf, Germany.*

Yoshida, T., Iino, M., Takanohashi, T. and Katoh, K. 2000. Study on Thermoplasticity of Coals by Dynamic Viscoelastic Measurement: Effect of Coal Rank and Comparison with Gieseler Fluidity. Fuel. ***79***(3-4), pp.399-404.

Chapter 6

A Comprehensive High Temperature ^1H NMR Study to Understand the Mobile Molecular Behaviour of a Range of Coals and Their Blends

Abstract

High temperature ^1H NMR has been used to understand the mobile molecular behaviour of a varied range of 10 coals where the percentage fluid hydrogen of the total hydrogen (%fluid H) and mobility (as determined by the spin-spin relaxation time, T_2) have been studied to quantify changes in such moieties. The proportion of fluid hydrogen and its mobility at maximum fluidity increased as a function of volatile matter content and bulk fluidity, apart from coal 3. Fluid hydrogen only exhibited Lorentzian behaviour for high volatile coals. Non- and medium fluidity coals exhibited maximum mobility at low temperature between 360 – 400 ^oC, followed by a decay as a function of temperature. Both additive and non-additive behaviour was exhibited by the blends tested, where the highest MVR coal and anomalous behaving coal 3 featured heavily in additive deviating blends with respect to % fluid H. For the fluid H mobility, T_{2L}, fewer blends displayed additive behaviour, with the majority of blends containing non-fluid coals exhibited deviations from additive behaviour, due to the significant difference in mobility profiles of such entities compared with high fluidity coals. Consequently, it was evident that the micro-fluidity of coal 3, displaying little bulk softening, was segregated from other coals, displaying high micro-fluidity.

6.1. Introduction

As coking coal fluidity is fundamental to the porosity and subsequent strength of the carbonised product, an understanding of the development of this phase is paramount to produce high quality metallurgical coke. Although this has been studied comprehensively using direct measurements of fluidity, such as Gieseler plastometry and high temperature rheometry, this cannot necessarily provide a quantitative measurement of the amount of fluid material generated by the coals. In some cases, coals can exhibit fluidity which does not correlate with coal properties, and hence cannot be rationalised through bulk measurements. High temperature proton nuclear magnetic resonance (^{1}H NMR) was developed to determine the percentage of material in a coal sample that was fluid (Dufour et al, 2012). This information could then be used to infer changes involving structural changes involving hydrogen (Lewitt & Lowe, 1997). From the use of this technique to study coals, it was found that mobile hydrogen containing entities form a major component of the metaplast. Additionally, these species can bind to and stabilise free radicals, preventing crosslinking and subsequent resolidification and hence sustaining the fluid range (Neavel, 1982). Therefore, the knowledge of these hydrogen species and their generation profiles is paramount to understanding the fluid behaviours of coking coals.

High temperature ^{1}H NMR has been used extensively to study coals to understand how the mobile hydrogen generation profiles correlate with measured fluidity (Steel et al, 2006), where the following has been found. *Maroto-Valer et al (1997)* found that half of hydrogen containing fluid species were generated from thermal breakdown of macromolecules, and half from pyridine soluble fractions. *Sakurovs (2000)* found that increasing the heating rate pushed the maximum in mobile hydrogen generation to a higher temperature, along with a more mobile fluid phase. This latter effect was thought to be due to better retention of the fluid phase within the structure with increased heating rate (Maroto-Valer, Andresen & Snape, 1997). This was also found in rheological studies on coals and biomass blends (Castro-Diaz et al, 2012). Building on this, *Tahmasebi et al (2012)* found that aliphatic groups were impacted more significantly by heating rate, compared with aromatic groups, suggesting that mobile fluid species were donated by aliphatic functionalities. Although the fluid phase has been found to be mainly comprised of small molecular entities, *Fletcher et al (1990)* suggested that, at high enough heating rates, macromolecules can be cleaved to afford lighter constituents which contribute directly to the fluid phase.

This technique has also been used to confirm observations from rheological studies. In particular, the effect of particle size, where NMR also shown that reduced particle size affords reduced fluidity. *Maroto-Valer, Andresen & Snape (1997)* showed that reducing the particle size to 45 μm significantly reduces the fluidity but increasing to, and above, 200 μm had little impact. *Sakurovs (2000)* also came to a similar conclusion, but interestingly reducing the particle size of charcoal benefitted the fluidity of coal-charcoal blends. Reasons for the correlations between particle size and fluidity have been rationalised as increased surface area of coal particle surface, affording increased rates of oxidation (Liu et al, 2011; Liu et al, 2016). Additionally, it was found that reducing the particle size through crushing and sieving reduced the number of protonated aliphatic groups, where long chain alkyl groups are fractured and afford crosslinks with aromatic groups (replacing C-H with C-C bonds) (Liu et al, 2016).

Along with particle size, the impacts of additives have been studied. Biomass has been intensively studied in a push to reduce the CO_2 emissions from the coke making process. However, all studies have shown that, in agreement with rheological findings, adding even small amounts of biomass significantly reduces the blend fluidity to a point at which poor coke is afforded (Castro-Diaz et al, 2005; Castro-Diaz et al, 2012; Kokonya et al, 2013). This was due to the high surface area of the additive biomass, leading to suppression of the mobile fluid phase of the coking coal. Conversely, adding components such as pitch and tar to coal has been found to benefit the fluidity due to the high molecular weight of these additives (Diez et al, 1999; Miyazawa, Yokono & Sanada, 1979; Xie et al, 2018). Additionally, it was clarified that these additives donate fluid hydrogen entities to the sample, stabilising the thermoplastic phase (Diez et al, 1999).

Despite the wide-ranging research upon single coals and blending with biomass and other additives, there has been very little work on blends of coals using high temperature ^{1}H NMR. Of the studies performed, only a limited number of coals have been used and only blends using high rank – low rank coals have been studied (Sakurovs, 2000; Steel et al, 2004). Therefore, there is need to better understand the interactions between a range of coals and to help develop better models to predict blend fluidity.

6.2. Experimental

The suite of 10 coals tested in chapters 4 and 5 were used here to understand the micro-fluid behaviour of the samples and additive behaviour in blends (Table 3.1 lists the coal properties). 100 mg - 200 mg of coal were packed into boron nitride capsules and capped with a screw lid to contain samples. Capsules were inserted horizontally into the stator within the Doty 200 MHz ^{1}H probe and used with a Bruker MLS 300 MHz instrument. Dry nitrogen was blown through the capsule region at 35 dm^{3}min^{-1} to heat the sample. Air was blown at a heating rate of 60 dm^{3}min^{-1} to ensure that the region below the capsule was maintained below 50 ^{o}C, and 20 dm^{3}min^{-1} of air was used to keep the region below the sample container and probe exterior to maintain the temperature below 110 ^{o}C. The sample region temperature was monitored via an independent thermocouple, and the temperature controlled via an independent temperature controller. A solid echo pulse sequence ($90^o – \tau – 90^o$) was used to determine the difference in peak width with increasing temperature. 100 scans were performed with a cycle delay of 0.3 s. As temperature was controlled independently and acquisitions performed manually, acquisitions were performed every 10 ^{o}C from 360 to 500 ^{o}C. The spectra were deconvoluted into Gaussian and Lorentzian components (the only samples to not exhibit a Lorentzian component for the fluid - less rigid - were coal 4 and 5 between 360 – 390 ^{o}C). The proportions of these components determined the quantities of mobile and rigid phases with their respective mobilities. Figure D1, appendix D, details the deconvolution of the spectra. Samples were tested in duplicate to ensure repeatability due to the low mass used here (100 - 200 mg). A blend of C5-C6(50wt%) has been tested 4 times to obtain a relative standard deviation (RSD) to understand the repeatability of the technique and differences between experimental and predicted values for blends.

The same 18 blends of coals tested in the previous chapter have been analysed using NMR, however some compositions have varied due to lack of bulk fluidity in rheometry. Due to the low sample mass permittable in the boron nitride capsule, each sample was tested in duplicate. All values presented in the text are averages of the duplicate runs. Here, each blend has been tested with compositions of CX-CY(25wt%), CX-CY(50wt%) and CX-CY(75wt%). Blend experimental %fluid H and T_{2L} were measured against the polymer blending rule to assess the accuracy of this model. Absolute values of %fluid H and T_{2L} for the individual coals were used to obtain predicted values using the following relationship.

$$\%Fluid\ H = \varphi_1\%Fluid\ H_1 + \varphi_2\%Fluid\ H_2 \tag{6.1}$$

$$T_{2L} = \varphi_1 T_{2L} + \varphi_2 T_{2L} \tag{6.2}$$

Where:

T_{2L} = *Spin-spin relaxation time of the fluid H.*

φ = *Component fraction in blend by either mass or hydrogen.*

For calculating predicted %fluid H, the fractional mass of hydrogen should be used, however discrepancies will only arise for coals with vastly differing hydrogen contents, with respect to the differences between predicted values calculated from the fractional mass content as opposed to wt% of coal addition. Two examples have been provided here, one with very similar fractional mass of hydrogen between the coals, and one with the greatest difference between fractional mass of hydrogen between the two coals of the blends tested here.

Percentage differences were calculated between experimental and predicted values for both maximum %fluid H and T_{2L} (at maximum %fluid H) and agreement with additive behaviour determined when the values were within the RSD of the experimental values, determined through 95% confidence limits (1.96 times the RSD).

6.3. Results and Discussion

6.3.1. Single Coals

As there has been very little work using high temperature proton NMR to study coking coal blends, a comprehensive study of blends was performed to understand what impacts blending had upon the amount and mobility of molecular mobile entities. However, in order to do this the %fluid H and mobility of such mobile species for single coals had to be measured so that predicted profiles could be obtained. Each single coal was tested to provide %fluid hydrogen and mobility of fluid species as a function of temperature. Spin-spin relaxation times of the rigid phase (T_{2G}) as a function of temperature are provided in Figures D2b – D11b, Appendix D where little change was observed for these profiles (where values ranged between 13.9 and 16.5 μs). %Rigid is not discussed, as this parameter can be directly calculated from %fluid H (i.e., % rigid H = 100 - %fluid H) but has been detailed in plots as a function of temperature in Figures D2b – D11b, Appendix D).

Plots of %Fluid and Rigid H as well as T_{2L} and T_{2G} (as a function of temperature plots) for single coals 1 – 10 can be found in Figures D2 – D11 (Appendix D), respectively (these are presented as averages of the duplicate tests). Table 6.1 details the maximum %fluid H, and mobility (T_{2L}) (note that non – softening and medium fluidity coals exhibit maximum mobility before softening, as opposed to maximum mobility at or near maximum %fluid hydrogen for high fluidity coals). Values have been provided for both duplicate tests to highlight the deviations. T_{2L} has been used to denote mobility of fluid moieties, where only coals 4 and 5 did not show any Lorentzian component between 360 – 390 °C. All other samples tested here exhibited a Lorentzian component.

Table 6.1: Duplicate Tests showing Maximum %fluid H, T_{2L} at maximum %fluid hydrogen, temperature for coals 1 – 10

Coal	Maximum %fluid H (%)		T_{2L} (at maximum %fluid H) (μs)		Temperature of maximum %fluid hydrogen (oC)	
	Run 1	Run 2	Run 1	Run 2	Run 1	Run 2
1	24.0	22.1	37.8	37.5	500	500
2	26.8	28.1	52.3	52.3	490	490
3	44.5	41.1	115	123	430	440
4	31.6	31.0	59.9	56.3	470	490
5	41.8	40.3	54.5	51.1	500	500
6	57.6	53.3	107	105	460	450
7	48.0	49.7	81.6	80.7	460	470
8	68.6	65.9	116	110	460	470
9	62.2	61.0	119	126	460	460
10	47.0	51.3	97.5	97.5	460	460

Deconvoluted spectra, at 360 °C and maximum %fluid H, of a non-softening coal (coal 2, Figure 6.1a & b), medium fluidity coal (coal 5, Figure 6.1c & d) and high fluidity coal (coal 8, Figure 6.e & f) have been provided for examples of the three types of coal tested here. These spectra show the Lorentzian (mobile phase), Gaussian (rigid phase), predicted and experimental profiles. For coal 5 at 360 °C there was no Lorentzian component, hence the experimental and predicted spectra were fit to a Gaussian component (Lorentzian component was exhibited from 400 °C for both medium fluidity coals 4 and 5. These were the only examples where Lorentzian components were not found). The non-softening coal 2 generated less than 5% fluid H at 360 ^{o}C, where the experimental and predicted profiles are very similar to the Gaussian profile. At 490 ^{o}C (maximum %fluid H), the Lorentzian profile is significantly higher compared with 360 ^{o}C due to the increase in mobile hydrogen species, with 27% fluid H generated. However, rigid hydrogen is still dominant, as shown by the Gaussian profile. Coal 5 shows a very similar profile to that of coal 2 at the two temperatures, although the Lorentzian peak is significantly greater for the medium fluidity coal at maximum %fluid H temperature. Coal 8 showed significantly different profiles at the two temperatures, where the Lorentzian peak was significantly greater. Additionally, at 470 ^{o}C the experimental and predicted spectra were very similar to that of the Lorentzian component, with only 33% rigid H.

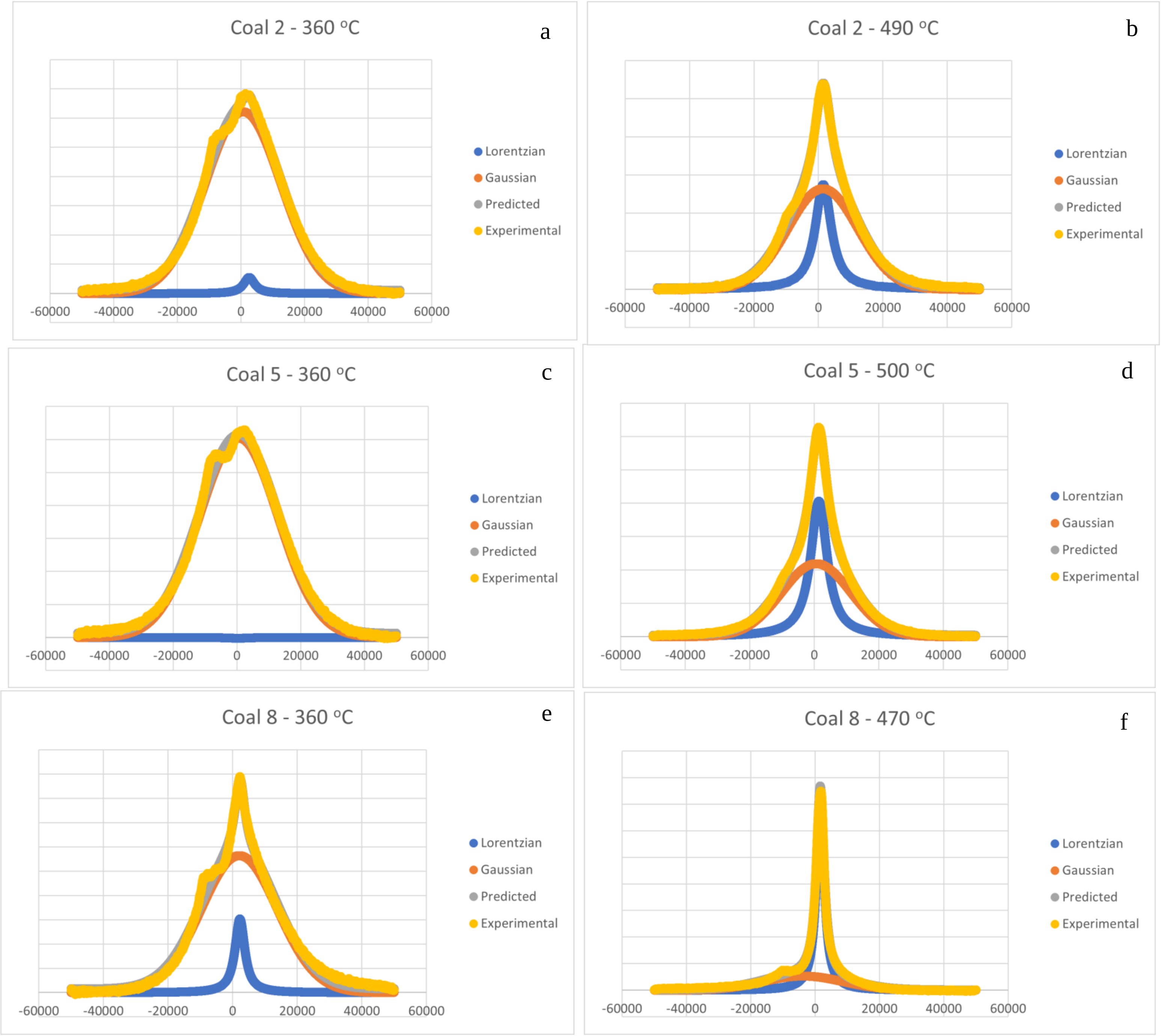

Figure 6.1: Deconvoluted ^{1}H NMR spectra at 360 °C and temperature of measured maximum %fluid H for coal 2 (a & b), coal 5 (c & d) and coal 8 (e & f).

Additionally, to the duplicate tests, to understand the repeatability of the NMR, a blend of C5-C6(50wt%) was tested 4 times. Surprisingly good repeatability was found for duplicate samples despite the low mass, particularly for binary blends. At maximum %fluid H of C5-C6(50wt%), RSD of 4.9% (%difference, rather than absolute difference in %fluid H) was found, and 4.3% for T_{2L}. Lower RSDs of 3.8% (%difference, rather than absolute difference

%rigid H) and 0.7% for %rigid H and T_{2G} at maximum %fluid H were found. The RSDs for maximum %fluid H and T_{2L} have been used to determine agreement between experimental and predicted values for blends. Using 95% confidence limits (1.96 RSDs), agreement could be classified as being within 9.6% for %fluid H (%difference, rather than absolute difference in %fluid H) and 8.4% for T_{2L}.

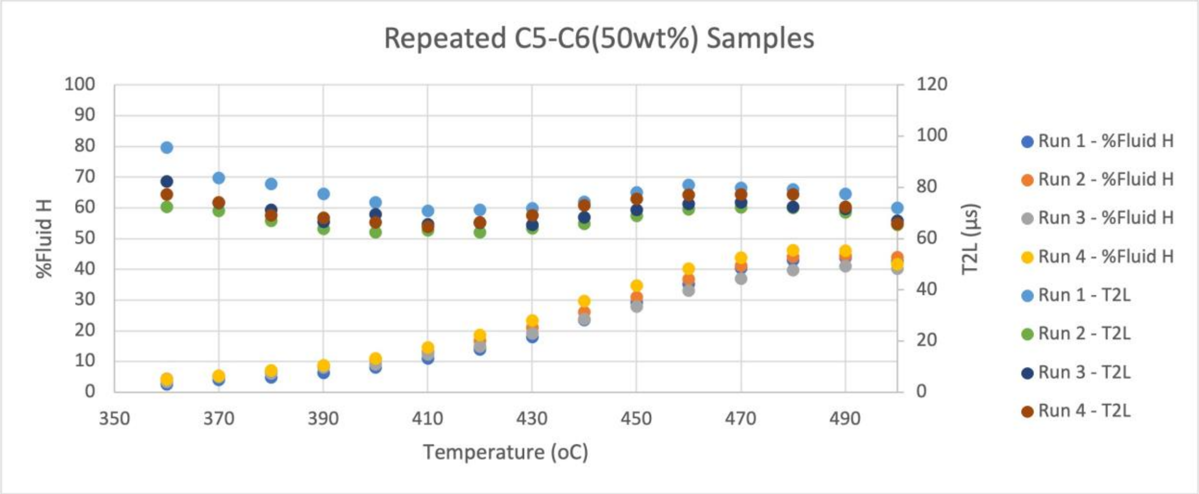

Figure 6.2: Repeat tests of C5-C6(50wt%) showing %fluid H and T_{2L} as a function of temperature

There was a consistent distinction between non-, medium and high fluidity coals with respect to %fluid H (apart from coal 3). Non-fluid coals exhibited maximum %fluid H below 30%, medium fluidity coals exhibited between 30% and 45% maximum %fluid H, and high fluidity coals exhibited greater than 45% maximum fluid H. Additionally, T_{2L} exhibited increasing values with %fluid H due to increased mobility of the fluid phase. Interestingly, coal 3 exhibited surprisingly high micro fluidity, with %fluid H of a medium fluidity coal, along with the second highest value of T_{2L} of the 10 coals tested here but showed low macroscopic fluidity in chapter 4. It should also be noted that the medium fluidity coals 4 and 5 exhibited low T_{2L} at maximum %fluid H, suggesting that the molecular fluid entities were localised and relatively immobile. Maximum T_{2L} for these moieties occurred at 400 ^{o}C and decreased with temperature thereafter. For high fluidity coals, high T_{2L}, along with high maximum %fluid H, gave rise to very mobile molecular fluid entities. This would suggest that such high fluid coals generate fluid material which can link and is not segregated to pockets, which can be found in non-softening and medium fluidity coals.

There was some variation in the duplicate tests for all 10 coals and the three parameters tabulated (maximum %fluid H, T_{2L} at maximum %fluid H and temperature of maximum %fluid H) in Table 6.1. However, all variation between duplicate runs was within the confidence limits of the repeat tests.

Coal 3 was identified as the outlying specimen. It was obvious that this coal showed very high mobility of the fluid phase along with sufficient fluid hydrogen to, theoretically, generate bulk fluidity. As Gieseler fluidity exhibited almost no fluidity (22 ddpm) and dilatation showed almost no swelling (17%), the ^{1}H NMR suggested that this coal generated micro-fluidity segregated into small pockets. Consequently, significant effort has gone towards understanding how this coal interacts with other specimens to understand if this segregation theory is the reason for lack of bulk fluidity.

6.3.1.1. Correlations between NMR Parameters and Coking Properties

Maximum %fluid H and T_{2L} (at maximum %fluid hydrogen) were correlated with coal properties to understand if these parameters could infer any more information about the samples. Due to the anomalous behaviour of coal 3, correlations were made with and without coal 3 to understand the differences between correlations. R^2 values for both sets of correlations are presented in Table 6.2 below.

Removing coal 3 from correlations improved R^2 values of %fluid H for all coking parameters apart from gas pressure. Conversely, T_{2L} showed improved correlations with coal 3 included for ash content, MVR, inertinite content, vitrinite content and gas pressure. Additionally, T_{2L} exhibited good correlations ($R^2 > 0.9$) for volatile matter content and MVR, suggesting that this NMR parameter could be used in blends to understand how volatile matter and lamellar structure could impact the fluidity on the molecular level of these samples. In this instance, as T_{2L} increases, volatile matter content increases and MVR decreases. This was true for correlations both with and without coal 3. For %fluid hydrogen, there were no correlations with $R^2 > 0.9$. However, without coal 3 the %fluid H expressed an R^2 value of 0.89 with volatile matter content, showing the same trend as T_{2L}.

Table 6.2: Correlations R^2 values for T_{2L} and %fluid H (with coal 3 and without coal 3) with coking properties

NMR Parameter	Volatile Matter Content (%)	Gieseler Fluidity (ddpm)	Free Swelling Index	Ash Content (%)	Mean Vitrinite Reflectance	Inertinite Content (%)	Vitrinite Content (%)	Gas Pressure
With Coal 3								
%Fluid H	0.69	0.77	0.58	0.40	0.57	0.73	0.67	0.14
T_{2L}	0.97	0.59	0.37	0.53	0.92	0.88	0.84	0.22
Without Coal 3								
%Fluid H	0.89	0.78	0.58	0.58	0.75	0.86	0.82	0.13
T_{2L}	0.98	0.81	0.49	0.37	0.91	0.85	0.80	0.10

6.3.2. Coal Blends

Plots of maximum %fluid H and T_{2L} at maximum %fluid H have been provided as a function of composition to highlight agreements and deviations from additive behaviour (these are provided as averages of duplicate runs). Plots of %fluid H and T_{2L} as a function of temperature (provided as averages of duplicate runs) are shown in Figures D12 – D29, Appendix D.

6.3.2.1. Blends with Similar Coals

Blending similar coals with respect to softening profile and η^*_{min} was tested to understand if any deviations occurred, where it has been assumed hitherto that such blends would afford additive behaviour. C4-C5 and C6-C10 were tested, where plots of maximum %fluid H and T_{2L} as a function of composition are displayed below in Figure 6.3 for the two blends. Plots of %fluid H and T_{2L} as a function of temperature (provided as averages of duplicate runs) are shown in Figures D12 and D13 (Appendix D).

Interestingly, different conclusions were drawn for the two blends. C4-C5 exhibited agreement with additive behaviour at all compositions for both %fluid H and T_{2L}, showing that there were no interactions between the fluid phases of coals 4 and 5. From plots of

%fluid H as a function of temperature, there was good overlap between coal 4 and coal 5, with good progression of change in profile from coal 4 to coal 5 (Figure D12a, Appendix D). In order to understand any difference between predicted values when using wt% addition of coals, or when using fractional mass of hydrogen, the two were compared. For this blend of two medium fluidity coals the predicted values were almost identical due to the similarities in fractional mass of hydrogen in the two coals (Figure D30a). Fractional masses of coals 1 – 10 of hydrogen are presented in Table D1, Appendix D.

C6-C10 also exhibited additive behaviour for %fluid H and T_{2L} at all compositions, apart from a significant reduction in T_{2L} at C6-C10(50wt%) of 9.4 µs (see Table 6.4). This suggested that there was a reduction in the mobility of the fluid phase due to interactions between the two high fluidity coals at this composition. For %fluid hydrogen profiles as a function of temperature, there was good overlap between the coals, giving rise to agreement between the experimental and predicted values (see Figure D13a in Appendix D).

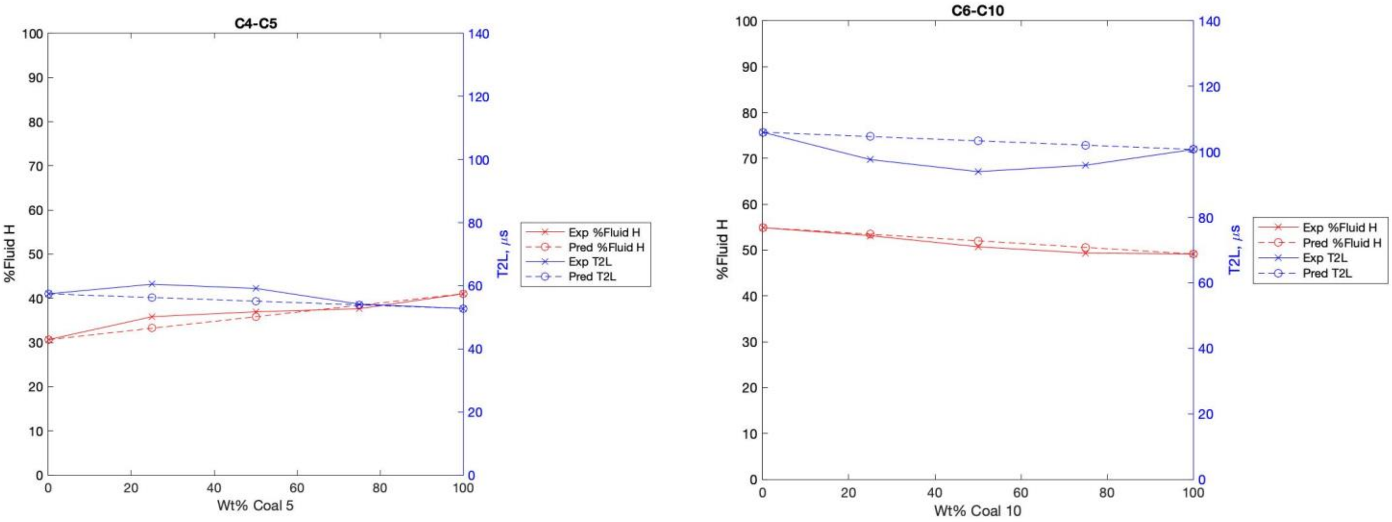

Figure 6.3: Maximum %fluid H and T_{2L} (at maximum %fluid hydrogen) for blend compositions of a (left)) C4-C5 and b (right)) C6-C10.

6.3.2.1.1. Differences to Predicted Behaviour

Table 6.3 and 6.4 detail the absolute error (determined from RSDs from repeated C5-C6(50wt%), where 95% confidence limits provided a percentage error in measured values of 9.6% for maximum %fluid H and 8.37% for maximum T_{2L}), absolute difference between experimental and predicted values for all blends for maximum %fluid H (Table 6.3) and T_{2L} (Table 6.4) value, along with confirmation of agreement with additive behaviour.

Table 6.3: Differences in %fluid H for the coal blends

Blend	75:25wt%			50:50wt%			25:75wt%		
	Error (%Fluid H)	Diff (%Fluid H)	Agree? (Y/N)	Error (% Fluid H)	Diff (%Fluid H)	Agree? (Y/N)	Error (%Fluid H)	Diff (%Fluid H)	Agree? (Y/N)
C4-C5	3.4	2.6	Y	3.53	1.12	Y	3.6	0.8	Y
C6-C10	5.2	0.3	Y	5.1	1.3	Y	4.8	1.3	Y
C1-C4	2.9	5.0	N	2.9	3.4	N	3.1	4.1	N
C1-C10	2.3	5.4	N	3.1	3.4	N	3.8	2.8	Y
C2-C6	4.0	7.9	N	3.9	0.3	Y	4.8	2.6	Y
C2-C8	3.6	0.2	Y	4.7	2.2	Y	5.7	3.1	Y
C4-C6	3.8	3.3	Y	4.5	4.3	Y	4.7	0.7	Y
C4-C10	3.9	5.2	N	4.1	2.6	Y	4.4	1.3	Y
C5-C6	4.0	2.3	Y	4.2	4.1	Y	4.8	0.8	Y
C5-C8	4.1	4.1	Y	4.6	5.6	N	5.5	2.4	Y
C5-C10	3.5	6.1	N	3.5	8.0	N	4.1	4.2	N
C3-C4	3.8	0.4	Y	3.8	3.0	Y	3.8	5.6	N
C3-C5	3.9	1.2	Y	3.3	7.0	N	3.3	6.7	N
C3-C6	4.8	4.6	Y	5.1	4.0	Y	5.2	2.3	Y
C3-C7	4.4	1.5	Y	3.9	4.8	N	3.9	6.2	N
C3-C8	5.3	7.0	N	5.6	3.4	Y	6.1	3.6	Y
C3-C9	5.1	5.8	N	5.1	1.4	Y	5.6	1.4	Y
C3-C10	4.8	6.1	N	5.0	6.2	N	4.9	4.2	Y

N.B. Error determined through RSD of repeated C5-C6(50wt%), determined to be 9.6%

Table 6.4: Percentage differences in T_{2L} for the coal blends

Blend	75:25wt%			50:50wt%			25:75wt%		
	Error (μs)	Diff (μs)	Agree? (Y/N)	Error (μs)	Diff (μs)	Agree? (Y/N)	Error (μs)	Diff (μs)	Agree? (Y/N)
C4-C5	5.06	4.20	Y	5.0	4.1	Y	4.5	0.2	Y
C6-C10	7.0	7.0	Y	7.9	9.4	N	8.0	6.2	Y
C1-C4	4.0	5.1	N	4.3	4.4	N	4.8	6.1	N
C1-C10	4.3	8.5	N	5.7	5.8	N	7.0	4.0	Y
C2-C6	5.0	6.2	N	6.5	2.1	Y	7.5	3.3	Y
C2-C8	5.1	6.9	N	7.0	1.0	Y	8.7	5.4	Y
C4-C6	5.5	3.4	Y	7.0	2.3	Y	7.7	2.3	Y
C4-C10	6.2	6.3	N	6.5	0.2	Y	7.1	3.2	Y
C5-C6	5.0	6.6	N	6.1	6.4	N	7.5	3.4	Y
C5-C8	5.0	8.8	N	6.9	0.6	Y	8.6	4.8	Y
C5-C10	4.6	8.9	N	5.7	7.0	N	6.9	4.5	Y
C3-C4	7.6	12.6	N	6.7	8.4	N	6.2	1.3	Y
C3-C5	9.1	5.8	Y	7.4	2.8	Y	4.7	13.3	N
C3-C6	9.2	5.8	Y	8.8	7.5	Y	8.2	11.1	N
C3-C7	9.2	0.3	Y	7.8	8.5	N	7.4	4.3	Y
C3-C8	10.2	4.0	Y	9.9	1.9	Y	9.6	0.5	Y
C3-C9	11.2	13.4	N	10.6	4.7	Y	10.7	4.4	Y
C3-C10	8.6	10.6	N	9.5	4.9	Y	10.8	26.6	N

N.B. Error determined through RSD of repeated C5-C6(50wt%), determined to be 8.4%

6.3.2.2. Individual Blend Compositions

Of the 18 blends tested, there were only two blends that exhibited agreement with additive behaviour for both %fluid hydrogen and T_{2L} at all compositions, which were C4-C5 and C4-C6. All other blends exhibited variations for at least one blend composition which are now discussed. However, of the 54 compositions tested, 34 exhibited predictive behaviour with respect to %fluid H, and 32 with respect to T_{2L}. Where significant differences have been found, the absolute difference (% for %fluid H and μs for T_{2L}) between experimental and predicted values have been provided (as shown in Tables 6.3 and 6.4 above).

6.3.2.3. Blends Containing Non – Softening Coals 1 & 2

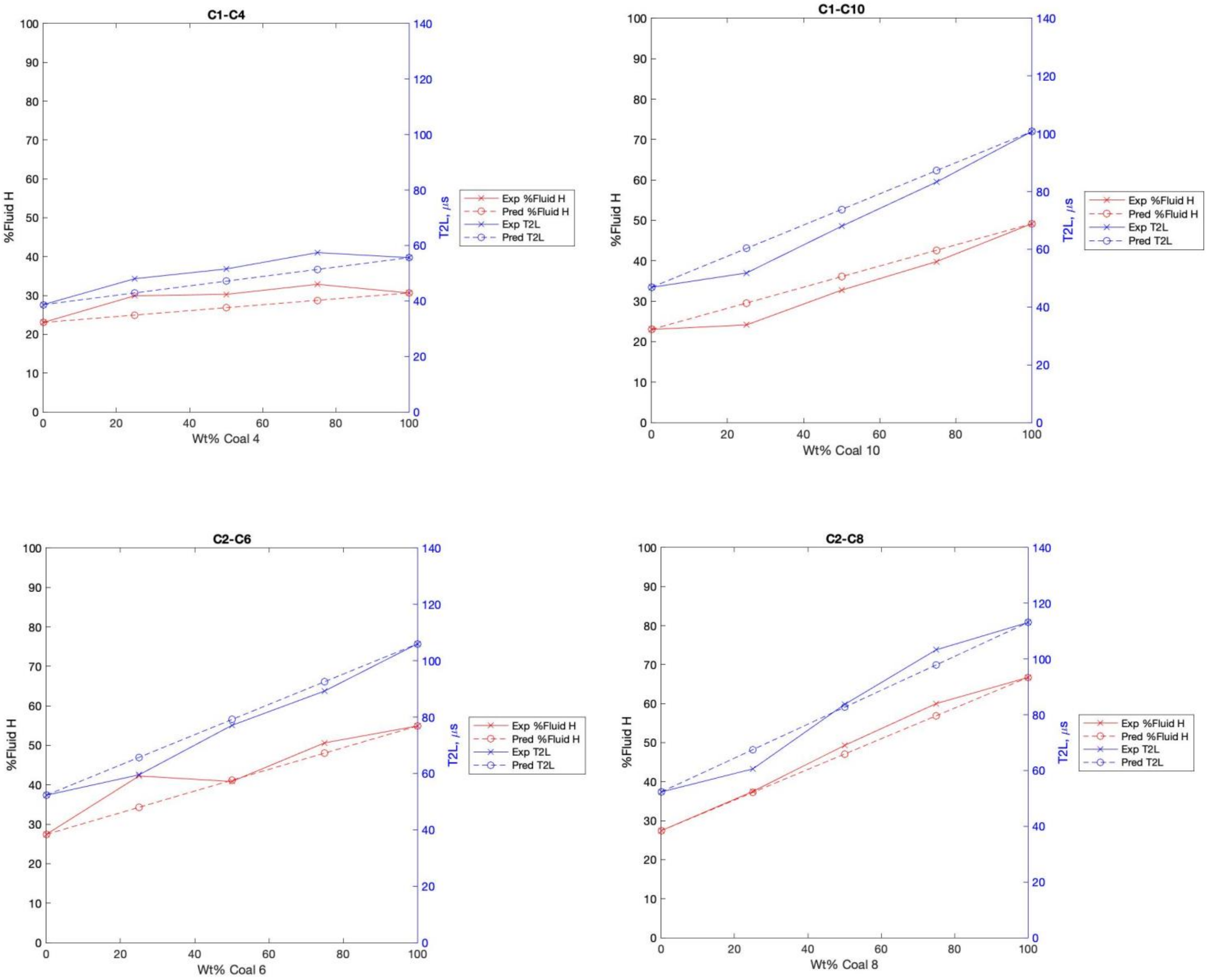

Figure 6.4: Maximum %fluid H and T_{2L} (at maximum %fluid hydrogen) for blend compositions of a (top left)) C1-C4, b (top right)) C1-C10, c (bottom left)) C2-C6 and d (bottom right)) C2-C8

Plots of %fluid H as a function of temperature are presented in Figures D14a – 17a (Appendix D) for C1-C4, C1-C10, C2-C6 and C2-C8. Plots of T_{2L} as a function of temperature are presented in Figures D14b – 17b (Appendix D) for C1-C4, C1-C10, C2-C6 and C2-C8.

Comparing C1-C4 with C1-C10, the following was found. *%Fluid H:* Coal 1 blends showed significant deviations at all compositions apart from C1-C10(75wt%) (see Figure 6.4b). Such deviations were found to be 5.0%, 3.4% and 4.1% for C1-C4(25-75wt%), and 5.4% and 3.4% for C1-C10(25-50wt%) (see Table 6.3). Enhanced %fluid H was found for C1-C4 (see Figure 6.4a) but reduced %fluid H for C1-C10 (see Figure 6.4b). This was likely a function of differences in temperature of maximum %fluid H; 20 °C between coals 1 and 4, compared with 40 °C between coals 1 and 10. *T_{2L}:* The same overall differences were found for mobility, which was likely due to differences in T_{2L} profiles; decreasing T_{2L} as a function of temperature for coals 1 and 4 (see Figures D2a and D5a, Appendix D), compared with maximum mobility near the temperature of maximum %fluid H for coal 10 (see Figure D11a, Appendix D). Deviations were found to be 5.1, 4.4 and 6.1 μs for C1-C4(25-75wt%), and 8.5 and 5.8 μs for C1-C10(25-50wt%) (see Table 6.4).

As C1-C10 exhibited the greatest difference in fractional mass of hydrogen between the coals, predicted values were calculated using the fractional mass of hydrogen, as well as that from wt% addition of the coals. As can be seen from Figure D30b (Appendix D), there was no significant difference between the predicted values of the two methodologies. Wt% addition of coal 10 is shifted higher along the x-axis for predicted values using fractional mass of hydrogen due to greater overall hydrogen content donated from coal 10 to the blend.

For coal 2 blends, agreement was found for all compositions apart from C2-C6(25wt%) for %fluid H (see Figure 6.4c), and C2-C6(25wt%) (see Figure 6.4c) and C2-C8(25wt%) (see Figure 6.4d) for T_{2L} (see Table 6.3 and 6.4). Increased %fluid H at C2-C6(25wt%), of 7.9% (see Table 6.3), could possibly have been due to increased inertinite content, where it has been found that inertinite can enhance volatile evolution (Xie et al, 2019). Reduction in T_{2L}, of 6.2 and 6.9 μs for C2-C6(25wt%) and C2-C8(25wt%) (see Table 6.4), was possibly due to fluid material adsorption.

6.3.2.4. Blends with Medium Fluidity Coal 4

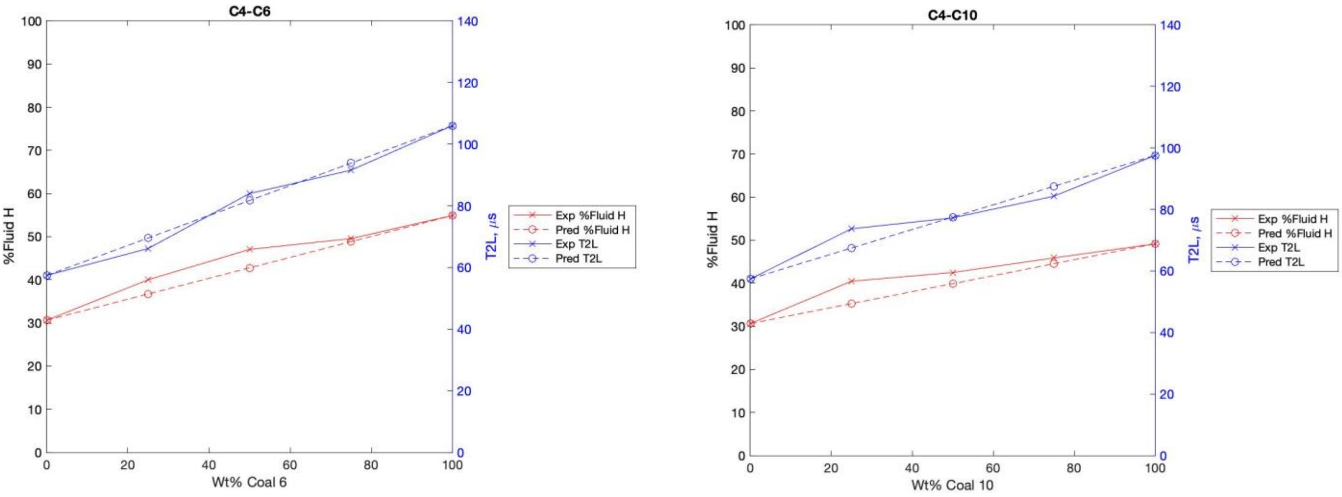

Figure 6.5: Maximum %fluid Hand T_{2L} (at maximum %fluid hydrogen) for blend compositions of a (left)) C4-C6 and b (right)) C4-C10

Plots of %fluid H as a function of temperature are presented in Figures D18a & 19a (Appendix D) for C4-C6 & C4-C10. Plots of T_{2L} as a function of temperature are presented in Figures D18b & D19b (Appendix D) for C4-C6 & C4-C10.

Good agreement was found with additive behaviour for C4-C6 and C4-C10 (see Figures 6.5a and 6.4b), apart from C4-C10(25wt%) for both %fluid H and T_{2L}. Increases in both %fluid H (of 5.2%) (Table 6.3) and T_{2L} (of 6.3 μs) (Table 6.4) were found at these compositions, suggesting an early mobilisation of some of the organic matter.

6.3.2.5. Blends with Prime Coking Coal 5

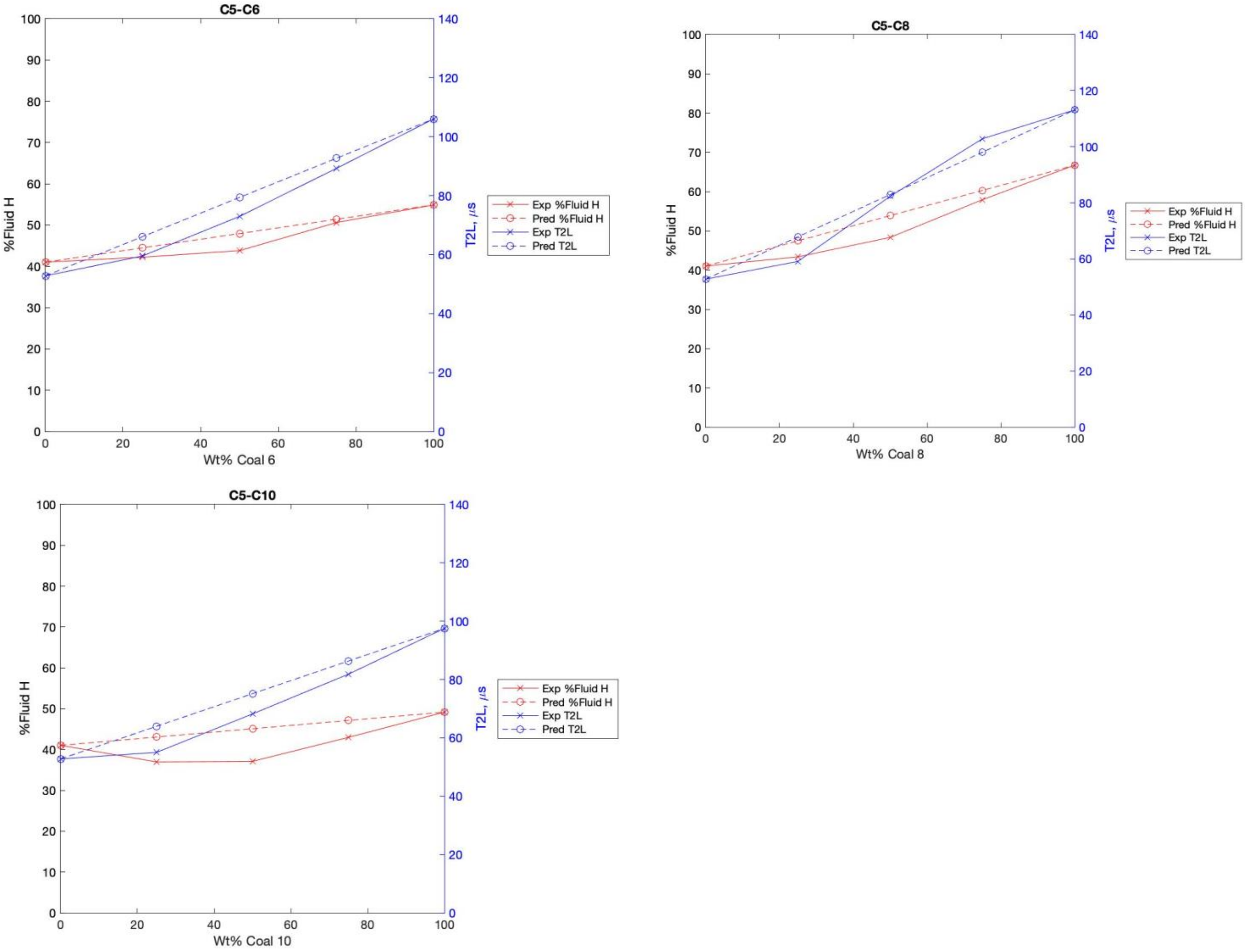

Figure 6.6: Maximum %fluid Hand T_{2L} (at maximum %fluid H) for blend compositions of a (top left)) C5-C6, b (top right)) C5-C8 and c (bottom left)) C5-C10

Plots of %fluid H as a function of temperature are presented in Figures D20a – D22a (Appendix D) for C5-C6, C5-C8 & C5-C10. Plots of T_{2L} as a function of temperature are presented in Figures D20b – D22b (Appendix D) for C5-C6, C5-C8 & C5-C10.

Significant differences were found between experimental and predicted values for coal 5 blended with high fluidity coals (see Figures 6.6a, 6.6b and 6.6c). *%Fluid H:* Deviations were found at C5-C8(50wt%) (see Figure 6.6b), and all C5-C10 blends (see Figure 6.6c) of 5.6%, 6.1%, 8.0% and 4.2% for the four aforementioned compositions (see Table 6.3). In all cases, reduced %fluid H was found, likely due to adsorption of fluid material. *T_{2L}:* Deviations were found at C5-C6(25wt%), C5-C6(50wt%), C5-C8(25wt%), C5-C10(25wt%) and C5-

C10(50wt%) (Figures 6.6a, 6.6b and 6.6c) of 6.6 µs, 6.4 µs, 8.8 µs, 8.9 µs and 7.0 µs (see Table 6.4). Reductions in T_{2L} were found in all cases, again likely due to adsorption of fluid material. The adsorption mechanisms likely had a pronounced effect due to the difference of 30 ^{o}C or more in maximum %fluid H between coal 5 and the high fluidity coals 6, 8 and 10, along with the differences in T_{2L} profiles between coal 5 and the high fluidity coals.

6.3.2.6. Blends with Non – Softening Coal 3

Coal 3 has been blended here with all of the softening coals as this sample exhibited very different behaviour in NMR when compared with rheometry. There was no apparent bulk fluidity measured by the sample in both rheometry and Gieseler plastometry, however this coal possessed the highest volatile matter content and vitrinite content of the suite of coals. Testing with NMR showed that there was a relatively high %fluid H throughout the heating regime and exhibited the highest mobility of the 10 samples at maximum %fluid H. Therefore, NMR has been used to understand if any explanatory behaviour was elucidated through blending and subsequent interactions.

6.3.2.6.1. Blends of Non – Softening Coal 3 with Medium Fluidity Coals 4 and 5

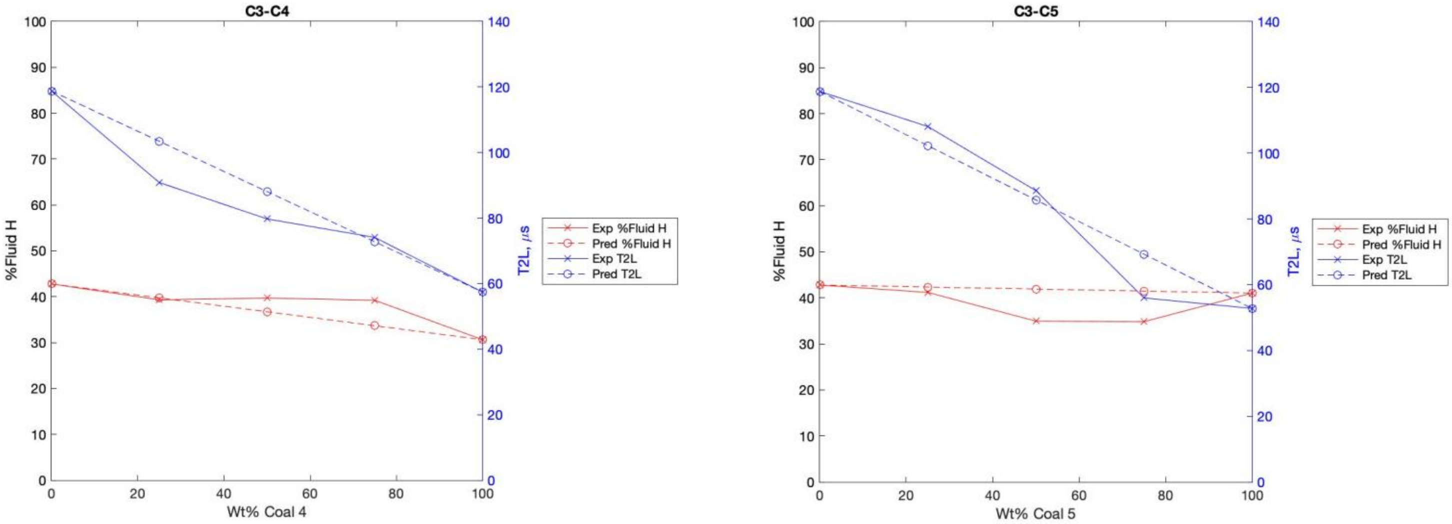

Figure 6.7: Maximum %fluid H and T_{2L} (at maximum %fluid hydrogen) for blend compositions of a (left)) C3-C4 and b (right)) C3-C5

Plots of %fluid H as a function of temperature are presented in Figures D23a & D24a (Appendix D) for C3-C4 & C3-C5. Plots of T_{2L} as a function of temperature are presented in Figures D23b & D24b (Appendix D) for C3-C4 & C3-C5.

%Fluid H: Deviations were found at C3-C4(75wt%)), C3-C5(50wt%) and C3-C5(75wt%) (see Figure 6.7a and 6.7b) of 5.6%, 7.0% and 6.7% respectively (see Table 6.3). C3-C4 exhibited increased %fluid H, possibly due to coal 4 maceral mobilisation. C3-C5 exhibited reduced %fluid H, likely due to fluid material adsorption. Additionally, coal 3 could have developed segregated micro-fluidity, with high surface area, and hence a high adsorption efficiency (Sakurovs, 2000). Enhanced %fluid H generation for C3-C4 was possibly due to reduced difference in temperature of maximum %fluid H, and subsequent hydrogen donation (Sakurovs, 2003).

T_{2L}: Significant deviations were found at C3-C4(25wt%), C3-C4(50wt%) and C3-C5(75wt%) of 12.6 μs, 8.4 μs and 13.3 μs, respectively, where reduced mobility was found in all cases (see Table 6.4). This was possibly due to the significant differences in T_{2L} profiles as a function of temperature (see Figures D23b and D24b, Appendix D) between coal 3 and the medium fluidity coals 4 and 5. At maximum T_{2L} for coal 3 (440 ^{o}C), mobility in coals 4 and 5 were decreasing and below 80 μs.

6.3.2.6.2. Blends of Non – Softening Coal 3 with High Fluidity Coals

Non – softening coal 3 exhibited a T_{2L} profile of a high fluidity coal, along with a relatively high maximum %fluid hydrogen. Therefore, there was interest to find out how the non – softening coal interacted with high fluidity coals. Blends of C3-C6, C3-C7, C3-C8, C3-C9 and C3-C10 were analysed to understand such interactions.

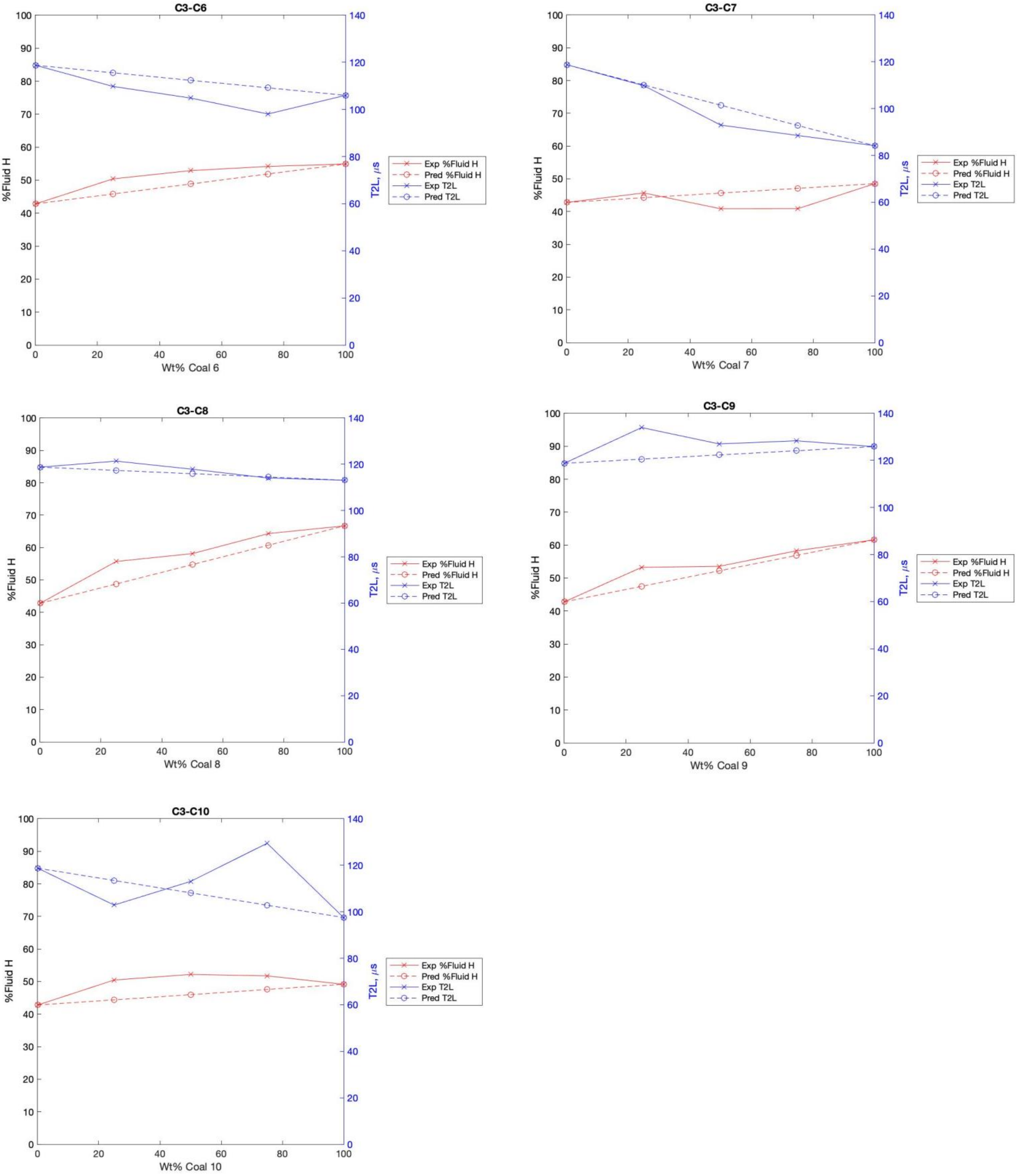

Figure 6.8: Maximum %fluid Hand T_{2L} *(at maximum %fluid H) for blend compositions of a) C3-C6, b) C3-C7, c) C3-C8, d) C3-C9 and e) C3-C10*

Plots of %fluid H as a function of temperature are presented in Figures D25a - D29a (Appendix D) for C3-C6, C3-C7, C3-C8, C3-C9 & C3-C10. Plots of T_{2L} as a function of temperature are presented in Figures D25a - D29a (Appendix D) for C3-C6, C3-C7, C3-C8, C3-C9 & C3-C10.

C3-C6 (Figure 6.8a): The only deviation found here was for C3-C6(75wt%) with respect to T_{2L}, where reduced mobility was found of 11.1 μs (see Table 6.3). Coal 6 exhibited a significantly lower maximum T_{2L} compared with coal 3 of 106 μs, compared with 119 μs. Additionally, adsorption of fluid material could have occurred.

C3-C7 (Figure 6.8b): Deviations were found at C3-C7(50wt%) and C3-C7(75wt%) for %fluid H of 4.8% and 6.2% (see Table 6.3), and at C3-C7(50wt%) for T_{2L} of 8.5 μs (Table 6.4). In all cases, reduced values were found, likely due to adsorption of fluid material, where coal 3 could have had enhanced adsorption efficiency due to micro-porosity generated by microfluidity.

C3-C8 (see Figure 6.8c): The only deviation found here was C3-C8(25wt%) with respect to %fluid H, where an increased value was found, 7.0% greater than predicted (see Table 6.3). This could have been due to hydrogen donation from coal 3 to coal 8, where the mobile fluid entities were retained within the metaplast of coal 8.

C3-C9 (Figure 6.8d): For both %fluid H and T_{2L}, deviations were found at C3-C9(25wt%), where increased values were found in both cases of 5.8% (Table 6.3) and 13.4 μs (Table 6.4) greater than predicted, respectively. Again, this was likely due to hydrogen donation from coal 3 to coal 9.

C3-C10 (Figure 6.8e): Deviations were found at C3-C10(25wt%) and C3-C10(50wt%) for %fluid H of 6.1% and 6.2% (see Table 6.3), respectively, and C3-C10(25wt%) and C3-C10(75wt%) for T_{2L} of 10.6 μs and 26.6 μs (see Table 6.4), respectively. Increased values were found for %fluid H, likely due to hydrogen donation. The same mechanism was likely for increased mobility at C3-10(75wt%), however reduced mobility at C3-C10(25wt%) was likely due to fluid material adsorption.

6.4. Conclusions

For the individual coals, it was found here that %fluid H afforded some correlation with volatile matter content, vitrinite content and inertinite content ($R^2 = 0.8 – 0.9$). Conversely, T_{2L} exhibited good correlation with volatile matter content and MVR ($R^2 > 0.9$), along with some correlation with Gieseler fluidity, inertinite and vitrinite content ($R^2 = 0.8 – 0.9$). High fluidity coals exhibited maximum T_{2L} close in temperature to maximum %fluid H, whereas non- and medium fluidity coals exhibited maxima at low temperature (360 – 400 ^{o}C), with decay as a function of temperature, affording very low mobility at maximum %fluid H. The only exception to this was coal 3, which afforded %fluid H and T_{2L} profiles of high fluidity coals, despite a Gieseler fluidity of only 22 ddpm.

For blends of similar coals, %fluid H and T_{2L} experimental and predicted values were close, with only one deviation, at C6-C10(50wt%) for T_{2L}. Reviewing the accuracy of the polymer blending rule when compared with experimental maximum %fluid H, 34 of the 54 compositions tested exhibited agreement with additive behaviour. 32 compositions exhibited agreement with additive behaviour when concerning T_{2L} at maximum %fluid hydrogen. Overall, for %fluid H, the blends to show deviations were C5-C10 and the majority of blends with C3 (excluding C3-C6 and C3-C7). Of these blends, C5-C10, C3-C5 and C3-C7 exhibited decreases in %fluid hydrogen at deviations from additive behaviour, where other blends exhibited increased %fluid hydrogen. This would suggest that coal 5 (highest rank coal of the suite) was very susceptible to fluid absorption mechanisms as a function of its high softening temperature (comparative to other coals tested here). For T_{2L}, most deviations afforded reduced mobility, which was thought to be due to fluid matter adsorption. The only blend to show no additive behaviour at all compositions with respect to T_{2L} was C1-C4, where increased mobility was likely due to maceral mobilisation in coal 4. However, there was overall good agreement between experimental and additive behaviour.

6.5. References

Castro Díaz, M., Zhao, H., Kokonya, S., Dufour, A. and Snape, C.E. 2012. The Effect of Biomass on Fluidity Development in Coking Blends Using High-Temperature SAOS Rheometry. *Energy & Fuels*. ***26***(3), pp.1767-1775.

Castro-Díaz, M., Edecki, L., Steel, K.M., Patrick, J.W. and Snape, C.E. 2008. Determination of the effects caused by different polymers on coal fluidity during carbonization using high-temperature ^{1}H NMR and rheometry. *Energy & fuels*. ***22***(1), pp.471-479.

Castro-Díaz, M., Steel, K.M., Drage, T.C., Patrick, J.W. and Snape, C.E. 2005. Determination of the Effect of Different Additives in Coking Blends using a Combination of In Situ High-Temperature ^{1}H NMR and Rheometry. *Energy & fuels*. ***19***(6), pp.2423-2431.

Dıez, M.A., Domınguez, A., Barriocanal, C., Alvarez, R., Blanco, C.G. and Canga, C.S. 1999. Hydrogen Donor and Acceptor Abilities of Pitches from Coal and Petroleum Evaluated by Gas Chromatography. *Journal of Chromatography A*. ***830***(1), pp.155-164.

Duffy, J.J., Mahoney, M.R. and Steel, K.M. 2010. Influence of Coal Thermoplastic Properties on Coking Pressure Generation: Part 2–A Study of Binary Coal Blends and Specific Additives. *Fuel*. ***89***(7), pp.1600-1615.

Dufour, A., Castro-Díaz, M., Marchal, P., Brosse, N., Olcese, R., Bouroukba, M. and Snape, C. 2012. In Situ Analysis of Biomass Pyrolysis by High Temperature Rheology in Relations with ^{1}H NMR. *Energy & Fuels*. ***26***(10), pp.6432-6441.

Fletcher, T.H., Kerstein, A.R., Pugmire, R.J. and Grant, D.M. 1990. Chemical Percolation Model for Devolatilization 2: Temperature and Heating Rate Effects on Product Yields. *Energy & Fuels*. ***4***(1), pp.54-60.

Kokonya, S., Castro-Díaz, M., Barriocanal, C. and Snape, C.E. 2013. An Investigation into the Effect of Fast Heating on Fluidity Development and Coke Quality for Blends of Coal and Biomass. *Biomass and bioenergy*. ***56***, pp.295-306.

Lewitt, M.W. and Lowe, A.J. 1997. Proton Magnetic Resonance Thermal Analysis in Coal Research: A Users Overview. *Thermochimica acta*. ***294***(1), pp.13-21.

Liu, J., Jiang, X., Huang, X., Shen, J. and Wu, S. 2011. Investigation of the Diffuse Interfacial Layer of Superfine Pulverized Coal and Char Particles. *Energy & Fuels*. ***25***(2), pp.684-693.

Liu, J., Luo, L., Ma, J., Zhang, H. and Jiang, X. 2016. Chemical Properties of Superfine Pulverized Coal Particles 3: Nuclear Magnetic Resonance Analysis of Carbon Structural Features. *Energy & Fuels*. ***30***(8), pp.6321-6329.

Maroto-Valer, M.M., Andrésen, J.M. and Snape, C.E. 1997. In-Situ ^{1}H NMR Investigation of Particle Size, Mild Oxidation, and Heating Regime Effects on Plasticity Development during Coal Carbonization. *Energy & fuels*. ***11***(1), pp.236-244.

Maroto-Valer, M.M., Andrésen, J.M. and Snape, C.E. 1997. Quantification by In Situ ^{1}H NMR of the Contributions from Pyridine-Extractables and Metaplast to the Generation of Coal Plasticity. *Fuel*. ***76***(13), pp.1301-1308.

Maroto-Valer, M.M., Atkinson, C.J., Willmers, R.R. and Snape, C.E. 1998. Characterization of partially carbonized coals by solid-state ^{13}C NMR and optical microscopy. *Energy & fuels*, ***12***(5), pp.833-842.

Maroto-Valer, M.M., Taulbee, D. N., Andresen, J. M., Hower, J. C. and Snape, C. E. 1998. The Role of Semifusinite in Plasticity Development for a Coking Coal. *Energy and Fuels.* ***12 (****1)*, pp.1040 – 1046.

Miyazawa, K., Yokono, T. and Sanada, Y. 1979. High Temperature ^{1}H-NMR Study of Coal and Pitch at the Early Stages of Carbonization. *Carbon*. ***17***(3), pp.223-225.

Neavel, R. C 1982. Coal Plasticity Mechanism: Inferences from Liquefaction Studies. In: Gorbaty, M.L., Larsen, J.W. and Wender, I. ed(s). *Coal Science Volume 1.* 1st Edition. Cambridge, MA: Academic Press.

Sakurovs, R. 2000. Some Factors Controlling the Thermoplastic Behaviour of Coals. *Fuel*. ***79***(3-4), pp.379-389.

Sakurovs, R. 2003. Interactions between coking coals in blends. *Fuel*. ***82***(4), pp.439-450.

Steel, K.M., Diaz, M.C., Patrick, J.W. and Snape, C.E. 2004. Use of Rheometry and ^{1}H NMR Spectroscopy for Understanding the Mechanisms behind the Generation of Coking Pressure. *Energy & fuels*. ***18***(5), pp.1250-1256.

Steel, K.M., Diaz, M.C., Patrick, J.W. and Snape, C.E. 2006. Evidence for Network Formation during the Carbonization of Coal from the Combination of Rheometry and ^{1}H NMR Techniques. *Fuel*. ***85***(12-13), pp.1821-1830.

Tahmasebi, A., Yu, J., Han, Y. and Li, X. 2012. A Study of Chemical Structure Changes of Chinese Lignite during Fluidized-Bed Drying in Nitrogen and Air. *Fuel Processing Technology*. ***101***, pp.85-93.

Xie, W., Stanger, R., Tran, Q.A., Mahoney, M., Lucas, J., Yu, J. and Wall, T. 2019. Impact of large sized inertinite particles on thermo-swelling and volatile release of coking coals. *Fuel Processing Technology*. ***193***, pp.63-72.

Xie, W., Stanger, R., Tran, Q.A., Smith, N., Wall, T. and Lucas, J. 2018. Impact of Coal Pyrolysis Products as a Rheological Additive on Thermoplasticity of a Coking Coal. *Energy & Fuels*. ***32***(4), pp.4382-4390.

Chapter 7

Discussion

Summary

As the novel cup geometry at 3 g was used to test blends for bulk fluidity, correlations have been made for both single coals and blends between NMR and the cup geometry, which has also shown to be beneficial as a possible proxy for gas pressure (compared with lower mass and sample displacement from the PP). With limited studies using high temperature rheometry and ^{1}H NMR for the analysis of coking coal blends, there have been no comprehensive comparisons of the two techniques to understand if there is any link between micro-fluidity upon phenomena on the bulk scale. Correlations were made between the parameters of the two techniques to confirm if changes in fluid hydrogen causes anomalous behaviour in rheological measurements. Correlations were found for medium fluidity coal blends between high temperature rheometry and ^{1}H NMR, but only with respect to G" and η* with %fluid H. Hence, viscous behaviour was predominantly dictated by mobile molecular entities, whereas elastic behaviour was dictated by bulk phenomena. From chapters 5 and 6, where better agreement was found between high temperature ^{1}H NMR and predicted values, compared with rheological measurements, suggested that non-additive behaviour was determined by a multitude of factors, including mechanisms such as volatile absorption, hydrogen donation, maceral crosslinking and suspension formation. Macroporosity and total porosity exhibited good correlations with maximum plate gap, where the cup geometry could be used in future studies to predict porosity. This was due to good sample retention from the novel cup geometry, not possible for the PP geometry due to sample displacement. Microporosity confirmed that coal 3 generated significant micro-fluidity, which could not propagate through the sample, with high microporosity, but low meso- and macroporosity.

7.1. NMR Correlations with Rheometry

7.1.1. Single Coals

Although results from ^{1}H NMR would not intrinsically correlate with rheological parameters due to the differences of the fluid phases (macro- vs micro-fluidity), correlations were performed to compare the two techniques. As η*, G' and G" were plotted on log axes, %fluid H and T_{2L} were correlated against log(η*), log(G') and log(G"). Linear viscoelastic correlations have been provided with log(viscoelastic parameters) in Appendix E in Figures E1 – E6, and Tables E1 – E3 in Appendix E. Due to lack of bulk fluidity for coals 1 – 3 for rheological measurements, correlations were made with and without these coals to understand if R^2 values were impacted, and an additional set of correlations were plotted excluding coal 3 as this specimen afforded anomalous bulk fluidity. Correlations were made between η*, G' and G" with %fluid hydrogen and T_{2L} to understand if there were deviations between the viscoelastic parameter correlations with the two NMR parameters, and hence if micro-fluidity directly impacted complex viscosity, elastic behaviour or viscous behaviour.

Tables 7.1 – 7.3 and Figures E1 – E6 (Appendix E) detail the correlations between rheological parameters (η*, G' and G") and NMR parameters (%fluid hydrogen and T_{2L}) for all coals 1-10 (Figures E1 & E2, Appendix E), softening coals only (4 – 10) (Figure E3 & E4, Appendix E) and all coals without coal 3 (Figures E5 & E6, Appendix E). From the correlations between rheometry and NMR for single coals, the following was found. Including all coals in the correlation (1 – 10) afforded better R^2 values compared with only softening coals (4 - 10), suggesting that there could have been some link between the fluid hydrogen and lack of bulk fluidity. However, the best correlations were found when only excluding coal 3 from correlations, confirming that this coal did exhibit anomalous rheological behaviour.

The following R^2 values were found between rheological and NMR parameters for the 3 sets aforementioned.

All coals: R^2 values of between 0.72 and 0.87 were found with %fluid hydrogen and the viscoelastic parameters, with the best correlation with G". This was also found for T_{2L}, but with much reduced R^2 values of 0.35 – 0.54. *Coals 4 – 10:* Correlations were poorer compared with the complete set of coals (1 – 10) with respect to both %fluid H and T_{2L}. *Without Coal 3:* removing coal 3 afforded the best correlations of the three sets (R^2 values of 0.88 and 0.87 for G" and η*), confirming the anomalous behaviour of coal 3 with respect to rheological measurements. G' consistently exhibited the lowest R^2 value for all correlations. This is in line with the proposition in chapter 5 that micro-fluid behaviour contributes primarily to viscous behaviour (G"), as opposed to elastic behaviour (G').

These correlations have shown that there is a reasonable correlation between %fluid hydrogen and viscous behaviour (G”), along with η*. Therefore, it was likely that the micro-fluidity of the coals dictated the viscous behaviour of coals. Additionally, with these correlations also improving with the use of non-softening coals, it would also suggest that the theory that G” provides information about molecular mobile species and their mechanisms in coal fluidity is confirmed by these correlations. With the lack of correlation between either %fluid hydrogen or T_{2L} with G’, this also confirmed that mobile molecular species do not contribute to elastic behaviour. Therefore, as stated in chapter 5, elastic behaviour is controlled by bulk effects such as suspension formation (from fluid pocket linking through channels) and maceral crosslinking.

Table 7.1: Correlations between rheological parameters G’, G” and η measured with the cup geometry (3 g sample) with %fluid hydrogen and T_{2L} for coals 1 – 10*

	%Fluid H	T_{2L}
Log(G’)	0.72	0.35
Log(G”)	0.87	0.54
Log(η*)	0.84	0.49

Table 7.2: Correlations between rheological parameters G’, G” and η measured with the cup geometry (3 g sample) with %fluid hydrogen and T_{2L} for coals 4 – 10*

	%Fluid H	T_{2L}
Log(G’)	0.31	0.09
Log(G”)	0.73	0.51
Log(η*)	0.71	0.48

Table 7.3: Correlations between rheological parameters G’, G” and η measured with the cup geometry (3 g with %fluid hydrogen and T_{2L} for coals 1 – 2, 4 – 10 (excluding coal 3)*

	%Fluid H	T_{2L}
Log(G’)	0.75	0.63
Log(G”)	0.88	0.76
Log(η*)	0.87	0.74

7.1.2. Blends

Correlations were made between ^{1}H NMR parameters (%fluid hydrogen and T_{2L}) with the rheological parameters (η*, G’ and G”) for blends to understand if the same links carried as those found for single coals. For these correlations, the same compositions had to be correlated (i.e., C5-C6(75wt%) measured by the NMR was correlated against C5-C6(75wt%) measured by the rheometer). Therefore, not all blends could be correlated due to the lack of bulk fluidity for coal 1 – 3 blends, where for example C1-C4(25wt%) did not exhibit a minimum in any of the viscoelastic parameters. Correlations have been divided into groups to understand the relationship between blend and bulk-to-micro-fluidity correlations. Linear viscoelastic correlations, along with log(viscoelastic correlations), can be found in Figures E7 – E13, Appendix E, and Tables E4 – E10.

7.1.2.1.All Blends

The R^2 values of correlations for all the blends are listed in Table 7.4. Figure E7 (Appendix E) shows the correlation plot of rheological parameters (η*, G' and G") and NMR parameters (%fluid H and T_{2L}) for all blends. Table E4 details both linear and log viscoelastic parameters correlated with %fluid H and T_{2L}. There were no viscoelastic parameters that afforded any reasonable correlation with %fluid H or T_{2L} when making correlations across all of the blends together (R^2 between 0.07 – 0.50), in contrast to the individual coals (R^2 between 0.35 – 0.87). This lack of correlation was likely due to the vast range of bulk fluidity exhibited by the coals, ranging from 10^3 - 10^5 Pa s, where coal 3 exhibited a relatively high %fluid hydrogen and T_{2L} despite lack of significant bulk fluidity. Additionally, coals 1 and 2 did not exhibit minima in η* but did show maxima in %fluid hydrogen and T_{2L}.

Table 7.4: Correlations between rheological parameters G', G" and η measured with the cup geometry at 3 g with %fluid hydrogen and T_{2L} for all blends*

	%Fluid H	T_{2L}
Log(G')	0.40	0.07
Log(G")	0.48	0.14
Log(η*)	0.50	0.16

N.B. %Fluid hydrogen vs T_{2L} correlation afforded R^2 value of 0.83

7.1.2.2.Similar Coal Blends

Table 7.5 below details the correlation R^2 values between rheological parameters and NMR parameters for similar coal blends (C4-C5 and C6-C10). Figure E8 (Appendix E) details the correlation plot of rheological parameters and NMR parameters for similar coal blends. Table E5 details the linear and log viscoelastic parameters correlated against %fluid H and T_{2L}.

Similar coal blends (C4-C5 and C6-C10) exhibited good correlations ($R^2 > 0.9$) for both %fluid hydrogen and T_{2L} for both G” and η*, but R^2 values below 0.9 for G’. This again showed that micro-fluidity significantly contributed to the viscous behaviour of the blend, but little towards the elastic behaviour.

Table 7.5: Correlations between rheological parameters G’, G” and η measured with the cup geometry (3g sample) with %fluid hydrogen and T_{2L} for similar coal blends*

	%Fluid H	T_{2L}
Log(G’)	0.76	0.78
Log(G”)	0.98	0.97
Log(η*)	0.95	0.95

N.B. %Fluid H vs T_{2L} correlation afforded R^2 value of 0.98

7.1.2.3.Non-Softening Coal Blends

Table 7.6 details the correlation R^2 values between rheological parameters (η*, G’ and G”) and NMR parameters (%fluid hydrogen and T_{2L}) for non-softening coal blends. Figure E9 (Appendix E) details the correlation plot of rheological parameters and NMR parameters for non-softening coal blends. Table E6, Appendix E, details the linear and log viscoelastic parameters correlated against %fluid H and T_{2L}. For blends with non-softening coals 1 and 2 (C1-C4, C1-C10, C2-C6 and C2-C8) there were no correlations with $R^2 > 0.9$ for the viscoelastic parameters with %fluid H and T_{2L}. However, G’, G” and η* did exhibit R^2 values of 0.86, 0.83 and 0.88 with %fluid H. Reduced correlations were due to the presence of non-fluid coals, where such specimens exhibit little viscous behaviour.

Table 7.6: Correlations between rheological parameters G’, G” and η measured with the cup geometry (3 g sample) with %fluid hydrogen and T_{2L} for non-softening coal blends*

	%Fluid H	T_{2L}
Log(G’)	0.86	0.74
Log(G”)	0.83	0.66
Log(η*)	0.88	0.73

N.B. %Fluid H vs T_{2L} correlation afforded R^2 value of 0.88

7.1.2.4.Medium Fluidity Coal 4 Blends

Table 7.7 below details the correlation R^2 values between rheological parameters (η*, G’ and G”) and NMR parameters (%fluid Hand T_{2L}) for coal 4 blends (C4-C6 and C4-C10). Figure

E10 (Appendix E) details the correlation plot of rheological parameters and NMR parameters for coal 4 blends. Table E7, Appendix E, details the linear and log viscoelastic parameters correlated against %fluid H and T_{2L}. For blends with coal 4 (C4-C6 and C4-C10) there were good correlations ($R^2 > 0.9$) for G" and η* (linear and log), but R^2 values below 0.8 were found for G'.

Table 7.7: Correlations between rheological parameters G', G" and η measured with the cup geometry (3 g samples) with %fluid hydrogen and T_{2L} for coal 4 blends*

	%Fluid H	T_{2L}
Log(G')	0.74	0.65
Log(G")	0.96	0.90
Log(η*)	0.98	0.91

N.B. %Fluid hydrogen vs T_{2L} correlation afforded R^2 value of 0.96

7.1.2.5. Medium Fluidity Coal 5 Blends

Table 7.8 details the correlation R^2 values between rheological parameters (η*, G' and G") and NMR parameters (%fluid hydrogen and T_{2L}) for coal 5 blends (C5-C6, C5-C8 and C5-C10). Figure E11 (Appendix E) details the correlation plot of rheological parameters and NMR parameters for coal 5 blends. Table E8 details the linear and log viscoelastic parameters correlated against %fluid H and T_{2L}. For blends with coal 5 (C5-C6, C5-C8 and C5-C10) there were no correlations with $R^2 > 0.9$, signifying that macro-fluidity for these samples was completely independent of the micro-fluidity detected by ^{1}H NMR.

Table 7.8: Correlations between rheological parameters G', G" and η measured with the cup geometry (3 g sample) with %fluid hydrogen and T_{2L} for coal 5 blends*

	%Fluid H	T_{2L}
Log(G')	0.64	0.63
Log(G")	0.81	0.63
Log(η*)	0.80	0.65

N.B. %Fluid H vs T_{2L} correlation afforded R^2 value of 0.75

7.1.2.6. Medium Fluidity Coals Blends (Collated Coal 4 and Coal 5 Blend Correlations)

Table 7.9 details the correlation R^2 values between rheological parameters and NMR parameters for all the medium fluidity coal blends (coal 4 and 5 blends). Figure E12 (Appendix E) details the correlation plot of rheological parameters and NMR parameters for medium fluidity coal blends. Table E9, Appendix E, details the linear and log viscoelastic parameters correlated against %fluid H and T_{2L}. Due to the differences in correlations for the medium fluidity coal blends (C4-CX and C5-CX blends), the results from both sets were collated to understand if the correlations were maintained. There were no R^2 values above 0.9 here, showing that coals 4 and 5 exhibited different behaviours with respect to macro- and micro-fluidity. It should also be highlighted that, again, G' exhibited the lowest R^2 value.

Table 7.9: Correlations between rheological parameters G', G" and η measured with the cup geometry (3 g sample) with %fluid hydrogen and T_{2L} for collated medium fluidity coal blends*

	%Fluid H	T_{2L}
Log(G')	*0.68*	*0.67*
Log(G")	*0.83*	*0.74*
Log(η*)	*0.85*	*0.76*

N.B. %Fluid hydrogen vs T_{2L} correlation afforded R^2 value of 0.80

7.1.2.7.Coal 3 Blends

Table 7.10 below details the correlation R^2 values between rheological parameters and NMR parameters for coal 3 blended with coals 4 – 10. Figure E13 (Appendix E) details the correlation plot of rheological parameters and NMR parameters for coal 3 with high fluidity coal blends. Table E10, Appendix E, details the linear and log viscoelastic parameters correlated against %fluid H and T_{2L} Correlations between viscoelastic parameters with %fluid hydrogen and T_{2L} for coal 3 blends (C3-C4 to C3-C10) did not afford any good or reasonable correlations. All R^2 values were below 0.5, due to the lack of bulk fluidity for coal 3.

Table 7.10: Correlations between rheological parameters G', G" and η measured with the cup geometry (3 g samples) with %fluid hydrogen and T_{2L} for coal 3 blends*

	%Fluid	T_{2L}
Log(G')	*0.27*	*0.09*
Log(G")	*0.30*	*0.05*
Log(η*)	*0.42*	*0.07*

N.B. %Fluid hydrogen vs T_{2L} correlation afforded a R^2 value of 0.82

7.2. Comparing Rheological – NMR Parameter Correlations

From the correlations in the previous section, it was found that some blends did exhibit a correlation between NMR and viscoelastic parameters. It was clear that the use of non – softening coals, along with the anomalous behaving coal 3, provided lower correlation R^2 values compared with the other blends tested. The overall lack of correlations when collating all blends was likely due to these aforementioned blends. The lack of correlations for the non-softening coal blends was found to be due to lower %fluid H and T_{2L} than predicted when compared with the viscoelastic parameters.

R^2 values of 0.9 or above when correlating G" with %fluid H for blends with medium fluidity and high fluidity coals suggested that the molecular mobile entities were responsible for the viscous behaviour of these blends. This agrees with the mechanisms proposed in chapter 5 on causes of interactions through measured G". Such interactions involving molecular mobile entities included absorption (reduced fluidity) and hydrogen donation (increased fluidity).

T_{2L} exhibited generally poor correlations with viscoelastic parameters (compared with %fluid H), which was primarily due to the relatively low R^2 value between %fluid hydrogen and T_{2L}, along with low mobility of medium fluidity coals. Therefore, increased %fluid hydrogen did not necessarily provide increased mobility. This was most noticeable for coal 3, which possessed one of the highest mobilities of the 10 coals (119 μs), with a maximum %fluid H of 42.8% (compared with coal 8, the highest %fluid H of the 10 coals, with T_{2L} of 113 μs and maximum %fluid H of 66.7%). Of the correlations between the viscoelastic parameters and T_{2L} with $R^2 > 0.9$, the following was found. Only similar coal blends and coal 4 blends provided such correlations. G' afforded R^2 values below 0.9, hence little link between micro-fluidity mobility and elastic behaviour.

As %fluid H appeared to provide the best correlation with G" of the three viscoelastic parameters for blends with two softening coals (on bulk scale), this could help in understanding other mechanisms. The lack of correlations with G' suggested that elastic behaviour was dictated by macromolecular effects and bulk effects. This provided more evidence that such mechanisms could include crosslinking (Das, 2001) between macromolecular structures (Kidena et al, 2002), where free radicals on the macromolecular structures are required for this to occur, as opposed to smaller distinct molecular free radicals

(Chen et al, 2022). Linking of fluid pockets and the formation of suspensions could also be clarified as a bulk effect not linked to mobile molecular entities. Here, the significant amount of fluid material generated can suspend inert solid particles, reduce the elastic behaviour through clustering and ultimately reduce the measured viscosity, as found in systems such as colloids (Kovalchuk et al, 2009).

As there has been no comprehensive study of the use of both high temperature rheometry and NMR to study blends, this shows that mobile molecular species can play a direct role in the fluidity of blends with softening coals. Blends with non-softening coals were more susceptible to bulk effects due to inert solid particles. Armed with this information that %fluid hydrogen contributes directly to the viscous behaviour of the coal, the mechanisms behind non-additive bulk behaviour can be confirmed.

7.3.Comparing Rheometry and NMR with Respect to Additive Behaviour

The individual comparisons between η^*_{min} and %fluid H with respect to additive behaviour, have been discussed in detail in chapters 5 and 6, respectively. Here the differing trends between the η^*_{min} and %fluid H are discussed to help outline the mechanisms that caused deviations in bulk fluidity, where fair agreement was found for %fluid H experimental values with additive behaviour, unlike η^*_{min}.

7.3.1. Similar Coal Blends

C4-C5: η^*_{min} exhibited non-additive behaviour with increased values (reduced fluidity, see Figure 5.2a), whereas %fluid H exhibited agreement (it should be noted that the polymer blending rule only applies to η^*_{min}, where additive behaviour for %fluid H was calculated by linear addition of %fluid H as a function of component addition to the blend, as shown in Equation 6.1) (see Figure 6.3a). Therefore, reduced fluidity was likely due to a bulk fluidity effect (not microfluidity induced) such as maceral crosslinking, with high MVR for both coals. *C6-C10:* Enhanced fluidity was found for η^*_{min} (see Figure 5.2b) as opposed to additive behaviour for %fluid H (see Figure 6.3b). Again, a bulk effect was likely due to such changes in rheological behaviour, such as suspension formation, due to abundance of low viscosity material in the blend at maximum fluidity, suspending any inert material. In fact, it has been found that suspensions can form in viscoelastic media, such as polymers, where the viscosity of the suspension medium can vary widely (Mewis & Wagner, 2012).

7.3.2. Non-Softening Coal Blends

C1-C4: Increased η^*_{min} was found for this blend (Figure 5.3a), which could not be rationalised by %fluid H (increases of between 3.4% - 5% compared with additive behaviour, with errors between 2.9 – 3.1%, were found for %fluid H). In fact, at C1-C4(25wt%) there was an increased value for maximum %fluid H (Figure 6.4a), but no η^*_{min} was measured due to lack of bulk fluidity. Therefore, a bulk effect such as crosslinking, or the significant amount of inert material blocking fluid propagation, where any fluid material was segregated (this can be seen as the opposite effect to suspension formation), were the likely causes of reduced fluidity (it should be noted that coal 1 possessed a high inertinite content of 48.4%). It should also be noted that increased R^2 value was found between G' and %fluid H, compared with G", for the non-fluid coal blends (Table 7.6). *C1-C10:* Increased η^*_{min} values were found at all compositions (Figure 5.3b), which was aligned with reduced %fluid H at C1-C10(25wt%) and C1-C10(50wt%) (suggesting reduced fluidity was in part due to fluid matter adsorption and reduced micro-fluidity), but %fluid H additive behaviour at C1-C10(75wt%) was found (Figure 6.4b). Therefore, macromolecular crosslinking and fluid pocket segregation were possible causes of reduced bulk fluidity at the latter composition. C1-C10(25wt%) did not exhibit a η^*_{min}. *C2-C6:* The only composition where the two techniques displayed additive behaviour was for C2-C6(50wt%), where rheological behaviour could have been directly influenced by mobile molecular entities (Figure 5.3c (η^*_{min}) and Figure 6.4c (%fluid H and T_{2L})). For the other compositions, the %fluid H could not rationalise agreements (C2-C6(25wt%) and deviations (C2-C6(75wt%)) from additive behaviour for rheological measurements. Therefore, bulk effects were likely the cause (crosslinking, and subsequent segregation of fluid material for the agreement, along with suspension formation for increased fluidity). *C2-C8:* %Fluid H (Figure 6.4d) provided evidence for additive behaviour for η^*_{min} (Figure 5.3d) at C2-C8(25wt%), with agreements for both parameters. At C2-C8(50wt%) and C2-C8(75wt%) reductions in η*min were found when %fluid H exhibited agreement with additive behaviour, and hence it was possible that a suspension formed at these compositions.

7.3.3. Coal 4 Blends

C4-C6: Direct links between the two techniques (Figure 5.4a (η^*_{min}) and Figure 6.5a (%fluid H)) were found at C4-C6(25wt%) with additive behaviour displayed. However, at C4-C6(50wt%) and C4-C6(75wt%) suspension formation is likely to have reduced $\eta^*_{min,}$ where additive behaviour was found for %fluid H.

C4-C10: Increased %fluid H at C4-C10(25wt%) was found (5.2% greater than predicted with an error of 3.9%) when agreement was found (Figure 6.5b) with additive behaviour evident for η^*_{min} (Figure 5.4b), hence it was possible that there was a high concentration of less rigid, macromolecular material. At C4-C10(50wt%) and C4-C10(75wt%), the additive behaviour for %fluid H could not rationalise the reduction in η^*_{min}. Hence a suspension likely could have formed at these compositions to afford enhanced bulk fluidity.

7.3.4. Coal 5 Blends

C5-C6: Direct link between the two techniques (see Figure 5.5a (η^*_{min}) and Figure 6.6a (%fluid H)) was found at C5-C6(75wt%), with agreement with additive behaviour for both η^*_{min} and %fluid H. Fluid material segregation, through macromolecular segregation and maceral crosslinking, was the likely cause of the differences between the two techniques, with increased η^*_{min} but agreement with additive behaviour for %fluid H, at the other two compositions.

C5-C8: A link was found at C5-C8(25wt%) and C5-C8(50wt%). For the former, reduced fluidity was reflected in both parameters (increased η^*_{min} (see Figure 5.5b) and reduced %fluid H (see Figure 6.6b)), hence a possible fluid material adsorption mechanism. For the latter, agreement was found for both η^*_{min} (see Figure 5.5b) and %fluid H (Figure 6.6b) (N.B. C5-C8(75wt%) could not be measured due to excess force applied to the rheometer transducer).

C5-C10: Links could be made at C5-C10(25wt%) and C5-C10(50wt%) with reduced fluidity for both parameters (see Figure 5.5c (η^*_{min}) and Figure 6.6c (%fluid hydrogen)). At C5-C10(75wt%), bulk effects were likely, such as suspension formation (C5-C10(75wt%)) where reduced %fluid H was found at this composition, compared with reduced η^*_{min}.

7.3.5. Coal 3 with Medium Fluidity Coal Blends

C3-C4: There were no links between the NMR and rheological parameters, where fluid material segregation was the likely cause with only greater η^*_{min} than predicted (or agreement with additive behaviour at C3-C4(85wt%)) when concerning η^*_{min} (Figure 5.6a (η^*_{min}). For %fluid hydrogen (see Figure 6.7a), the close to predicted values were found at C3-C4(25wt%) and C3-C4(50wt%) but a higher value than predicted at C3-C4(75wt%).

C3-C5: For the blends tested in the rheometer (C3-C5(25wt%) could not be measured due to the lack of bulk fluidity) agreement was found between the rheological and NMR parameters (Figure 5.6b (η^*_{min}) and Figure 6.7b (%fluid H)). Increased η^*_{min} was matched with reduced %fluid hydrogen at both C3-C5(50wt%) and C3-C5(75wt%), hence molecular mobile entity absorption was a possible mechanism for reduced fluidity.

7.3.6. Coal 3 blended with High Fluidity Coals

C3-C6: Bulk effects were likely due to the changes in rheological behaviour at C3-C6(50wt%) such as fluid material segregation, where η^*_{min} exhibited higher than predicted values (by 91.4%), but agreement with additive behaviour was found for %fluid H (Figure 5.7a (η^*_{min}) and Figure 6.8a (%fluid H). Both η^*_{min} and %fluid H exhibited additive behaviour at C3-C6(75wt%).

C3-C7: Agreement between %fluid H and η^*_{min} was found at C3-C7(50wt%), where η^*_{min} exhibited increased values (see Figure 5.7b) and %fluid H exhibited reduced values (4.8% lower with 3.9% error) (Figure 6.8b), compared with additive behaviour. At C3-C7(75wt%), agreement with additive behaviour was found for η^*_{min} where reduced %fluid H was found. Hence a possible suspension formation mechanism could have arisen here.

C3-C8: At C3-C8(50wt%) and C3-C8(75wt%), both %fluid H and η^*_{min} showed agreement with additive behaviour (see Figure 5.7c (η^*_{min}) and Figure 6.8c (%fluid hydrogen)).

C3-C9: Increased η^*_{min} at C3-C9(50wt%) and C3-C9(75wt%) was not due to mobile molecular entities (agreement with additive behaviour for %fluid H), therefore fluid material segregation was the likely cause of reduced bulk fluidity (see Figure 5.7d (η^*_{min}) and Figure 6.8d (%fluid hydrogen)).

C3-C10: For both C3-C10(50wt%) and C3-C10(75wt%), there was no agreement between %fluid H and η^*_{min} (see Figure 5.7e (η^*_{min}) and Figure 6.8e (%fluid hydrogen)). Increased η^*_{min} at both compositions was likely due to fluid material segregation where increased values of %fluid H was found (6.2% greater than predicted with 5% error) at C3-C10(50wt%) and agreement with additive behaviour at C3-C10(75wt%).

For the majority of the compositions tested here, the rheological behaviour could not be rationalised by the %fluid H changes. Of the 54 blends where η^*_{min} and %fluid H could be compared, only 14 compositions showed agreement between the two parameters. 8 of these instances occurred where agreement with additive behaviour occurred, confirming that %fluid H showed fair agreement with additive behaviour. Interestingly, the other 6 instances of agreement between η^*_{min} and %fluid H were found when reduced fluidity occurred, possibly suggesting that adsorption of fluid material led to reductions in both micro- and macrofluidity. Additionally, no agreement was found between the parameters where increased fluidity was found. Hence, for such circumstances, bulk fluidity was likely controlled by elastic forces and mechanisms such as suspension formation.

7.4.Porosity Studies

A selection of single coals and blends were selected to be studied for porosity measurements to understand and confirm the link between pore generation and fluidity. Blends were chosen based on expansion behaviour in the cup geometry, which were selected due to enhanced expansion or very little expansion. Additionally, such information could elucidate more information about the anomalous behaviour of coal 3. All samples were carbonised to 1000 ^{o}C at 3 ^{o}C/min using 3 g of sample (by Umaru Musa, see section 3.2.4) to directly compare with rheological studies. The samples tested were as follows where the η^*_{min} and plate gap measurements were (see Table 7.11 below):

Table 7.11: Semi-coke samples tested for porosity

Sample	η^*_{min} (Pa s)	Maximum Plate Gap Expansion (mm)
Coal 1	1.07×10^{5}	5.6
Coal 3	3.98×10^{4}	5.4
Coal 4	8.77×10^{3}	9.3
Coal 5	3.64×10^{3}	12.2
50% Coal 5 50% Coal 6	8.07×10^{3}	10.7
50% Coal 2 50% Coal 8	3.47×10^{3}	11.9
25% Coal 3 75% Coal 5	1.23×10^{4}	5.4
25% Coal 2 75% Coal 6	4.37×10^{3}	13.1

Single coals 1 and 3, along with the blend of C3-C5(50wt%) were selected due to the high η^*_{min} (above $1x10^4$ Pa s) with very little expansion, where the starting pellet thickness was 5 mm. Single coals 4 and 5, along with C5-C6(50wt%), C2-C8(50wt%) and C2-C6(75wt%) were selected due to the low η^*_{min} (below $1x10^4$ Pa s) along with their high degree of expansion.

Figure 7.1 below details the η^*_{min} as a function of maximum plate gap to initially understand if any relationship existed between η^*_{min} and maximum plate gap. It can be seen that at $\eta^*_{min} > 10^4$ Pa s there was almost no change in maximum plate gap (found for coals 1, 3 and blend of 50% coal 3 75% coal 5), where insufficient fluidity was generated to allow pores to generate. At $\eta^*_{min} < 10^4$ Pa s, small changes in fluidity provided significant increases in maximum plate gap.

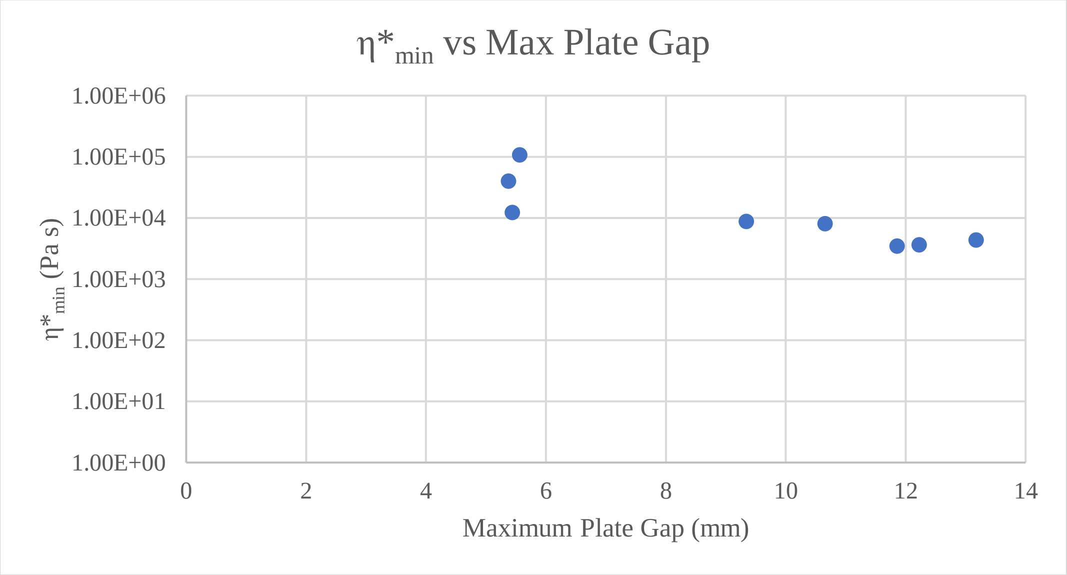

Figure 7.1: η^*_{min} as a function of maximum plate gap for samples tested in the porosity studies

The data from the porosity tests can be found in Tables 7.12a and 7.12b.

Table 7.12a: Pore area, inter-particulate void volume, macropore volume, mesopore volume, micropore volume and total pore volume

Coal Blends	Pore Area (m^2/g)	Inter particlulate void volume (cm^3/g)	Macropore Volume (cm^3/g)	Mesopore Volume (cm^3/g)	Micropore volume (cm^3/g)	Total Pore Volume (cm^3/g)
100% Coal 1	17.1	0.037	0.19	0.036	0.071	0.35
100% Coal 3	7.5	0.061	0.31	0.021	0.095	0.52
100% Coal 4	6.1	0.000	0.78	0.016	0.068	0.89
100% Coal 5	11.3	0.000	1.29	0.024	0.057	1.40
C2-C6(75wt%)	8.6	0.000	1.17	0.018	0.072	1.29
C2-C8(50wt%)	17.0	0.000	1.04	0.036	0.075	1.17
C3-C5(75wt%)	14.2	0.000	0.33	0.030	0.072	0.46
C5-C6(50wt%)	16.5	0.000	1.58	0.034	0.069	1.70
C6-C7(50wt%)	4.8	0.000	1.21	0.010	0.074	1.32

Table 7.12b: Total pore volume-inter, average pore diameter, bulk density, skeletal density and porosity

Coal Blends	Total Pore Volume - inter (cm^3/g)	Average Pore diameter (nm)	Bulk Density (g/cm^3)	Skeletal Density (g/cm^3)	Porosity (%)
100% Coal 1	0.32	74.0	1.05	1.63	35.1
100% Coal 3	0.46	242	0.92	1.62	43.4
100% Coal 4	0.89	585	0.68	1.66	59.1
100% Coal 5	1.40	495	0.47	1.58	70.3
C2-C6(75wt%)	1.29	598	0.52	1.64	68.2
C2-C8(50wt%)	1.17	276	0.57	1.59	64.4
C3-C5(75wt%)	0.46	129	0.85	1.60	46.8
C5-C6(50wt%)	1.70	414	0.42	1.58	73.4
C6-C7(50wt%)	1.32	1106	0.52	1.62	67.6

From the porosity tests, the following was found. C2-C8(50wt%) exhibited the greatest surface area (17.0 m^2g^{-1}), which corresponded with the lowest η^*_{min} of the samples tested. It should be noted that coal 1 did afford a pore area of 17.1 m^2g^{-1}, however this coal did not exhibit any bulk fluidity, and mobility of molecular fluidity was too low (37.6 μs) to provide sufficient micro-fluidity to develop significant porous structure. In comparison, single coal 4 exhibited a pore volume of 6.1 m^2g^{-1}.

Only coals 1 and 3 afforded inter particular void volume. This reinforced the findings from rheological studies that insufficient bulk fluidity was generated by these samples to bind all particles together, affording void space between solid particles. This could possibly suggest that, when blending coals 1 and 3 with fluidity exhibiting coals, these void spaces provide high surface area regions which could catalyse oxidation reactions and radical recombination reactions to bind to fluid contributing species (Cimadevilla, Alvarez & Pis, 2005).

7.4.1. Macropore Volume and Total Pore Volume

Total pore volume could provide information about which pores dictated the overall porosity of the coal samples, and the subsequent bulk behaviour such as maximum plate gap. η^*_{min} exhibited no relationship with total pore volume ($R^2 = 0.62$).

Conversely, there was a linear relationship between maximum plate gap and total pore volume, as shown in Figure 7.2 below which details maximum plate gap as a function of total pore volume. Therefore, plate gap measurements from the cup can provide a reliable prediction of the total pore volume of a coal sample. The equation (Equation 7.1) from this linear regression was found to follow as such:

$$dL = aV_M + b \tag{7.1}$$

Where:

a = *constant (6.47 gm^{-3})*

b = *constant (2.92 mm)*

V_M = *Pore volume (cm^3g^{-1})*

dL: Maximum plate gap (mm)

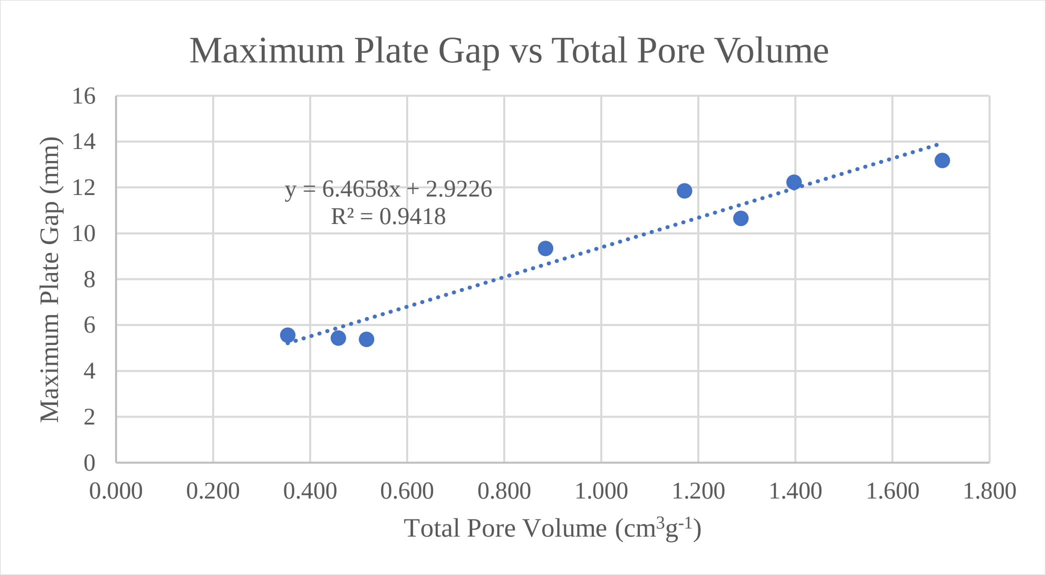

Figure 7.2: Maximum plate gap as a function of total pore volume

Studying the impact of macropore volume, relationships were found between maximum plate gap and macroporosity. Figures 7.3 and 7.4 present η^*_{min} and maximum plate gap as a function of macropore volume, respectively. It was found that there was no relationship between η^*_{min} and macropore volume. There were significant reductions in η^* as function of increasing macropore volume to 0.4 cm^3g^{-1}, but little change thereafter. Therefore, as the fluidity increases through the range of $1x10^5$ to $1x10^4$ Pa s, macropores generate slowly. However, once at $1x10^4$ Pa s, macroporosity generates almost exponentially.

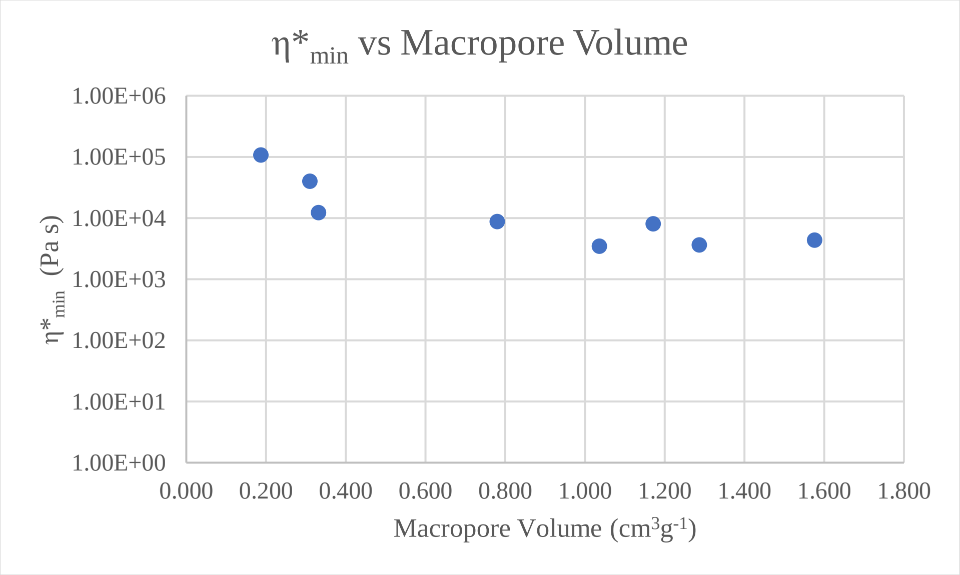

Figure 7.3: Minimum complex viscosity as a function of macropore volume

As might be expected, there was a linear relationship between maximum plate gap and macropore volume ($R^2 = 0.95$), as porosity was created by the fluid phase generating internal pressure as gas vapours were released. The following equation (Equation 7.2) was found between plate gap and macropore volume:

$$dL = aV_M + b \tag{7.2}$$

Where:

a = constant (6.233 gm^{-3})

b = constant (4 mm)

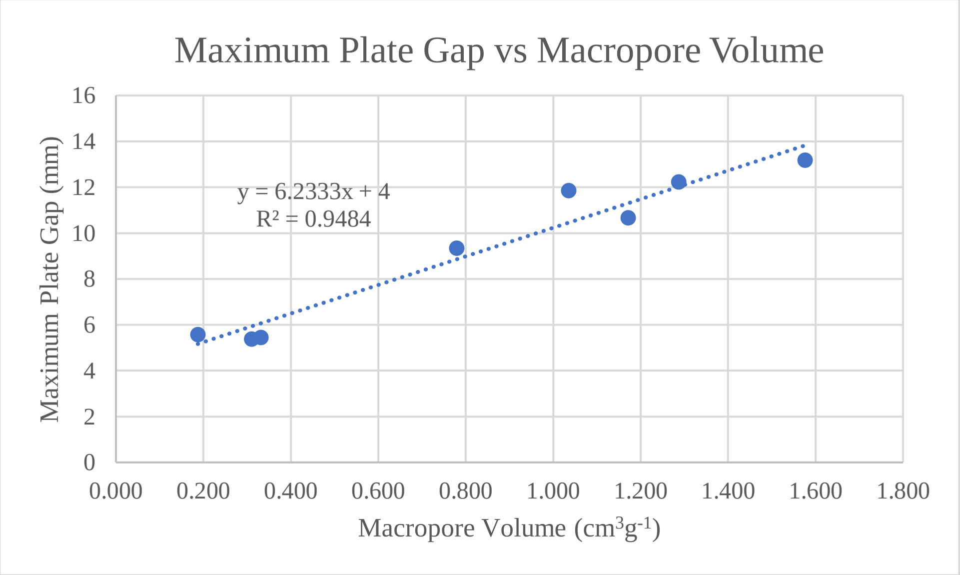

Figure 7.4: Maximum plate gap as a function of macropore volume

7.4.2. Micropore Volume

Due to the nature of coking coal, the volume of micropores was low, where larger pores tend to generate as fluidity is generated to a point at which porosity can form. However, comparing the values of micropore volume, coal 3 did exhibit the greatest micropore volume of 0.095 cm^{3}g^{-1}, correlating with having one of the highest mobilities (T_{2L}) of molecular entities in the suite of coals. All other samples exhibited micropore volumes of between 0.057 – 0.075 cm^{3}g^{-1}, hence the microporous volume of coal 3 was significantly higher than the other samples tested. Therefore, all fluidity generated by coal 3 was on a very localised level, confirmed here by microporous volume and fluidity of molecular entities. Due to the very small grouping of samples, apart from coal 3, there was no relationship between either

η^*_{min} or maximum plate gap with micropore volume ($R^2 = 0.046$ and $R^2 = 0.296$). However, there appeared to be some link between micropore volume and rank of the single coals. Coal 3 possessed the lowest rank of the suite (MVR = 0.65), along with the greatest micropore volume. Conversely, coal 5 exhibited the lowest micropore volume (0.0569 cm^3g^{-1}) and possessed the highest rank (MVR = 1.41).

7.4.3. %Porosity

As total pore volume and macropore volume have been discussed above, total porosity has been compared against bulk parameters to further solidify conclusions on the use of the cup geometry for coke quality predictions. Percentage porosity was calculated as such (Equation 7.3):

$$Porosity\ (\%) = 1 - \frac{Bulk\ Density}{Skeletal\ Density}\ x\ 100 \qquad (7.3)$$

η^*_{min} and maximum plate gap were plotted as a function of %porosity, as shown in Figures 7.5 and 7.6 . Although it would be expected that similar correlations would be found between fluidity measurements with total pore volume and porosity, η^*_{min} provided a relationship with %porosity ($R^2 = 0.917$). Consequently, this does show that η^*_{min} can be used to predict %porosity, as increased fluidity provides increased porosity. This exponential relationship can be described as such (Equation 7.4):

$$ln\eta^*_{Min} = lna - b(\%Porosity) \qquad (7.4)$$

Where:

A = constant (1.05x10^6 Pa s)

B = constant = 7.93x10^{-2} Pa s/%Porosity

The intercept, a, indicated that at 1.05x10^6 Pa s no porosity would form.

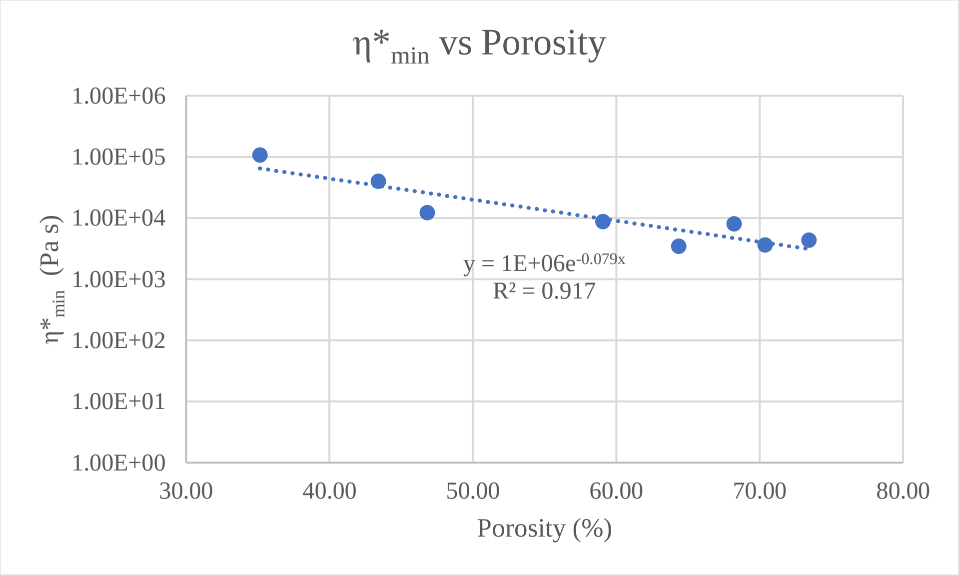

Figure 7.5: Minimum complex viscosity as a function of semi-coke porosity

As expected, there was a linear relationship between maximum plate gap and %porosity (R^2 = 0.914), as shown below in Figure 7.6 and Equation 7.5. Hence, maximum plate gap increased linearly with pore generation.

$$dL = a(\%Porosity) - b \tag{7.5}$$

Where:

A = constant (0.223 mm/(%Porosity))

B = constant (-3.65 mm)

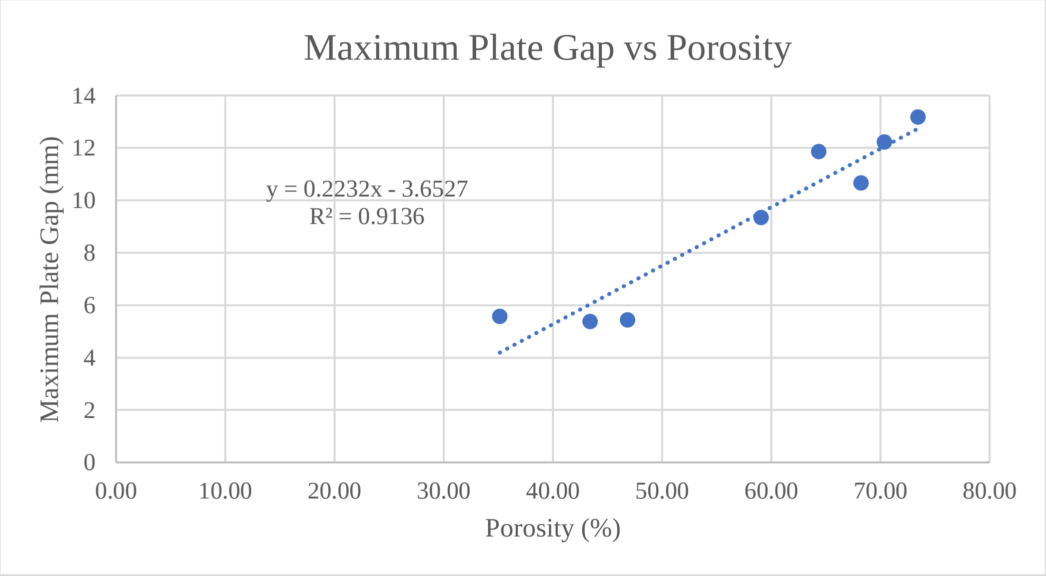

Figure 7.6: Maximum plate gap as a function of semi-coke porosity

There were few relationships between η^*_{min} and porosity measurements, with the only noticeable correlation with %porosity. Maximum plate gap measurements with the cup geometry afforded good correlations with macropore volume, %porosity and total pore volume, which was due to the presence of retaining walls. Gas and coke pressure was exerted primarily against the top plate, giving rise to direct measurement of pore growth (unlike sample displacement from the PP). Therefore, the cup geometry could be used to predict porosity and macropore volume, an added benefit to the rheological measurements of coking coals.

7.5.References

Chen, Y., Lee, S., Tahmasebi, A., Liu, M., Zhang, T., Bai, J., Tian, L. and Yu, J. 2022. Mechanism of carbon structure transformation in plastic layer and semi-coke during coking of Australian metallurgical coals. *Fuel*. ***315***, p.123205.

Cimadevilla, J.L.G., Álvarez, R. and Pis, J.J. 2005. Influence of coal forced oxidation on technological properties of cokes produced at laboratory scale. *Fuel processing technology*. ***87***(1), pp.1-10.

Das, T.K. 2001. Thermogravimetric characterisation of maceral concentrates of Russian coking coals. *Fuel*. ***80***(1), pp.97-106.

Kidena, K., Katsuyama, M., Murata, S., Nomura, M. and Chikada, T. 2002. Study on plasticity of maceral concentrates in terms of their structural features. *Energy & fuels*. ***16***(5), pp.1231-1238.

Kovalchuk, N., Starov, V., Langston, P. and Hilal, N. 2009. Formation of stable clusters in colloidal suspensions. *Advances in Colloid and Interface Science*. ***147***, pp.144-154.

Luo, P. and Gu, Y. 2007. Effects of asphaltene content on the heavy oil viscosity at different temperatures. *Fuel*. ***86***(7-8), pp.1069-1078.

Mewis, J. and Wagner, N.J. 2012. *Colloidal suspension rheology*. Cambridge: Cambridge University Press.

Chapter 8

Conclusions and Future Work

8.1. Conclusions

8.1.1. Novel Geometry Methodology Development

Throughout coking coal fluidity research, only the PP geometry has been used since the inception of rheometry for the study of such materials under high temperature. Hence it was identified that there was need for new methodologies and rheological geometries to expand the range of knowledge of the area and obtainable data. The use of a novel rheometric geometry was shown to provide viscoelastic measurements which showed agreement with the standardised PP geometry despite the differences in dimensions of the geometries. The significant differences were found within plate gap measurements due to the presence of a retaining wall for the cup, and subsequent direct application of volatile force against the top plate. Conversely, the PP, without retaining walls, was prone to sample displacement from the constant force of the top plate against the sample to retain contact. Hence, the PP only provided maxima in plate gap during softening. The cup, alternatively, provided a maximum plate gap at maximum fluidity of the sample due to retaining walls, and in some cases for high rank coals a continuous increase was found, hence this new methodology could act as a proxy for gas pressure.

Sample retention was a significant benefit of the cup geometry, when compared with the PP. The increase in mass, performed for non-softening, medium fluidity and high fluidity coals, showed that there was agreement with the lower mass measurements. Additionally, plate gap measurements highlighted that better sample retention was afforded due to the increased gas pressure against the top plate preventing sample displacement, compared with the PP. Therefore, the cup geometry was selected as the methodology of use for studying blends using rheometry at the increased mass of 3 g.

8.1.2. High Temperature Rheological Studies of Coal Blends

In the rheological testing of blends, the majority of the blends tested here showed significant deviations from the polymer blending rule. Interestingly, blending two similar coals did not result in additive behaviour. Two medium fluidity coals afforded reduced fluidity, whereas two high fluidity coals provided enhanced fluidity. The mechanisms behind these were thought to be the opposite of each other. For medium fluidity coals, maceral crosslinking possibly prevented fluid propagation through the sample. For high fluidity coals, the abundance of low viscosity material likely allowed a suspension to form. The same bulk phenomena were likely for non-softening coal blends, where both increases and decreases in η^*_{min} were found compared with predicted.

Coal 3 provided very intriguing results, where this coal was shown to provide no fluidity, yet possessed the highest volatile matter content and vitrinite content of the 10 coals. When blended with medium fluidity coals, significant reductions in fluidity were found. High fluidity coals provided two sets of results, where some blends afforded reduced fluidity, and others exhibited enhanced fluidity. It was thought that coal 3 either adsorbed a significant amount of fluid material but could also be suspended in a fluid matrix when blended with certain high fluidity coals.

Plate gap measurements provided additional confirmatory information about blends where increased swelling was indicative of increased fluidity and vice versa. Many samples exhibited a continuous increase in plate gap with no sample displacement, showing that these blends exerted significant gas pressure to resist the force of the top plate, and hence could provide useful information about coking pressure. Other blends, all of which contained a high fluidity coal, showed sample displacement. It was found that down to a particular η^*_{min} (approximately 2000 – 3000 Pa s) there was a significant increase in plate gap, suggesting that such blends could maintain segregated pores. For blends that exhibited η^*_{min} below this limit it was likely that a low viscosity suspension and large coalesced pores formed along with volatile escape, giving rise to a weak semi-coke and subsequent sample displacement.

8.1.3. High Temperature ^{1}H NMR for the Study of Coal Blends

High temperature ^{1}H NMR measurements of single coals afforded %fluid hydrogen which correlated with rheological measurements, apart from coal 3. This coal exhibited one of the highest mobility of the 10 coals, along with a maximum %fluid hydrogen akin to that of a medium fluidity coal. NMR also confirmed that high fluidity coals possessed the highest %fluid hydrogen and mobility of the fluid phase, suggesting a link with the low η^*_{min} of such specimens. Although NMR did not rationalise the bulk fluidity phenomena of coal 3, it did show that this coal could possess micro-fluidity which could not propagate through the sample.

For the majority of blends tested using high temperature ^{1}H NMR, %fluid hydrogen and T_{2L} exhibited additive behaviour with respect to composition. Deviations from additive behaviour were found for coal 3 and coal 5 (the highest MVR coal of the suite) blends with respect to %fluid H, and for non-fluid coals with respect to T_{2L} due to the significant difference in mobility profiles when compared with high fluidity coals. Although this did not rationalise cases where enhanced bulk fluidity was found, it confirmed that microfluidity was generated in agreement with additive behaviour. Conclusively, phenomena in rheological measurements were largely the result of bulk effects.

8.1.4. Comparing Rheometry with NMR

Correlating NMR and rheological parameters, no correlations were found for mobility (T_{2L}), however reasonable correlations were found for %fluid hydrogen, in particular for G" and η^*_{min}. This was true for single coals, where the link between viscous behaviour and micro-fluidity was confirmed here. For blends of coals, there was no overall correlation between rheological and NMR parameters. However, for blends including medium fluidity coals, along with blends of similar coals, provided correlation R^2 values above 0.9, confirming that viscous behaviour of these blends was dictated to an extent by microfluidity. Blends with non-softening coals, including coal 3, did not show such correlations, and hence other bulk fluidity phenomena were likely the cause of deviations from additive behaviour.

Comparing the two techniques with respect to additive behaviour, %fluid H exhibited fair agreement with the polymer blending rule, whereas η^*_{min} exhibited mostly deviations from additive behaviour. Consequently, it was found that only 14 of the 54 comparable compositions exhibited agreements between the two parameters with respect to additive behaviour. Of the 14 compositions, 8 provided additive behaviour in both η^*_{min} and %fluid H, and 6 provided reduced fluidity in the two parameters. Hence, rheological properties were only impacted significantly by microfluidity by adsorption of fluid material or in a few cases where additive behaviour was observed. In cases where enhanced bulk fluidity was observed, phenomena such as suspension formation were thought to give rise to such behaviour.

8.1.5. Porosity Testing

8 samples were tested to understand the effect of fluidity upon porosity and to solidify previous theories upon the relationship between these two parameters. There were good correlations between η^*_{min} and %porosity, but no relationship with total pore volume and macropore volume. Good correlations were found between macropore volume, total pore volume and %porosity with maximum plate gap, with $R^2 > 0.9$ in all cases. Consequently, the cup geometry could be used to provide accurate predictive measurements of porosity and total pore volume, consequently very useful for coke quality predictions.

Micropore volume exhibited no correlation with maximum plate gap or η^*_{min}, which confirmed that bulk fluidity dictated the macropore development, whereas only localized fluidity and volatile generation afforded microporous structural changes. However, coal 3 did exhibit the greatest micropore volume (but low meso- and macroporosity), corresponding with the high mobility of the low swelling coal, which reaffirmed that coal 3 could not generate bulk fluidity where any fluid material was segregated in micro-pockets and could not propagate through the sample. Additionally, coals 1 and 3 were the only samples to exhibit inter-particulate void volume, confirming that these coals did not generate sufficient bulk fluidity for particles to fuse.

8.2. Future Work

A significant amount of novel data has been generated from this research using the cup geometry, and the subsequent comparisons with high temperature NMR and porosity measurements. As such, the following studies could be performed in future research.

- To further study and examine the porosity of coals and their blends. From the porosity tests, the very good correlations found here can be confirmed on a very wide basis of coals, where the cup can then be used in a range of studies to predict porosity of coke samples.

- To obtain differential hydrogen generation profiles as a function of temperature for coals and their blends so that %fluid H experimental values can be compared against predicted values based on the hydrogen content of coals and blends at that specific temperature.

- To use the novel cup geometry to understand the impact of additives upon the fluid and expansion behaviour of coals and coal blends. Additionally, as this novel geometry has shown to be able to predict porosity and possibly act as a proxy for gas pressure, the impact of additives upon porosity and coking pressure can be studied to reduce the amount of sample used in pilot scale tests prior to industrial scale coking. On a similar vein, biomass blended with coal could be studied with the cup geometry. With the advantage of porosity prediction, the novel geometry would provide an additional layer of information about the use of biomass in industrial scale coking.

Nomenclature

η^*_{min}: Minimum complex viscosity (Pa s)
η^*: Complex viscosity (Pa s)
G’: Storage modulus (Pa)
G”: Loss Modulus (Pa)
Tanδ: Loss tangent (dimensionless)
dL: Plate gap (mm)
MVR: Mean vitrinite reflectance (dimensionless)

Appendix A

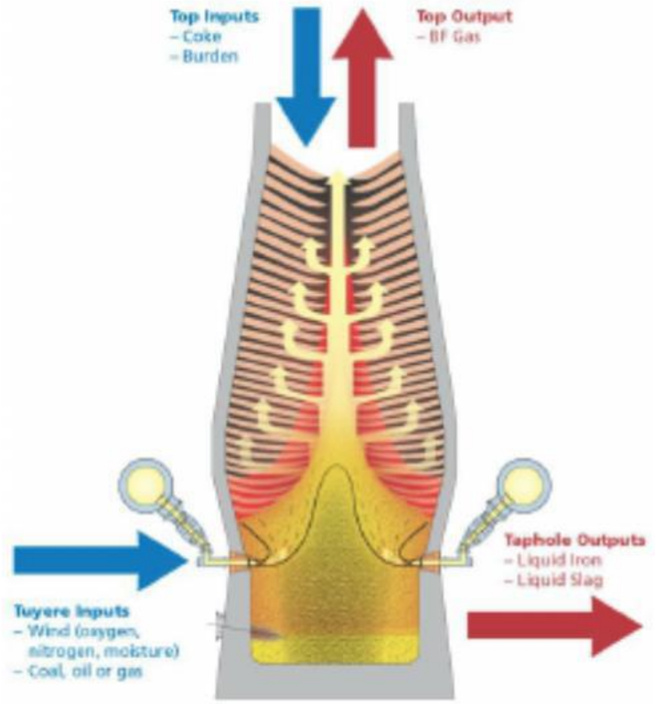

Figure A1: Cross-Section of a Basic Oxygen Furnace (BOF) (Geerdes, Chaigneau & Kurunov, 2015)

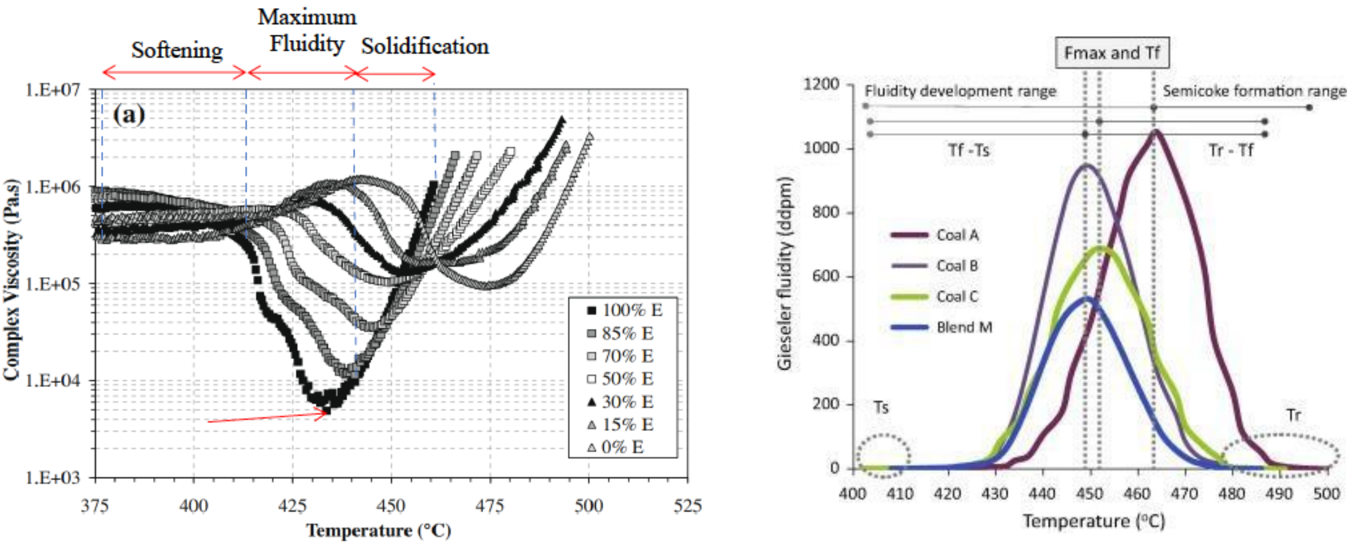

Figure A2: Plot of complex viscosity as a function of temperature for a binary blend of coals (left) (Duffy, Mahoney and Steel, 2010); Plot of Gieseler fluidity as a function of temperature (right) (Gavo, Garcia & Diez, 2016)

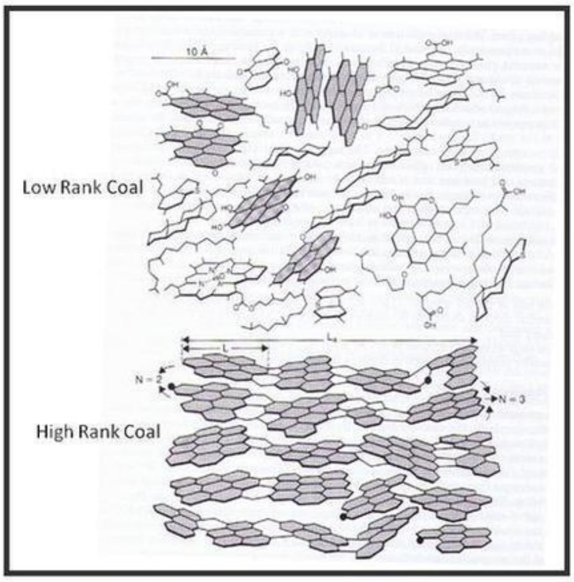

Increase and Alignment of Graphitic Ring Structures as Rank Increases

Figure A3: Difference in maceral composition and alignment in low rank and high rank coals (Bonijoly, Oberlin & Oberlin, 1982).

Appendix B

Table B1: Gieseler plastometer measurements of temperatures for softening (TSoft), maximum fluidity (TMF) and resolidification (TResol)

Coal	Fluidity (ddpm)	TSoft (ºC)	TMF (ºC)	TResol (ºC)
1	0	N/A	N/A	N/A
2	3	436	469	488
3	22	N/A	N/A	N/A
4	440	411	458	492
5	130	446	478	506
6	3700	388	442	482
7	8400	390	452	498
8	30000	364	440	492
9	29400	387	432	477
10	30000	388	440	480

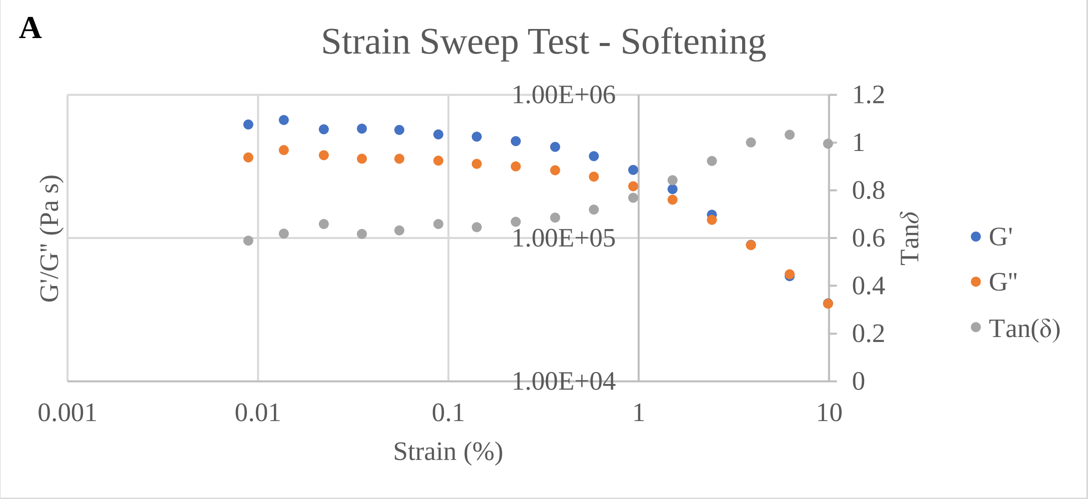

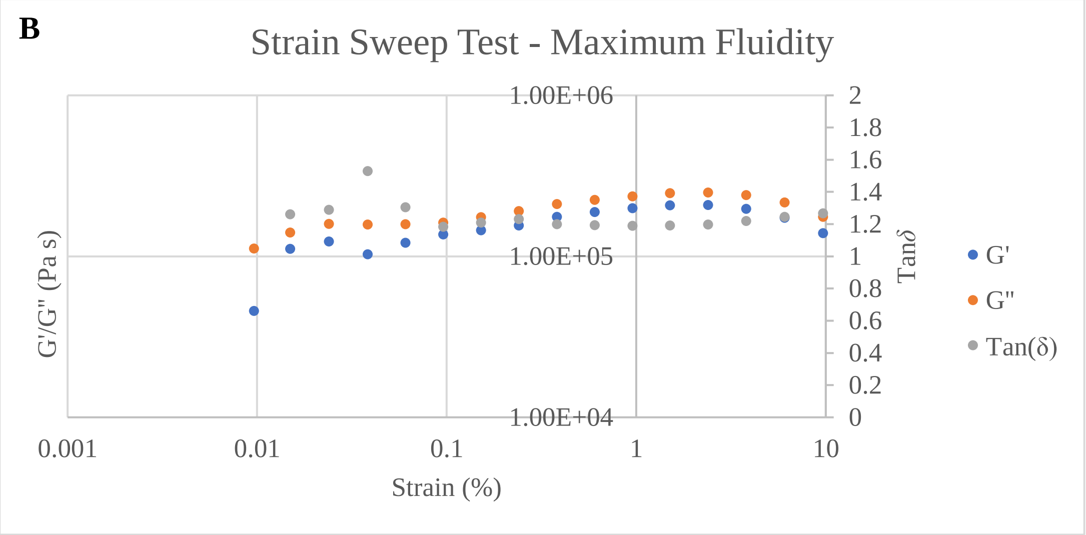

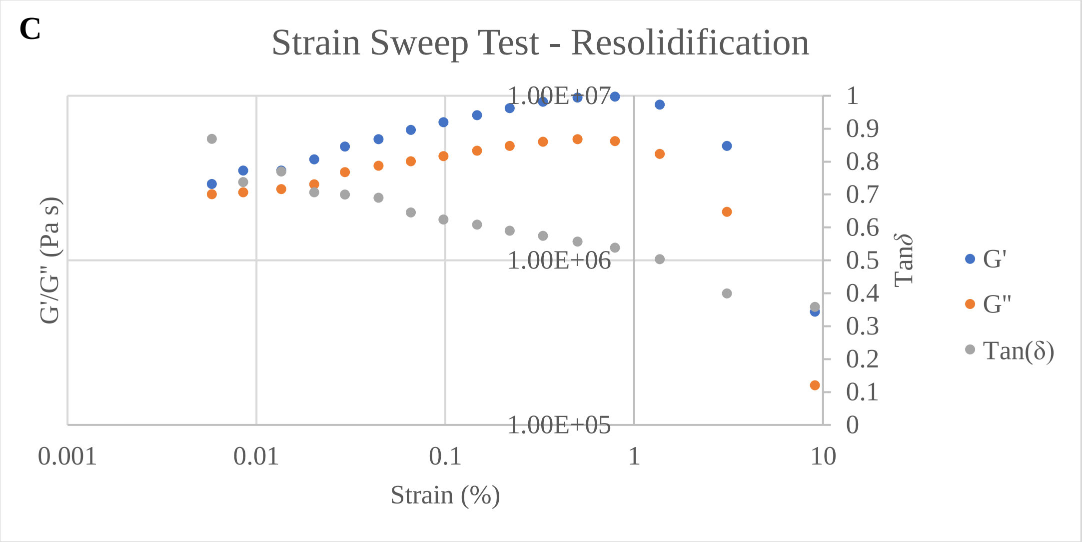

Figure B1: Strain sweep test of coal 4 to obtain the linear viscoelastic limit. Softening (A); Maximum Fluidity (B); Resolidification (C). For these events, there is no significant decrease in G' or G" up to a strain of 0.1%. Therefore, at this strain, the coals are still within the linear viscoelastic range (the material still behaves as a viscoelastic material). All tests performed in this research were tested with a strain of 0.1%. N.B. Tanδ decreases during resolidification due to the increased elastic behaviour (G' greater than G" with increasing difference with respect to strain) of the sample during this stage. The sample is still within the viscoelastic range, as storage and loss moduli do not decrease until 1% strain.

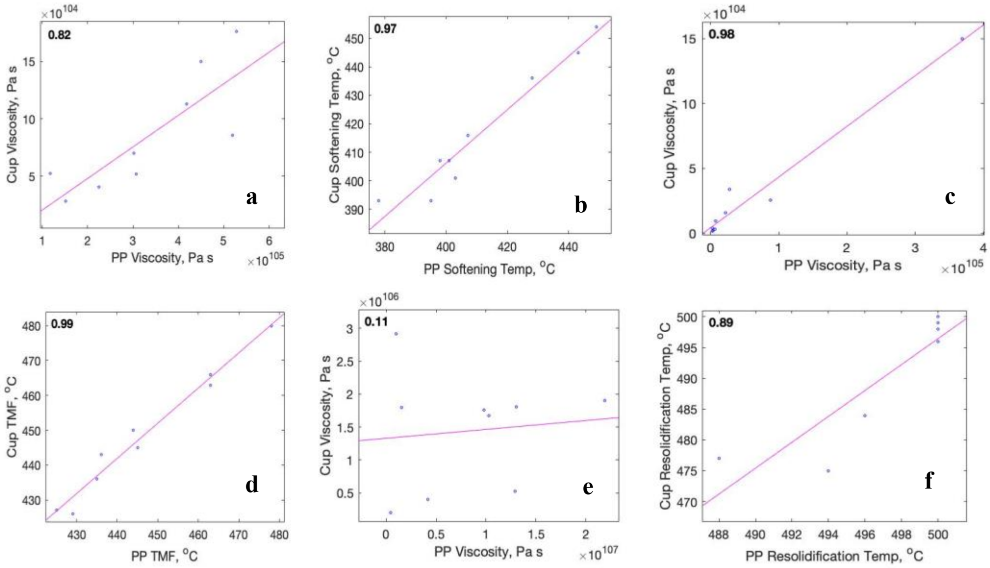

Figure B2: PP - Cup correlations for complex viscosity for a) softening complex viscosity (coals 2 – 10), b) temperature of softening (coals 2 – 10), c) minimum complex viscosity (coals 2 – 10), d) temperature of maximum fluidity (coals 2 – 10), e) resolidification complex viscosity (coals 2 – 10) and f) temperature of resolidification (coals 2 – 10).

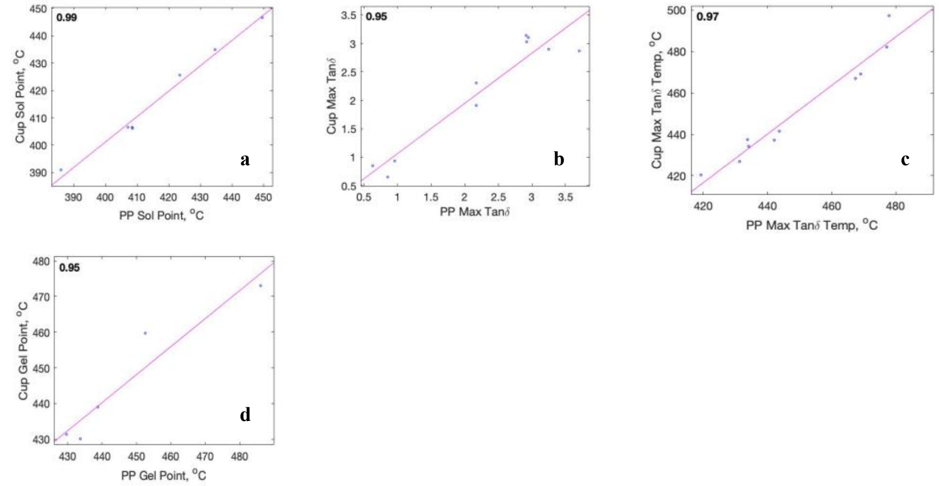

Figure B3: PP - cup tanδ correlations for a) sol point (coals 4 – 10), b) maximum tanδ (coals 1 – 10), c) temperature of maximum tanδ (coals 1 – 10) and d) gel point (coals 6 – 10)

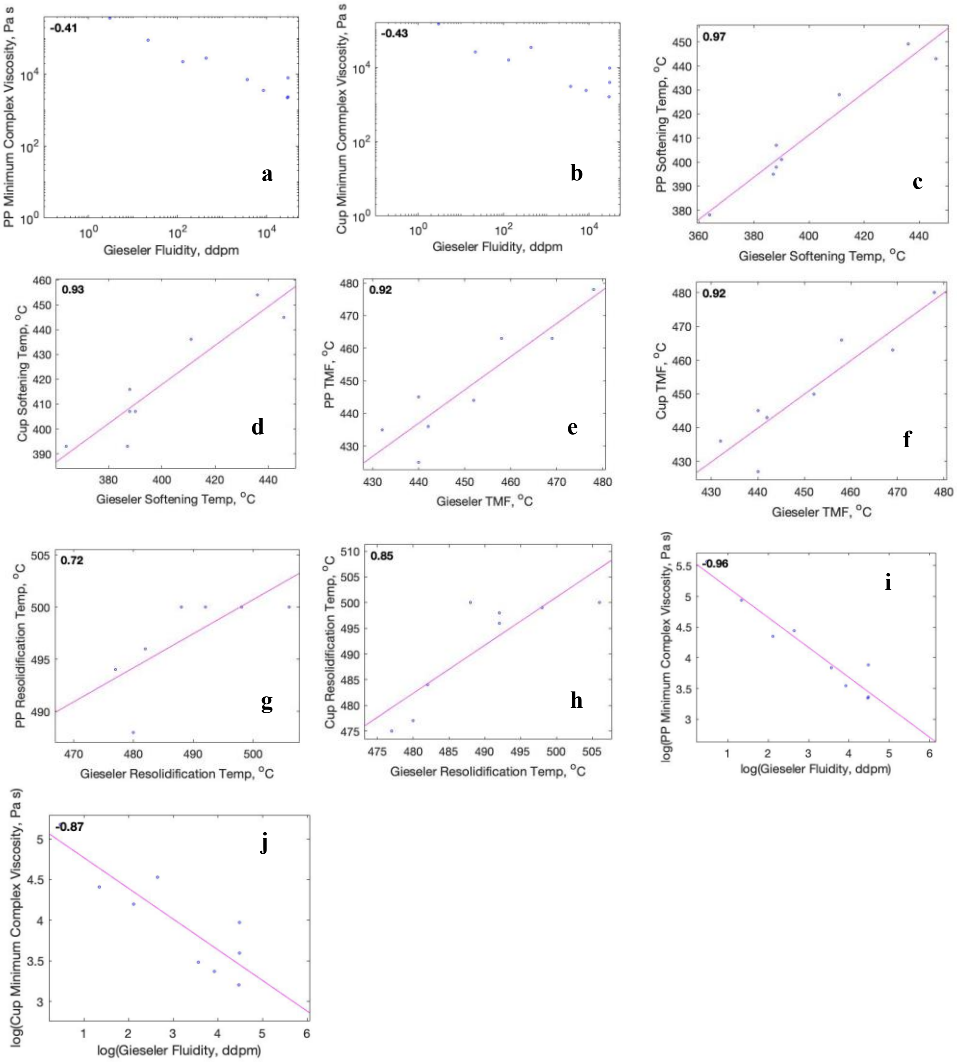

Figure B4: Complex viscosity vs Gieseler correlations for a) PP minimum complex viscosity vs Gieseler maximum fluidity (coals 2 – 10), b) cup minimum complex viscosity vs Gieseler maximum fluidity (coals 2 – 10), c) PP softening temperature vs Gieseler softening temperature (coals 2, 4 – 10), d) cup softening temperature vs Gieseler softening temperature (coals 2, 4 – 10), e) PP temperature of maximum fluidity vs Gieseler temperature of maximum fluidity (coals 2, 4 – 10), f) cup temperature of maximum fluidity vs Gieseler temperature of maximum fluidity (coals 2, 4 – 10), g) PP temperature of resolidification vs Gieseler temperature of resolidification (coals 2, 4 – 10), h) cup temperature of resolidification vs Gieseler temperature of resolidification (coals 2, 4 – 10), i) log(PP minimum complex viscosity vs log(Gieseler maximum fluidity) (coals 2 – 10) and j) log(cup minimum complex viscosity vs log(Gieseler maximum fluidity) (coals 2 – 10).

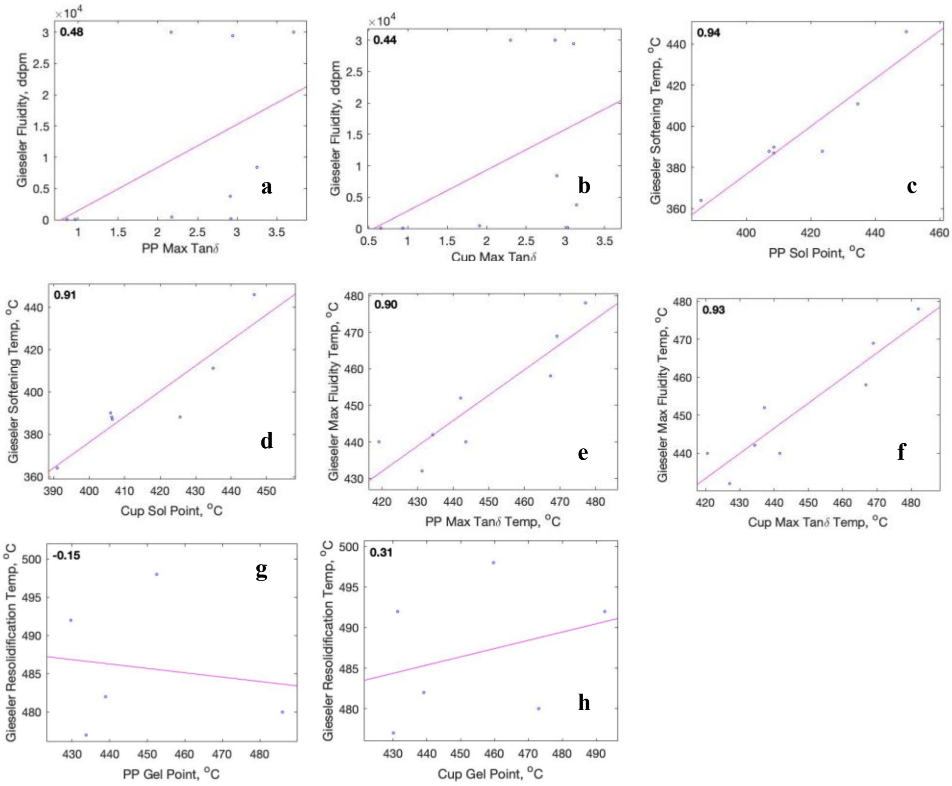

Figure B5: Tanδ vs Gieseler correlations for a) PP maximum tanδ vs Gieseler maximum fluidity, b) cup maximum tanδ vs Gieseler maximum fluidity, c) PP sol point vs Gieseler softening temperature (coals 4 – 10), d) cup sol point vs Gieseler softening temperature (coals 4 – 10), e) PP temperature of maximum tanδ vs Gieseler temperature of maximum fluidity (coals 2, 4 – 10), f) cup temperature of maximum tanδ vs Gieseler temperature of maximum fluidity (coals 2, 4 – 10), g) PP gel point vs Gieseler temperature of resolidification (coals 6 – 10) and h) cup gel point vs Gieseler temperature of resolidification (coals 6 – 10).

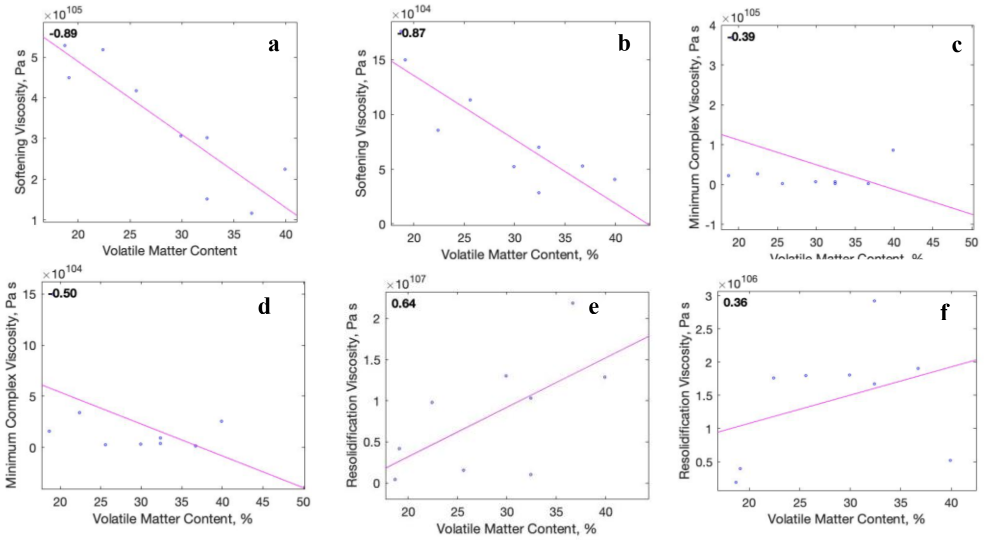

Figure B6: Complex viscosity – volatile matter correlations for a) PP softening viscosity (coals 2 – 10), b) cup softening viscosity (coals 2 – 10), c) PP minimum complex viscosity (coals 2 – 10), d) cup minimum complex viscosity (coals 2 – 10), e) PP resolidification viscosity (coals 2 – 10), f) cup resolidification viscosity (coals 2 – 10).

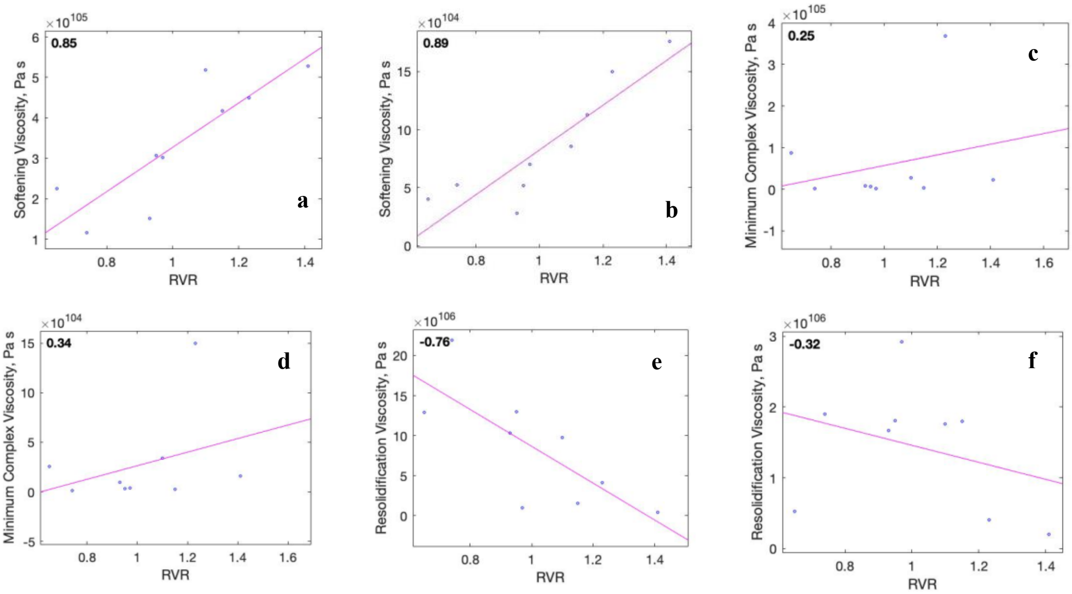

Figure B7: Complex viscosity – mean vitrinite reflectance correlations for a) PP softening viscosity (coals 2 – 10), b) cup softening viscosity (coals 2 – 10), c) PP minimum complex viscosity (coals 2 – 10), d) cup minimum complex viscosity (coals 2 – 10), e) PP resolidification viscosity (coals 2 – 10), f) cup resolidification viscosity (coals 2 – 10)

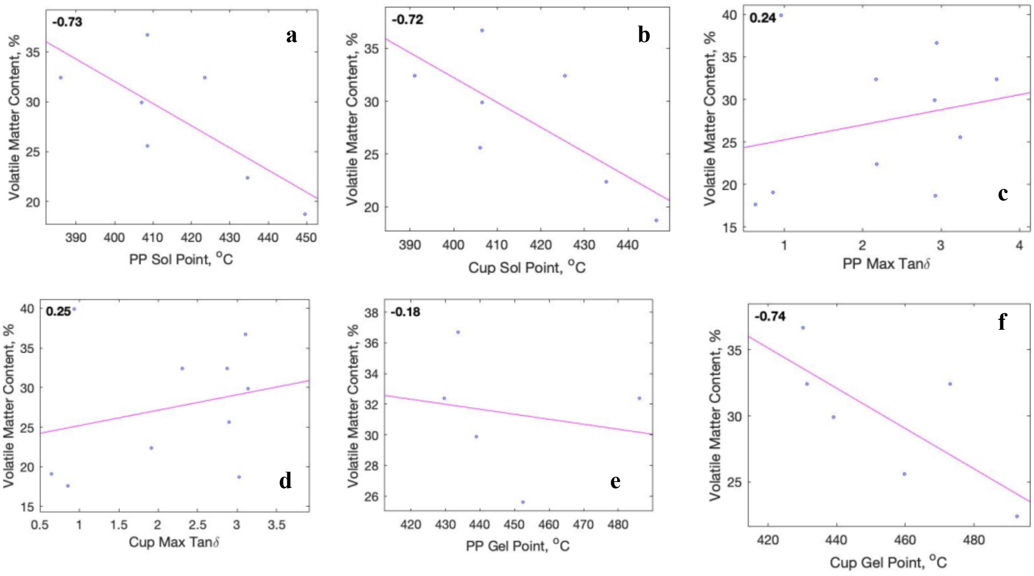

Figure B8: Tanδ – volatile matter correlations for a) PP sol point (coals 4 – 10), b) cup sol point (coals 4 – 10), c) PP maximum tanδ (coals 1 – 10), d) cup maximum tanδ (coals 1 – 10), e) PP gel point (coals 6 – 10) and f) cup gel point (coals 4, 6 – 10).

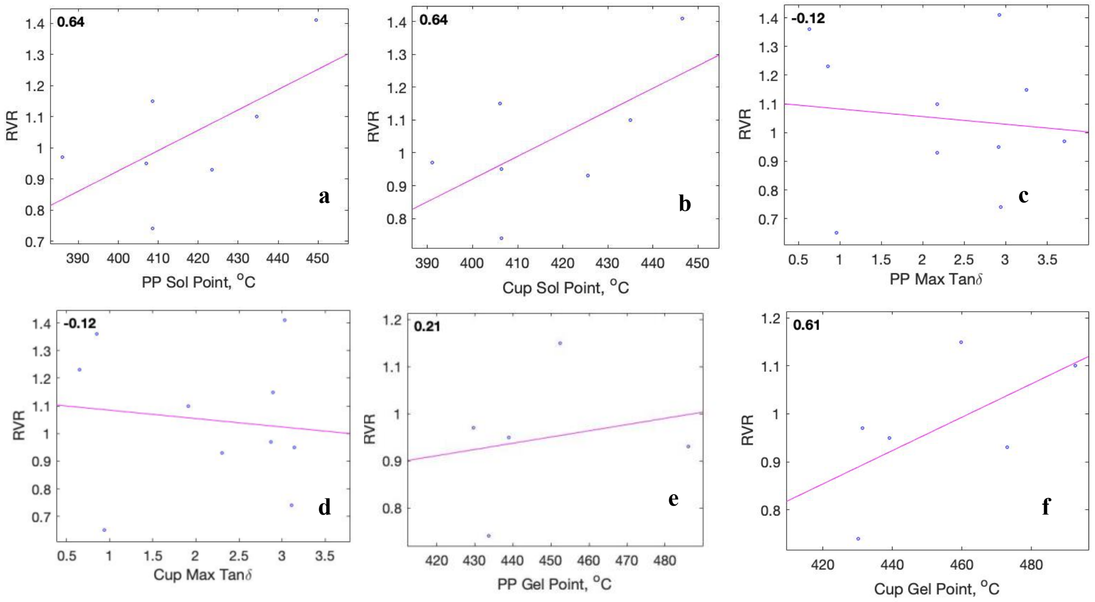

Figure B9: Tanδ – mean vitrinite reflectance correlations for a) PP sol point (coals 4 – 10), b) cup sol point (coals 4 – 10), c) PP maximum tanδ (coals 1 – 10), d) cup maximum tanδ (coals 1 – 10), e) PP gel point (coals 6 – 10) and f) cup gel point (coals 4, 6 - 10)

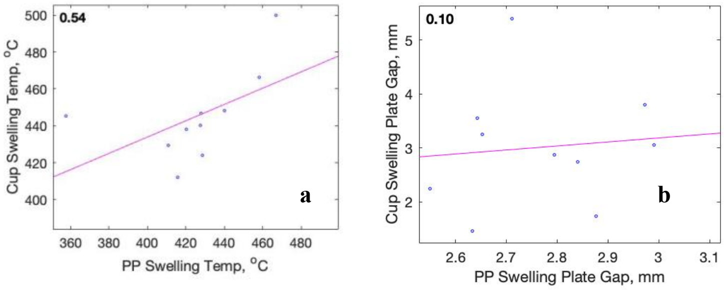

Figure B10: PP – cup plate gap correlations for a) swelling temperature (coals 1 – 10), b) swelling plate gap (coals 1 – 10)

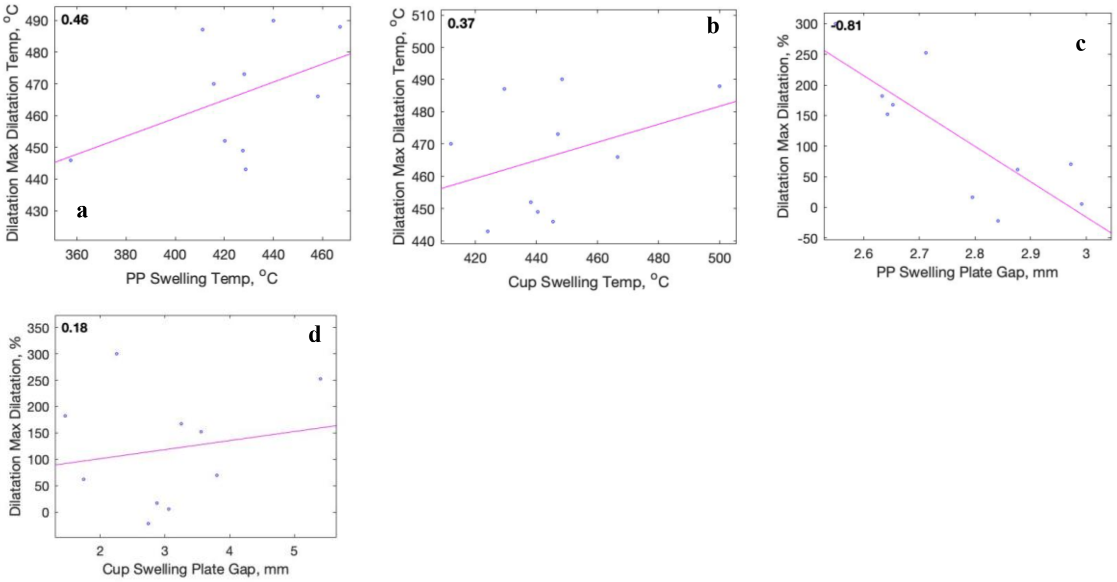

Figure B11: Plate gap – dilatation correlations for a) PP swelling temperature vs dilatation maximum dilatation temperature, b) cup swelling temperature vs dilatation maximum dilatation temperature, c) PP swelling plate gap vs dilatation maximum dilatation (coals 1 – 10), d) cup swelling plate gap vs dilatation maximum dilatation (coals 1 – 10)

Appendix C

Table C1: Gieseler plastometer measurements of temperatures for softening (TSoft), maximum fluidity (TMF) and resolidification (TResol)

Coal	Fluidity (ddpm)	TSoft (°C)	TMF (°C)	TResol (°C)
1	0	N/A	N/A	N/A
2	3	436	469	488
3	22	N/A	N/A	N/A
4	440	411	458	492
5	130	446	478	506
6	3700	388	442	482
7	8400	390	452	498
8	30000	364	440	492
9	29400	387	432	477
10	30000	388	440	480

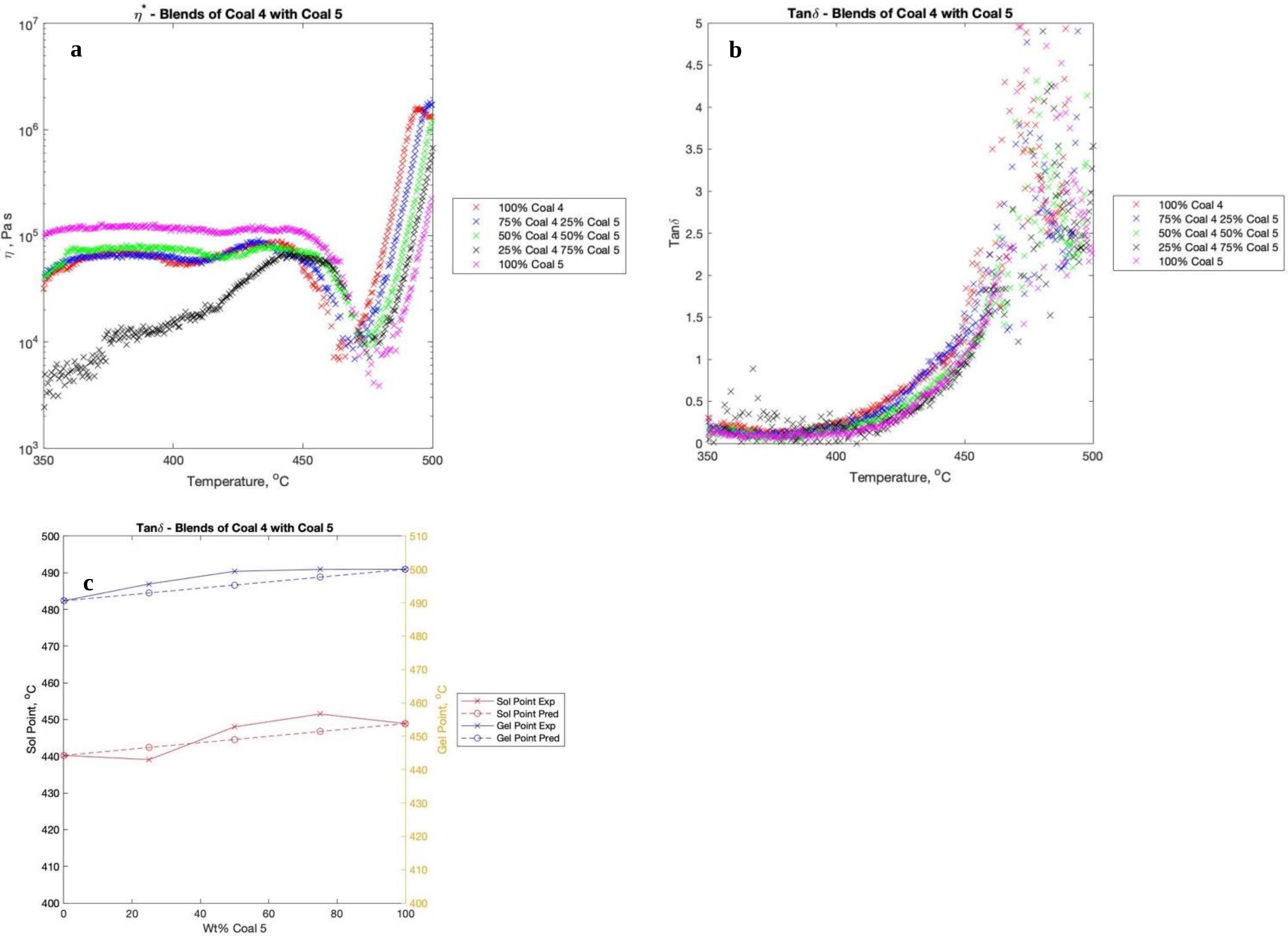

Figure C1: (a - left) Complex viscosity and (b - right) tanδ as a function of temperature for blends of C4-C5, c) gel point and sol point as a function of composition for C4-C5

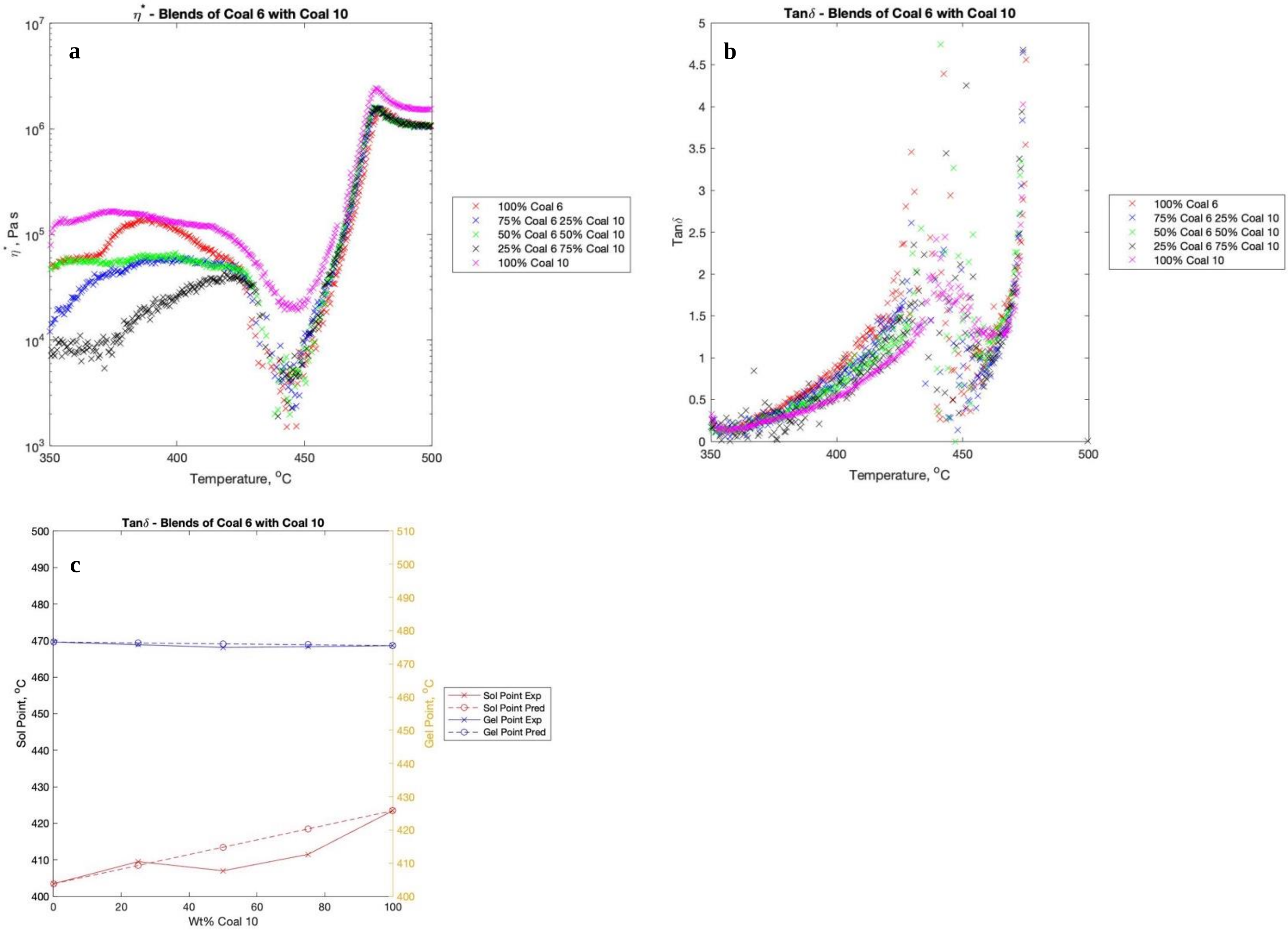

Figure C2: (a - left) Complex viscosity and (b - right) tanδ as a function of temperature for blends of C6-C10, c) gel point and sol point as a function of composition for C6-C10

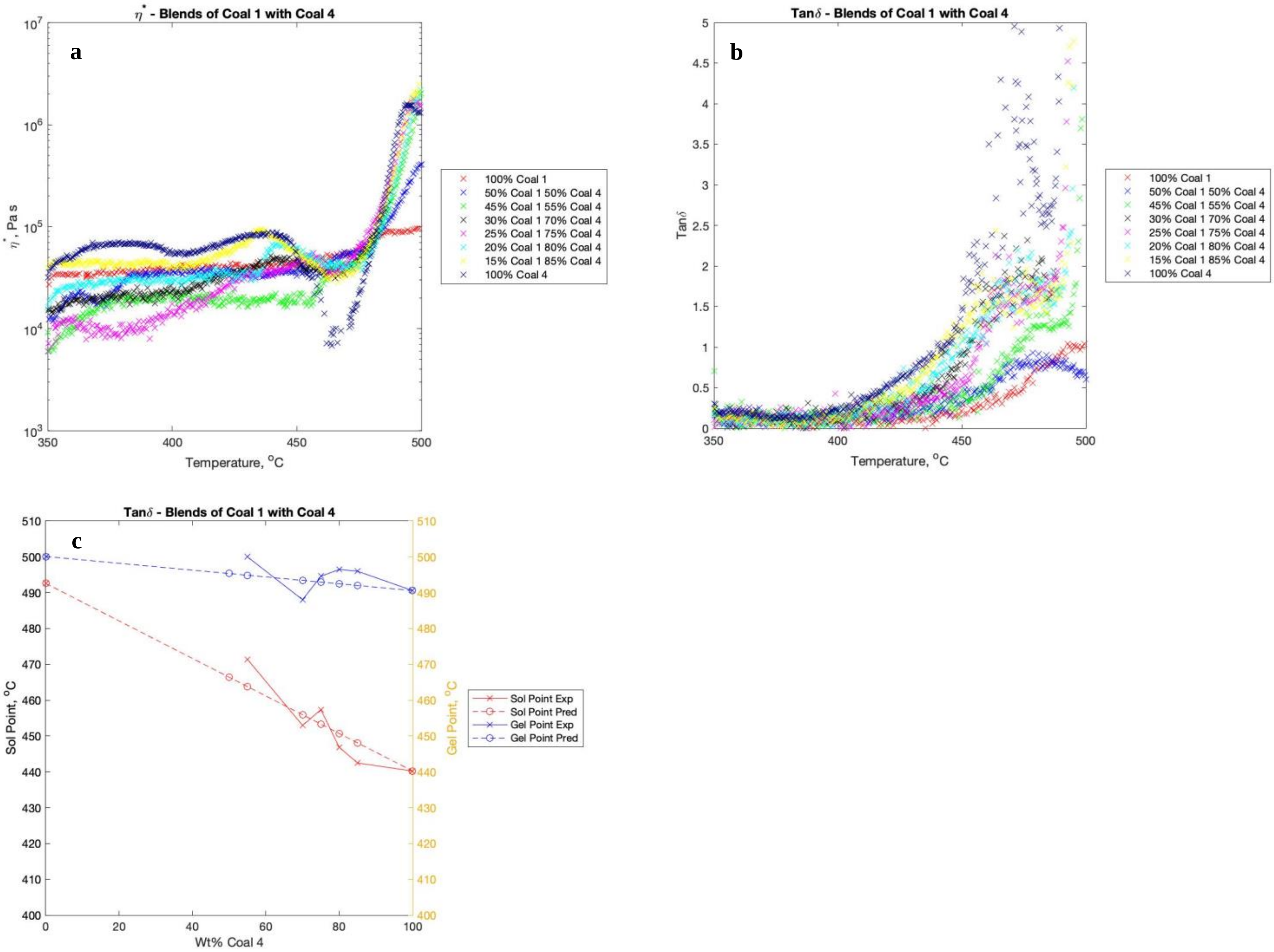

Figure C3: (a - left) Complex viscosity and (b - right) tanδ as a function of temperature for blends of C1-C4, c) gel point and sol point as a function of composition for C1-C4

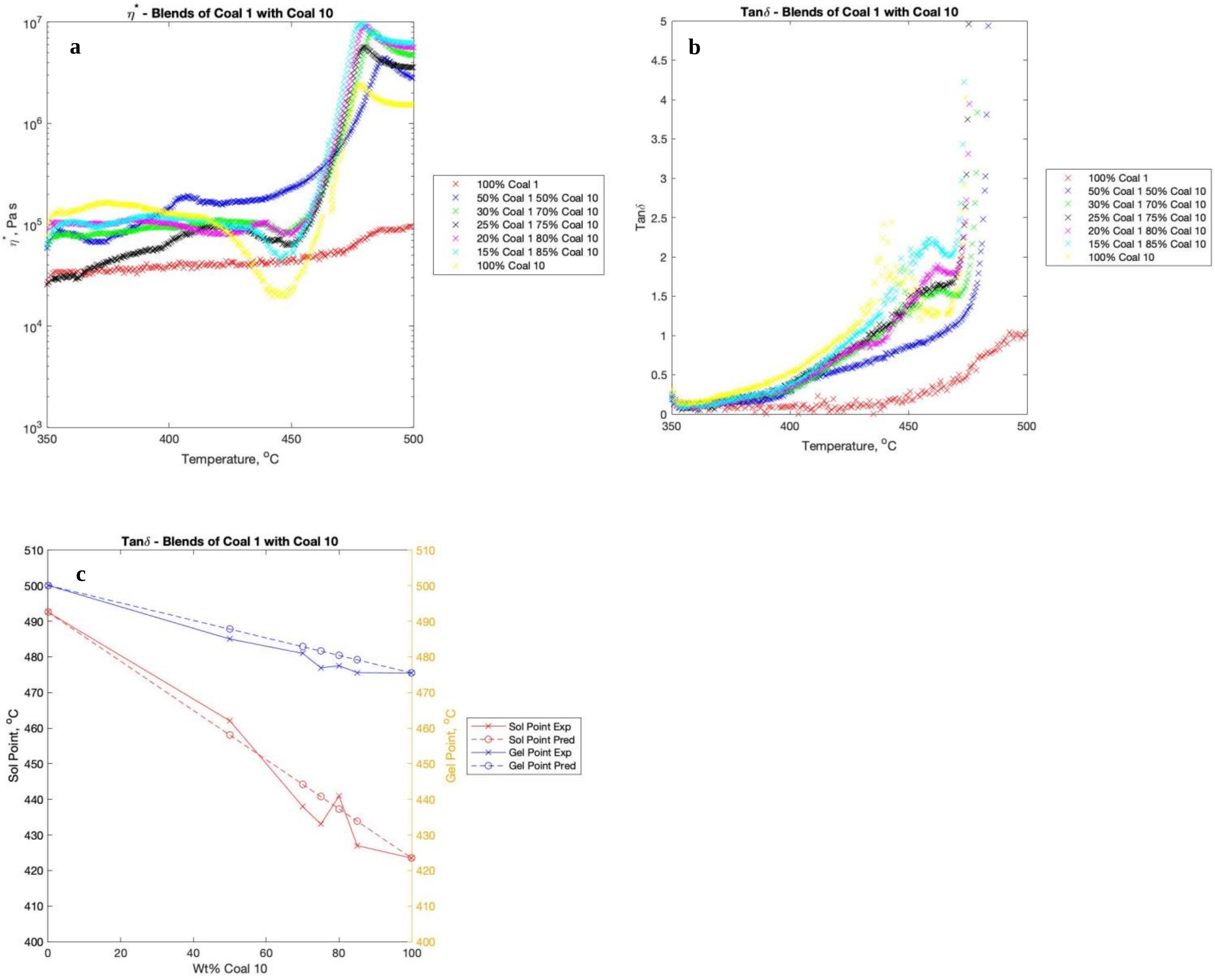

Figure C4: (a - left) Complex viscosity and (b - right) tanδ as a function of temperature for blends of C1-C10, c) gel point and sol point as a function of composition for C1-C10

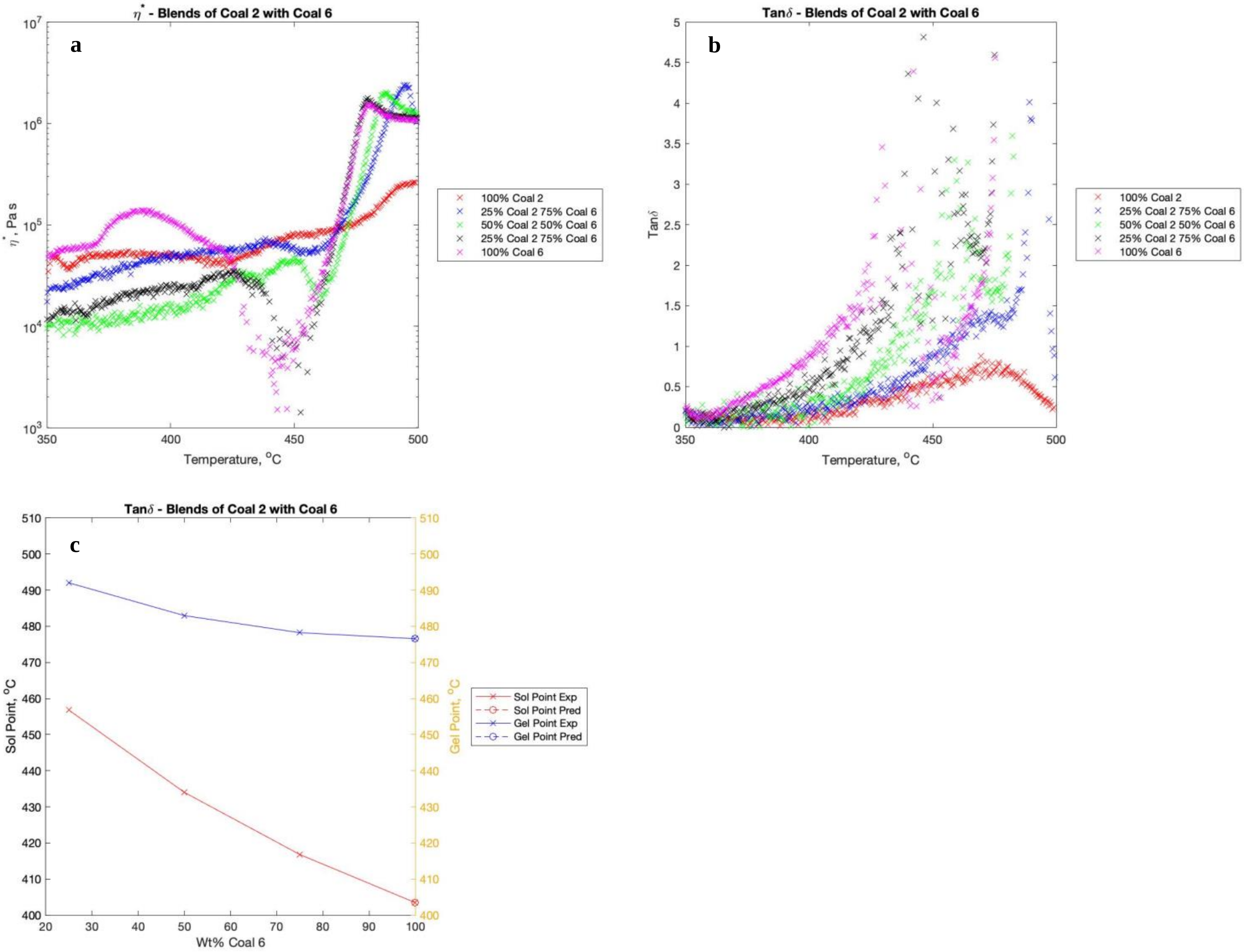

Figure C5: (a - left) Complex viscosity and (b - right) tanδ as a function of temperature for blends of C2-C6, c) gel point and sol point as a function of composition for C2-C6

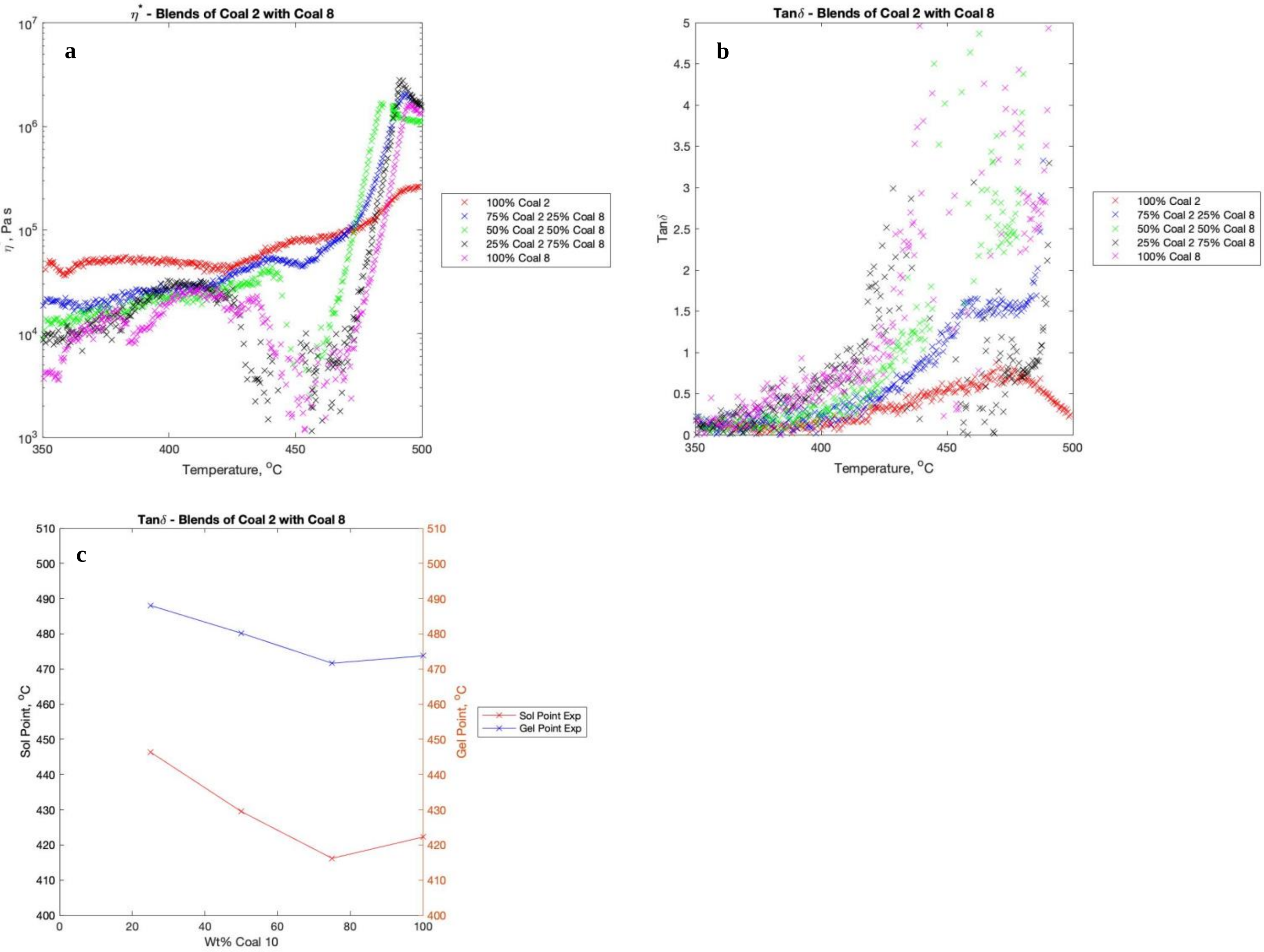

Figure C6: (a - left) Complex viscosity and (b - right) tanδ as a function of temperature for blends of C2-C8, c) gel point and sol point as a function of composition for C2-C8

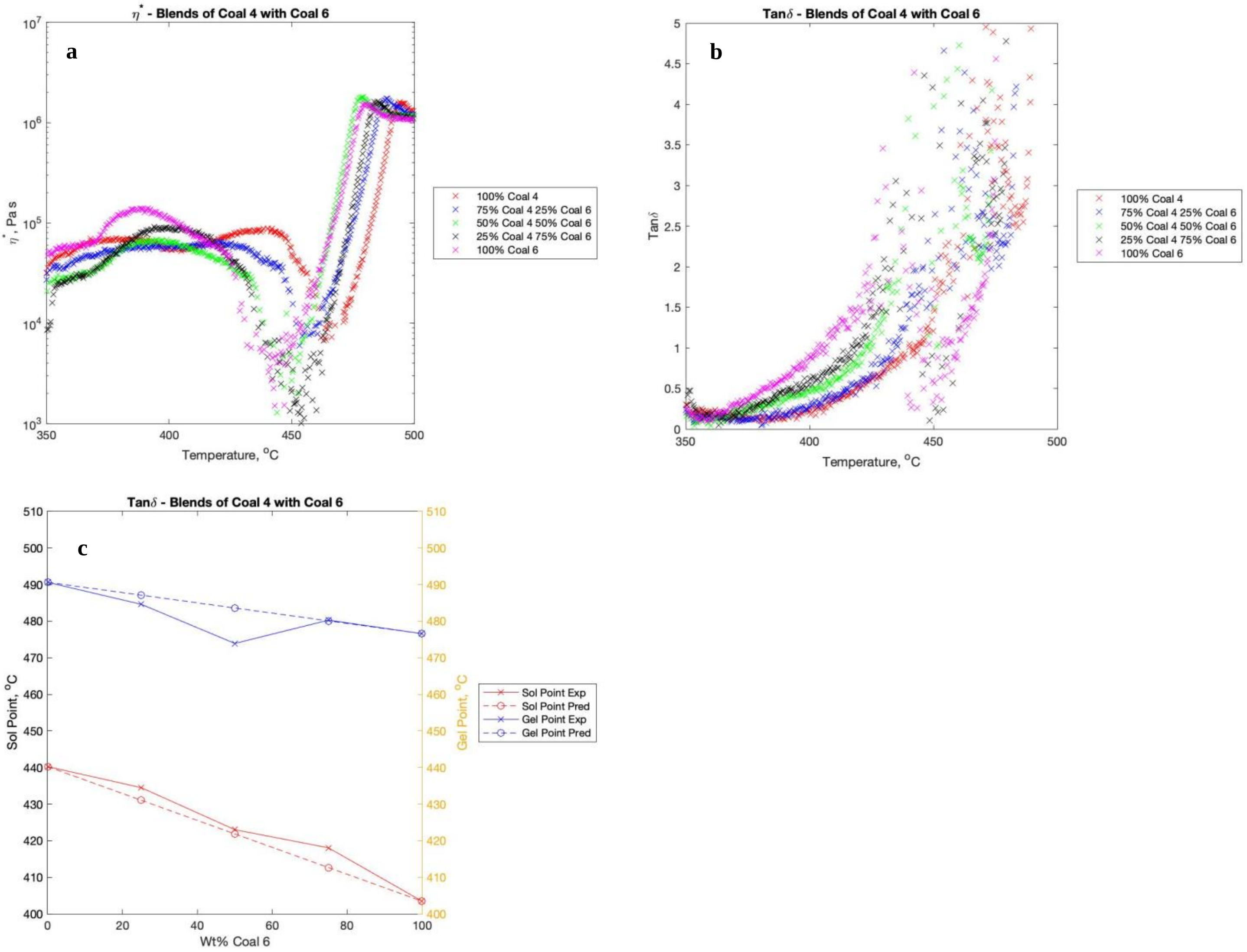

Figure C7: (a - left) Complex viscosity and (b - right) tanδ as a function of temperature for blends of C4-C6, c) gel point and sol point as a function of composition for C4-C6

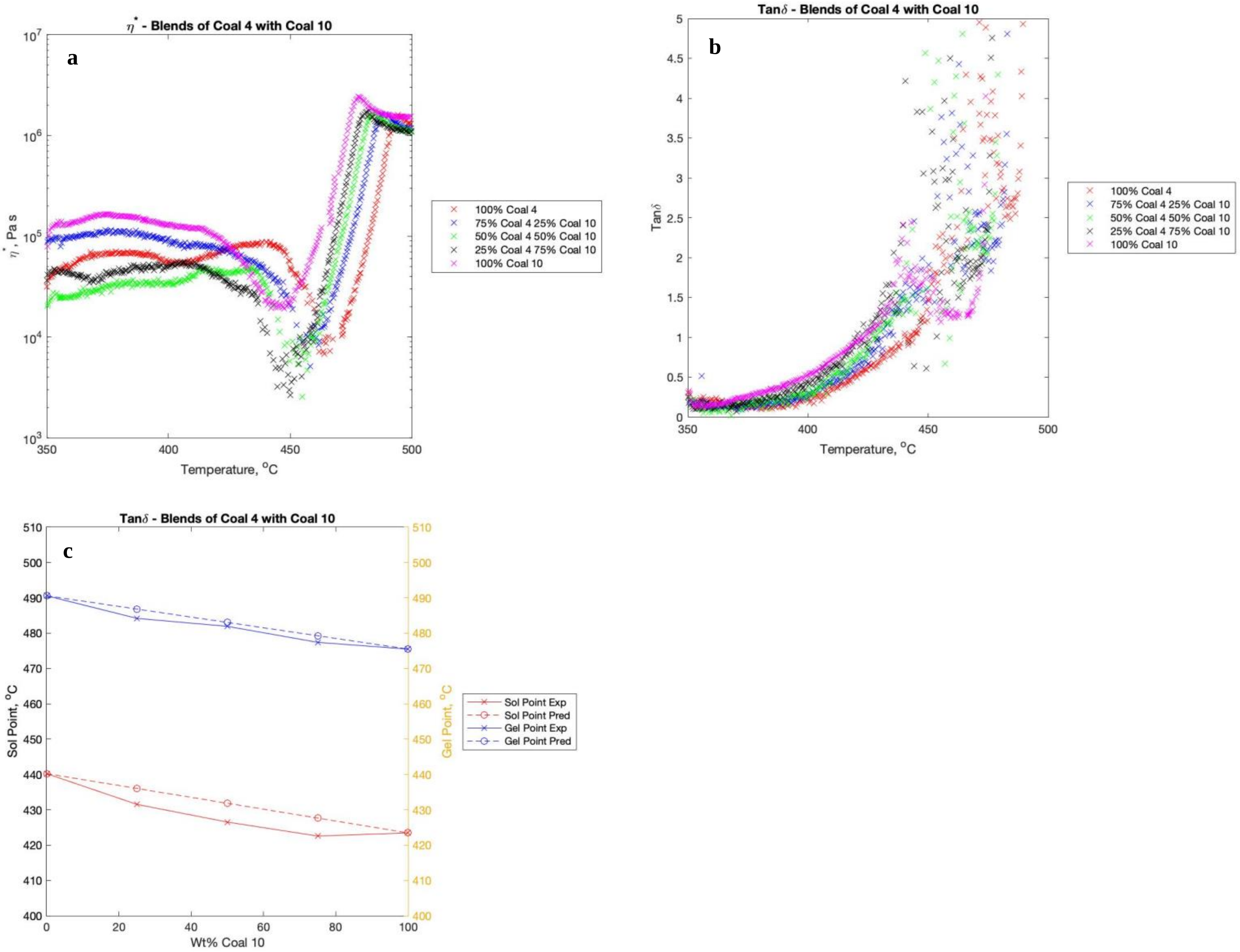

Figure C8: (a - left) Complex viscosity and (b - right) tanδ as a function of temperature for blends of C4-C10, c) gel point and sol point as a function of composition for C4-C10

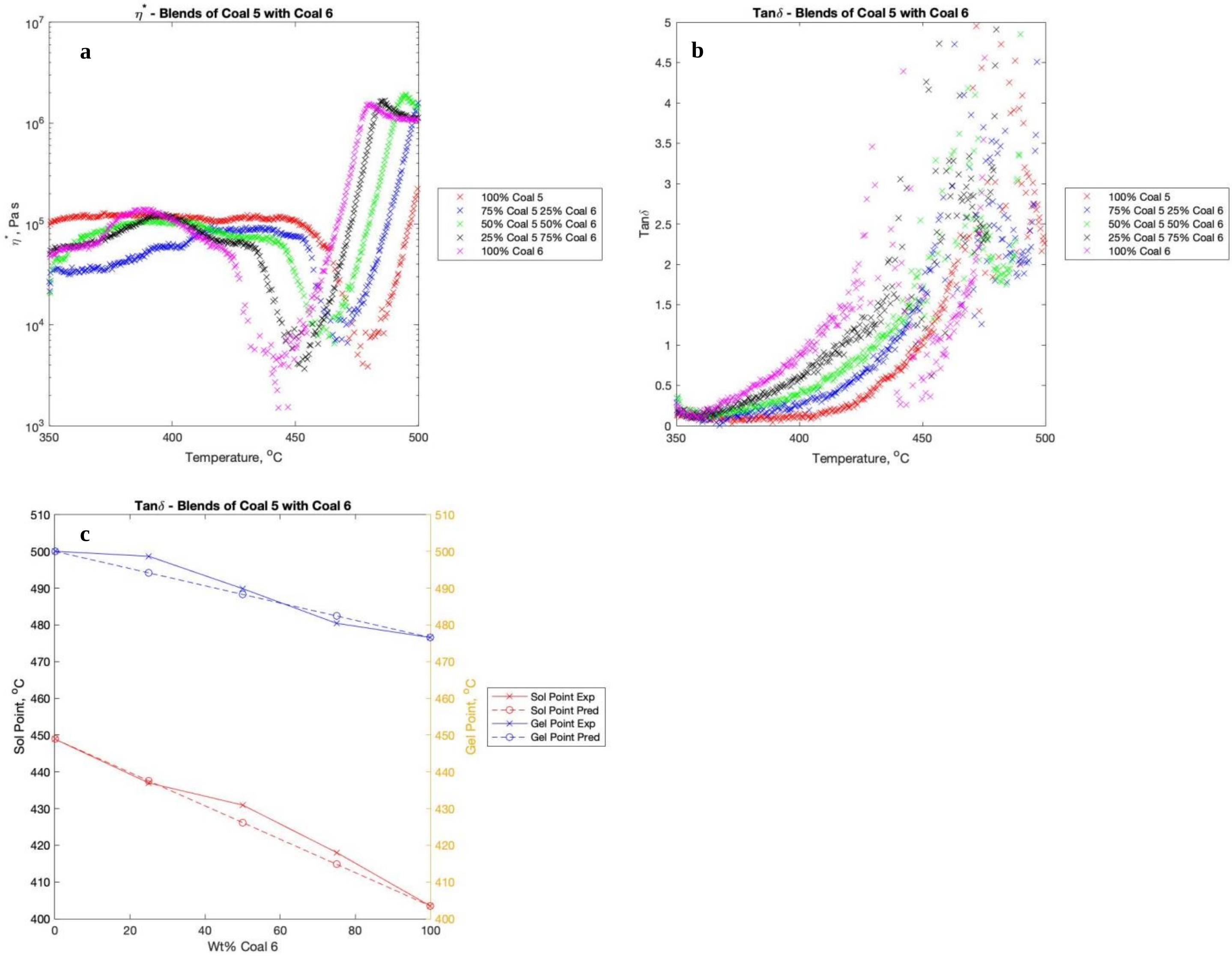

Figure C9: (a - left) Complex viscosity and (b - right) tanδ as a function of temperature for blends of C5-C6, c) gel point and sol point as a function of composition for C5-C6

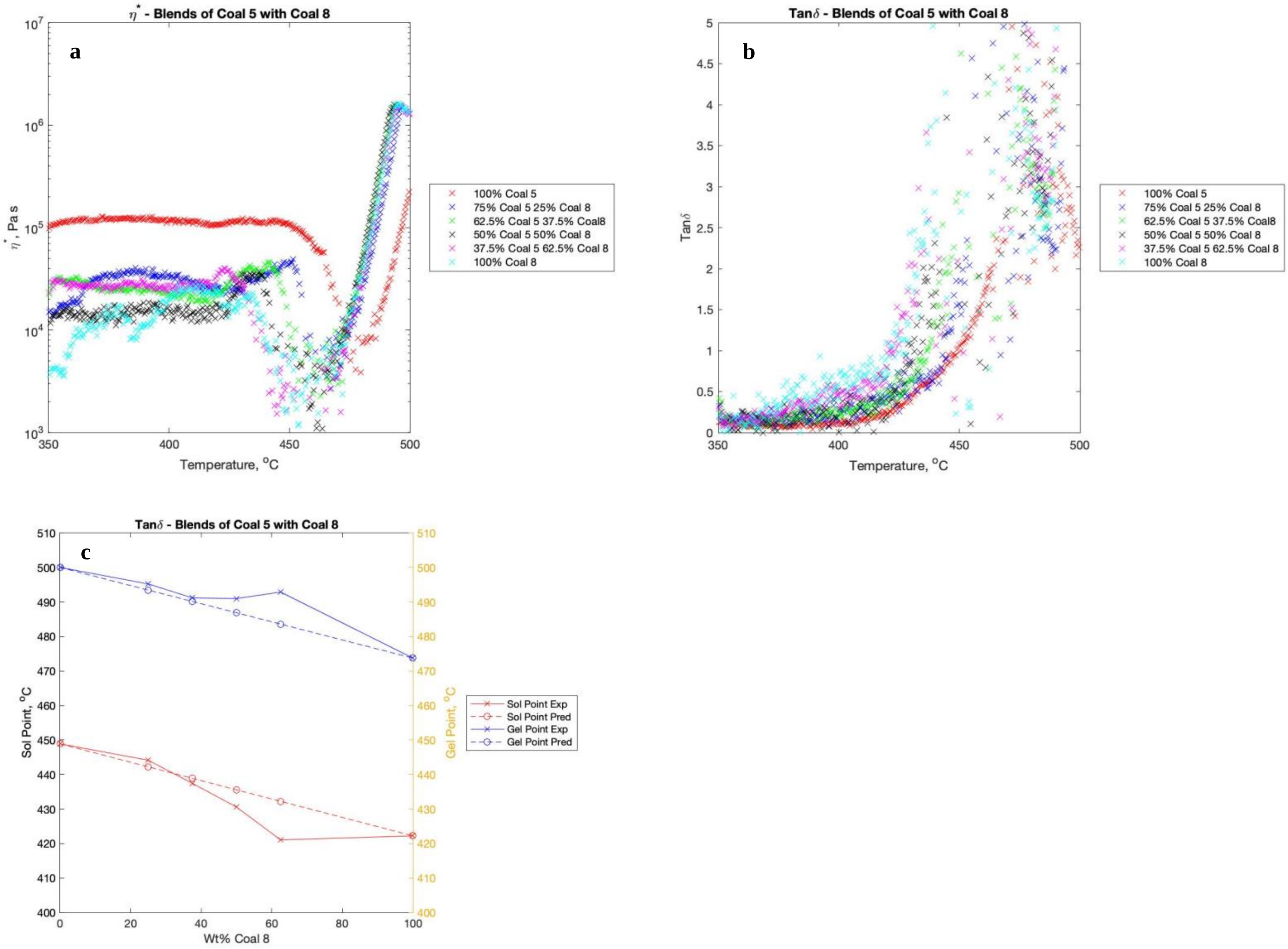

Figure C10: (a - left) Complex viscosity and (b - right) tanδ as a function of temperature for blends of C5-C8, c) gel point and sol point as a function of composition for C5-C8

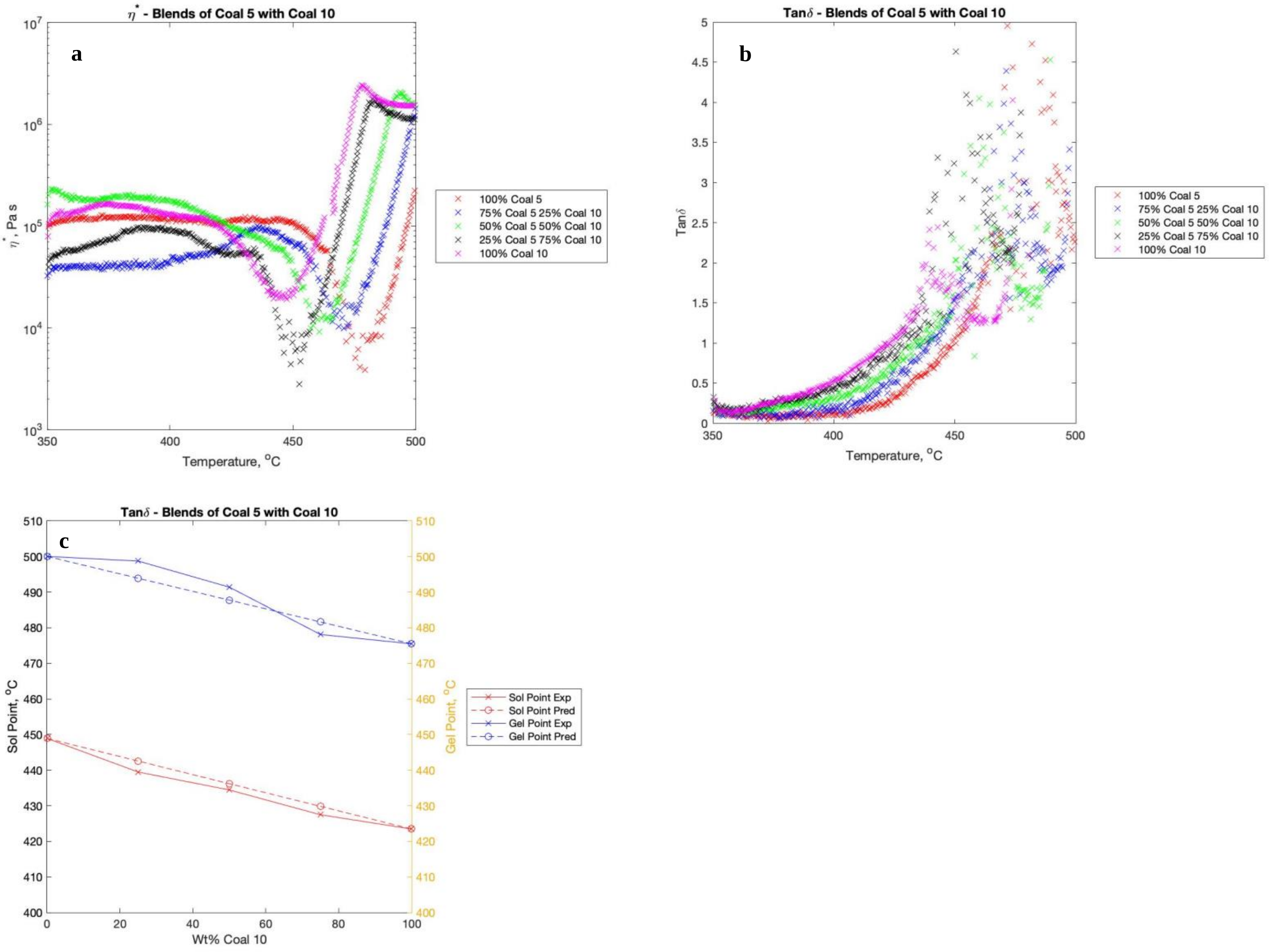

Figure C11: (a - left) Complex viscosity and (b - right) tanδ as a function of temperature for blends of C5-C10, c) gel point and sol point as a function of composition for C5-C10

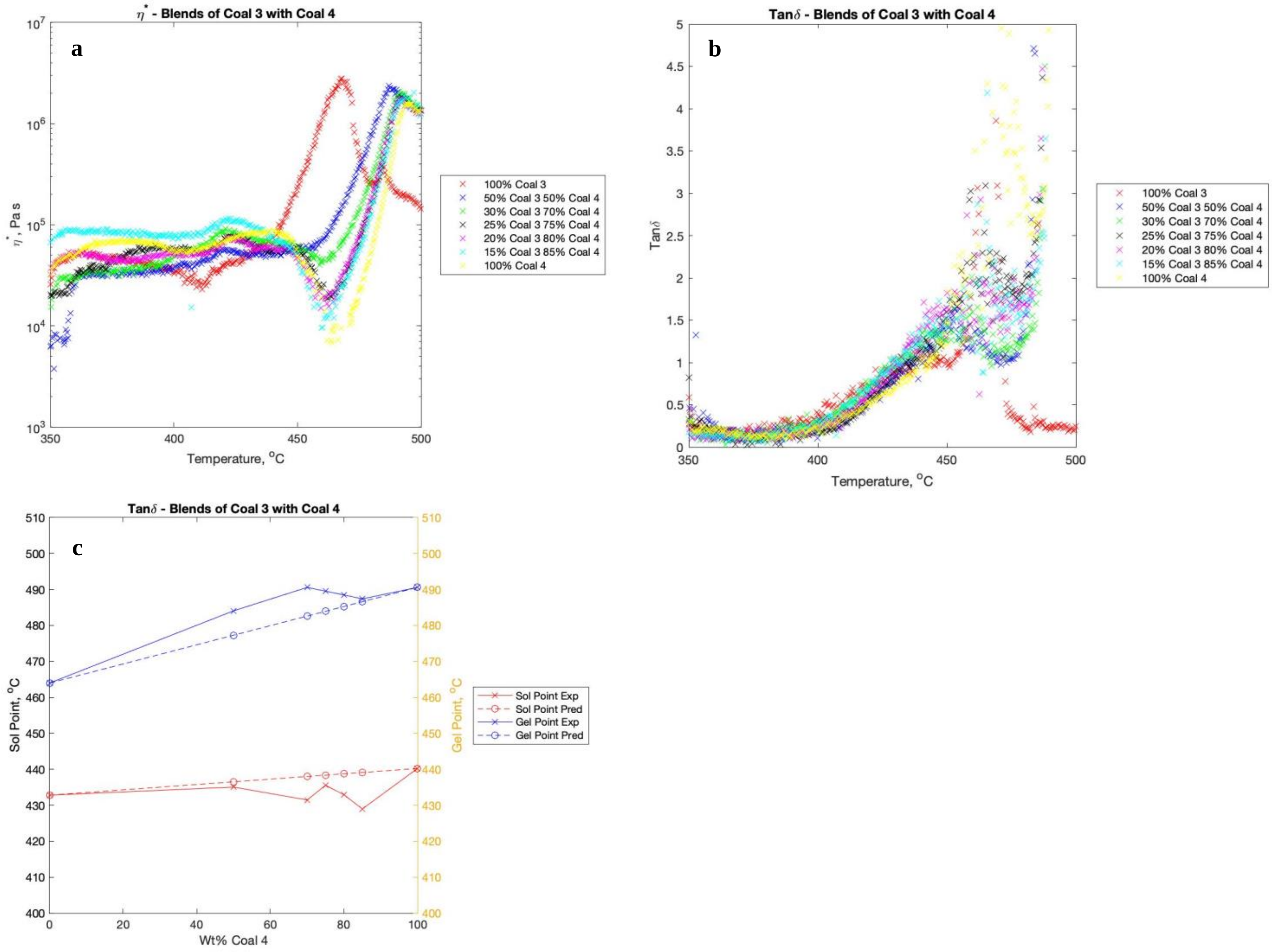

Figure C12: (a - left) Complex viscosity and (b - right) tanδ as a function of temperature for blends of C3-C4, c) gel point and sol point as a function of composition for C3-C4

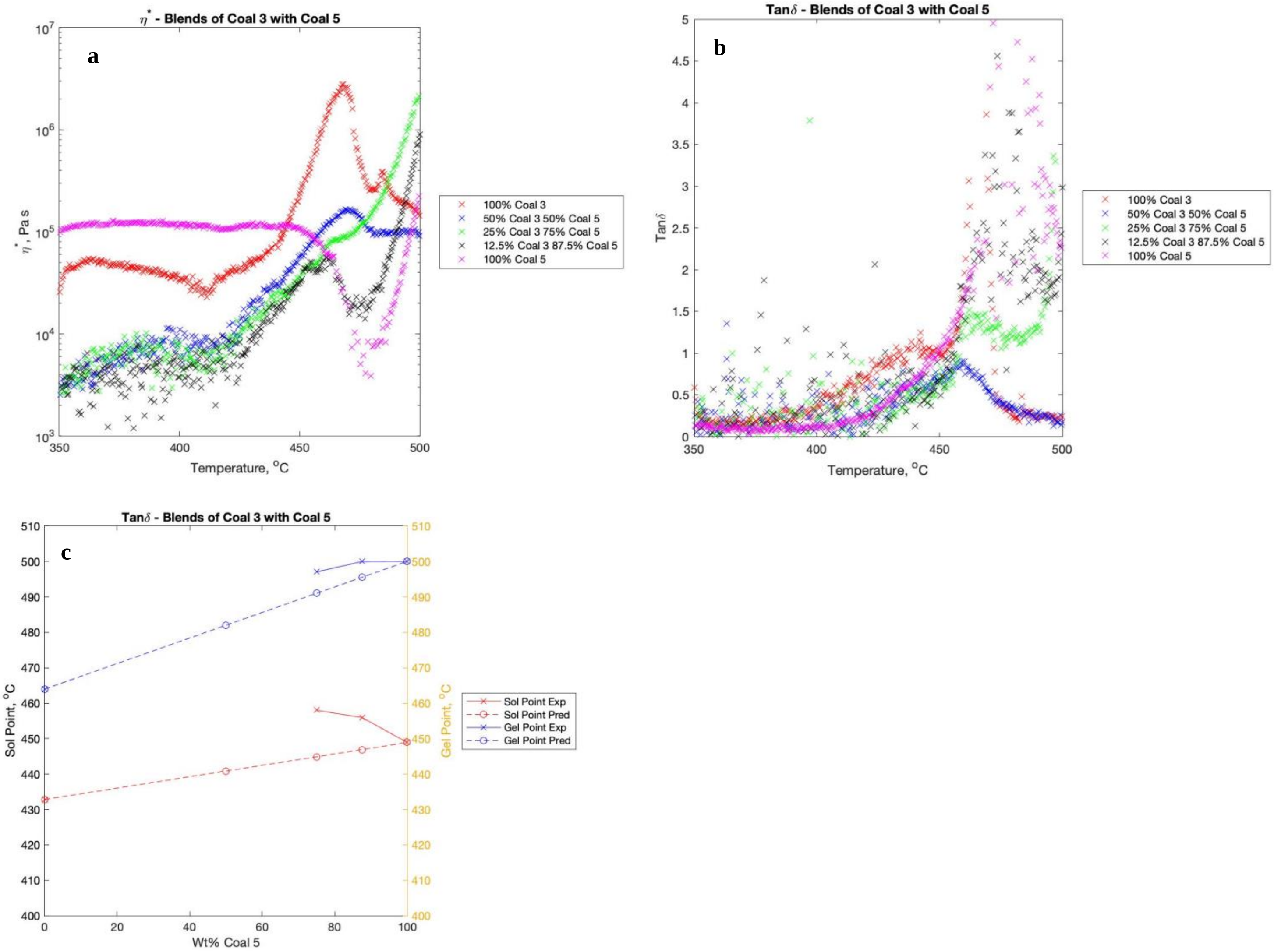

Figure C13: (a - left) Complex viscosity and (b - right) tanδ as a function of temperature for blends of C3-C5, c) gel point and sol point as a function of composition for C3-C5

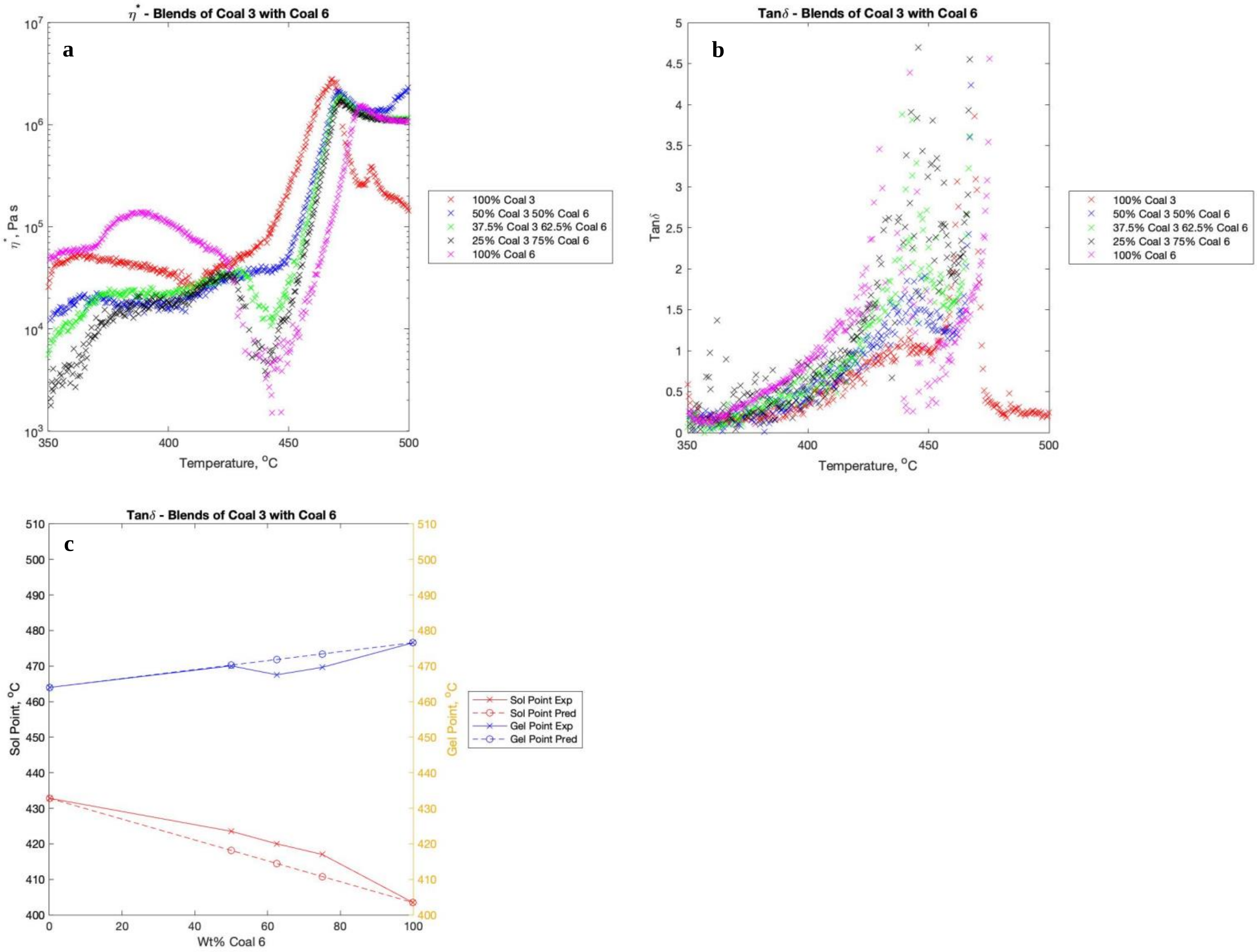

Figure C14: (a - left) Complex viscosity and (b - right) tanδ as a function of temperature for blends of C3-C6, c) gel point and sol point as a function of composition for C3-C6

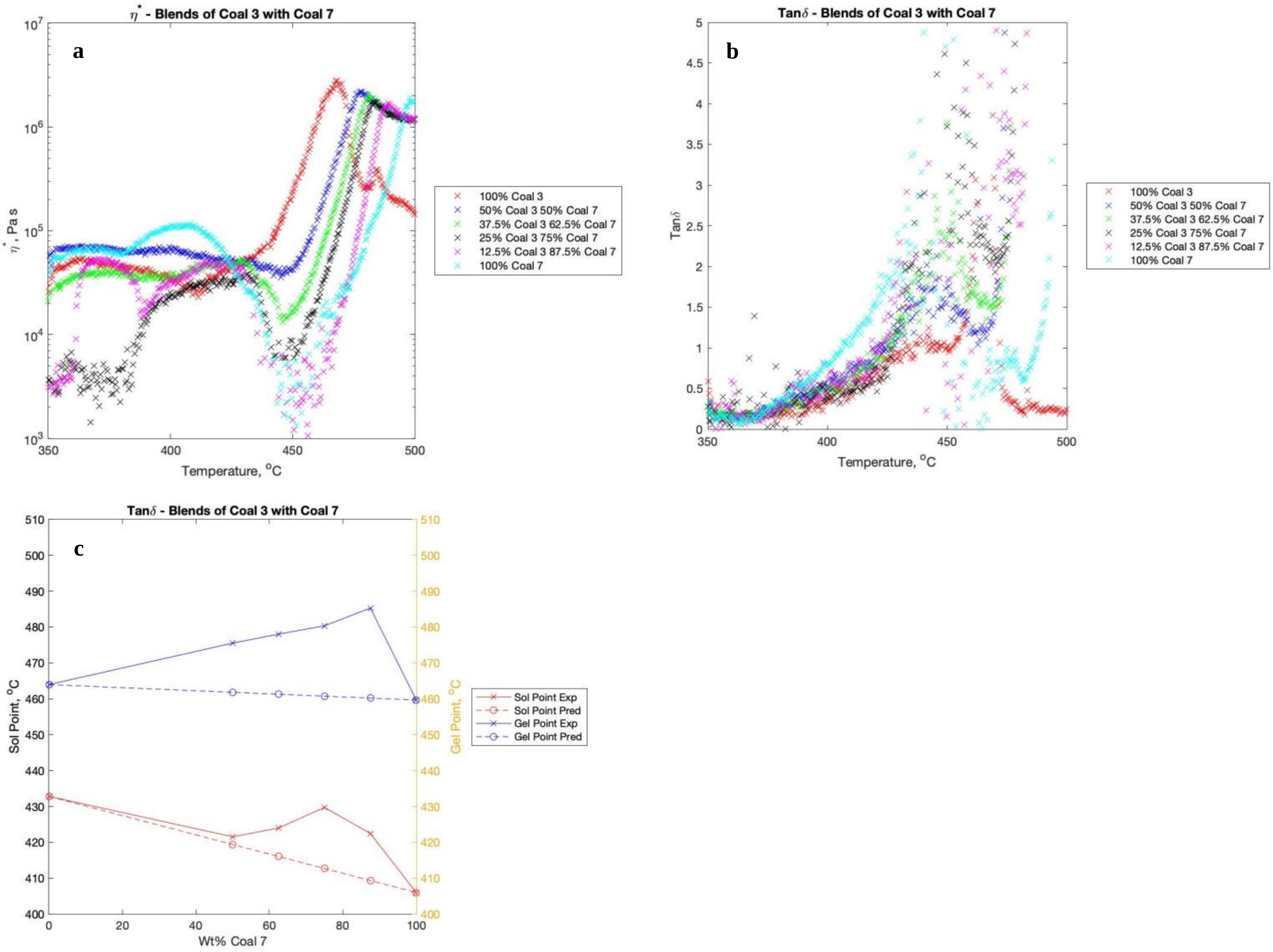

Figure C15: (a - left) Complex viscosity and (b - right) tanδ as a function of temperature for blends of C3-C7, c) gel point and sol point as a function of composition for C3-C7

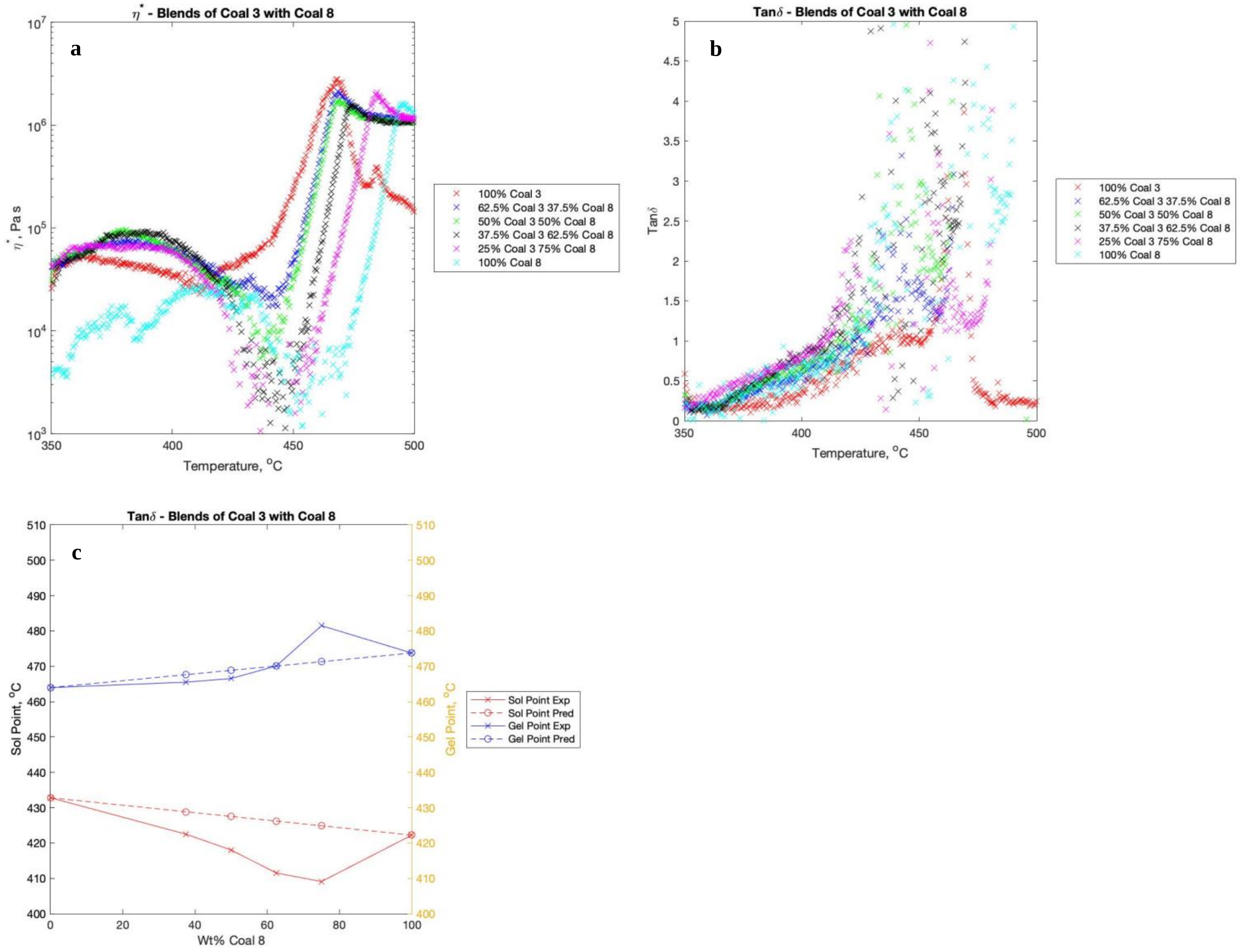

Figure C16: (a - left) Complex viscosity and (b - right) tanδ as a function of temperature for blends of C3-C8, c) gel point and sol point as a function of composition for C3-C8

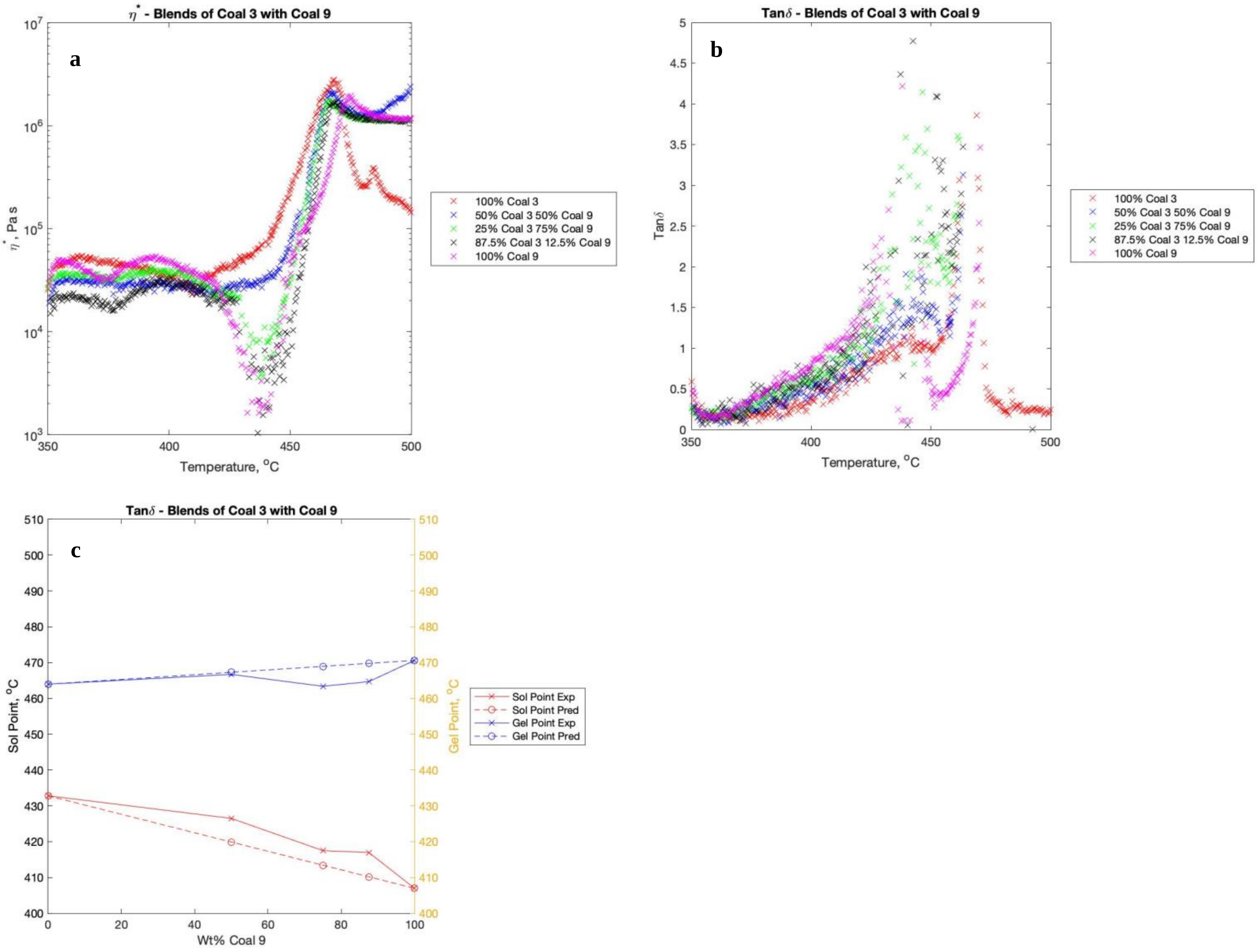

Figure C17: (a - left) Complex viscosity and (b - right) tanδ as a function of temperature for blends of C3-C9, c) gel point and sol point as a function of composition for C3-C9

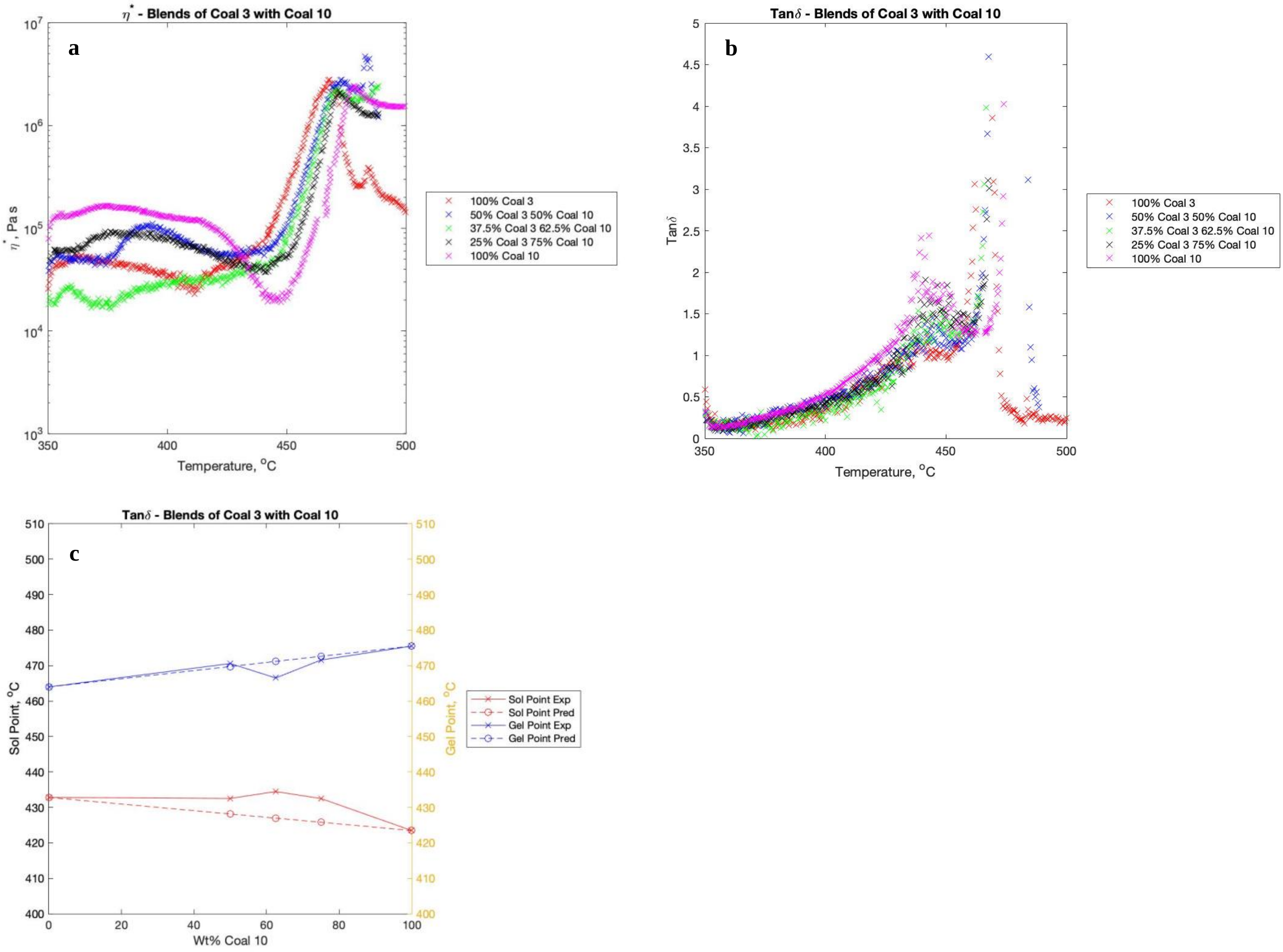

Figure C18: (a - left) Complex viscosity and (b - right) tanδ as a function of temperature for blends of C3-C10, c) gel point and sol point as a function of composition for C3-C10

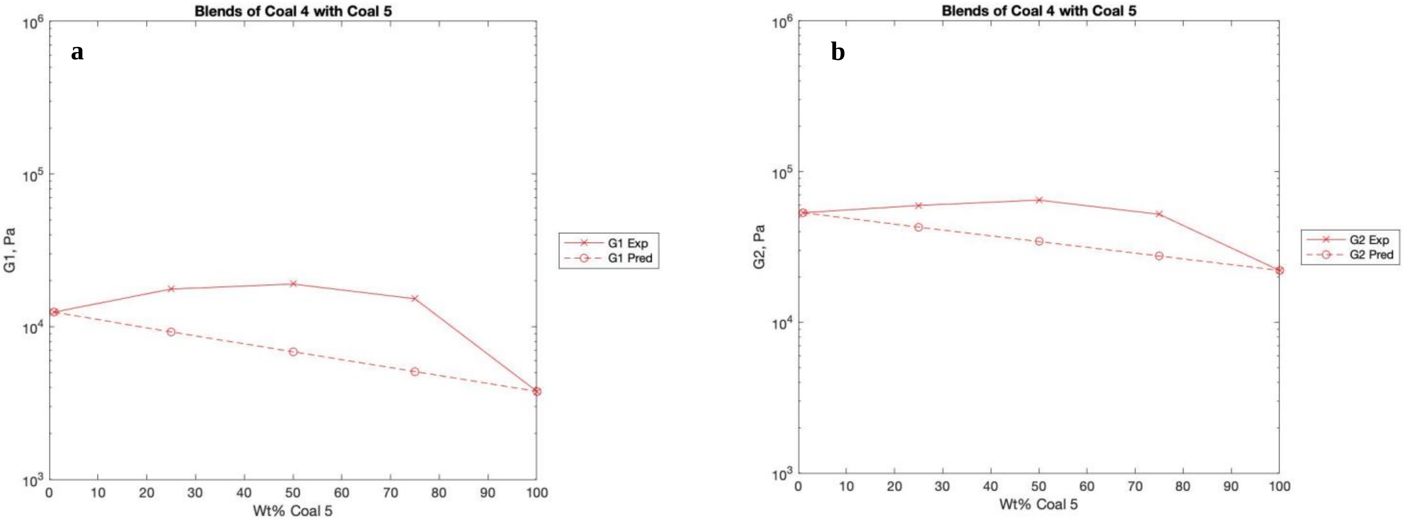

Figure C19: Minimum G' (a - left) and minimum G'' (b - right) as a function of composition for blends of C4-C5.

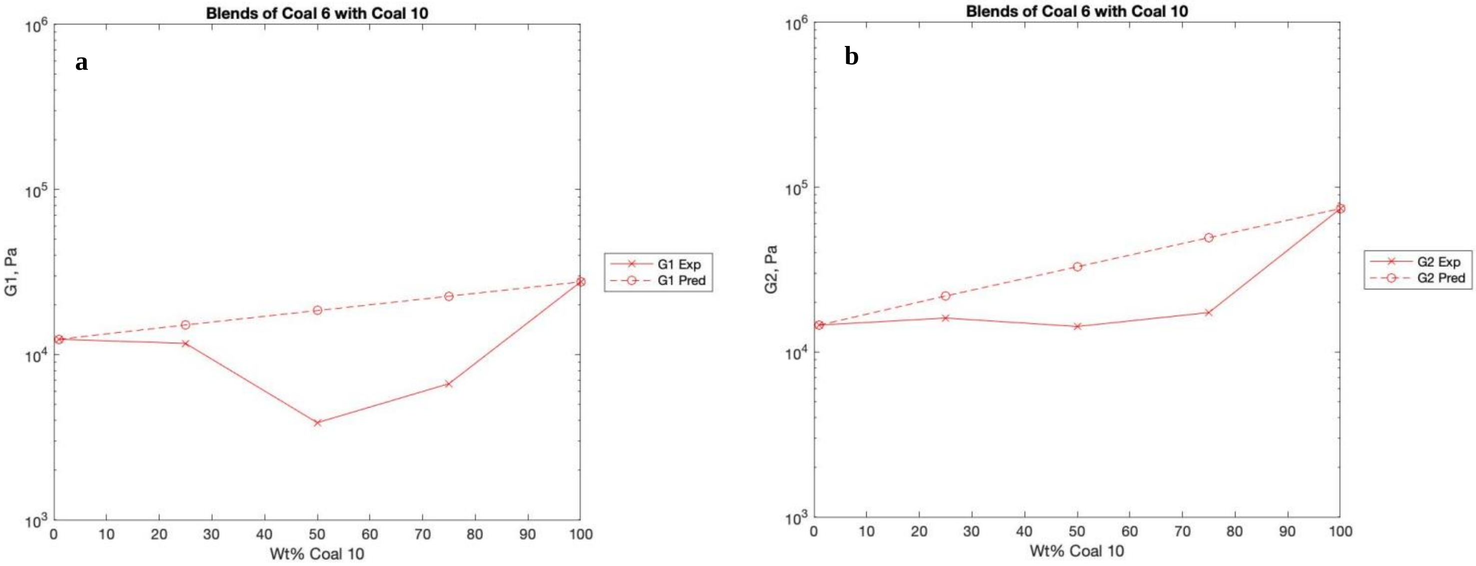

Figure C20: Minimum G' (a - left) and minimum G'' (b - right) as a function of composition for blends of C6-C10

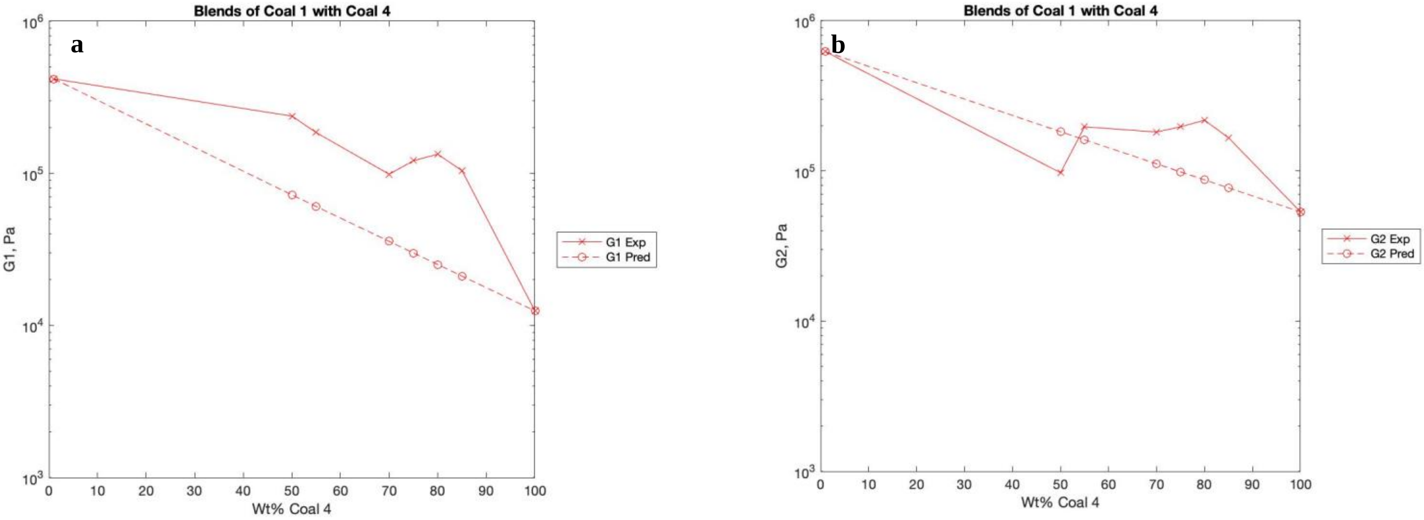

Figure C21: Minimum G' (a - left) and minimum G" (b - right) as a function of composition for blends of C1-C4

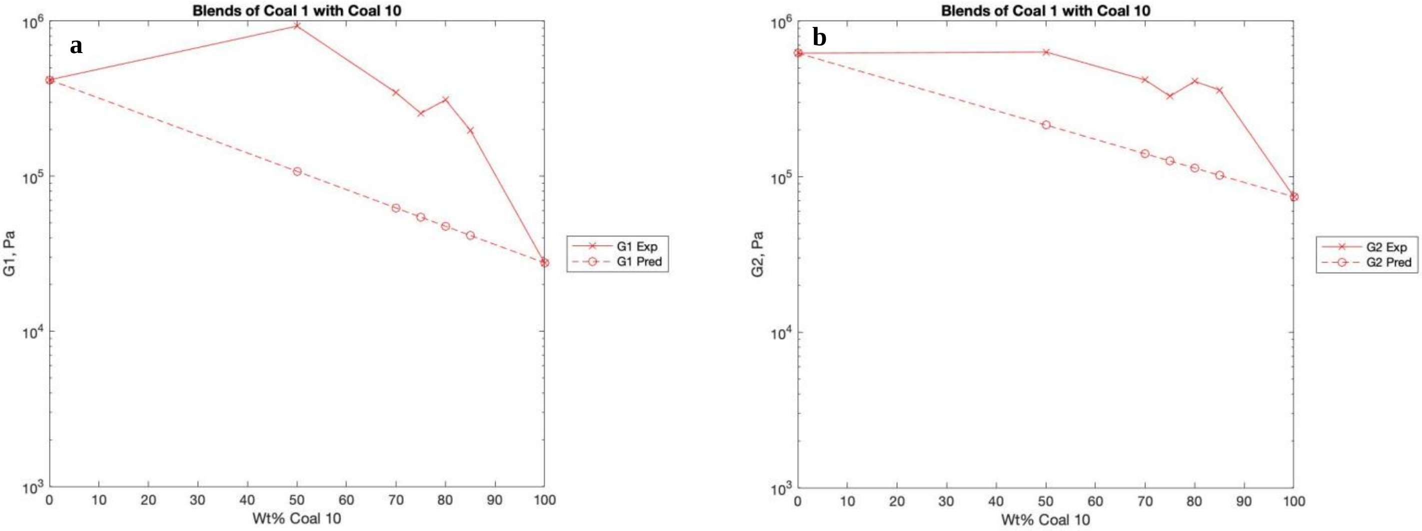

Figure C22: Minimum G' (a - left) and minimum G" (b - right) as a function of composition for blends of C1-10

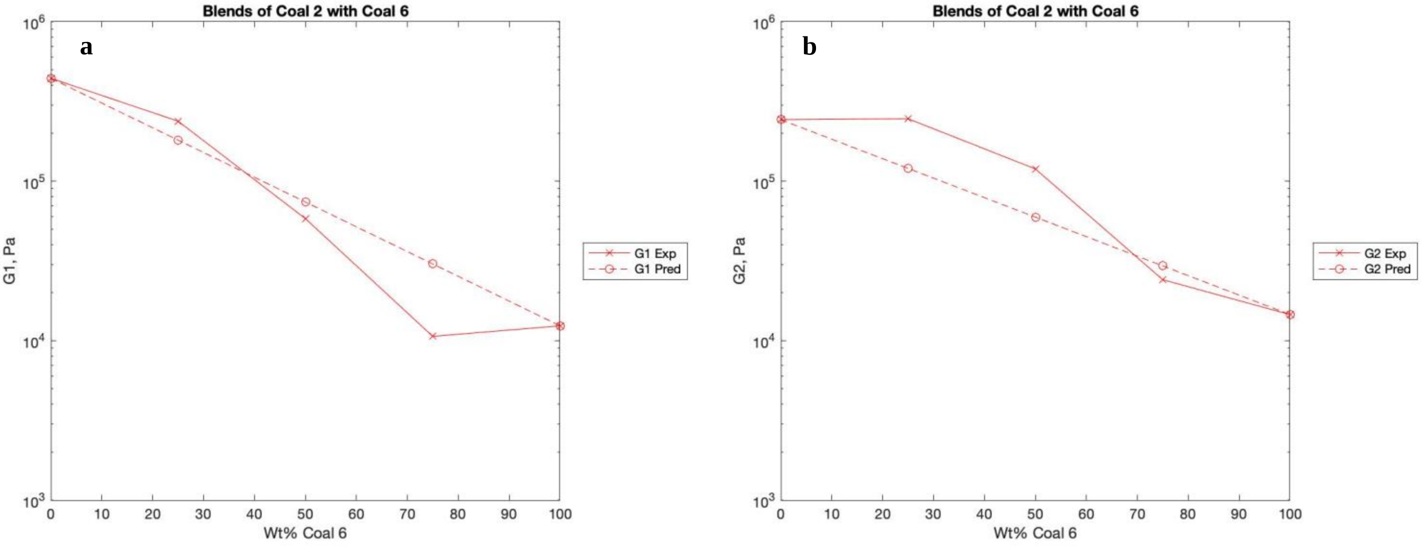

Figure C23: Minimum G' (a - left) and minimum G" (b - right) as a function of composition for blends of C2-C6

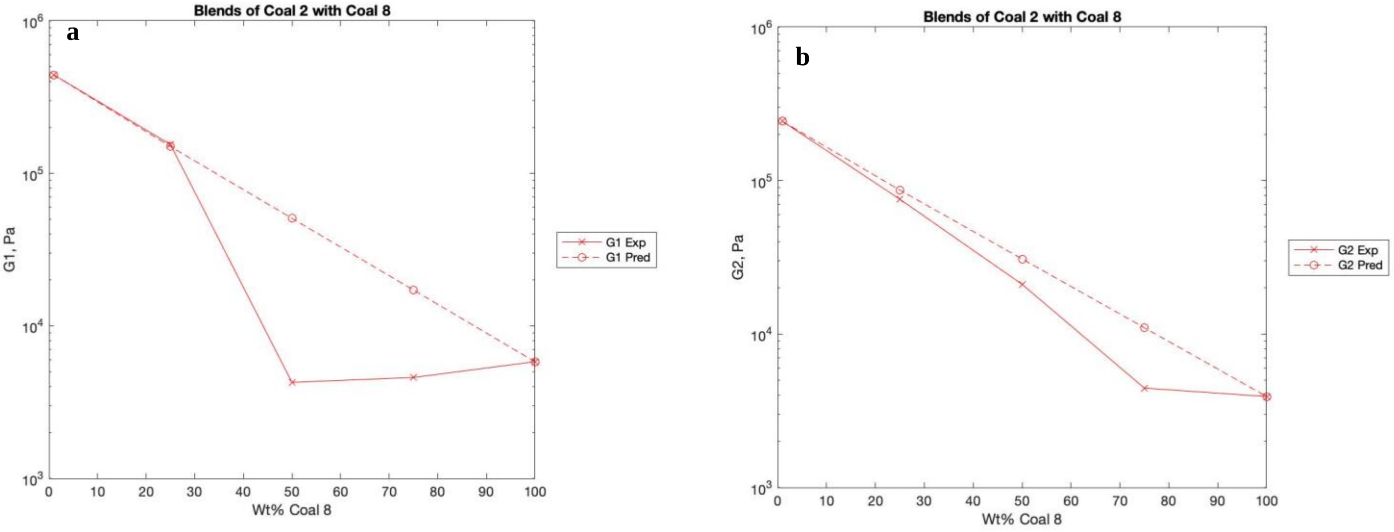

Figure C24: Minimum G' (a - left) and minimum G" (b - right) as a function of composition for blends of C2-C8

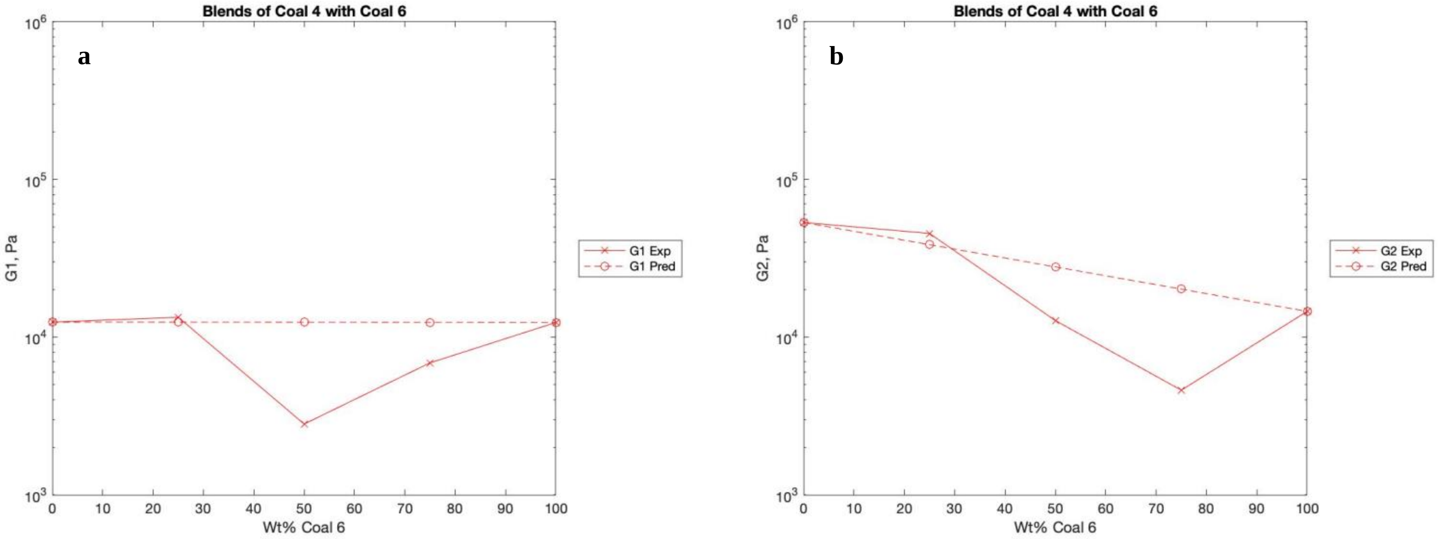

Figure C25: Minimum G' (a - left) and minimum G" (b - right) as a function of composition for blends of C4-C6

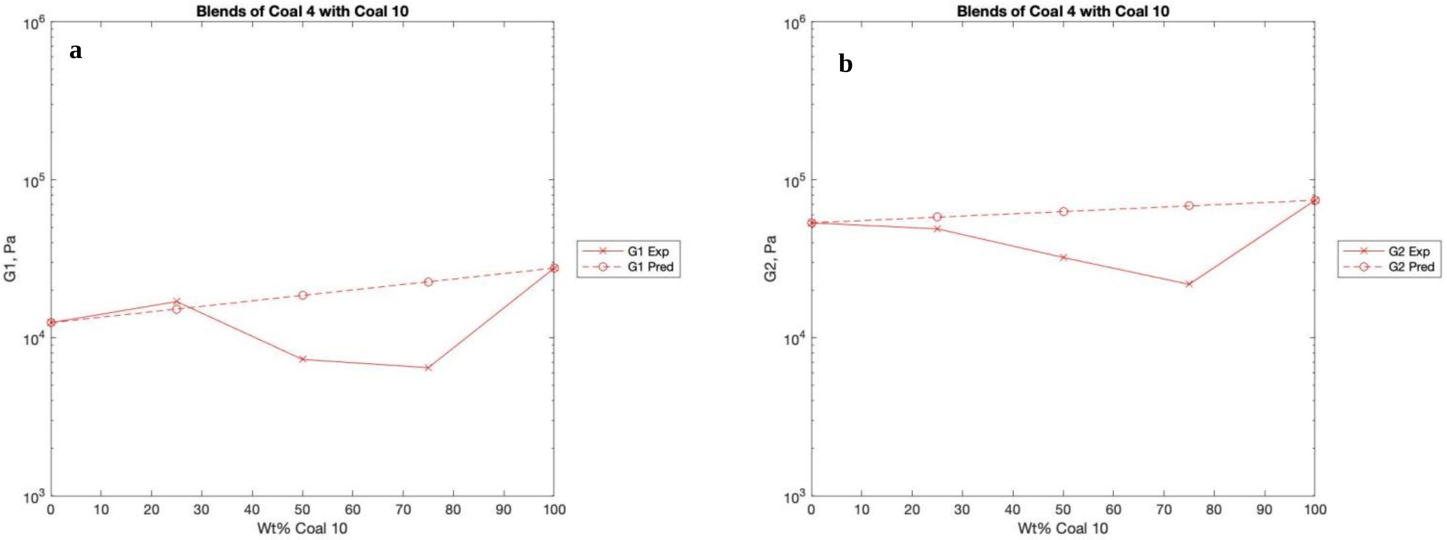

Figure C26: Minimum G' (a - left) and minimum G" (b - right) as a function of composition for blends of C4-C10

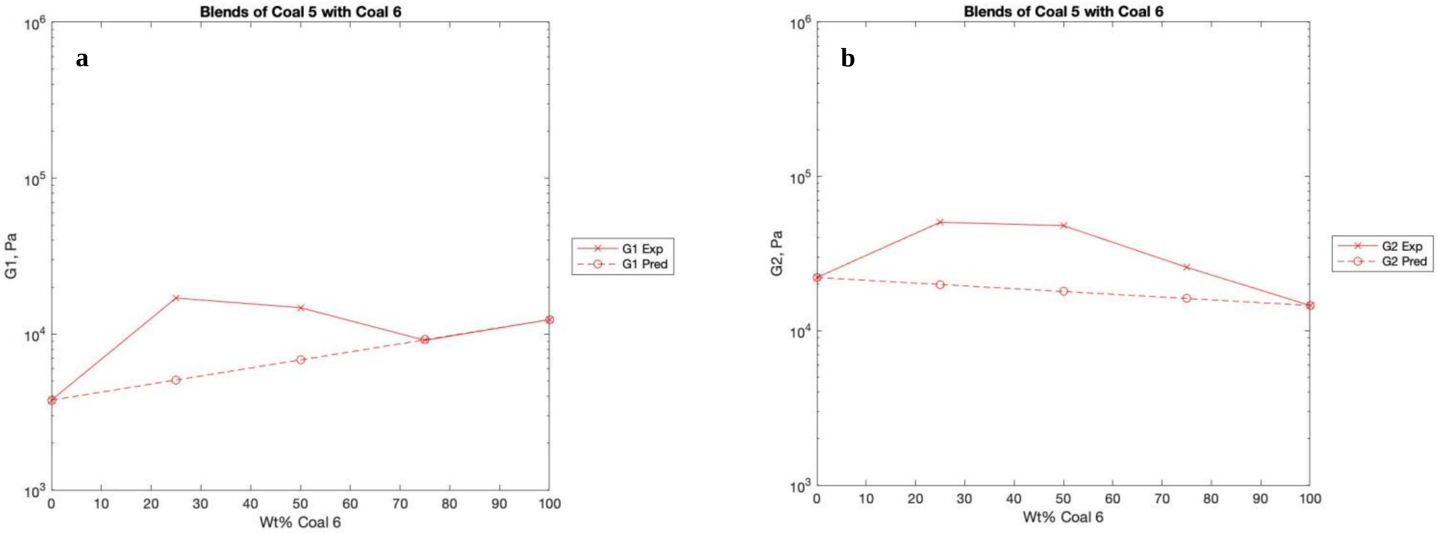

Figure C27: Minimum G' (a - left) and minimum G" (b - right) as a function of composition for blends of C5-C6

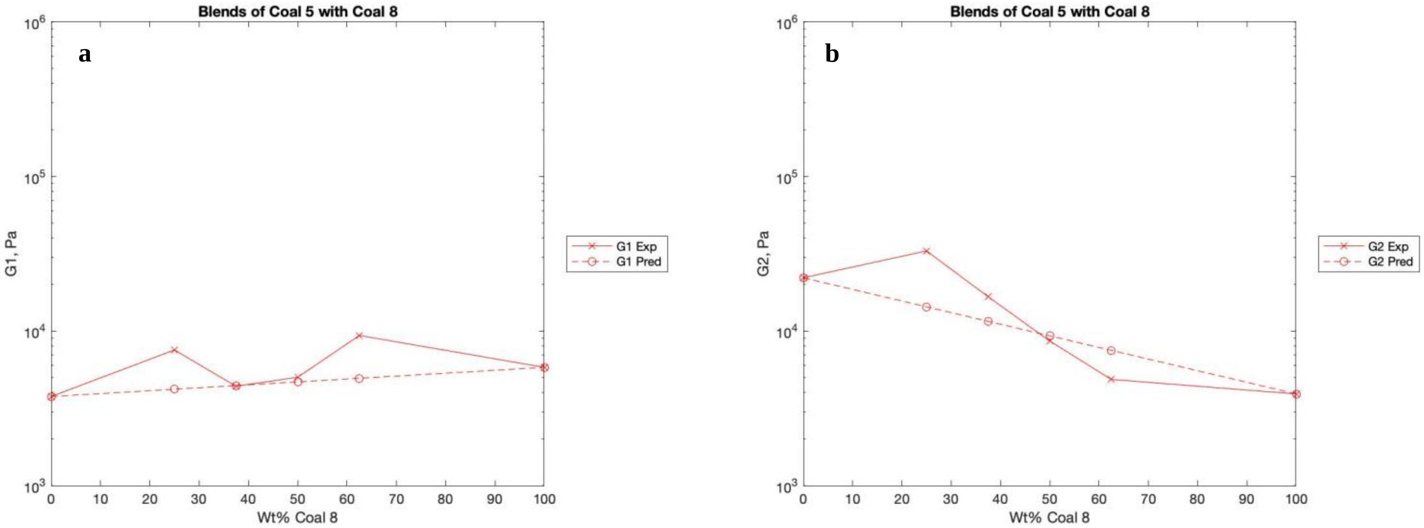

Figure C28: Minimum G' (a - left) and minimum G" (b - right) as a function of composition for blends of C5-C8

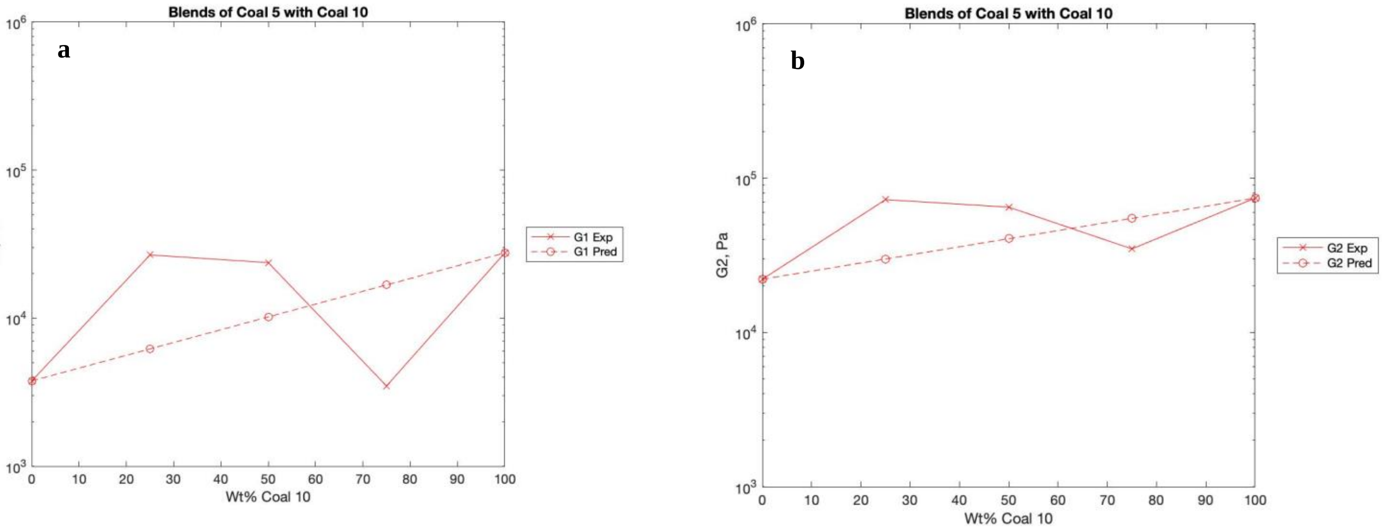

Figure C29: Minimum G' (a - left) and minimum G'' (b - right) as a function of composition for blends of C5-C10

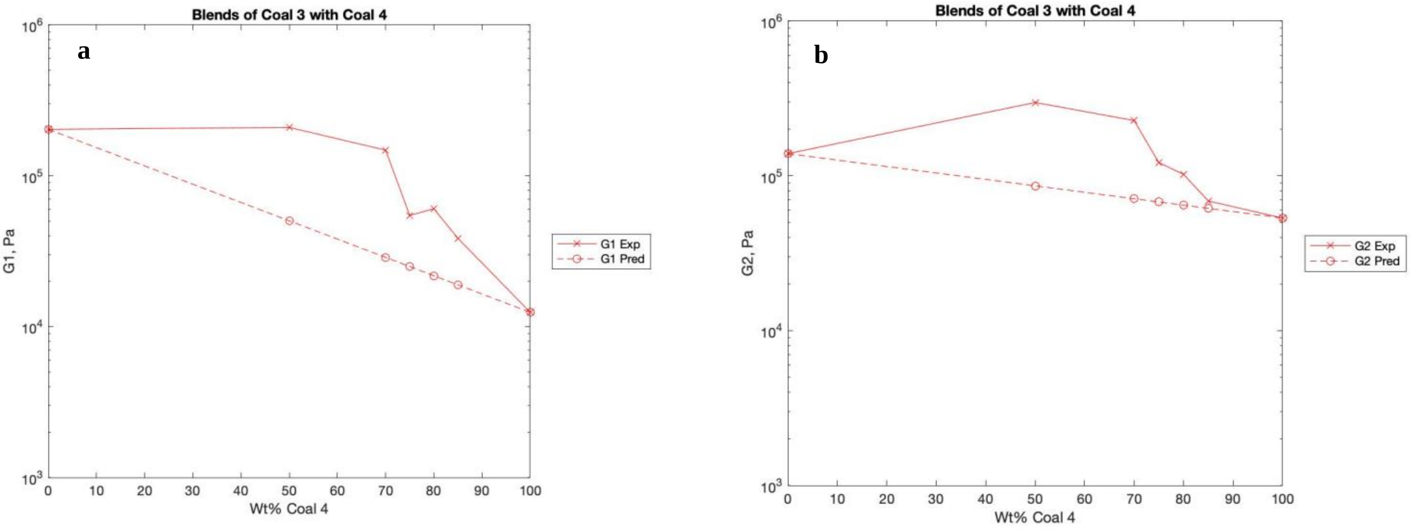

Figure C30: Minimum G' (a - left) and minimum G'' (b - right) as a function of composition for blends of C3-C4

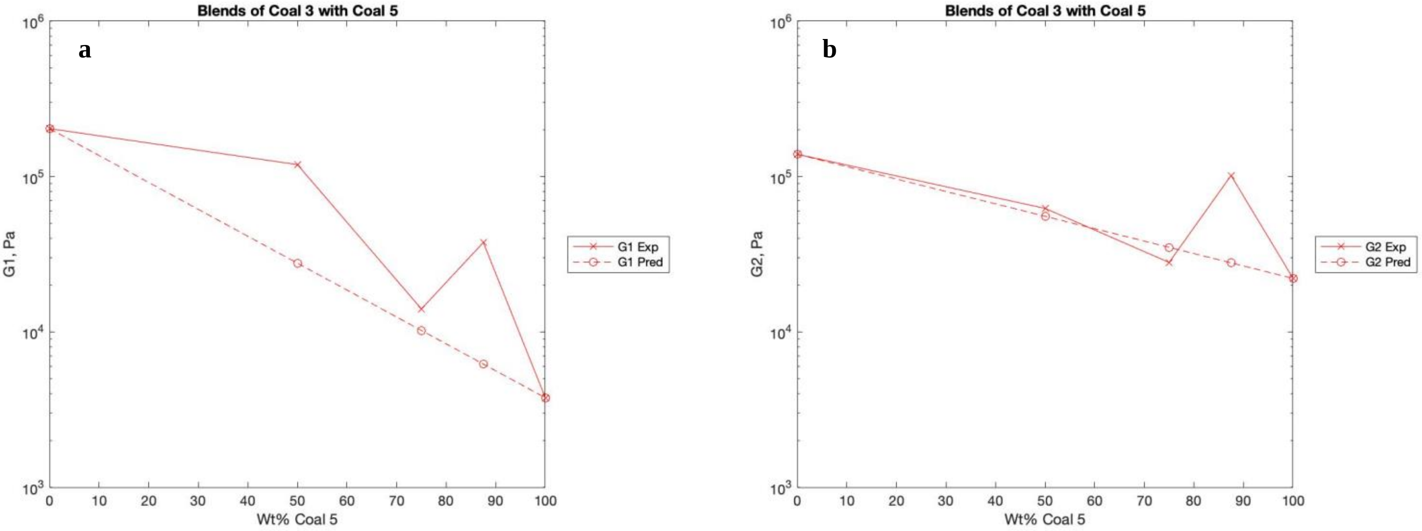

Figure C31: Minimum G' (a - left) and minimum G" (b - right) as a function of composition for blends of C3-C5

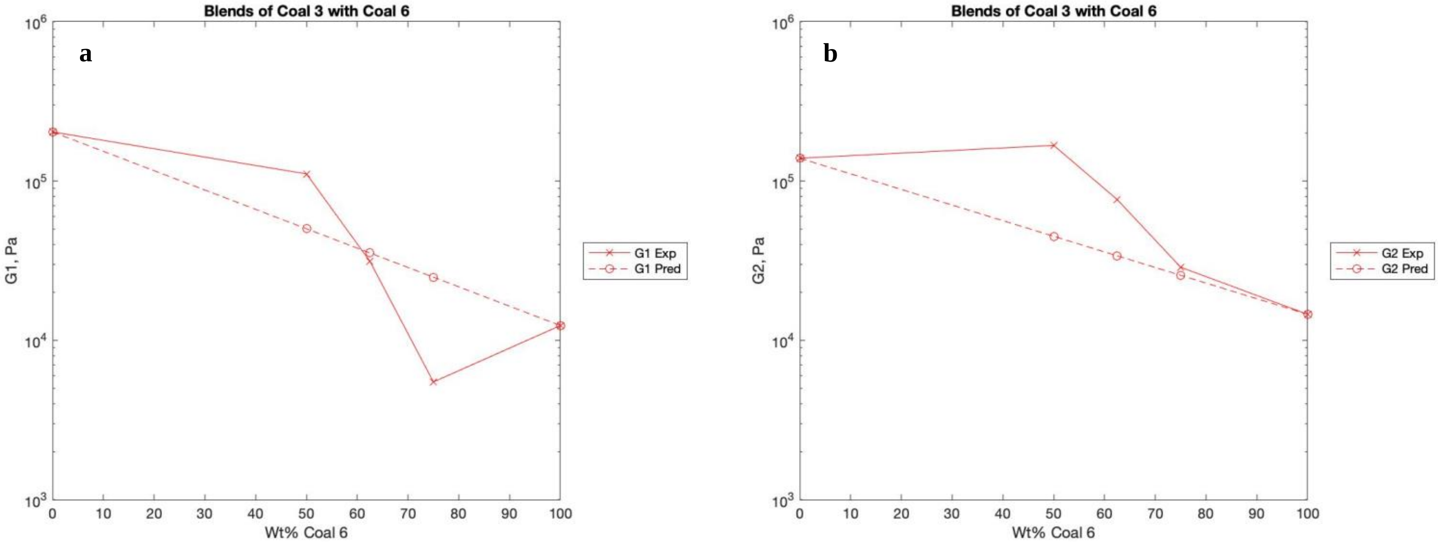

Figure C32: Minimum G' (a - left) and minimum G" (b - right) as a function of composition for blends of C3-C6

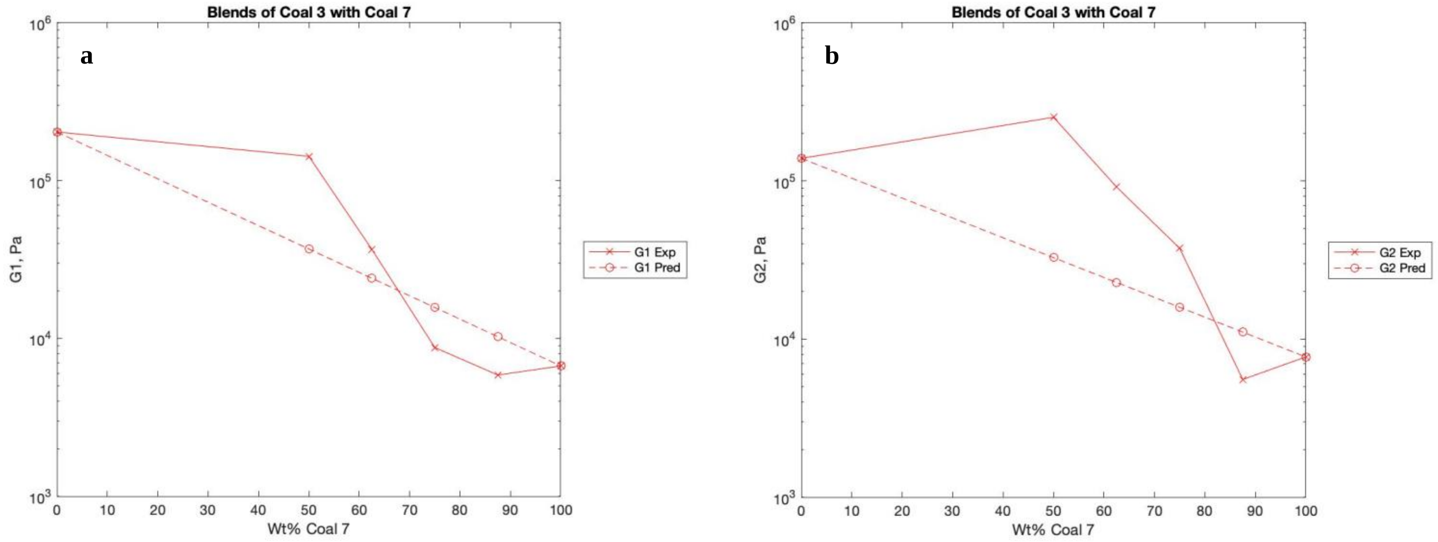

Figure C33: Minimum G' (a - left) and minimum G" (b - right) as a function of composition for blends of C3-C7

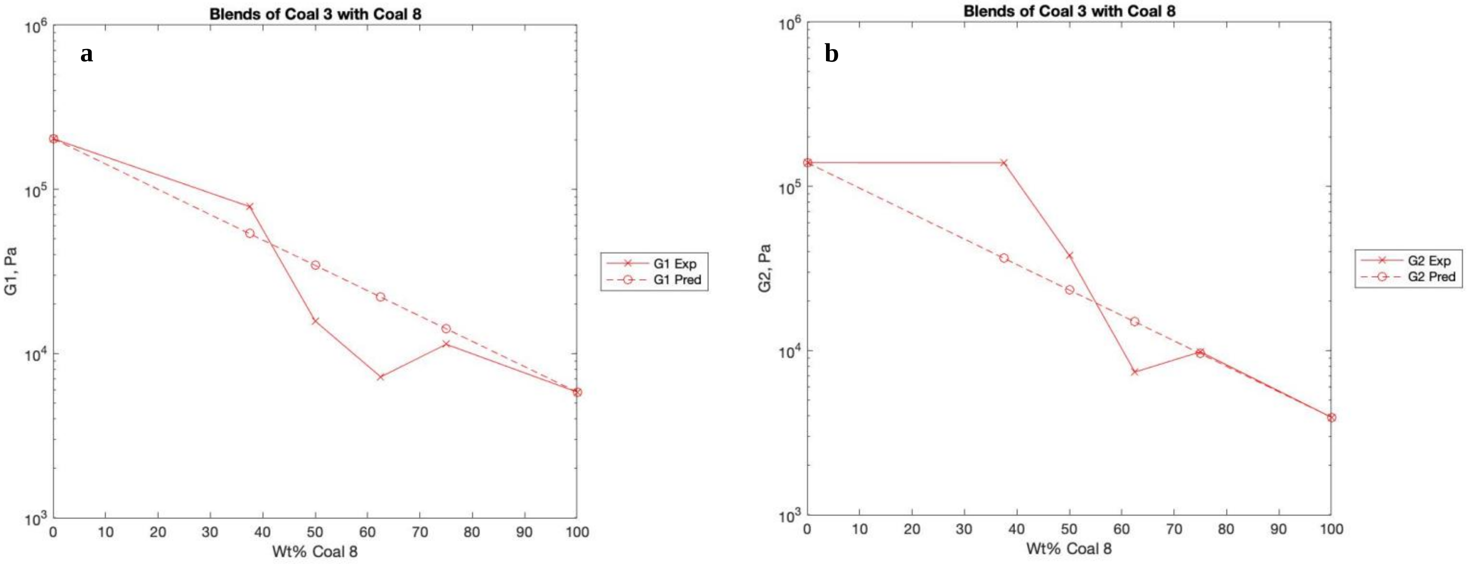

Figure C34: Minimum G' (a - left) and minimum G" (b - right) as a function of composition for blends of C3-C8

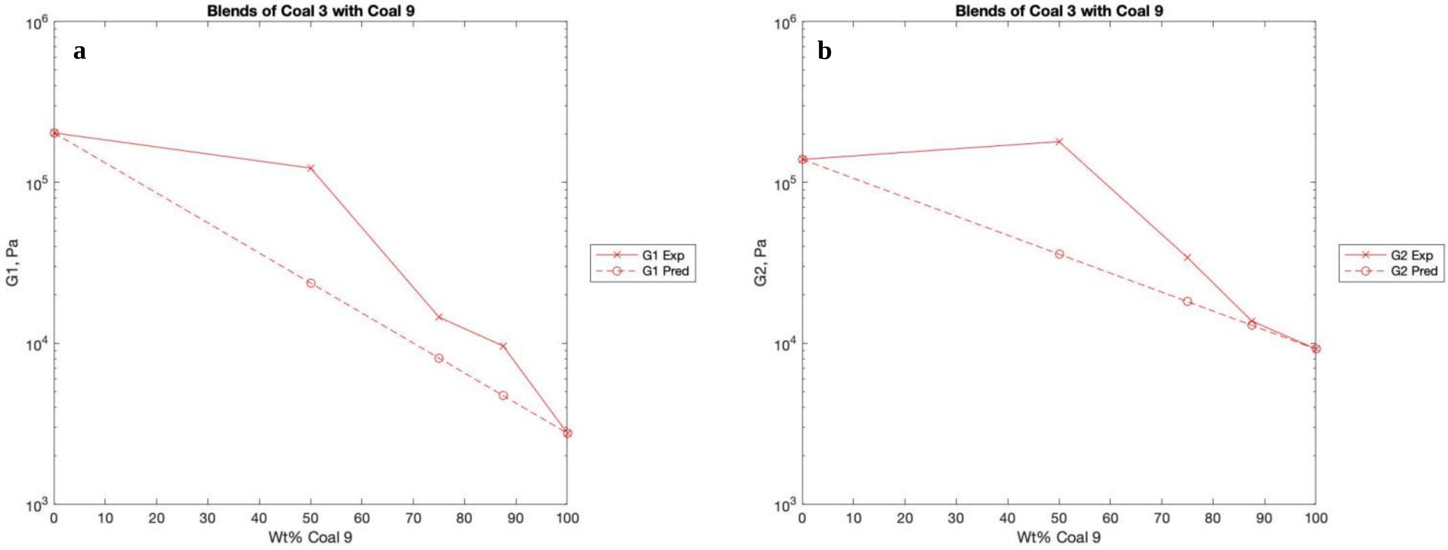

Figure C35: Minimum G' (a - left) and minimum G" (b - right) as a function of composition for blends of C3-C9

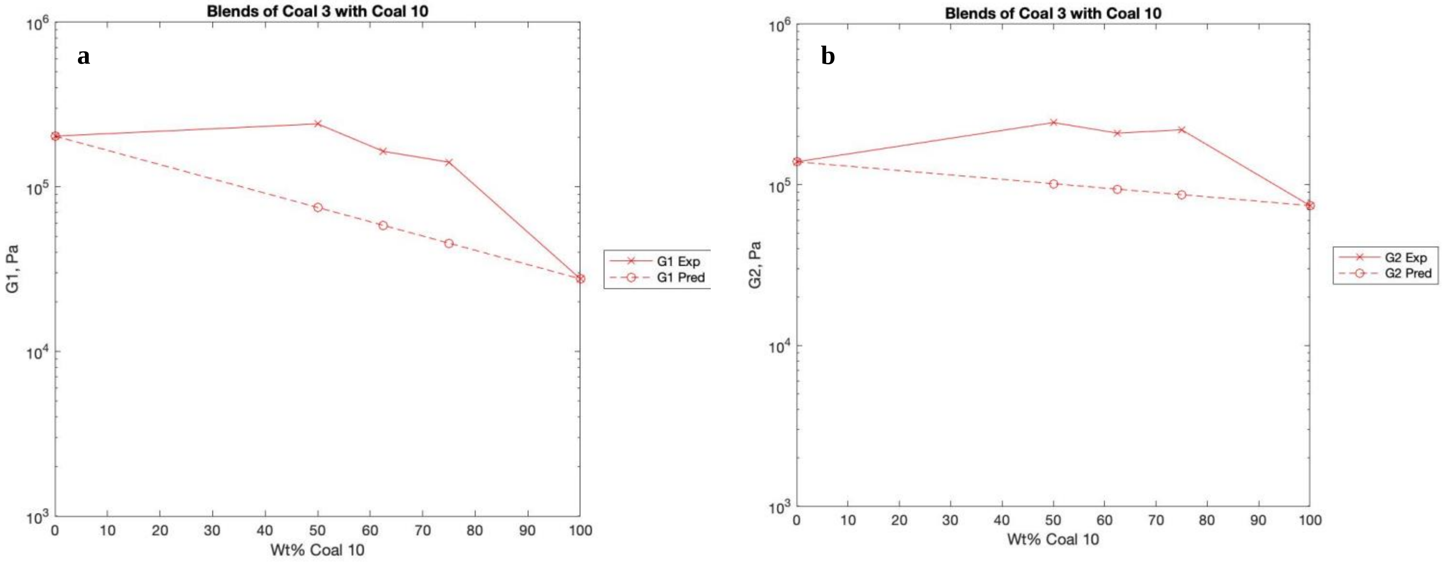

Figure C36: Minimum G' (a - left) and minimum G" (b - right) as a function of composition for blends of C3-10

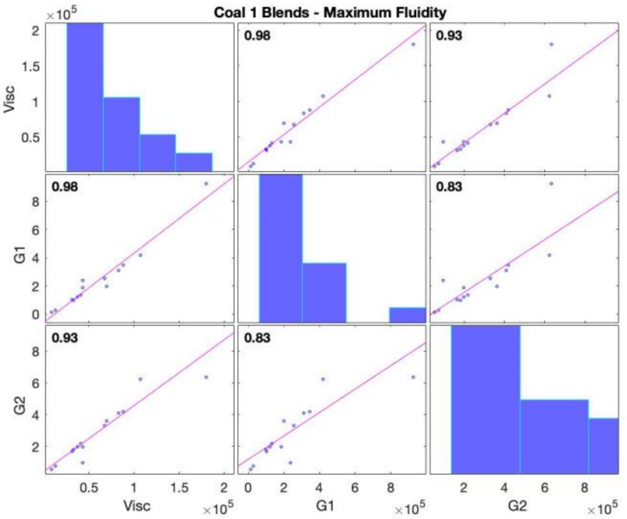

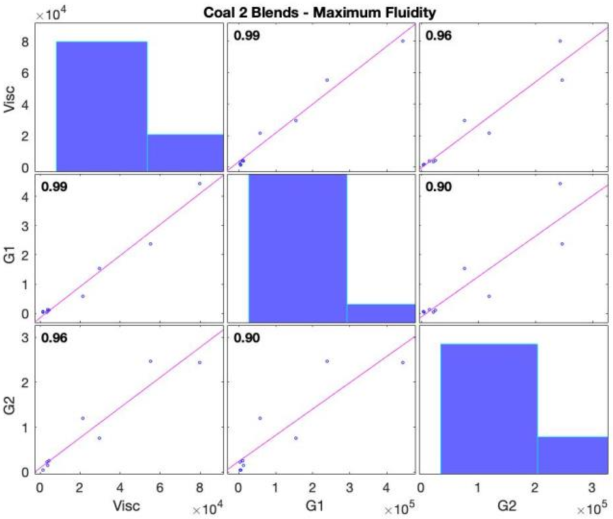

Figure C37 (left): Correlations between minimum η, G' and G" for coal 1 blends; Figure C38 (right): Correlations between minimum η*, G' and G" for coal 2 blends.*

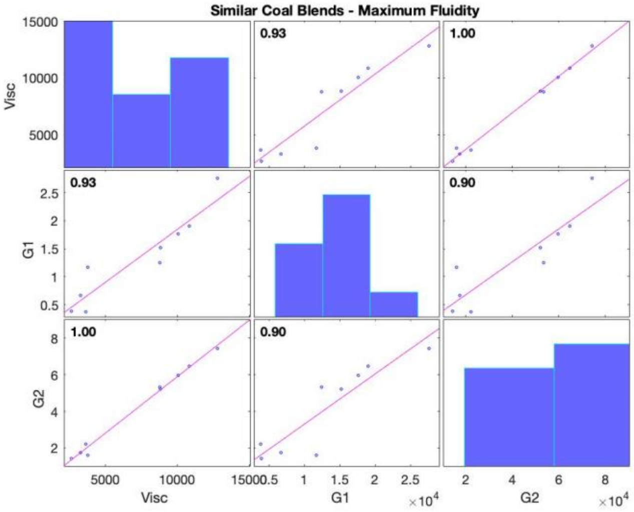

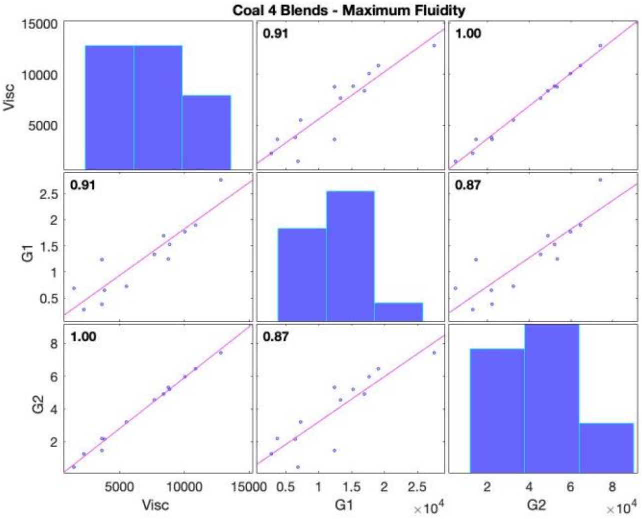

Figure C39 (left): Correlations between minimum η, G' and G" for similar coal blends (C4-C5 & C6-C10); Figure C40 (right): Correlations between minimum η*, G' and G" for coal 4 blends*

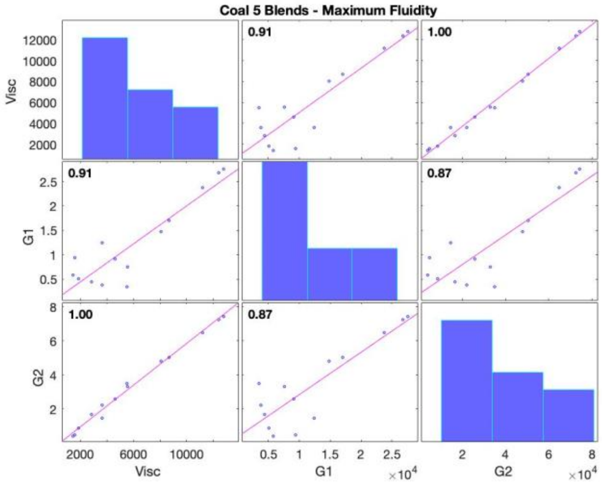

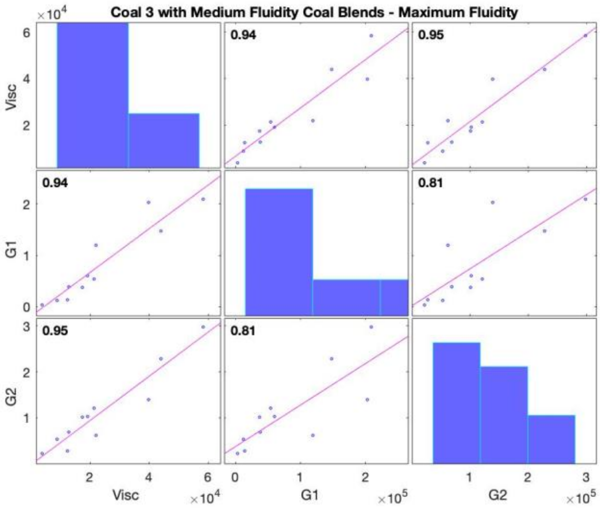

Figure C41 (left): Correlations between minimum η, G' and G'' for coal 5 blends; Figure C42 (right): Correlations between minimum η*, G' and G'' for blends of coal 3 with medium fluidity coals 4 and 5*

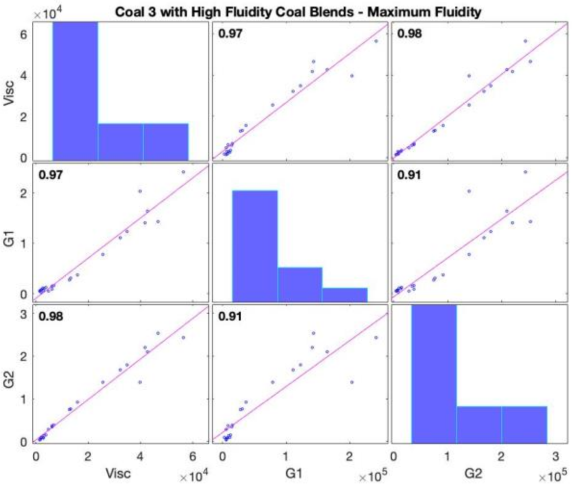

Figure C43 (left): Correlations between minimum η, G' and G'' for blends of coal 3 with high fluidity coals 6 – 10*

Table C2: Percentage (Diff (%)) and absolute difference (Diff (Pa s)) between experimental and predicted values of minimum complex viscosity for all blend compositions, along with log(percentage difference), where complex viscosity has been presented on log-axes. Agreement was defined as being within 38.8% of predicted values (or 1.59% for log(Diff)%).

Blend	Experimental η^*_{min} (Pa s)	Diff (Pa s)	Diff (%)	Log(Diff) %
C4-C5(25wt%)	10047	3010	35.2	1.55
C4-C5(50wt%)	10842	5193	63	1.80
C4-C5(75wt%)	8838	4302	64.3	1.81
C6-C10(25wt%)	3798	1169	26.7	1.43
C6-C10(50wt%)	2648	4163	88	1.94
C6-C10(75wt%)	3286	6051	95.9	1.98
C1-C4(50wt%)	43063	12401	33.6	1.53
C1-C4(55wt%)	43368	16315	46.3	1.67
C1-C4(70wt%)	32969	14388	55.8	1.75
C1-C4(75wt%)	37134	20740	77.5	1.89
C1-C4(80wt%)	41351	26886	96.3	1.98
C1-C4(85wt%)	31347	18584	84.3	1.93
C1-C10(50wt%)	180150	143099	131.8	2.12
C1-C10(70wt%)	87938	63719	113.6	2.06
C1-C10(75wt%)	67564	45787	102.5	2.01
C1-C10(80wt%)	83127	63546	123.7	2.09
C1-C10(85wt%)	69386	51779	119	2.08
C2-C6(25wt%)	55287	18423	40	1.60
C2-C6(50wt%)	21294	4281	22.4	1.35
C2-C6(75wt%)	4369	3482	57	1.76
C2-C8(25wt%)	29588	248	0.8	-0.10
C2-C8(50wt%)	3474	7304	102.5	2.01
C2-C8(75wt%)	1520	2439	89	1.95
C4-C6(25wt%)	7667	638	8.7	0.94
C4-C6(50wt%)	2252	3384	85.8	1.93
C4-C6(75wt%)	1483	3036	101.1	2.00
C4-C10(25wt%)	8386	1251	13.9	1.14
C4-C10(50wt%)	5535	5058	62.7	1.80
C4-C10(75wt%)	3802	7843	101.5	2.01
C5-C6(25wt%)	8677	5040	81.9	1.91
C5-C6(50wt%)	8071	4438	75.8	1.88
C5-C6(75wt%)	4628	1000	24.2	1.38
C5-C8(25wt%)	5536	2641	62.7	1.80
C5-C8(37.5wt%)	2856	275	10.1	1.00
C5-C8(50wt%)	1845	456	22	1.34
C5-C8(62.5wt%)	1578	474	26.1	1.42
C5-C10(25wt%)	12390	7404	85.2	1.93

C5-C10(50wt%)	11182	4355	48.4	1.68
C5-C10(75wt%)	5486	3862	52.1	1.72
C3-C4(50wt%)	58327	39657	103	2.01
C3-C4(70wt%)	43896	30099	104.3	2.02
C3-C4(75wt%)	21259	8466	49.7	1.70
C3-C4(80wt%)	19072	7211	46.6	1.67
C3-C4(85wt%)	12742	1745	14.7	1.17
C3-C5(50wt%)	21909	9876	58.2	1.76
C3-C5(75wt%)	12349	5729	60.4	1.78
C3-C5(87.5wt%)	17443	12534	112.1	2.05
C3-C6(50wt%)	32203	20200	91.4	1.96
C3-C6(62.5wt%)	13235	4338	39.2	1.59
C3-C6(75wt%)	4782	1813	31.9	1.50
C3-C7(50wt%)	46670	36045	125.8	2.10
C3-C7(62.5wt%)	15715	8075	69.1	1.84
C3-C7(75wt%)	6158	665	11.4	1.06
C3-C7(87.5wt%)	1519	2431	88.9	1.95
C3-C8(37.5wt%)	25560	14061	75.9	1.88
C3-C8(50wt%)	6776	828	11.5	1.06
C3-C8(62.5wt%)	1896	3132	90.5	1.96
C3-C8(75wt%)	2553	772	26.3	1.42
C3-C9(50wt%)	34842	26270	121	2.08
C3-C9(75wt%)	6037	2057	41.1	1.61
C3-C9(87.5wt%)	2978	266	9.3	0.97
C3-C10(50wt%)	56444	33884	85.8	1.93
C3-C10(62.5wt%)	42567	22988	74	1.87
C3-C10(75wt%)	41641	24648	84.1	1.92

N.B. Agreement between experimental and additive behaviour was defined as being within 38.8% (linear) and 1.59% (log), determined from 1.96 RSDs of repeated tests to provide 95% confidence limits

Table C3: Percentage (Diff(%)) and absolute (Diff (^{o}C)) difference between experimental and predicted values of sol point, gel point and softening range for all blend compositions.

Composition	Sol Point				Gel Point			
	Experimental Sol Point (^{o}C)	Diff (^{o}C)	Diff(%)	Agreement (Yes/No)	Experimental Gel Point (^{o}C)	Diff (^{o}C)	Diff (%)	Agreement (Yes/No)
C4-C5(25wt%)	439	3.3	0.8	No	491	2.7	0.5	No
C4-C5(50wt%)	448	3.5	0.8	No	496	4.1	0.8	No
C4-C5(75wt%)	452	4.8	1.1	No	499	2.3	0.5	No
C6-C10(25wt%)	410	1.1	0.3	Yes	476	0.5	0.1	Yes
C6-C10(50wt%)	407	6.4	1.6	No	475	1.1	0.2	Yes
C6-C10(75wt%)	411	7.0	1.7	No	475	0.6	0.1	Yes
C1-C4(50wt%)	N/A	N/A		N/A	N/A	N/A		N/A
C1-C4(55wt%)	471	7.6	1.6	No	500	5.1	1.0	No
C1-C4(70wt%)	453	3.0	0.7	Yes	488	5.4	1.1	No
C1-C4(75wt%)	457	4.0	0.9	No	495	1.6	0.3	No
C1-C4(80wt%)	447	3.9	0.9	No	497	4.0	0.8	No
C1-C4(85wt%)	442	5.6	1.3	No	496	4.0	0.8	No
C1-C10(50wt%)	462	4.0	0.9	No	485	2.8	0.6	No
C1-C10(70wt%)	438	6.2	1.4	No	481	1.9	0.4	No
C1-C10(75wt%)	433	7.7	1.8	No	477	4.7	1.0	No
C1-C10(80wt%)	441	3.6	0.8	No	478	2.9	0.6	No
C1-C10(85wt%)	427	6.8	1.6	No	476	3.6	0.8	No
C2-C6(25wt%)	457	N/A		N/A	492	N/A		N/A
C2-C6(50wt%)	434	N/A		N/A	483	N/A		N/A
C2-C6(75wt%)	417	N/A		N/A	478	N/A		N/A
C2-C8(25wt%)	446	N/A		N/A	488	N/A		N/A
C2-C8(50wt%)	430	N/A		N/A	480	N/A		N/A
C2-C8(75wt%)	416	N/A		N/A	472	N/A		N/A
C4-C6(25wt%)	434	3.4	0.8	No	485	2.5	0.5	No
C4-C6(50wt%)	423	1.2	0.3	Yes	474	9.7	2.0	No
C4-C6(75wt%)	418	5.4	1.3	No	480	0.2	0.0	Yes
C4-C10(25wt%)	432	4.5	1.0	No	484	2.6	0.5	No
C4-C10(50wt%)	427	5.3	1.2	No	482	1.1	0.2	Yes
C4-C10(75wt%)	423	5.1	1.2	No	477	1.9	0.4	No
C5-C6(25wt%)	437	0.6	0.1	Yes	499	4.5	0.9	No
C5-C6(50wt%)	431	4.8	1.1	No	490	1.6	0.3	Yes
C5-C6(75wt%)	418	3.2	0.8	No	480	2.0	0.4	No
C5-C8(25wt%)	444	1.9	0.4	Yes	495	1.8	0.4	No
C5-C8(37.5wt%)	437	1.5	0.3	Yes	491	1.0	0.2	Yes
C5-C8(50wt%)	431	5.0	1.2	No	491	4.1	0.8	No

C5-C8(62.5wt%)	421	11.2	2.7	No	493	9.3	1.9	No
C5-C10(25wt%)	439	3.1	0.7	Yes	499	4.8	1.0	No
C5-C10(50wt%)	434	1.8	0.4	Yes	491	3.6	0.7	No
C5-C10(75wt%)	427	2.4	0.6	Yes	478	3.5	0.7	No
C3-C4(50wt%)	435	1.5	0.3	Yes	484	6.8	1.4	No
C3-C4(70wt%)	431	6.5	1.5	No	491	8.0	1.6	No
C3-C4(75wt%)	436	2.8	0.6	Yes	490	5.6	1.1	No
C3-C4(80wt%)	433	5.8	1.3	No	488	3.2	0.7	No
C3-C4(85wt%)	429	10.1	2.4	No	487	0.8	0.2	Yes
C3-C5(50wt%)	N/A	N/A		N/A	N/A	N/A		N/A
C3-C5(75wt%)	458	13.1	2.9	No	497	6.0	1.2	No
C3-C5(87.5wt%)	456	9.1	2.0	No	500	4.5	0.9	No
C3-C6(50wt%)	424	5.4	1.3	No	470	0.2	0.0	Yes
C3-C6(62.5wt%)	420	5.5	1.3	No	468	4.3	0.9	No
C3-C6(75wt%)	417	6.2	1.5	No	470	3.8	0.8	No
C3-C7(50wt%)	422	2.1	0.5	Yes	476	13.7	2.9	No
C3-C7(62.5wt%)	424	7.9	1.9	No	478	16.8	3.5	No
C3-C7(75wt%)	430	17.0	4.0	No	480	19.6	4.1	No
C3-C7(87.5wt%)	422	13.1	3.1	No	485	25.1	5.2	No
C3-C8(37.5wt%)	422	6.3	1.5	No	466	2.1	0.5	No
C3-C8(50wt%)	418	9.5	2.3	No	467	2.3	0.5	No
C3-C8(62.5wt%)	412	14.7	3.6	No	470	0.0	0.0	Yes
C3-C8(75wt%)	409	15.8	3.9	No	481	10.2	2.1	No
C3-C9(50wt%)	426	6.6	1.5	No	467	0.6	0.1	Yes
C3-C9(75wt%)	417	4.1	1.0	No	463	5.6	1.2	No
C3-C9(87.5wt%)	417	6.8	1.6	No	465	5.1	1.1	No
C3-C10(50wt%)	433	4.4	1.0	No	471	0.8	0.2	Yes
C3-C10(62.5wt%)	434	7.5	1.7	No	467	4.7	1.0	No
C3-C10(75wt%)	432	6.7	1.5	No	472	1.0	0.2	Yes

Agreement between experimental and predicted sol point was defined as being within 0.733% (1.96 RSDs of repeated tests). Agreement between experimental and predicted gel point was defined as being within 0.325% (1.96 RSDs of repeated tests).

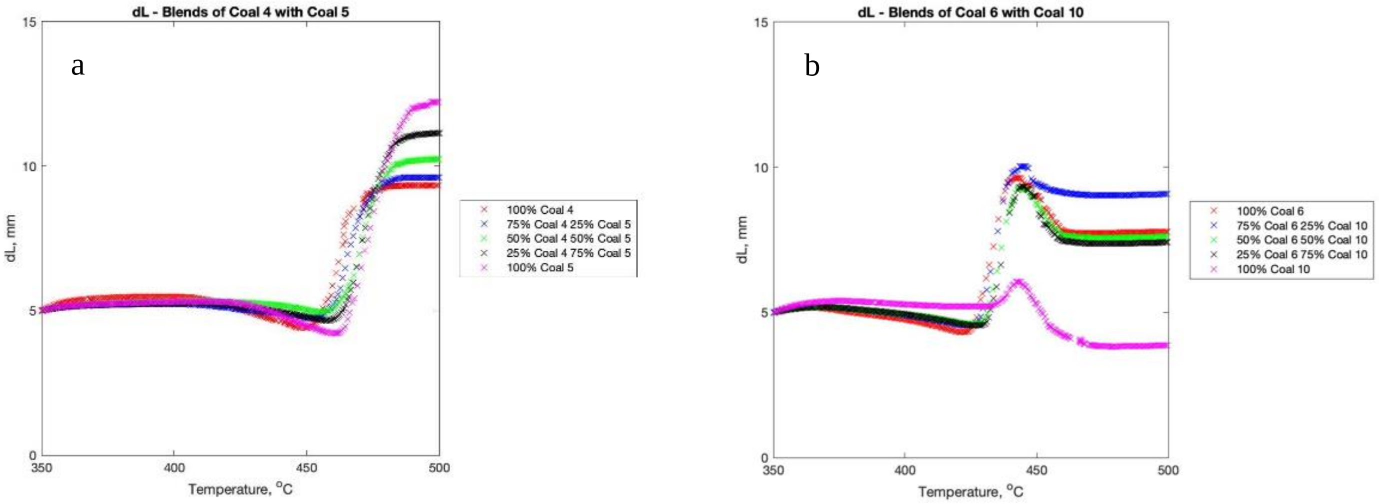

Figure C44: Plate gap as a function of temperature for blends of C4-C5 (a) and C6-C10 (b).

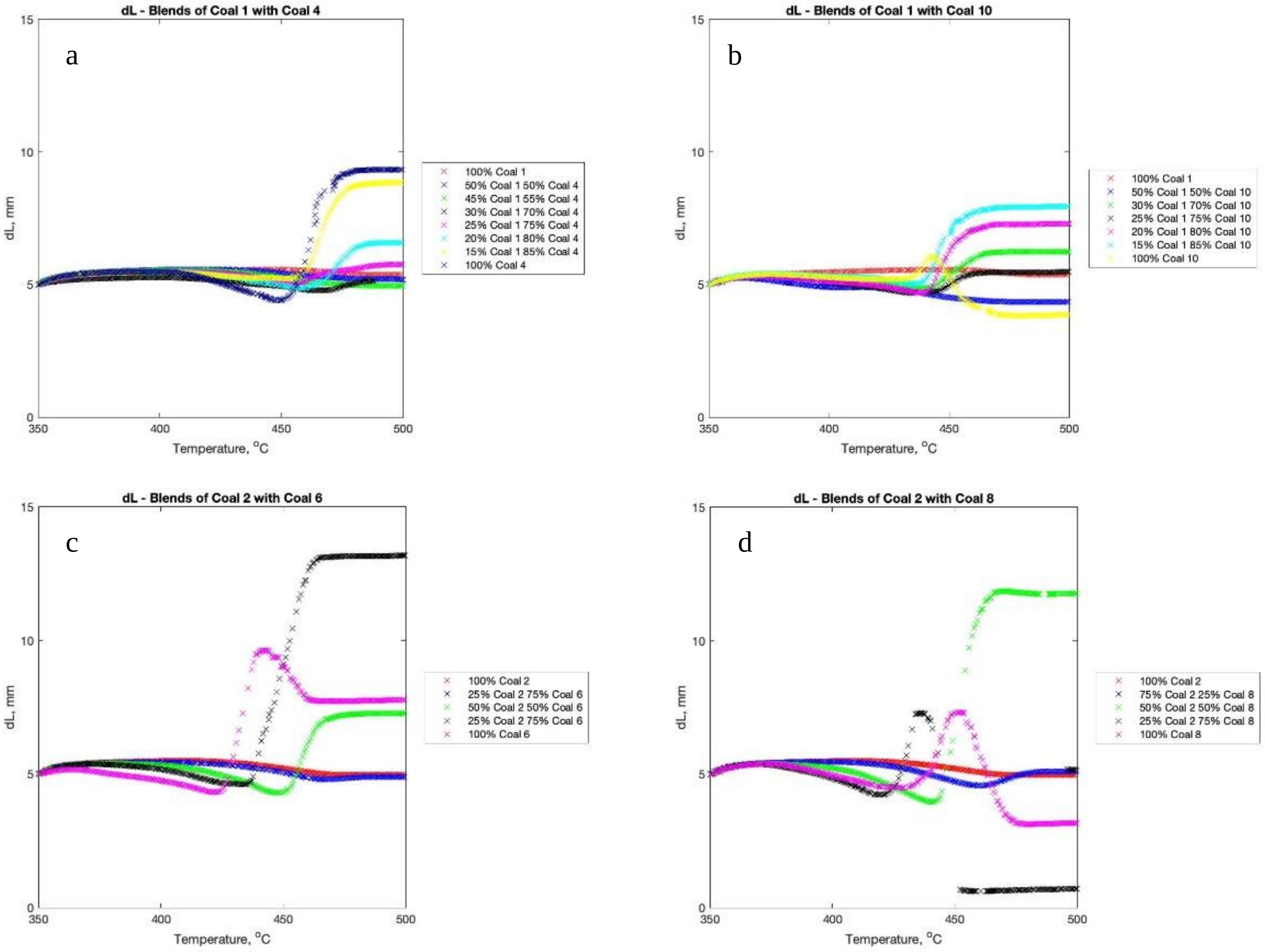

Figure C45: Plate gap as a function of temperature plots for C1-C4 (a), C1-C10 (b), C2-C6 (c) and C2-C8 (d)

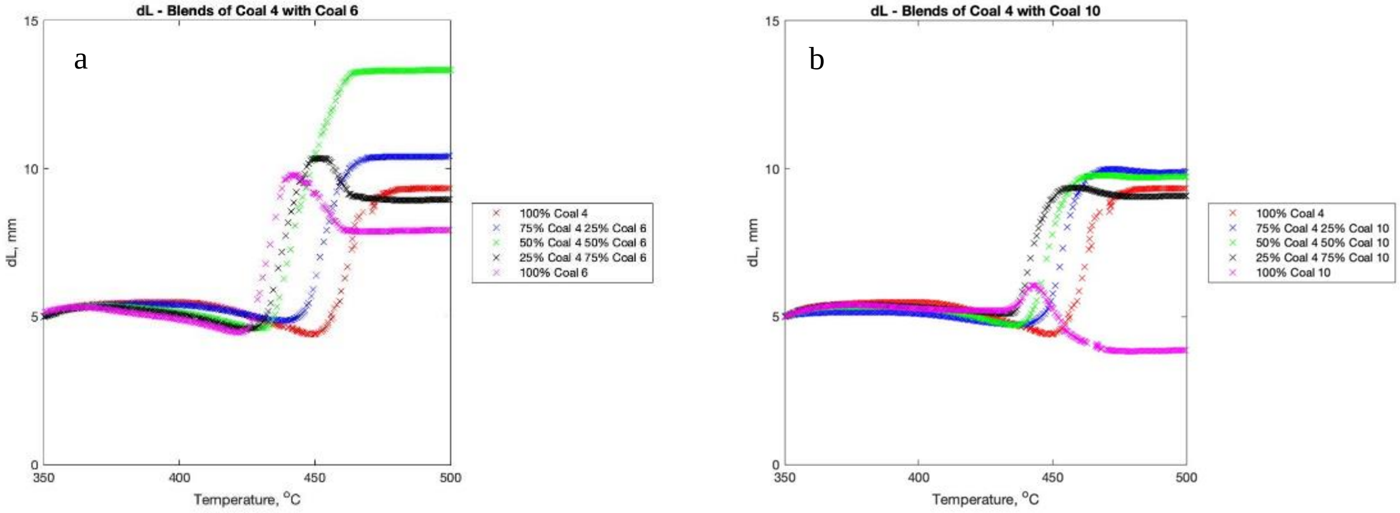

Figure C46: Plate gap as a function of temperature for C4-C6 (a) and C4-C10 (b).

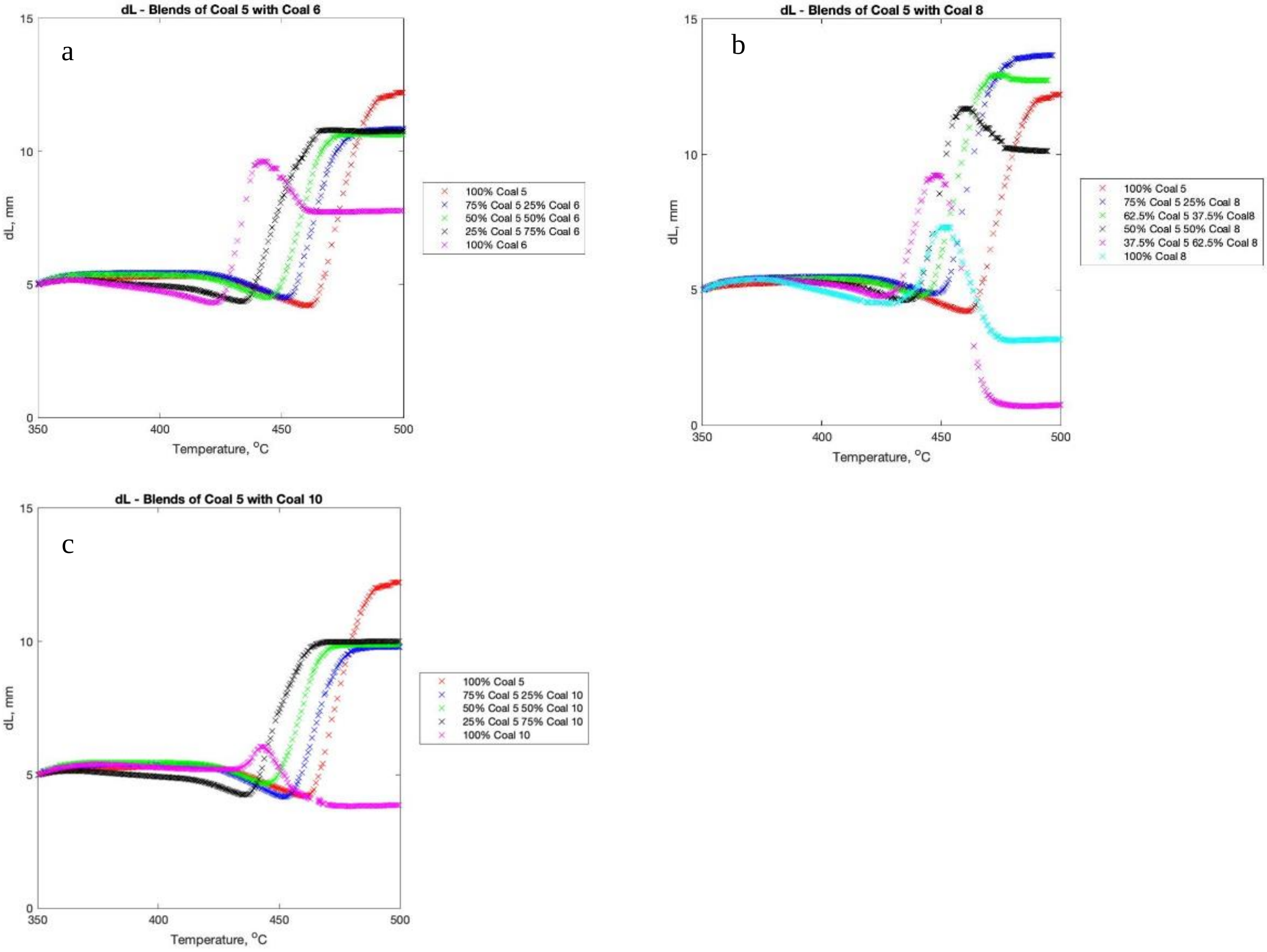

Figure C47: Plate gap as a function of temperature for C5-C6 (a), C5-C8 (b) and C5-C10 (c)

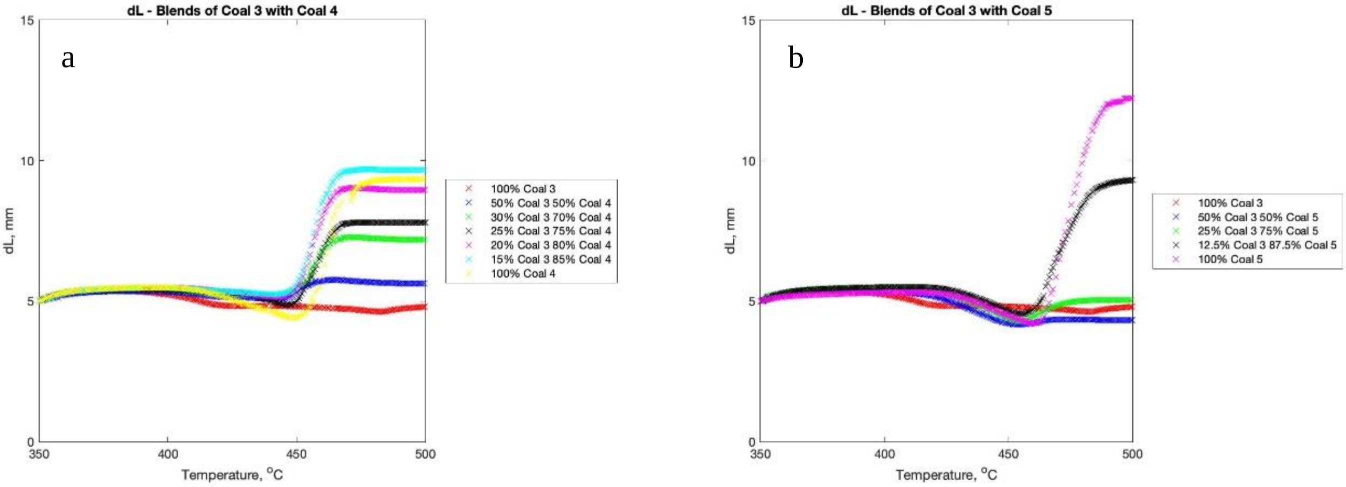

Figure C48: Plate gap as a function of temperature for C3-C4 (a) and C3-C5 (b).

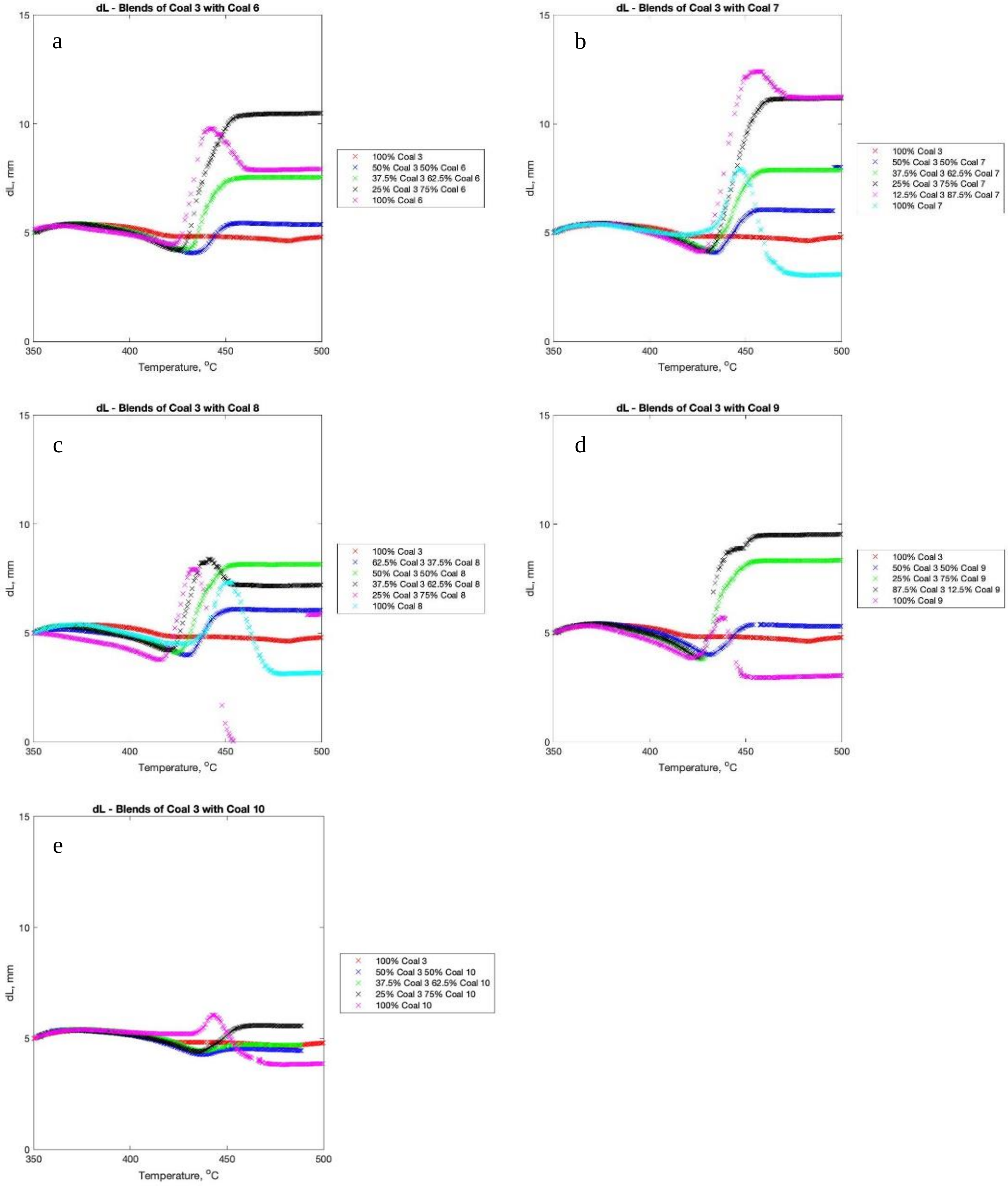

Figure C49: Plate gap as a function of temperature for C3-C6 (a), C3-C7 (b), C3-C8 (c), C3-C9 (d) and C3-C10 (e).

Table C4: Percentage (Diff (%)) and absolute (Diff (mm)) differences between experimental and predicted plate gaps at the temperature of maximum swelling for the blends and agreement with additive behaviour highlighted.

Composition	Experimental Max Plate Gap (mm)	Diff (mm)	Diff (%)	Agreement?
C4-C5(25wt%)	9.6	0.5	4.7	Yes
C4-C5(50wt%)	10.2	0.5	5.3	Yes
C4-C5(75wt%)	11.1	0.4	3.2	Yes
C6-C10(25wt%)	10.0	1.3	12.9	Yes
C6-C10(50wt%)	9.3	1.4	15.5	No
C6-C10(75wt%)	9.3	2.4	25.7	No
C1-C4(50wt%)	5.6	1.9	33.8	No
C1-C4(55wt%)	5.5	2.1	38.2	No
C1-C4(70wt%)	5.3	2.9	55.8	No
C1-C4(75wt%)	5.8	2.6	46.0	No
C1-C4(80wt%)	6.6	2.0	30.6	No
C1-C4(85wt%)	8.8	0.1	0.8	Yes
C1-C10(50wt%)	5.3	0.6	10.6	Yes
C1-C10(70wt%)	6.2	0.3	5.5	Yes
C1-C10(75wt%)	5.5	0.5	8.3	Yes
C1-C10(80wt%)	7.3	1.3	18.3	No
C1-C10(85wt%)	7.9	2.0	24.7	No
C2-C6(25wt%)	13.2	4.6	34.8	No
C2-C6(50wt%)	7.3	0.3	4.1	Yes
C2-C6(75wt%)	5.4	1.1	20.1	No
C2-C8(25wt%)	7.3	0.4	5.8	Yes
C2-C8(50wt%)	11.9	5.4	45.9	No
C2-C8(75wt%)	5.5	0.5	9.0	Yes
C4-C6(25wt%)	10.4	1.0	9.7	Yes
C4-C6(50wt%)	13.3	3.9	28.9	No
C4-C6(75wt%)	10.3	0.8	7.6	Yes
C4-C10(25wt%)	10.0	1.5	14.7	No
C4-C10(50wt%)	9.8	2.1	21.3	No
C4-C10(75wt%)	9.4	2.5	26.6	No
C5-C6(25wt%)	10.8	0.7	6.8	Yes
C5-C6(50wt%)	10.7	0.3	2.5	Yes

C5-C6(75wt%)	10.8	0.5	4.9	Yes
C5-C8(25wt%)	13.7	2.7	19.5	No
C5-C8(37.5wt%)	12.9	2.5	19.7	No
C5-C8(50wt%)	11.7	1.9	16.5	No
C5-C8(62.5wt%)	9.2	0.1	0.8	Yes
C5-C10(25wt%)	9.8	0.9	9.1	Yes
C5-C10(50wt%)	9.9	0.7	7.5	Yes
C5-C10(75wt%)	10.0	2.4	24.2	No
C3-C4(50wt%)	5.8	1.6	27.8	No
C3-C4(70wt%)	7.3	0.9	11.9	Yes
C3-C4(75wt%)	7.8	0.5	6.9	Yes
C3-C4(80wt%)	9.0	0.5	5.4	Yes
C3-C4(85wt%)	9.7	0.9	9.7	Yes
C3-C5(50wt%)	5.4	3.4	62.9	No
C3-C5(75wt%)	5.4	5.1	93.2	No
C3-C5(87.5wt%)	9.3	2.1	22.2	No
C3-C6(50wt%)	5.4	2.1	38.0	No
C3-C6(62.5wt%)	7.5	0.5	6.4	Yes
C3-C6(75wt%)	10.5	1.9	18.4	No
C3-C7(50wt%)	6.1	0.6	9.5	Yes
C3-C7(62.5wt%)	7.9	0.9	11.9	Yes
C3-C7(75wt%)	11.2	3.9	35.1	No
C3-C7(87.5wt%)	12.4	4.8	38.9	No
C3-C8(37.5wt%)	6.1	0.0	0.1	Yes
C3-C8(50wt%)	8.2	1.8	22.2	No
C3-C8(62.5wt%)	8.4	1.8	21.4	No
C3-C8(75wt%)	7.9	1.1	13.8	Yes
C3-C9(50wt%)	5.4	0.1	2.0	Yes
C3-C9(75wt%)	8.3	2.7	32.6	No
C3-C9(87.5wt%)	9.5	3.9	40.6	No
C3-C10(50wt%)	5.4	0.3	5.7	Yes
C3-C10(62.5wt%)	5.4	0.4	6.9	Yes
C3-C10(75wt%)	5.6	0.3	5.3	Yes

N.B: Agreement between experimental and additive behaviour values was defined as being within 14.3% determined from 1.96 RSDs of repeated tests

Appendix D

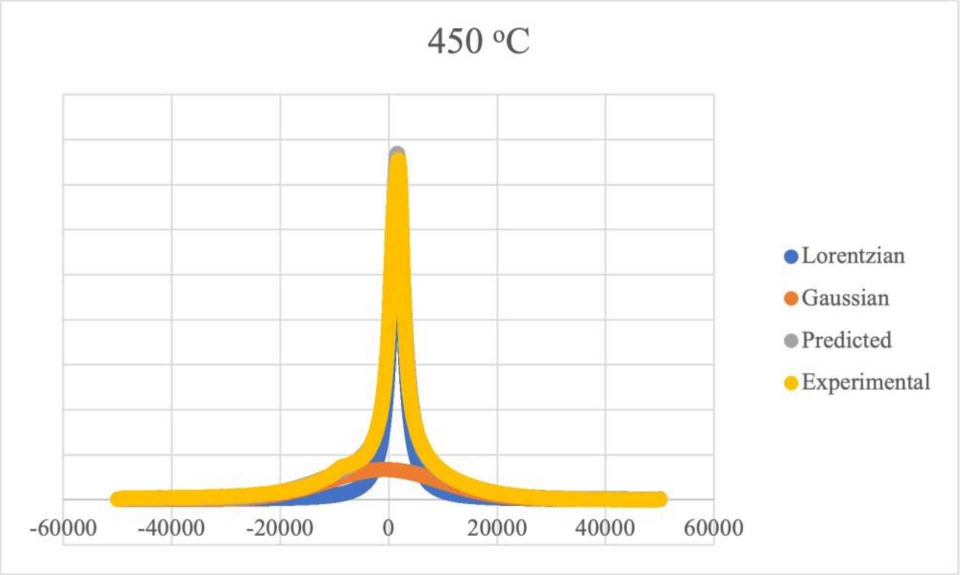

Figure D1: Plot of calculated Lorentzian (fluid component) and Gaussian (rigid component) with predicted spectrum and experimental spectrum for Coal 8 at 450 °C.

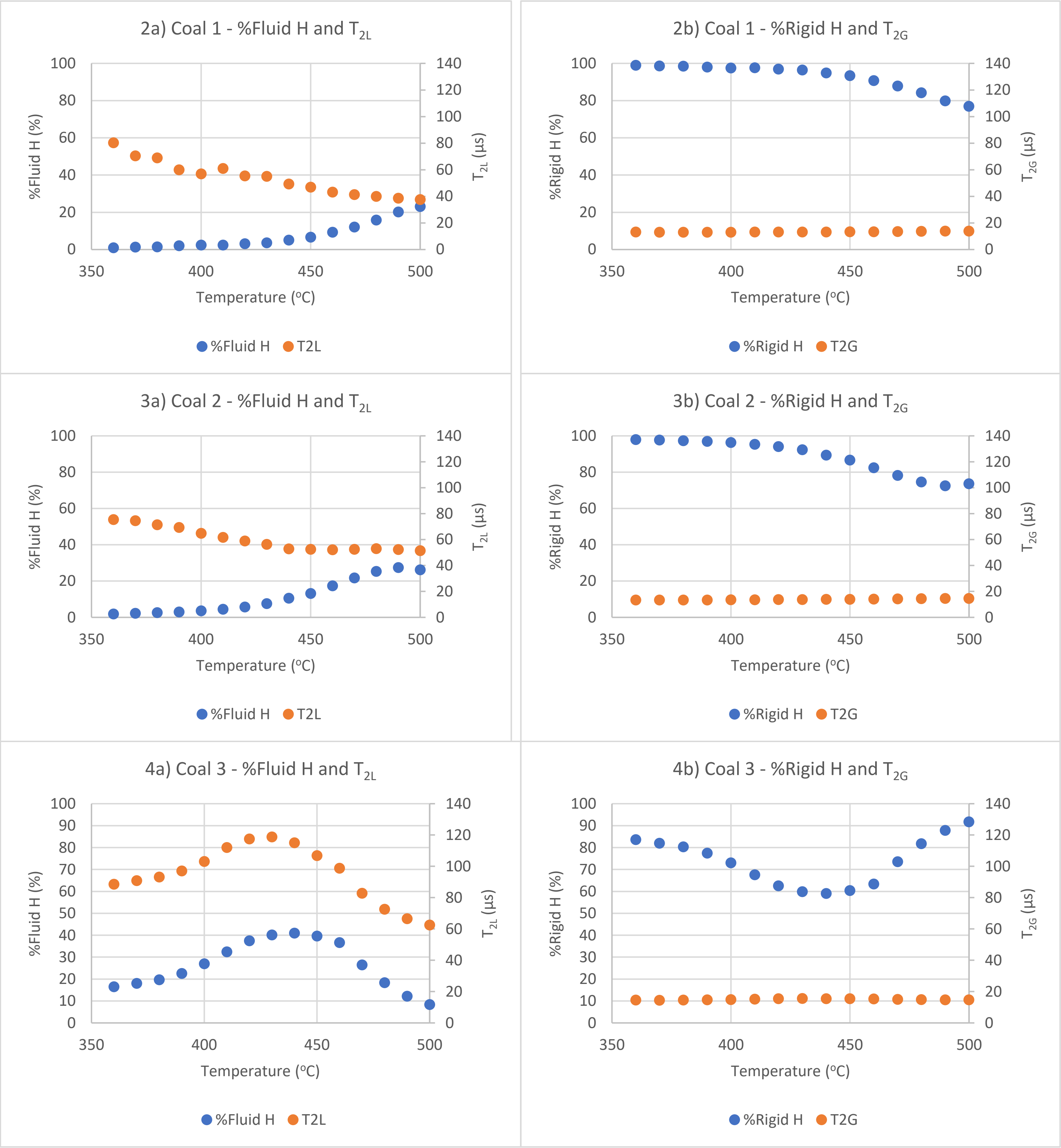

Figure D2: %Fluid hydrogen (a) and T_{2L} (b) as a function of temperature for coal 1; Figure D3: %Fluid hydrogen (a) and T_{2L} (b) as a function of temperature for coal 2; Figure D4: %Fluid hydrogen (a) and T_{2L} (b) as a function of temperature for coal 3.

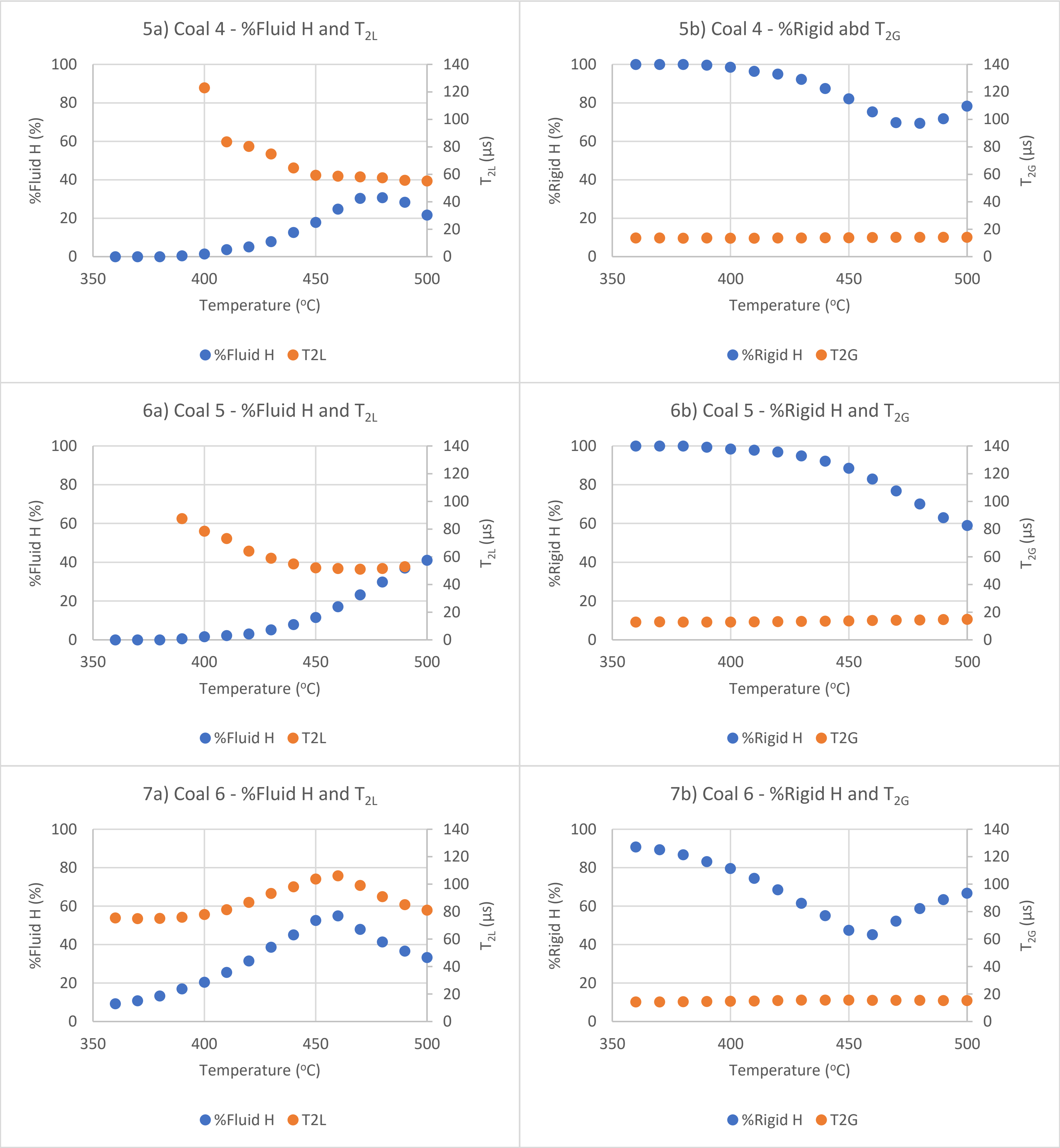

Figure D5: %Fluid hydrogen (a) and T_{2L} (b) as a function of temperature for coal 4; Figure D6: %Fluid hydrogen (a) and T_{2L} (b) as a function of temperature for coal 5; Figure D7: %Fluid hydrogen (a) and T_{2L} (b) as a function of temperature for coal 6.

Figure D8: %Fluid hydrogen (a) and T_{2L} (b) as a function of temperature for coal 7; Figure D9: %Fluid hydrogen (a) and T_{2L} (b) as a function of temperature for coal 8; Figure D10: %Fluid hydrogen (a) and T_{2L} (b) as a function of temperature for coal 9.

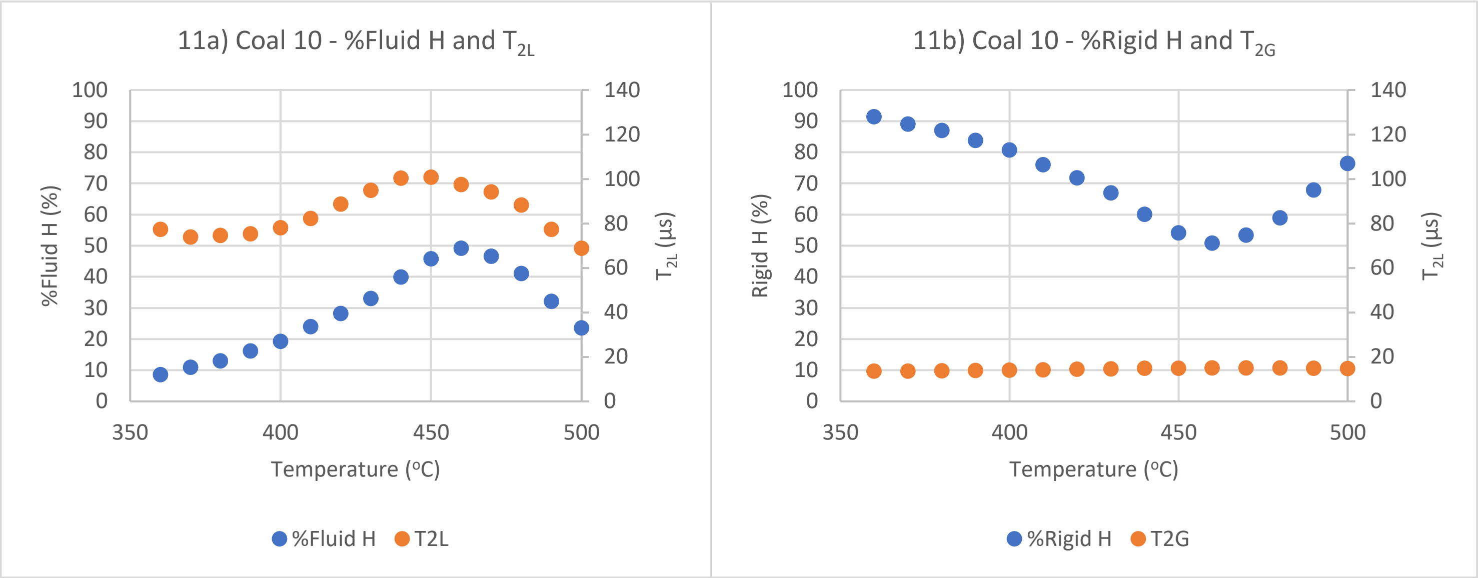

Figure D11: %Fluid hydrogen (a) and T_{2L} (b) as a function of temperature for coal 10

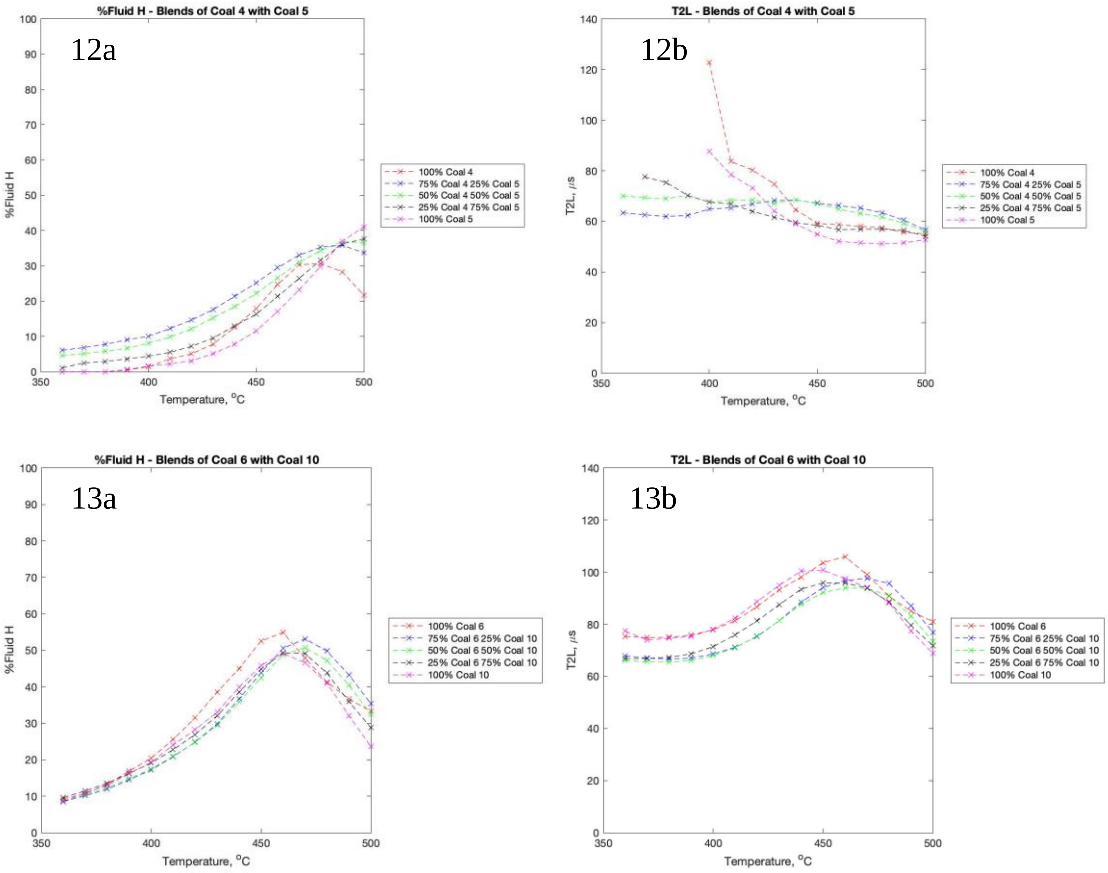

Figures D12 – D13: %Fluid hydrogen (a) and T_{2L} (b) as a function of temperature for C4-C5 (D12); C6-C10 (D13)

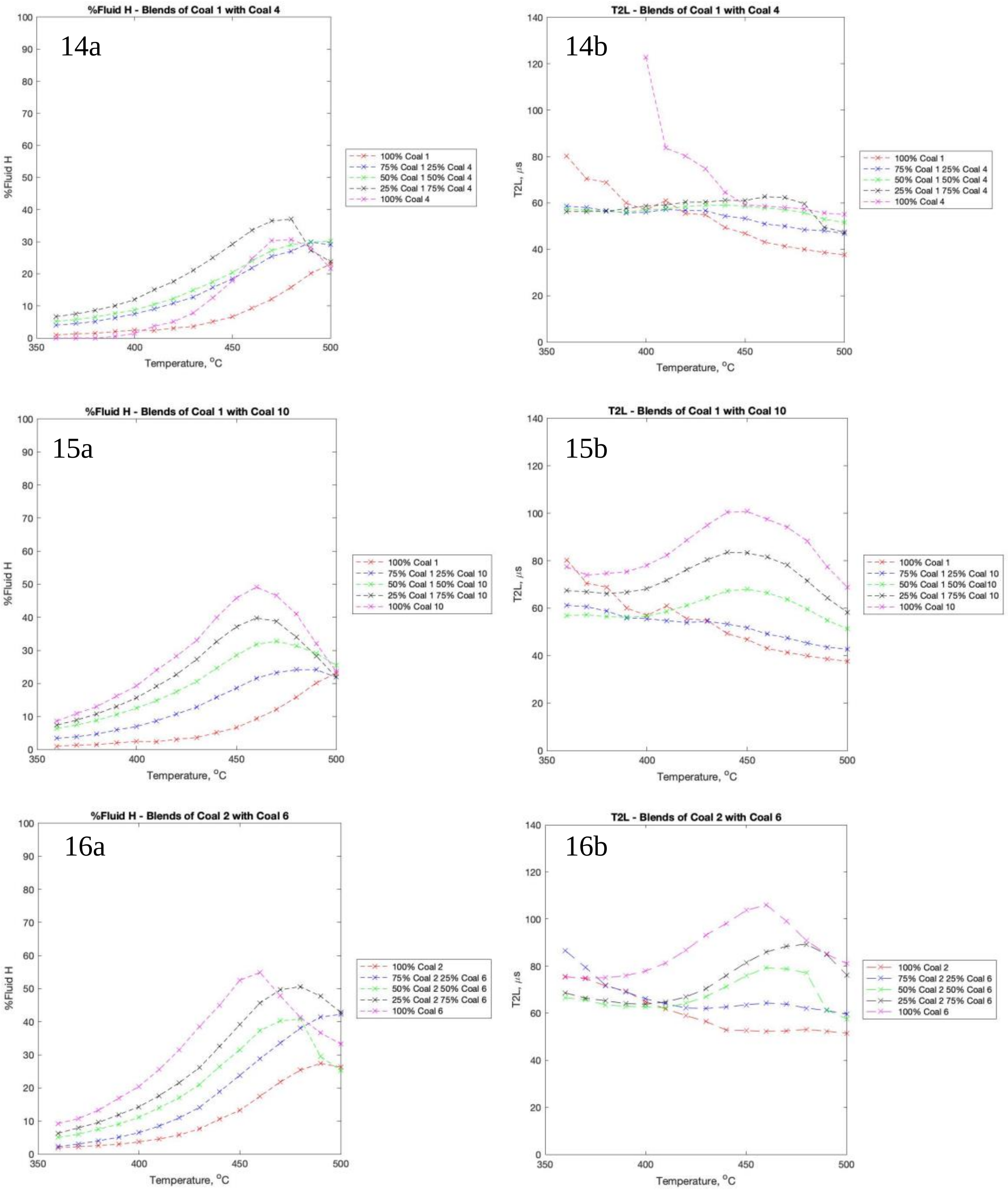

Figure D14-D16: %Fluid hydrogen (a) and T_{2L} (b) as a function of temperature for C1-C4 (D14); C1-C10 (D15); C2-C6 (D16).

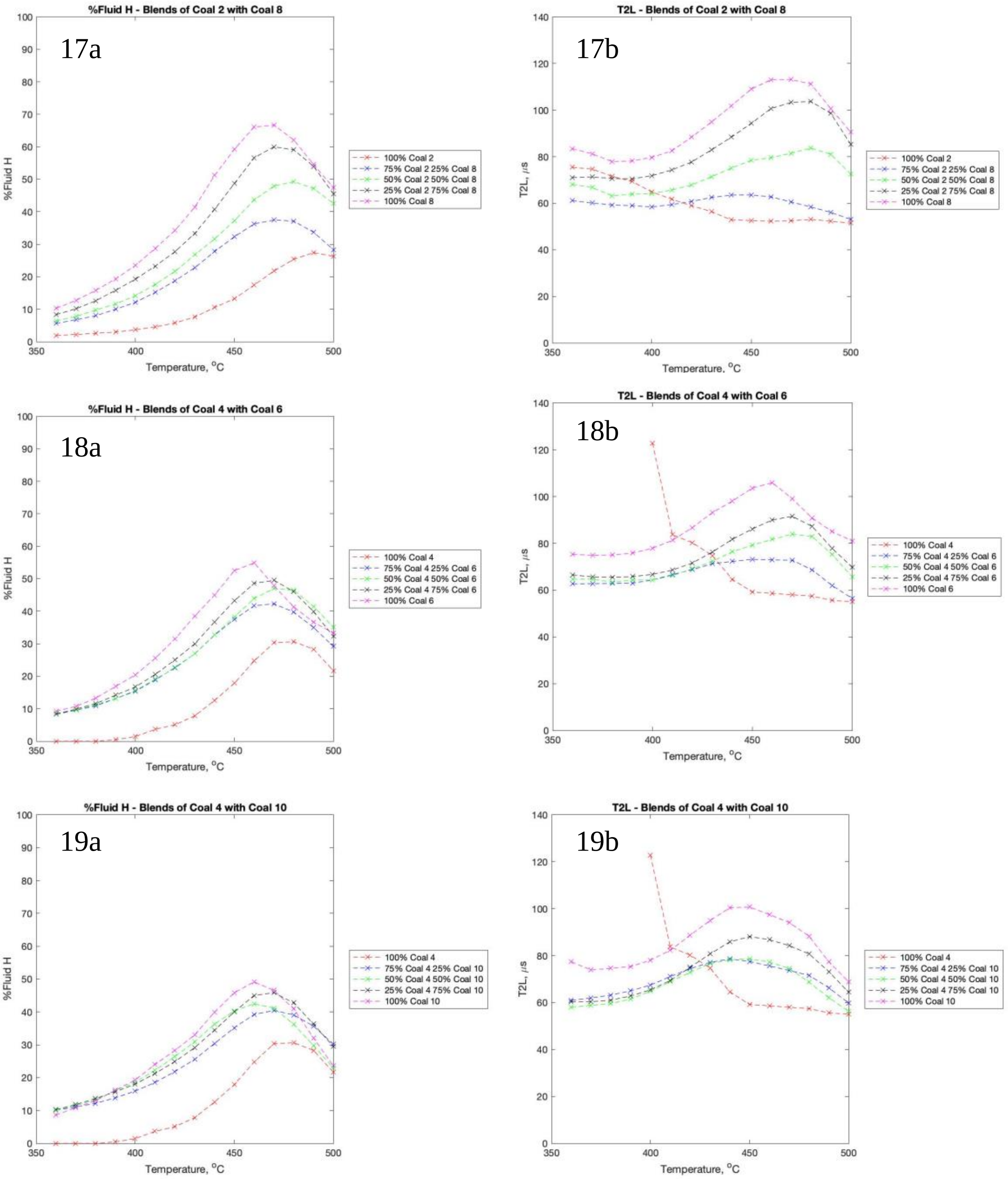

Figures D17 – D19: %Fluid hydrogen (a) and T_{2L} (b) as a function of temperature for C2-C8 (D17); C4-C6 (D18); C4-C10 (D19)

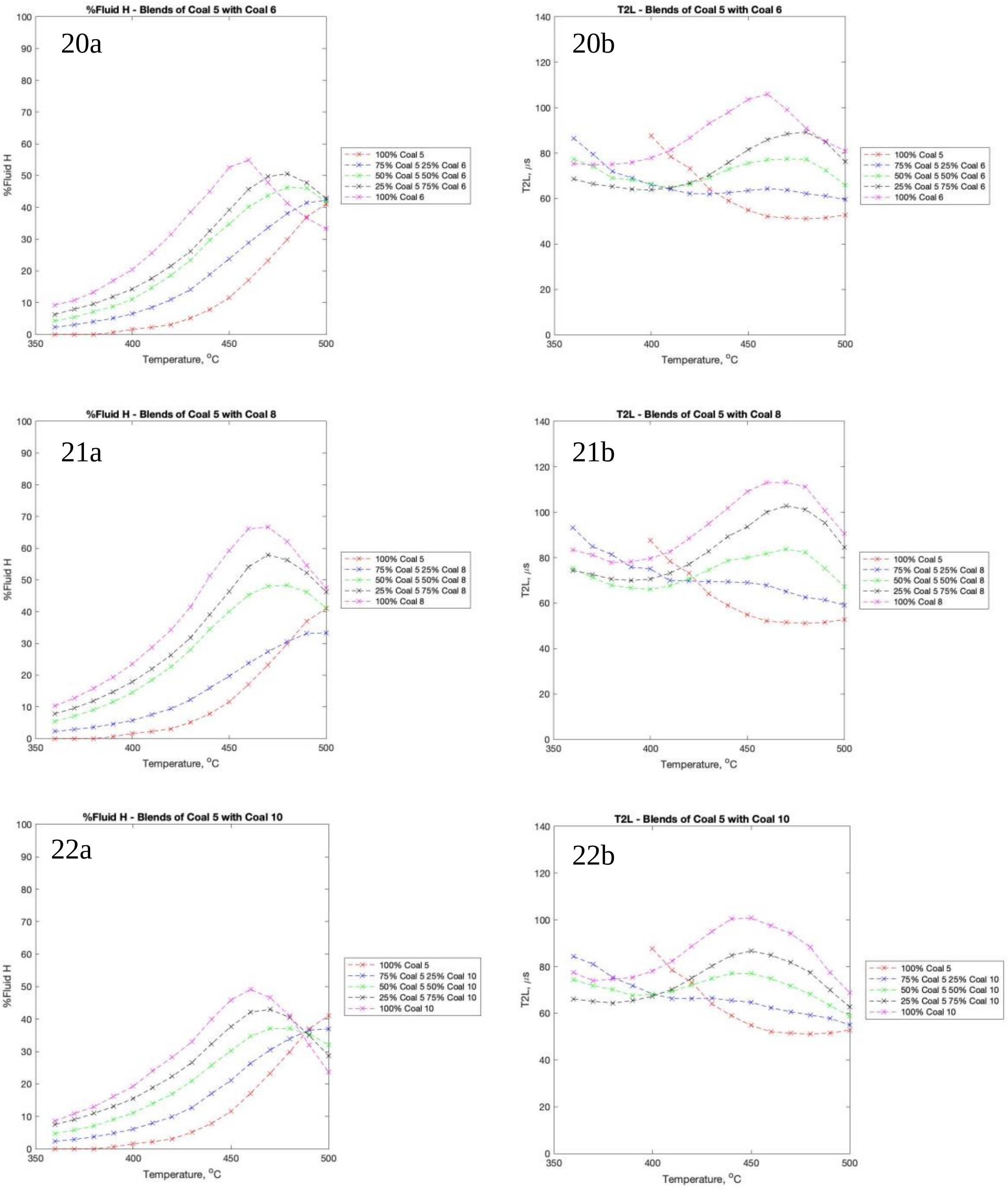

Figures D20 - D22: %Fluid hydrogen (a) and T_{2L} (b) as a function of temperature for C5-C6 (D20); C5-C8 (D21); C5-C10 (D22)

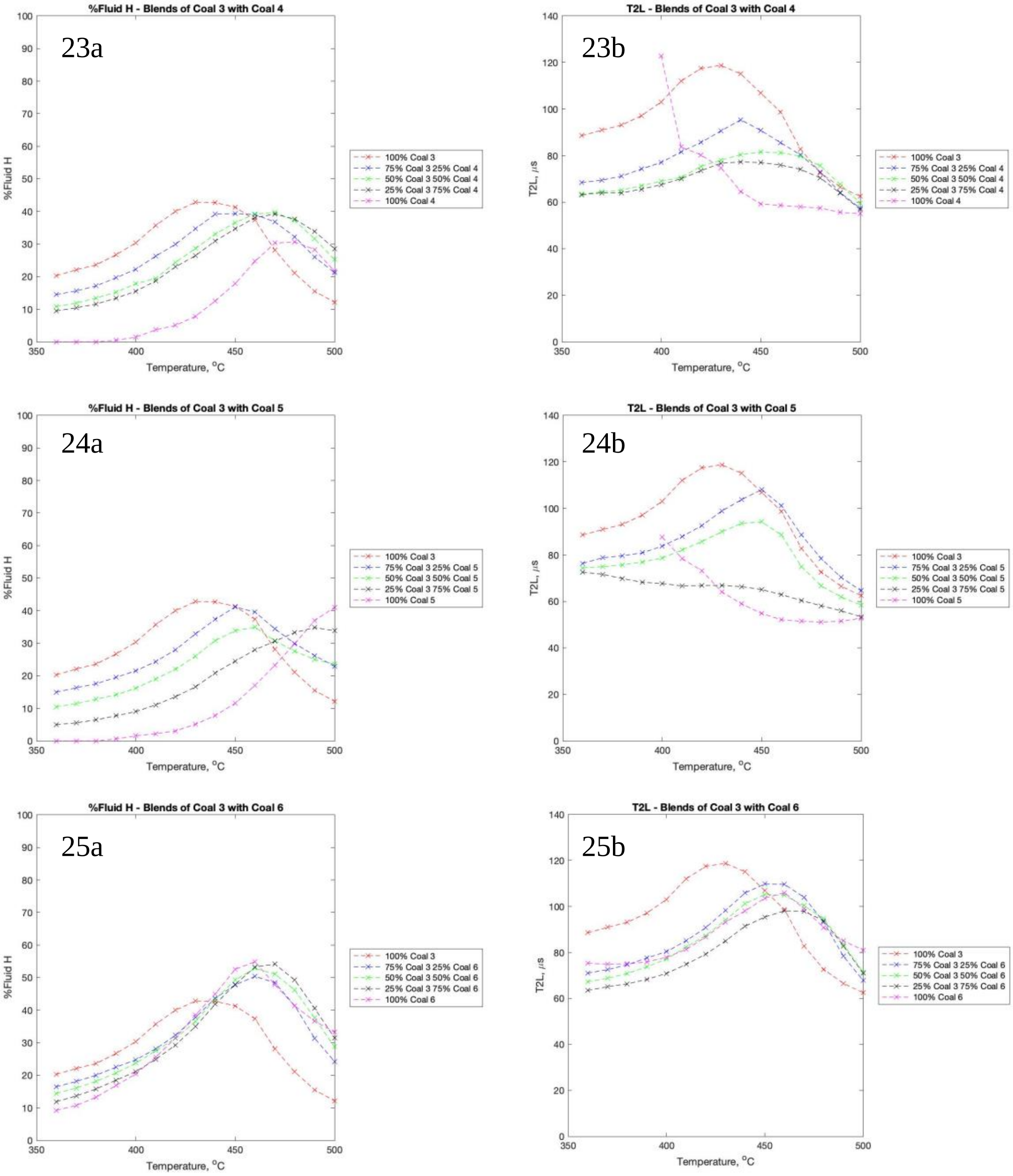

Figures D23 – D25: %Fluid hydrogen (a) and T_{2L} (b) as a function of temperature for C3-C4 (D23); C3-C5 (D24); C3-C6 (D25)

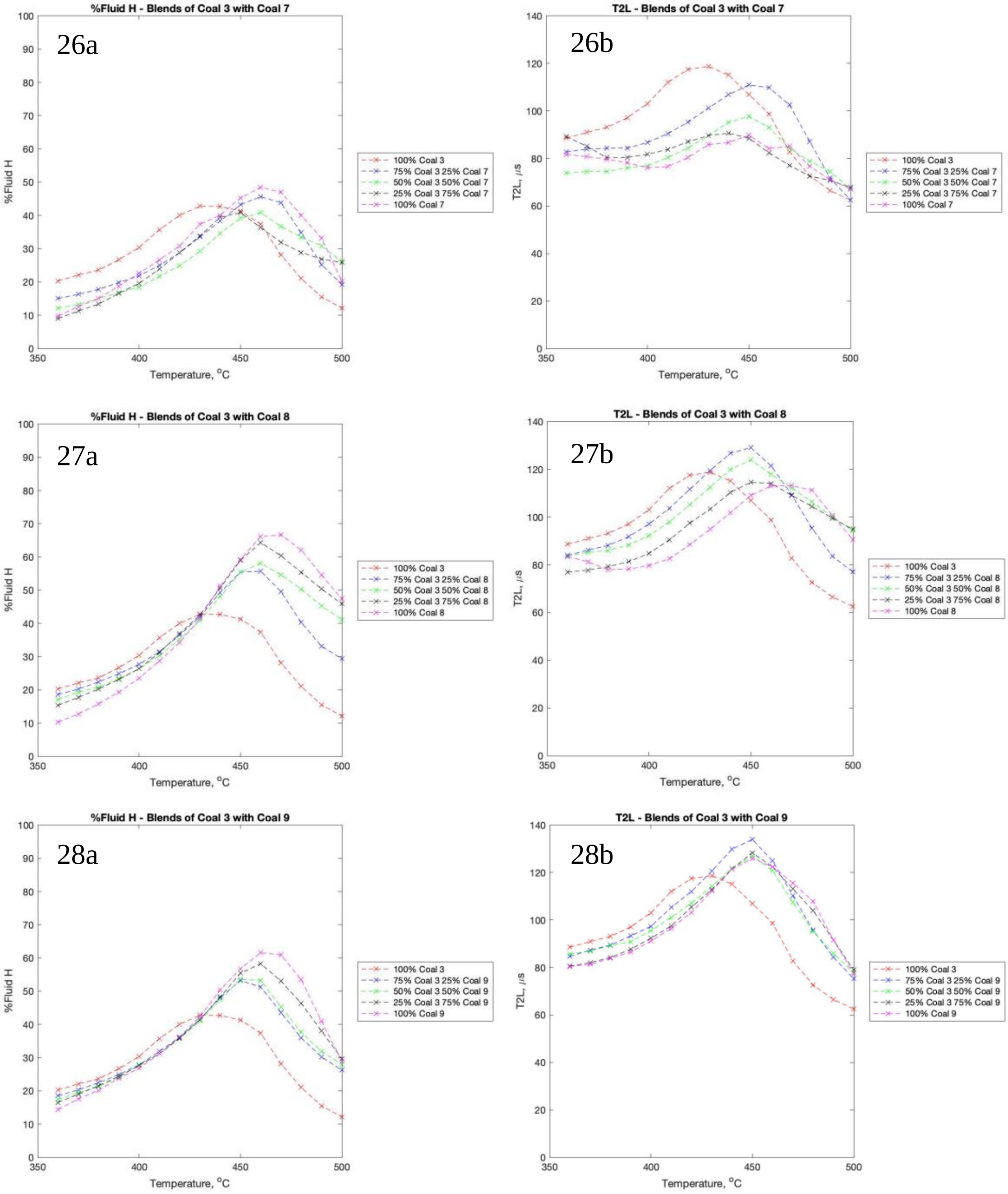

Figures D26 – D28: %Fluid hydrogen (a) and T_{2L} (b) as a function of temperature for C3-C7 (D26); C3-C8 (D27); C3-C9 (D28)

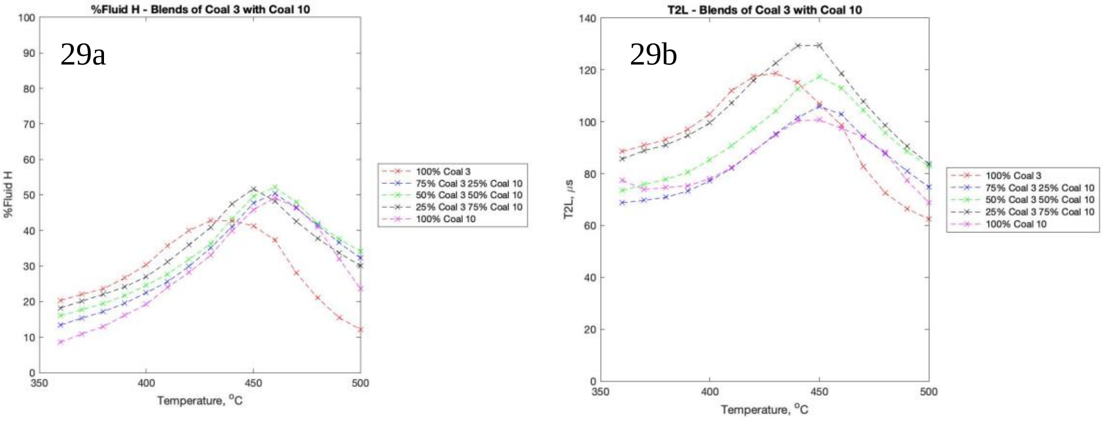

Figure D29: %Fluid hydrogen (a) and T_{2L} (b) as a function of temperature for C3-C10.

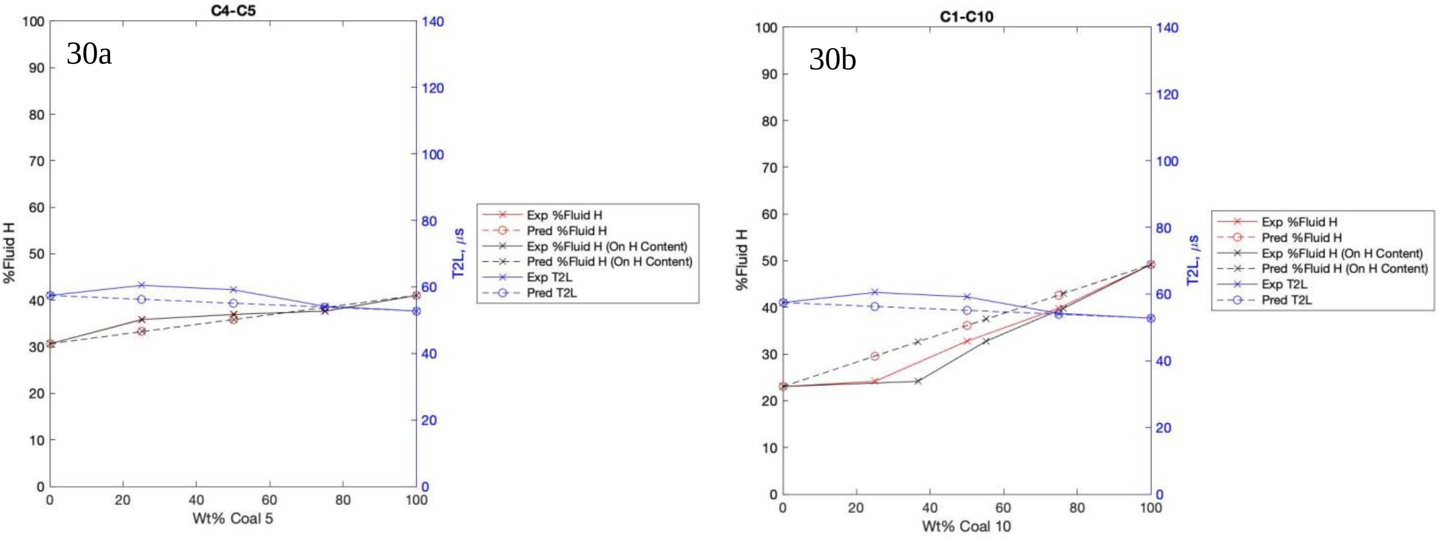

Figure D30: Experimental and predicted maximum %fluid H (based on wt% addition), experimental and predicted maximum %fluid H (based on fractional mass of hydrogen in the blend) and T_{2L} at maximum %fluid H for C4-C5 (a) C1-C10 (b)

Table D1: Hydrogen fraction for single coals determined from ultimate analysis

Coal	*Hydrogen Fraction (%)*
1	*4.2*
2	*5.0*
3	*5.8*
4	*4.9*
5	*4.8*
6	*5.0*
7	*5.1*
8	*5.3*
9	*5.5*
10	*5.4*

Appendix E

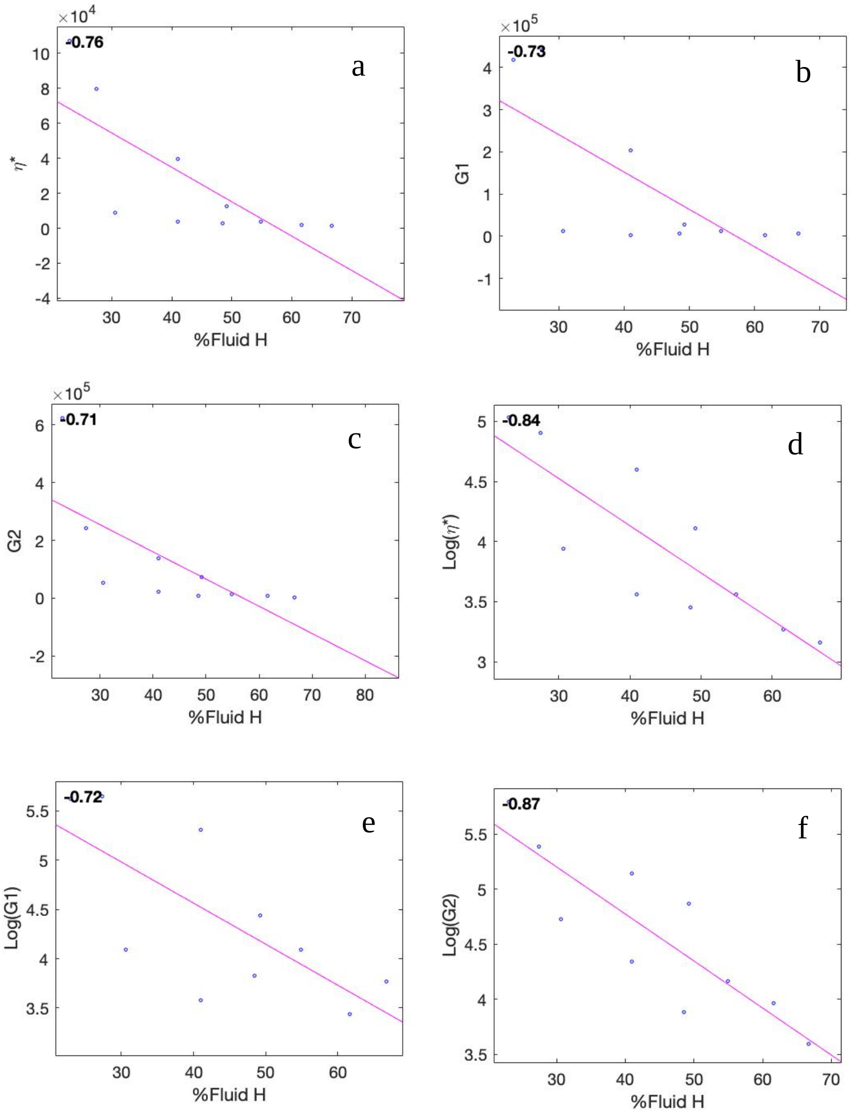

Figure E1: Correlations for coals 1 – 10 measured using 3 g samples by the cup geometry between maximum %fluid hydrogen and rheological parameters: η (a – top left), G' (b – top right), G'' (c – middle left), log(η*) (d – middle right), log(G') (e – bottom left) and log(G'') (f – bottom right).*

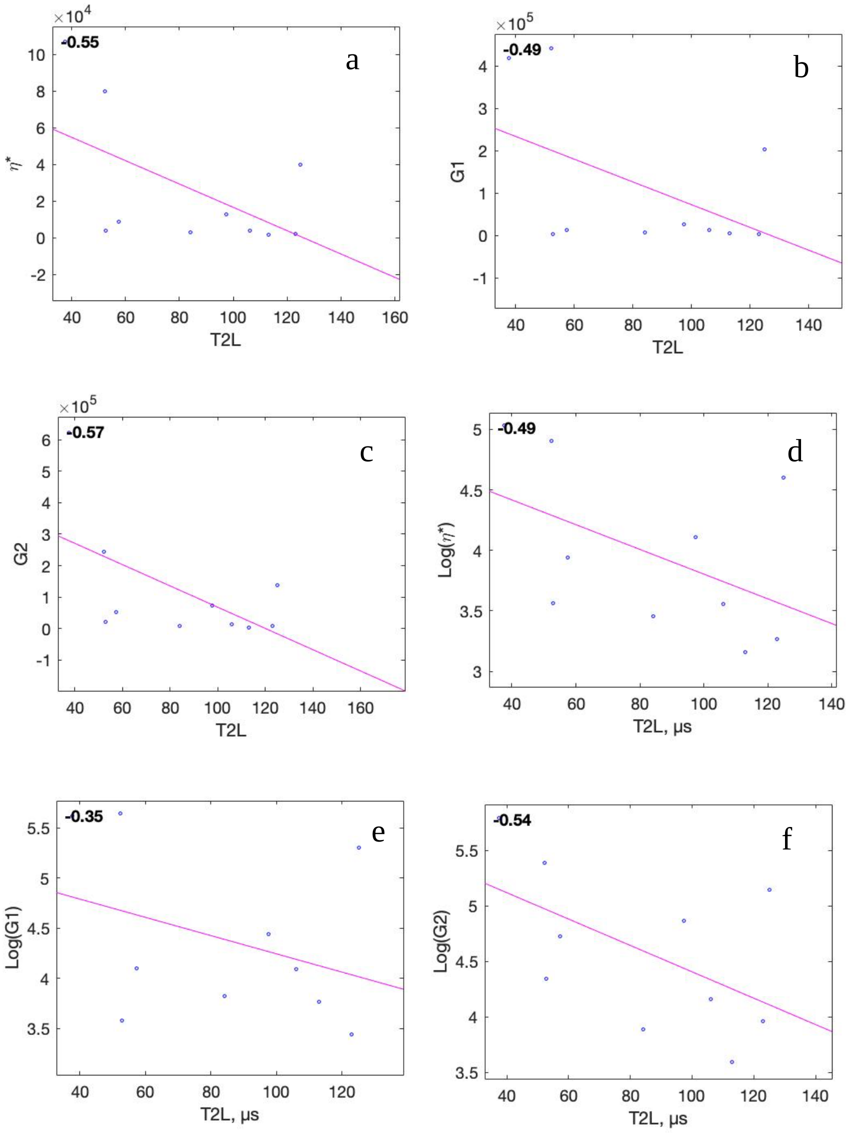

Figure E2: Correlations for coals 1 – 10 measured using 3 g samples by the cup geometry between T_{2L} (at maximum %fluid H) and rheological parameters: η (a – top left), G' (b – top right), G" (c – middle left), log(η*) (d – middle right), log(G') (e – bottom left) and log(G") (f – bottom right).*

Table E1: Correlations between rheological parameters G', G" and η measured with the Cup geometry using 3 g samples with %fluid hydrogen and T_{2L} for coals 1 – 10*

	%Fluid H	T_{2L}
G'	0.73	0.49
G"	0.71	0.57
η*	0.76	0.55
Log(G')	0.72	0.35
Log(G")	0.87	0.54
Log(η*)	0.84	0.49

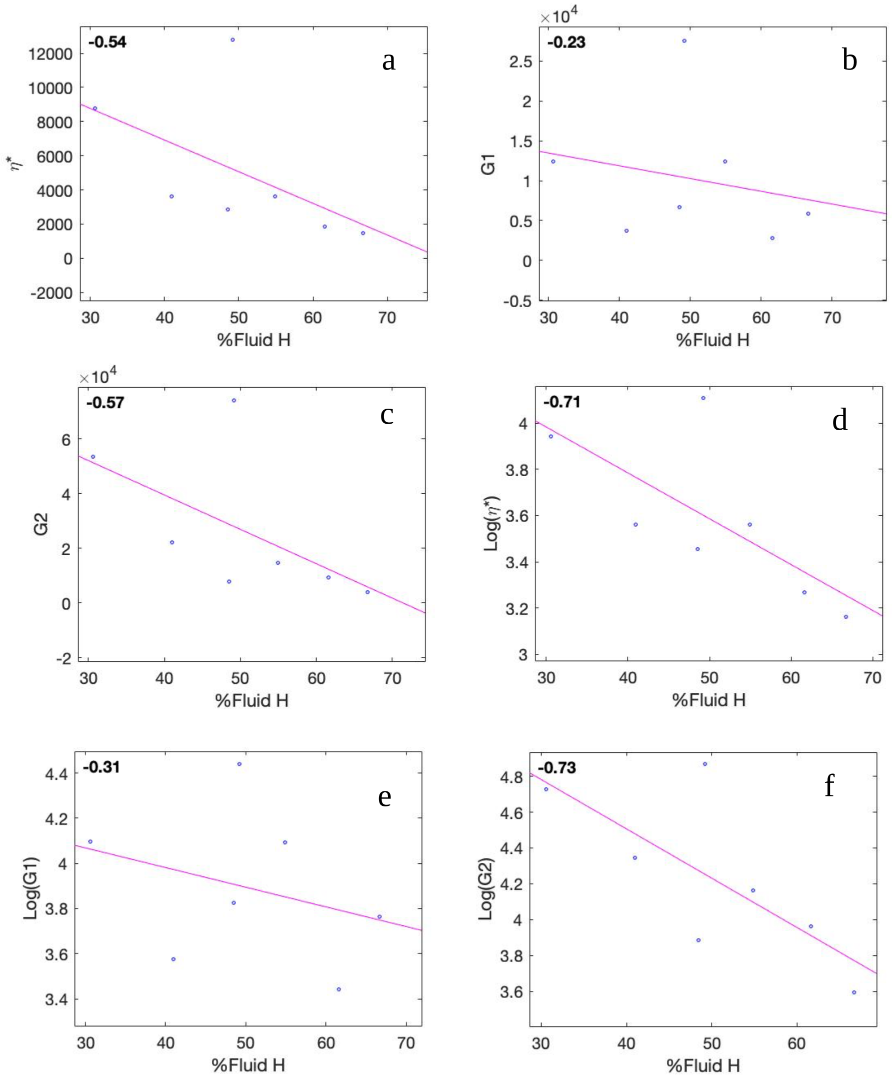

Figure E3: Correlations for coals 4 – 10 measured using 3 g samples by the cup geometry between maximum %fluid hydrogen and rheological parameters: η (a – top left), G' (b – top right), G" (c – middle left), log(η*) (d – middle right), log(G') (e – bottom left) and log(G") (f – bottom right).*

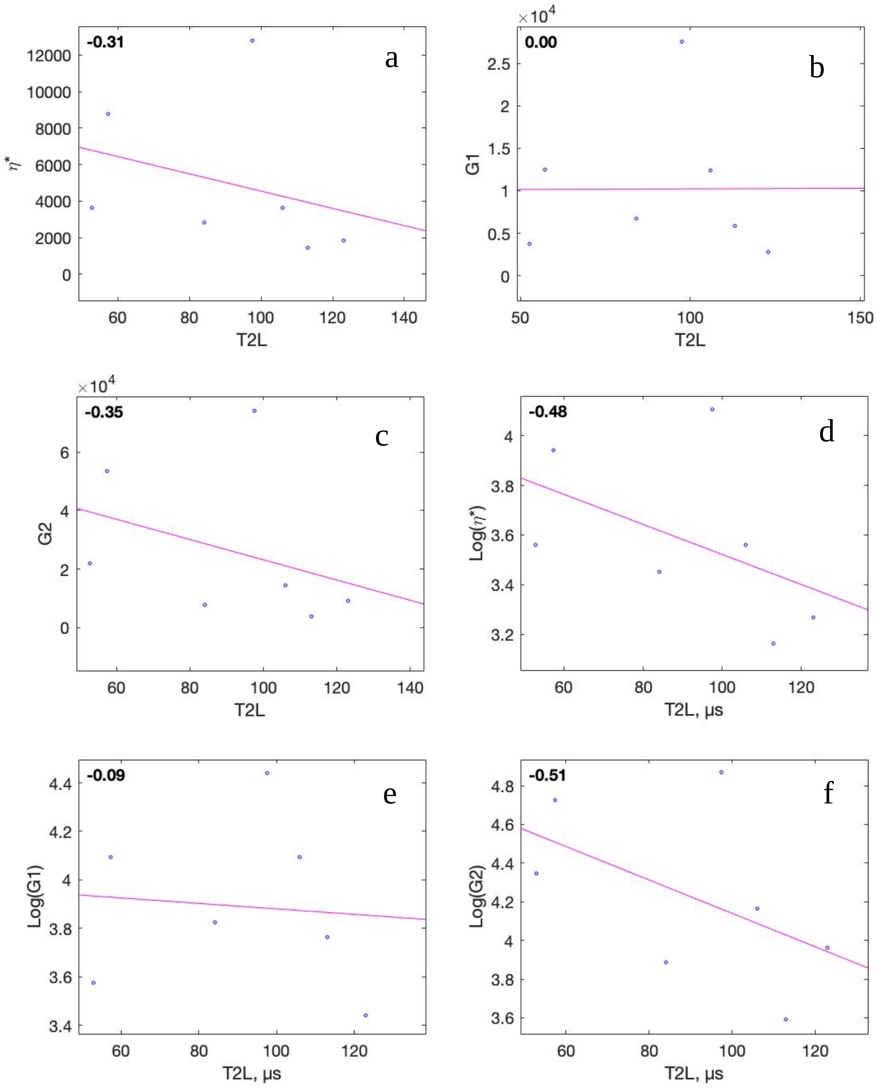

Figure E4: Correlations for coals 4 – 10 measured using 3 g samples by the cup geometry between T_{2L} (at maximum %fluid H) and rheological parameters: η (a – top left), G' (b – top right), G'' (c – middle left), log(η*) (d – middle right), log(G') (e – bottom left) and log(G'') (f – bottom right).*

Table E2: Correlations between rheological parameters G', G'' and η measured with the Cup geometry using 3 g samples with %fluid hydrogen and T_{2L} for coals 4 – 10*

	%Fluid H	T_{2L}
G'	0.23	0.00
G''	0.57	0.35
η*	0.54	0.31
Log(G')	0.31	0.09
Log(G'')	0.73	0.51
Log(η*)	0.71	0.48

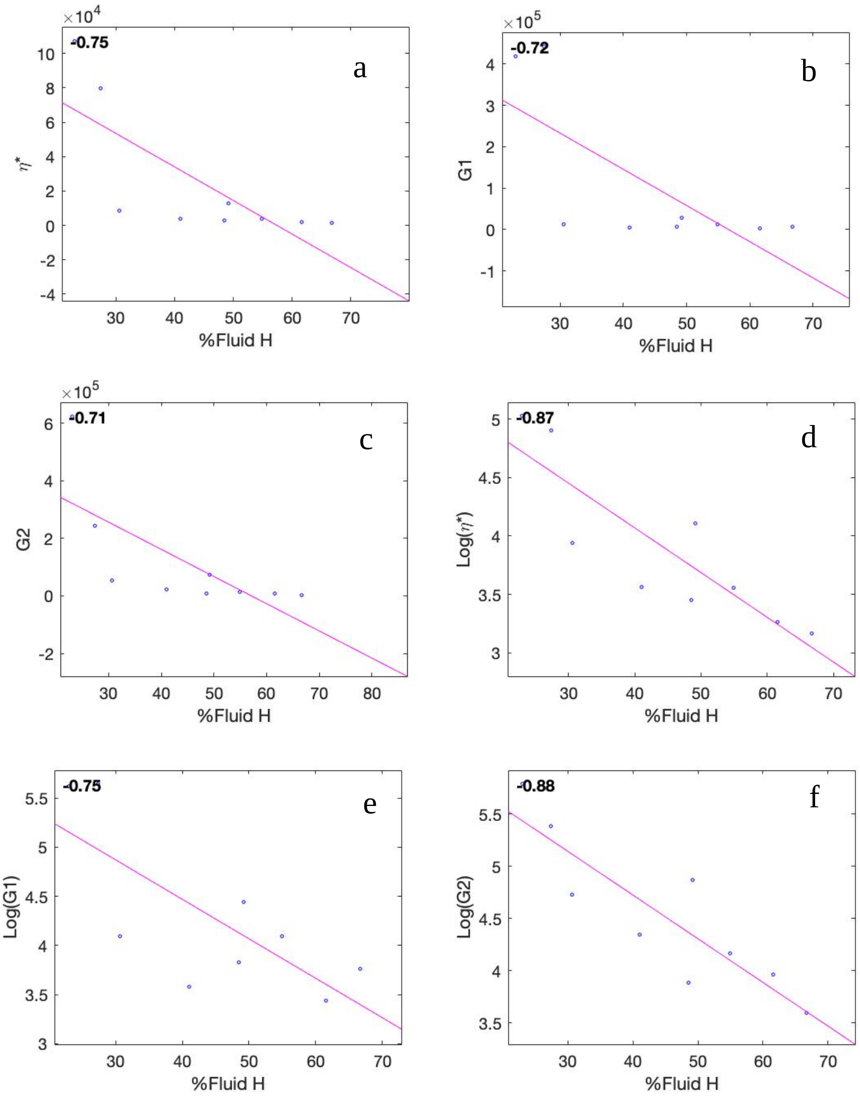

Figure E5: Correlations for coals 1 – 2 and 4 – 10 measured using 3 g samples by the cup geometry between maximum %fluid hydrogen and rheological parameters: η (a – top left), G' (b – top right), G" (c – middle left), log(η*) (d – middle right), log(G') (e – bottom left) and log(G") (f – bottom right).*

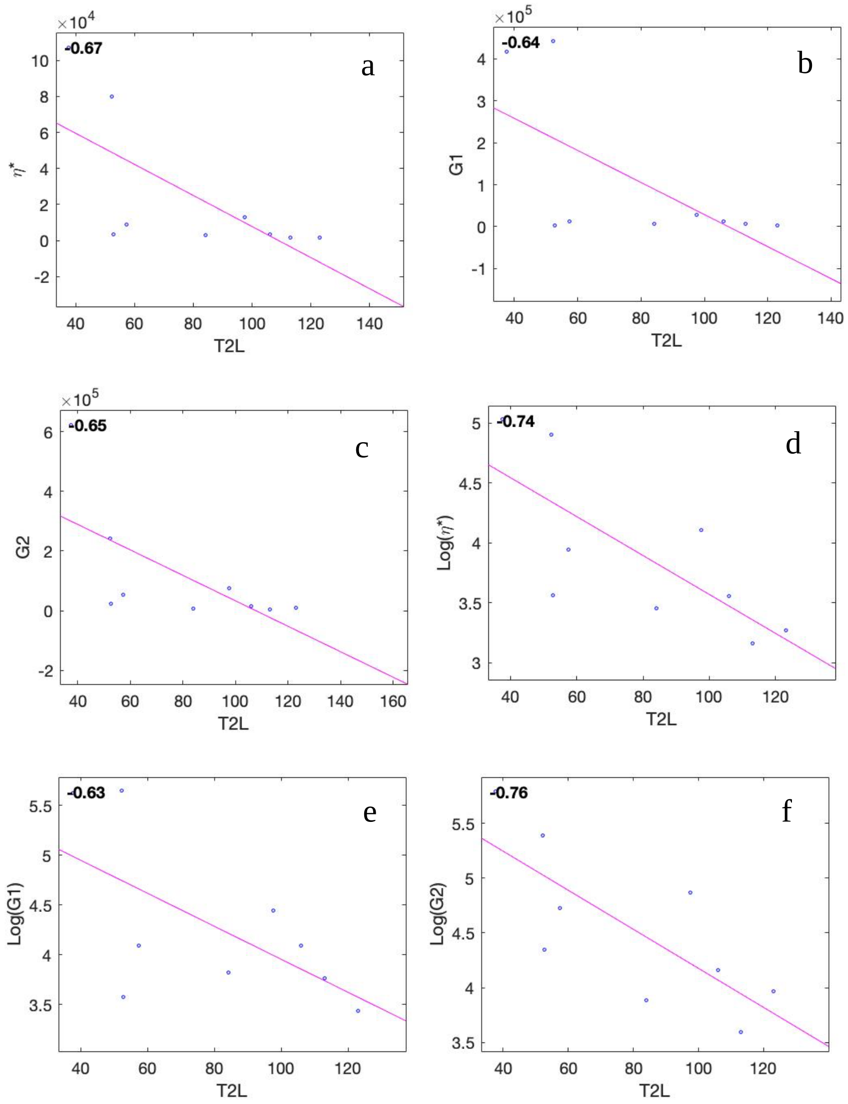

Figure E6: Correlations for coals 1 – 2 and 4 – 10 measured using 3 g samples by the cup geometry between T_{2L} (at maximum %fluid H) and rheological parameters: η (a – top left), G' (b – top right), G" (c – middle left), log(η*) (d – middle right), log(G') (e – bottom left) and log(G") (f – bottom right).*

Table E3: Correlations between rheological parameters G', G" and η measured with the Cup geometry using 3 g samples with %fluid hydrogen and T_{2L} for coals 1 – 2, 4 – 10 (excluding coal 3)*

	%Fluid H	T_{2L}
G'	0.72	0.64
G"	0.71	0.65
η*	0.75	0.67
Log(G')	0.75	0.63
Log(G")	0.88	0.76
Log(η*)	0.87	0.74

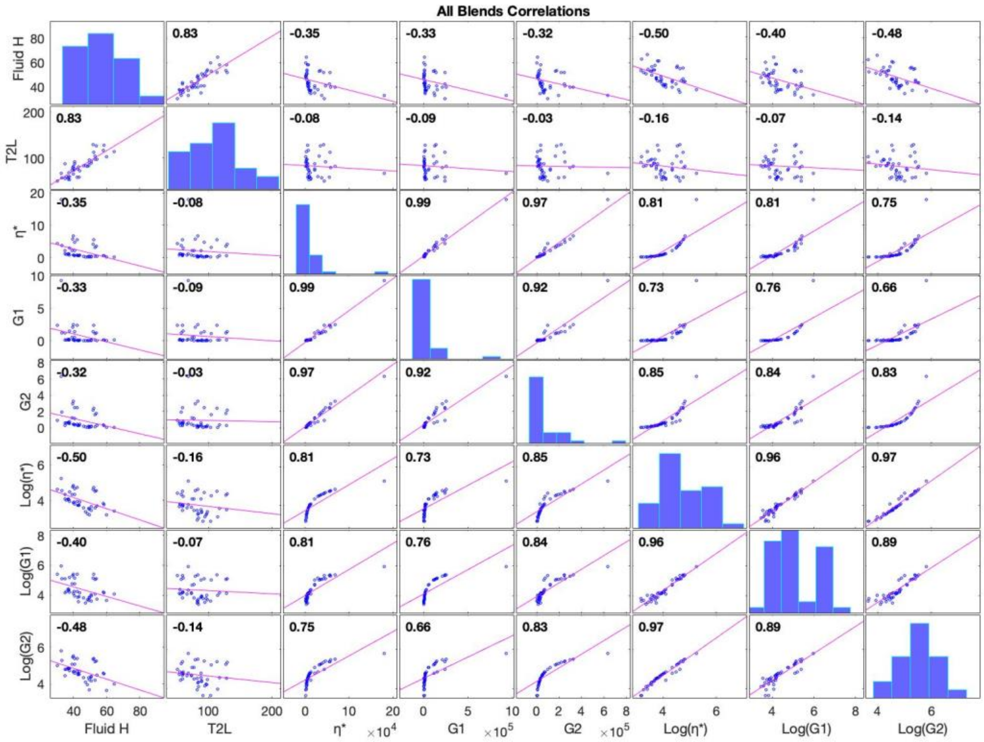

Figure E7: Matrix detailing correlations between maximum %fluid hydrogen, T_{2L} (at maximum %fluid H), η^*_{min}, minimum G', minimum G", log(η^*_{min}), log(G'), log(G") for all coal blends measured with 3 g samples in the cup geometry

Table E4: Correlations between rheological parameters G', G" and η measured with the Cup geometry using 3 g samples with %fluid hydrogen and T_{2L} for all blends*

	%Fluid Hydrogen	T_{2L}
G'	0.33	0.09
G"	0.32	0.03
η*	0.35	0.08
Log(G')	0.40	0.07
Log(G")	0.48	0.14
Log(η*)	0.50	0.16

N.B. %Fluid hydrogen vs T_{2L} correlation afforded R^2 value of 0.83

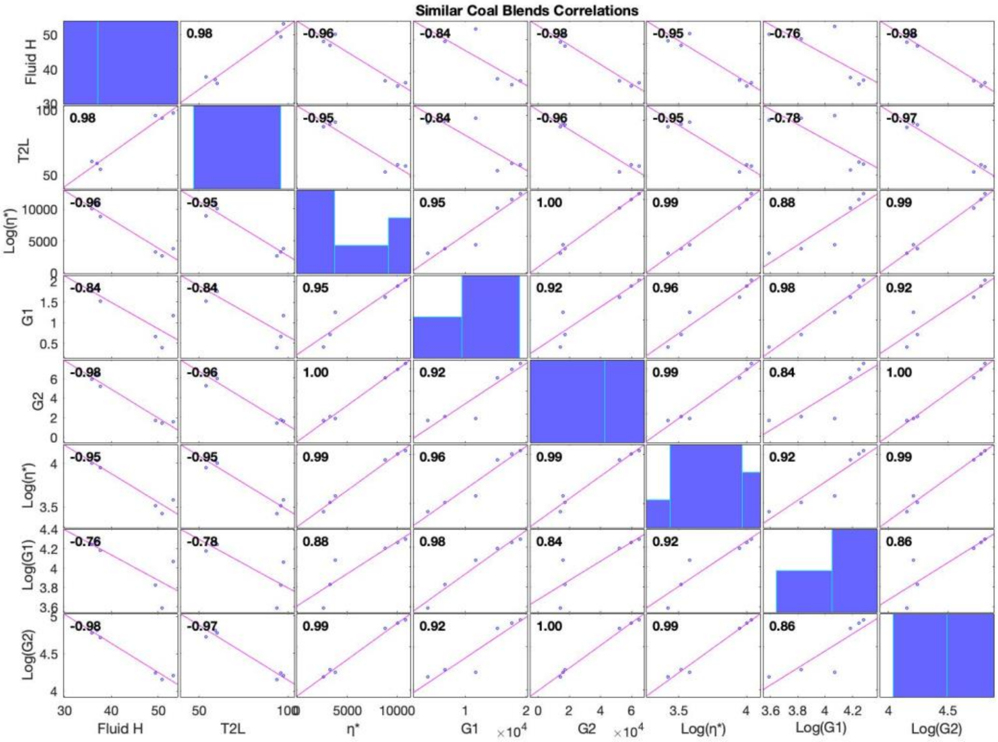

Figure E8: Matrix detailing correlations between maximum %fluid hydrogen, T_{2L} (at maximum %fluid H), η^*_{min}, minimum G', minimum G'', log(η^*_{min}), log(G'), log(G'') for similar coal blends measured using 3 g samples in the cup geometry

Table E5: Correlations between rheological parameters G', G'' and η measured with the Cup geometry using 3 g samples with %fluid hydrogen and T_{2L} for similar coal blends*

	%Fluid Hydrogen	T_{2L}
G'	0.84	0.84
G''	0.98	0.96
η*	0.96	0.95
Log(G')	0.76	0.78
Log(G'')	0.98	0.97
Log(η*)	0.95	0.95

N.B. %Fluid hydrogen vs T_{2L} correlation afforded R^2 value of 0.98

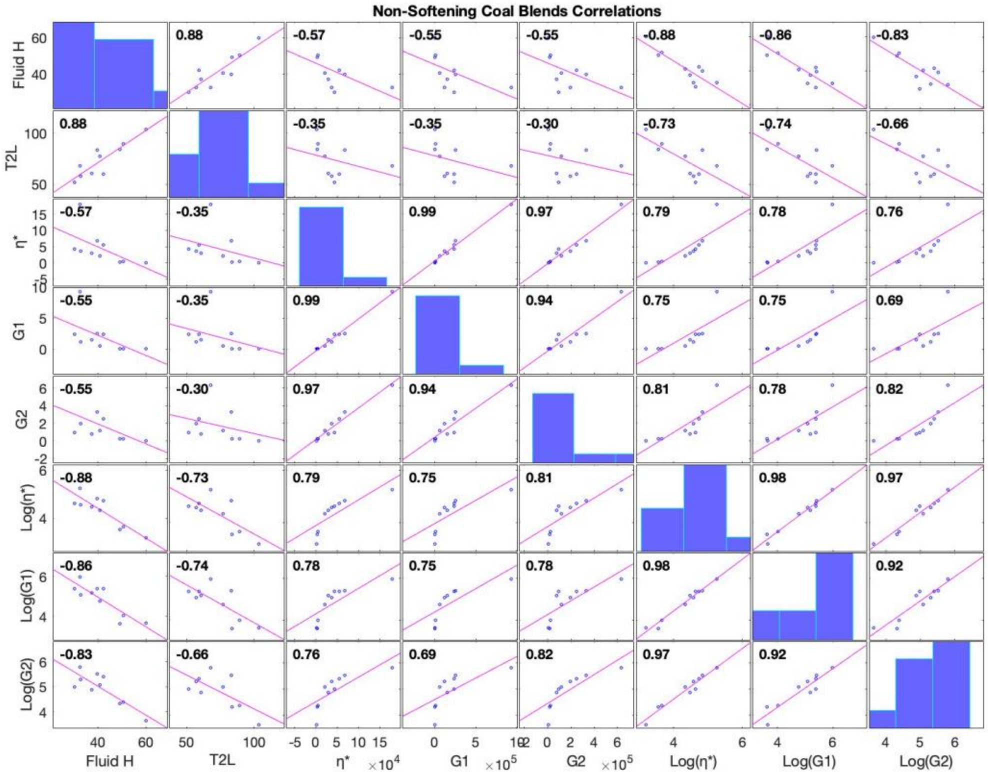

Figure E9: Matrix detailing correlations between maximum %fluid hydrogen, T_{2L} (at maximum %fluid H), η^*_{min}, minimum G', minimum G", $\log(\eta^*_{min})$, log(G'), log(G") for non-softening coal blends measured using 3 g samples in the cup geometry

Table E6: Correlations between rheological parameters G', G" and η measured with the Cup geometry using 3 g samples with %fluid hydrogen and T_{2L} for non-softening coal blends*

	%Fluid Hydrogen	T_{2L}
G'	0.55	0.35
G"	0.55	0.30
η*	0.57	0.35
Log(G')	0.86	0.74
Log(G")	0.83	0.66
Log(η*)	0.88	0.73

N.B. %Fluid hydrogen vs T_{2L} correlation afforded R^2 value of 0.88

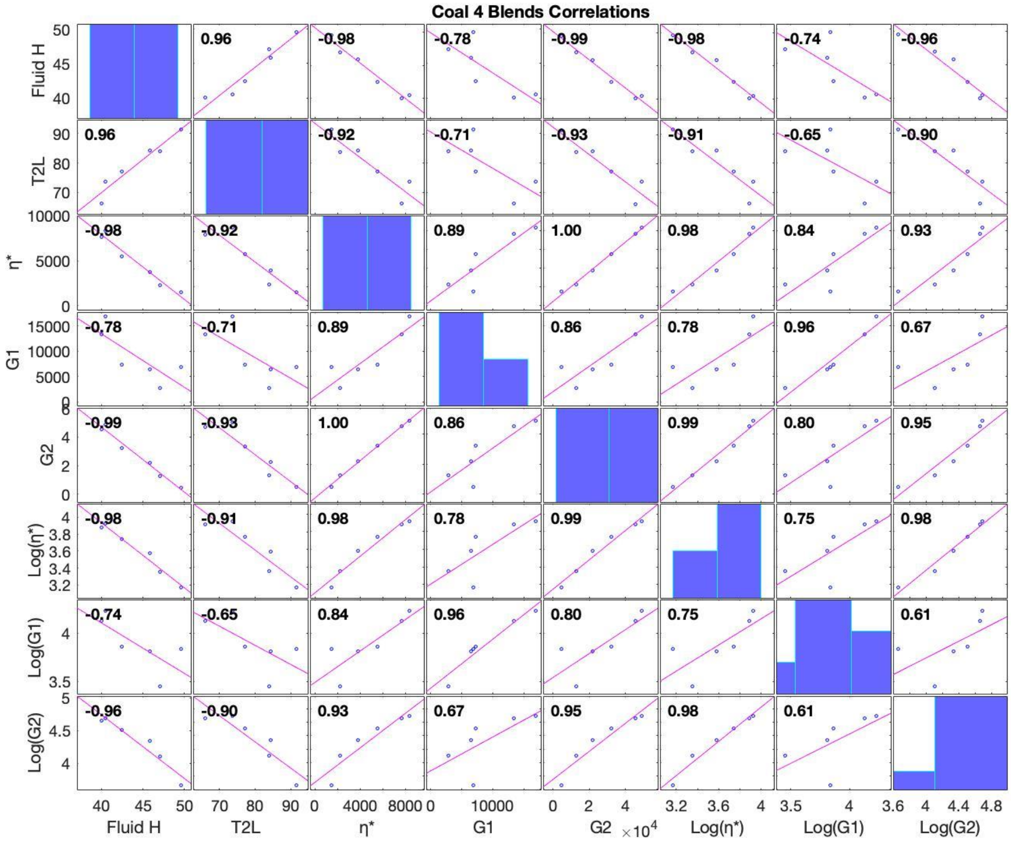

Figure E10: Matrix detailing correlations between maximum %fluid hydrogen, T_{2L} (at maximum %fluid H), η^*_{min}, minimum G', minimum G'', log(η^*_{min}), log(G'), log(G'') for coal 4 blends measured using 3 g samples in the cup geometry

Table E7: Correlations between rheological parameters G', G'' and η measured with the Cup geometry using 3 g samples with %fluid hydrogen and T_{2L} for coal 4 blends*

	%Fluid H	T_{2L}
G'	0.78	0.71
G''	0.99	0.93
η*	0.98	0.92
Log(G')	0.74	0.65
Log(G'')	0.96	0.90
Log(η*)	0.98	0.91

N.B. %Fluid hydrogen vs T_{2L} correlation afforded R^2 value of 0.96

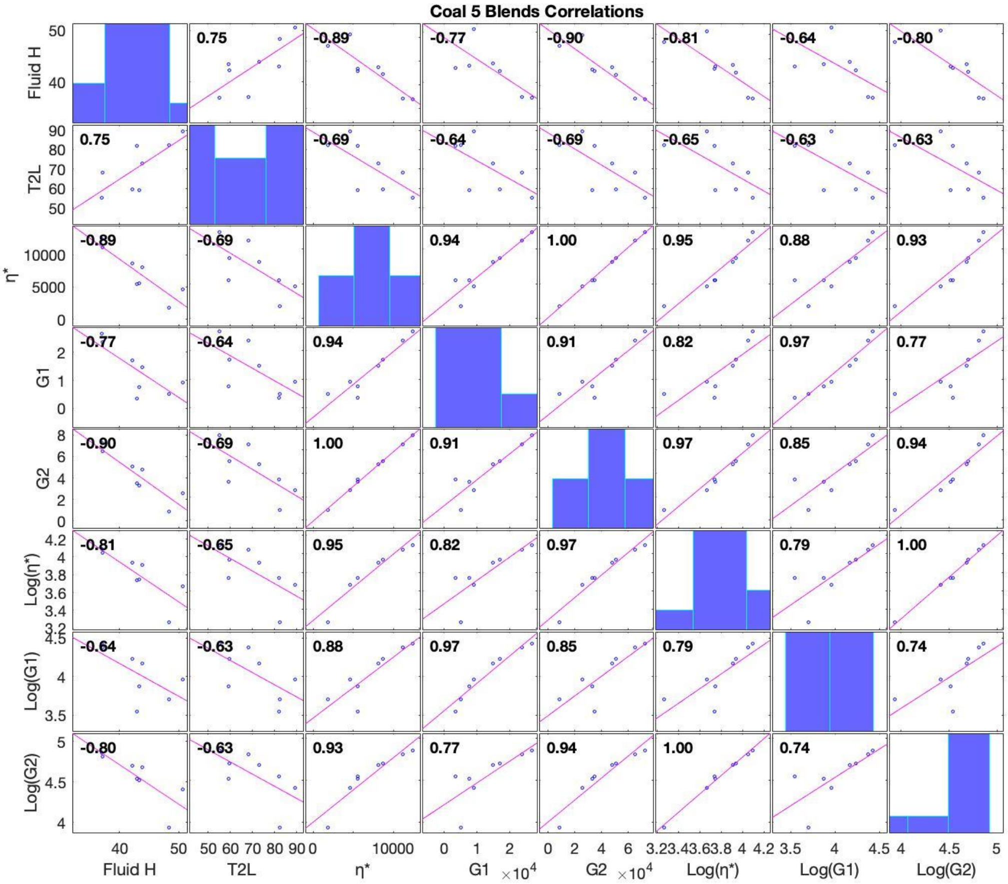

Figure E11: Matrix detailing correlations between maximum %fluid hydrogen, T_{2L} (at maximum %fluid H), η^*_{min}, minimum G’, minimum G”, log(η^*_{min}), log(G’), log(G”) for coal 5 blends measured using 3 g samples in the cup geometry

Table E8: Correlations between rheological parameters G’, G” and η measured with the Cup geometry using 3 g samples with %fluid hydrogen and T_{2L} for coal 5 blends*

	%Fluid H	T_{2L}
G’	0.77	0.64
G”	0.90	0.69
η*	0.89	0.69
Log(G’)	0.64	0.63
Log(G”)	0.81	0.63
Log(η*)	0.80	0.65

N.B. %Fluid hydrogen vs T_{2L} correlation afforded R^2 value of 0.75

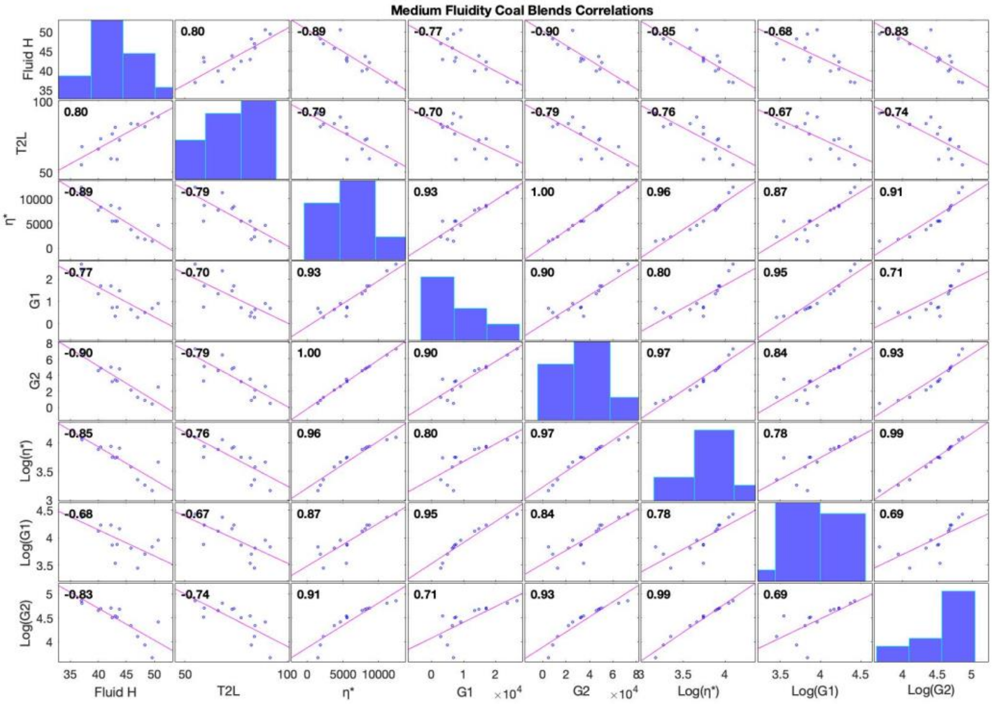

Figure E12: Matrix detailing correlations between maximum %fluid hydrogen, T_{2L} (at maximum %fluid H), η^*_{min}, minimum G’, minimum G”, log(η^*_{min}), log(G’), log(G”) for medium fluidity coal (coals 4 and 5) blends measured using 3 g samples in the cup geometry

Table E9: Correlations between rheological parameters G’, G” and η measured with the Cup geometry using 3 g samples with %fluid hydrogen and T_{2L} for collated medium fluidity coal blends*

	%Fluid H	T_{2L}
G’	*0.77*	*0.70*
G”	*0.90*	*0.79*
η*	*0.89*	*0.79*
Log(G’)	*0.68*	*0.67*
Log(G”)	*0.83*	*0.74*
Log(η*)	*0.85*	*0.76*

N.B. %Fluid H vs T_{2L} correlation afforded R^2 value of 0.80

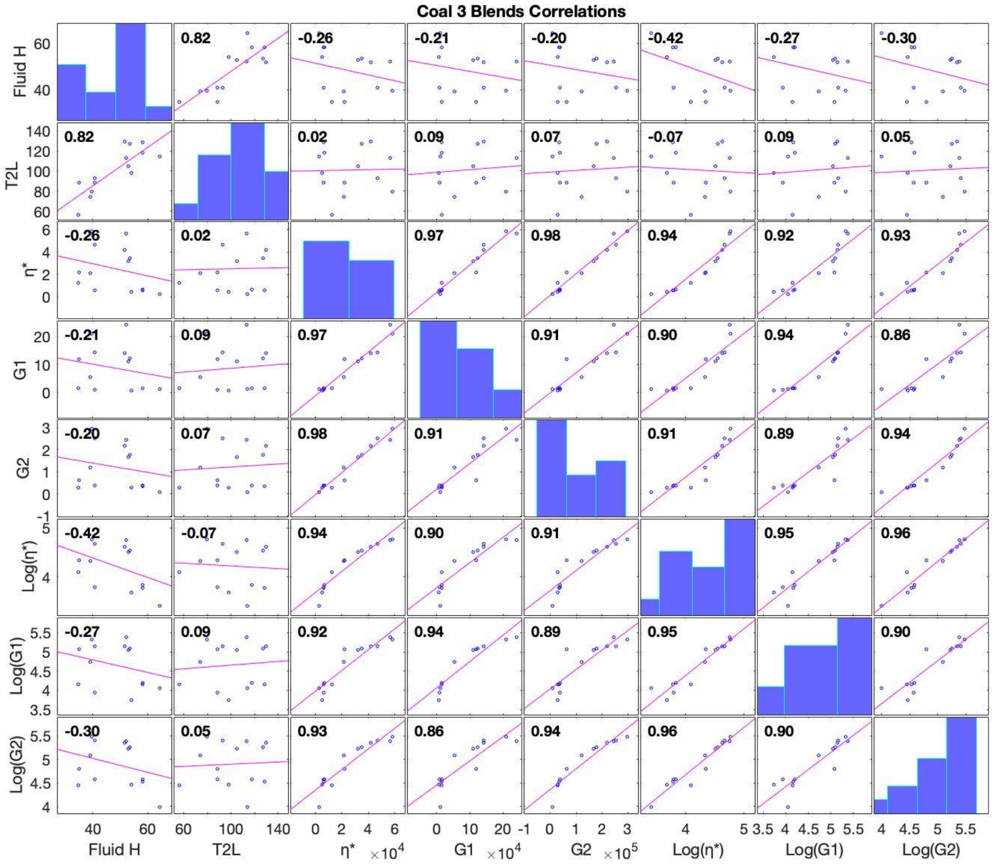

Figure E13: Correlation matrix detailing correlations between maximum %fluid hydrogen, T_{2L} (at maximum %fluid H), η^*_{min}, minimum G', minimum G", log(η^*_{min}), log(G'), log(G") for coal 3 blends measured using 3 g samples in the cup geometry

Table E10: Correlations between rheological parameters G', G" and η measured with the Cup geometry using 3 g samples with %fluid hydrogen and T_{2L} for coal 3 blends*

	%Fluid H	T_{2L}
G'	*0.21*	*0.09*
G"	*0.20*	*0.07*
η*	*0.26*	*0.02*
Log(G')	*0.27*	*0.09*
Log(G")	*0.30*	*0.05*
Log(η*)	*0.42*	*0.07*

N.B. %Fluid H vs T_{2L} correlation afforded R^2 value of 0.82